The Structure, Composition and Evolution of Mercury's Core

Amy Louise Edgington

A dissertation submitted in partial fulfillment

of the requirements for the degree of

Doctor of Philosophy

of

University College London.

Department of Earth Sciences

UCL

December, 2016

I, Amy Louise Edgington, confirm that the work presented in this thesis is my own. Where information has been derived from other sources, I confirm that this has been indicated in the thesis.

Abstract

This thesis presents the results of *ab initio* molecular dynamics calculations of the adiabatic gradient of pure liquid iron and a liquid Fe-S-Si mixture with the relative atomic percentages, 80:10:10. Laser-heated diamond-anvil-cell experiments have been conducted to measure the liquidus and solidus relationships of $Fe_{0.8}S_{0.1}Si_{0.1}$. First-principles molecular dynamics is combined with thermodynamic integration and free-energy minimisation to simulate the spin transition in pure liquid iron and liquid $Fe_{0.8}S_{0.1}Si_{0.1}$. From the magnetic transition, the equations of state, thermodynamic properties and adiabatic gradients of pure liquid iron and liquid $Fe_{0.8}S_{0.1}Si_{0.1}$ are determined. The calculated adiabatic gradients are used alongside the gradients of published melting curves of iron and the measured liquidus of $Fe_{0.8}S_{0.1}Si_{0.1}$ to provide insight into the crystallisation regime of the core of Mercury. The suggested crystallisation regime of a hypothetical pure iron or $Fe_{0.8}S_{0.1}Si_{0.1}$ Mercurian core depends strongly on the derivative of the melting curve. Results suggest that a $Fe_{0.8}S_{0.1}Si_{0.1}$ core of Mercury may start in a 'top-down' crystallisation regime resulting in a complex core structure with a possible stratified Fe-S layer at the top of the core, which, may in-part explain the observed weak magnetic field of Mercury.

Acknowledgements

This thesis is a testament to the endless support and guidance of my supervisors, Professor Lidunka Vočadlo, Professor Lars Stixrude and Professor Ian Wood. In particular, I must express my sincerest gratitude to Lidunka for her mentorship and encouragement.

I would also like to thank Dr Oliver Lord, Professor David Dobson, Professor John Brodholt and Professor Dario Alfè for their expertise and guidance throughout my studies and Dr Benjamí Martorell, Dr. Eero Holmström and Dr. Alex Lindsay Scott for their helpful advice with running VASP calculations.

I am eternally indebted to my family and friends, it is beyond words to describe my thanks for the encouragement and support they have given me. Lastly, my thanks go to my colleagues at UCL for making my PhD so enjoyable, and to Cherry for her friendship and support throughout.

This PhD was funded by the Science and Technology Facilities Council, and made use of the HECToR and ARCHER UK National Supercomputing Service (http://www.archer.ac.uk). I also wish to acknowledge the use of the UCL Grace High Performance Computing Facility (Grace@UCL), and associated support services, in the completion of this work.

Contents

List of Figures

List of Tables

Chapter 1

Introduction

As one of only five planets that can be seen in the night sky with the naked eye, Mercury's existence has been known since ancient times, yet research is on-going to try and unravel the mysteries associated with the planet. Littered with craters, and lying 50 million kilometres from the Sun, with an equatorial radius of 2439.7 km, Mercury is the smallest terrestrial planet in the solar system (Figure 1.1). Although relatively small, it is one of the densest planets, which suggests the planet is composed of a very high metal to silicate ratio, whilst also maintaining a highly surprising magnetic field. Mercury is the closest planet to the Sun, but the Mercurian day is very long. The planet is locked into a 3:2 spin orbit resonance, i.e. only three sidereal days will pass for every two orbits around the Sun (Mercury's day lasts 58 days, 15 hours on Earth, but the planet's year only lasts 88 Earth days).

From both ground based and orbital measurements, much has been learnt about the properties of Mercury, including the existence of its magnetic field, gravitational properties and surface composition. Comparatively less is known about the state of the planet's deep interior. Unlike Earth, where seismology can be used to directly investigate the state of the Earth's core, the study of Mercury's core is enabled only by surface expressions of the interior dynamics and modelling of core evolution and composition. As the smallest, innermost and one of the densest planets, Mercury resides in an end-member position, and hence, a better understanding of the Mercurian core may give greater insight in the generation of planetary magnetic fields in general, as well as the evolution of the terrestrial planets and the environment from which they formed. The aim of this study is to investigate the internal composition, evolution and structure of the planet Mercury. This will be achieved through

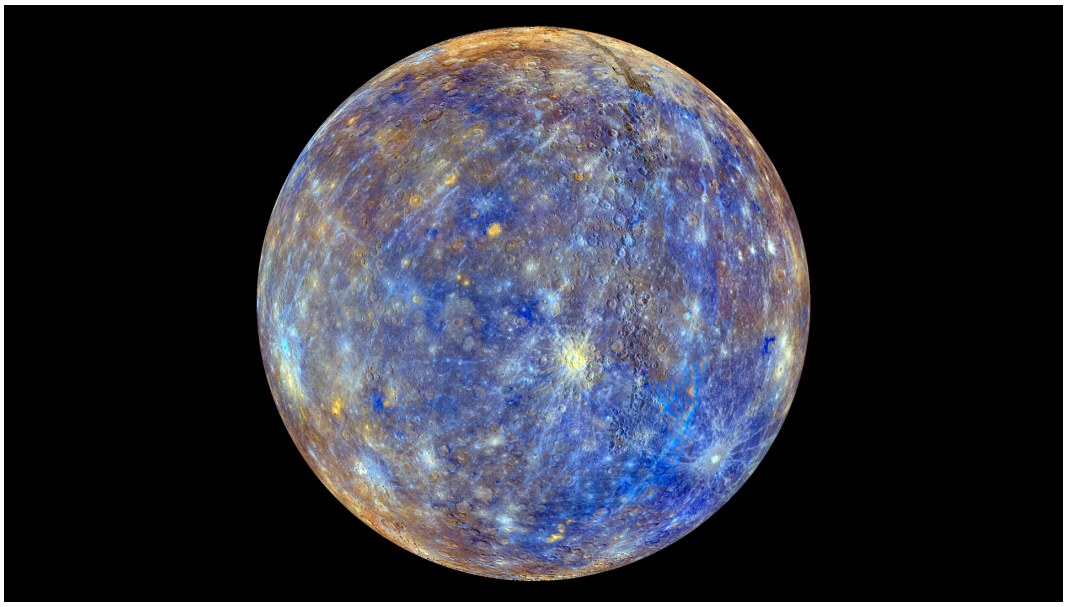

Figure 1.1: Mercury is the innermost planet in the solar system and is littered with craters from bombardment over its lifetime. This image is produced using images from the color base map imaging campaign during MESSENGER's mission. This is not the true colour of Mercury, the colours are used to highlight the chemical, mineralogical, and physical changes across the planet's surface. Image credit: NASA/Johns Hopkins University Applied Physics Laboratory/Carnegie Institution of Washington (2013).

the study of the physical properties of candidate materials likely to be present in the core, which will lead to an evolutionary model. In this chapter, the motivation for this work will be put forward, along with a detailed account of what is currently known.

1.1 Missions to Mercury

As of spring 2016, Mercury is the subject of two past NASA missions, Mariner 10 in 1974 (Figure 1.2) and the MErcury Surface, Space ENvironoment, GEochemisty and Ranging spacecraft, MESSENGER (Figure 1.2) which arrived over 30 years later in 2011. During its year-long stay, Mariner 10 performed three flybys, imaging half of the planet's heavily cratered surface, and revealed some intriguing properties of the planet, such as the presence of a magnetic field.

MESSENGER was the first spacecraft to orbit the innermost planet, and during its four year mission, which ended with its planned impact into the planet surface in April 2015,

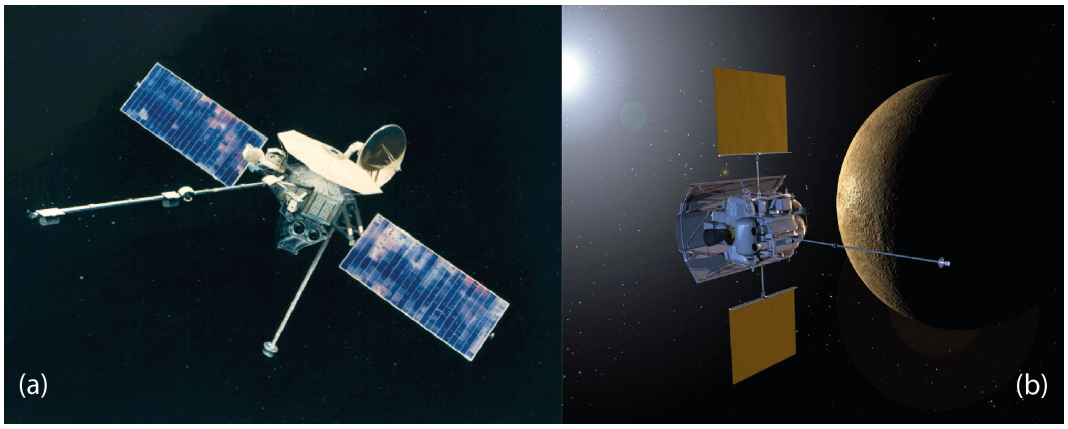

Figure 1.2: (a) The NASA Mariner 10 spacecraft, Mariner 10 performed three flybys of Mercury. (b) The MESSENGER spacecraft. Figure adapted from Mariner 10 and MESSENGER images from NASA (2016) and NASA (2014) respectively.

it mapped 100% of the planet's surface, characterised the planet's magnetic field (Section 1.2.4) and discovered water ice at Mercury's north pole. MESSENGER also mapped Mercury's gravity which revealed the planet's crustal thickness and provided insight into the internal structure of Mercury. The gravity field revealed a thicker crust at low latitudes of the planet's northern hemisphere, and thinner crustal thickness towards the poles (Smith et al., 2012). This was also accompanied by crustal thinning below some impact basins (Smith et al., 2012). The low-degree gravity field could also be used alongside Mercury's spin parameters to calculate the planet's moment of inertia and reveal the density distribution within the planet (Section 1.2.2). MESSENGER also found that Mercury is abundant in volatile elements that evaporate at moderately high temperatures, which then rule out some formation models for the solar system (Section 1.3.1). These missions will be followed by BepiColombo, an ESA mission to study Mercury in collaboration with JAXA, currently due for launch in 2017.

1.2 The State of Mercury's Core

1.2.1 Mercury's Density and Large Metallic Core

Before the arrival of Mariner 10 the known properties of Mercury were few and limited in their accuracy. The small size and proximity of the planet in relation to the Sun (it is never more than 28° away from the Sun in the sky) mean that ground based observations

are limited to the daytime, or at twilight. Mercury's mean density is 5430 ± 10 kgm^{-3} (Anderson et al., 1987), comparable to the Earth's whose mean density is approximately 5500 kgm^{-3}, however, Mercury is only a third of the size of the Earth. In terms of uncompressed density (the density a planet would have if it was not compressed, but still at high enough pressure to squeeze out all pore spaces; Kaula, 1986), Mercury's density is 5300 kgm^{-3} far exceeding that of Earth, which is only $\sim$ 4030 kgm^{-3} (Taylor and Scott, 2003; Strom and Sprague, 2003). The uncompressed density of Mercury combined with its small size suggests a planet highly enriched in metallic iron. This could mean that Mercury contains twice as much iron in its interior than any other planetary body in the solar system, and that Mercury consists of a core measuring 75% of the total radius of the planet and 42% of its volume (if the heavy metals are concentrated in its core; Strom and Sprague, 2003; Figure 1.3).

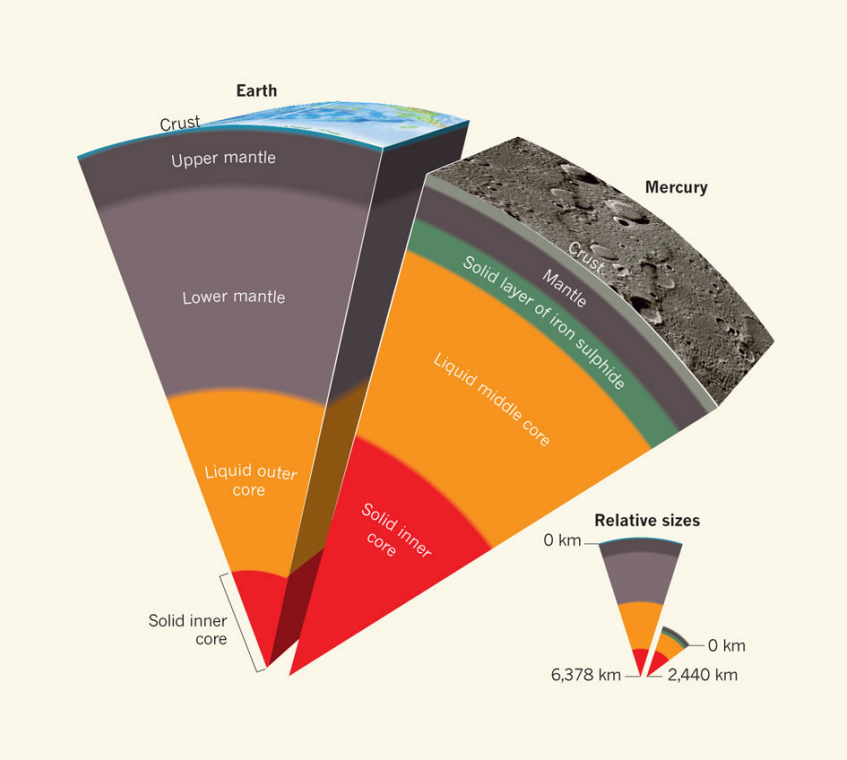

Figure 1.3: The comparison of core sizes between the Earth and the planet Mercury. The core of Mercury is suggested to fill $\sim$ 75 % of the planets radius, whereas the Earth's core is closer to 50 %. Reprinted by permission from Macmillan Publishers Ltd: Nature, (Stevenson, 2012), Copyright 2012.

1.2.2 Liquid Interior

One of the great mysteries associated with Mercury is the state and extent of its large core. Mariner 10 discovered the presence of Mercury's magnetic field, which, if of dynamo origin, would require at least a liquid layer in the planet's core. Peale (1976) described a method of determining the state of Mercury's core using the planet's forced physical libration. The source of the forced physical libration is a combination of Mercury's 3:2 orbit resonance and its non-spherical shape and eccentric orbit. These result in a periodic reversal of torques on the planetary body as it rotates relative to the Sun producing small changes in its spin rate, i.e. the length of day, from its resonant value (of 3/2 times the orbital frequency). It is the amplitude of the oscillations produced that are called the forced librations (Margot et al., 2007). The combination of the amplitude of the forced physical libration, alongside the second degree gravity field and obliquity can then be used to reveal the presence of a liquid outer core (more detail can be found in Margot et al., 2007). Ground based observations of the rotation of Mercury made by Margot et al. (2007) in combination with gravitational harmonic coefficients, determined by Mariner 10, revealed a molten core decoupled from the planet's mantle. However the errors associated with the Mariner 10 measurement of the gravitational harmonic coefficient C_{22} made the further determination of the size of the core impossible until the arrival of MESSENGER. The shape and size of Mercury's core could be found from an accurate knowledge of the planet's moment of inertia, MoI. For a uniform sphere of radius R and mass M, the ratio of the MoI, to the quantity MR^2 is 0.4; for the Earth this ratio is 0.3307, indicating that some of the density is gathered at the centre of the sphere, i.e. in the Earth's core. Margot et al. (2012) determined the MoI for Mercury, and made estimates of the planet's obliquity and libration amplitude, which have been confirmed by MESSENGER data (Stark et al., 2015). Margot et al. (2012) combined estimates of the obliquity and libration amplitude with the gravitational harmonics measured by MESSENGER (Smith et al., 2012) and precession rate and orbital inclination determined by Yseboodt and Margot (2006) and calculated the ratio of the MoI to the quantity MR^2 of Mercury's outer shell to be 0.149 +/- 0.006 and polar MoI ratio of 0.346 +/- 0.014 (Margot et al., 2012). Margot et al. (2012) used the MoIs of the relative components of Mercury in a two layer model, assuming a core and mantle, each of uniform density. They estimated a core radius for Mercury of 1998 km (82% of the planetary radius), a mean core density equal to 7254 kg/m^3 and mean mantle density of 3203 kg/m^3 (Margot et al., 2012). More

complicated models of Mercury's interior structure have been investigated by Hauck et al. (2007, 2013), described in Section 1.3.2.

1.2.3 Surface Expressions of the Core

The state of Mercury's core has implications for the planet's surface, influencing many features ranging from its composition to the creation of dramatic scarps and ridges on its surface. The size and extent of ridges on the planet's surface such as lobate scarps (Figure 1.4) can indicate the amount of cooling that the planet has undergone, as well as the solidification of a core and are therefore important constraints on the thermal history models for Mercury (Solomon, 1976, 1977; Schubert et al., 1988). Images from Mariner 10 revealed long striations across Mercury's surface and subsequent estimates of the decrease in radius of the planet on cooling ranged from $<$ 1 km to $\sim$ 2 km (Watters et al., 1998; Strom et al., 1975). Cooling and complete solidification of an initially liquid iron core would result in a $\sim$ 17 km decrease in radius (Solomon, 1976).

MESSENGER (Figure 1.2), the successor of Mariner 10, mapped 100% of the planet's surface, in comparison with the 45% mapped previously. MESSENGER imaged previously unobserved surface features and large lobate scarps, which resulted in revised estimates of radial decrease between 2.4 - 3.6 km (Di Achille et al., 2012). Even with this larger estimate of planetary contraction, it is far smaller than the planetary contraction predicted by a range of thermal evolution models, which suggested a decrease in radius of $\sim$ 4 - 10 km during long-term planetary cooling (e.g. Solomon, 1977; Schubert et al., 1988; Grott et al., 2011) or possibly up to 15 km (Van Hoolst and Jacobs, 2003). This discrepancy was partly resolved by Byrne et al. (2014), which included a greater number, and variety, of surface features, which suggested that the planet had contracted radially by up to 7 km (Byrne et al., 2014).

The planetary contraction indicated by Mercury's surface agrees with the observation of a liquid layer within the planet, but if the core of Mercury consisted of pure iron, the core would have completely solidified by the present day (e.g. Solomon, 1976, core temperature 2100 K). To reconcile the presence of a liquid layer with the high bulk density of the planet suggests that the core includes light elements. Light elements such as sulphur have been strongly favoured as they can dramatically reduce the melting temperature of iron (more

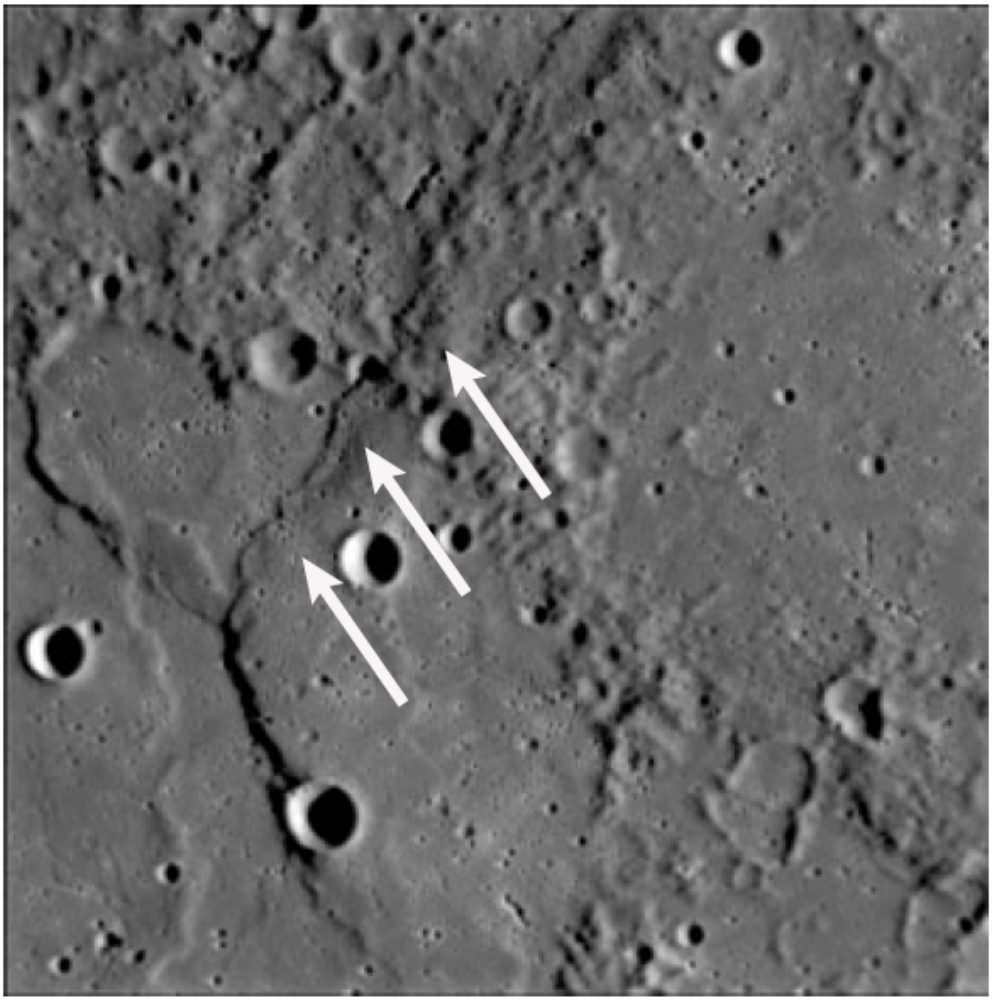

Figure 1.4: Picture taken by the Narrow Angle camera (NAC), part of the Mercury Dual Imaging System (MDIS) instrument, taken during a close flyby of Mercury by the MESSENGER spacecraft on January, 14 2008. A portion of a large crater can be seen in the lower left corner of the image. The "Y" shaped ridges which transect the crater floor and rim, of which the top right arm appears to be a classic "lobate scarp" (indicated by white arrows). Image adapted from an image by NASA/Johns Hopkins University Applied Physics Laboratory/Carnegie Institution of Washington (2008).

details in Section 1.3.2), thereby possibly enabling part of the core to remain molten to the present day. The surface composition of Mercury can place additional constraints on the composition of Mercury's core. MESSENGER X-ray spectroscopy (XRS) has determined an upper bound on the average surface abundance of Fe to be ~ 4 weight percent (Nittler et al., 2011) which suggests that iron has segregated into the core. MESSENGER also found a high sulphur content on the surface, in the form of Mg/Ca-rich sulfides, which are only stable under reduced conditions (Nittler et al., 2011). If Mercury formed in such highly reduced conditions, silicon more readily dissolves into iron, suggesting substantial amounts of Si as well as S in the core (Malavergne et al., 2010). Like the Earth, which may contain multiple light elements, it is also possible that other light elements not considered here may be present in the core of Mercury such as H and C.

1.2.4 Magnetic Field

Mariner 10 discovered a permanent magnetic field present at Mercury much weaker than Earth's with a field strength of 350 nT at the equator (Ness et al., 1974; Breuer et al., 2007). The limited data from Mariner 10 did not allow for a full characterisation of the field and its geometry, but did indicate a substantial dipole component nearly aligned with the rotation axis (Ness, 1979; Connerney and Ness, 1988) and the field was found to be sufficient to undergo similar behaviour to the Earth's geomagnetic field, with evidence indicating a bow-shock, magneto-sheath and magnetosphere (Strom, 1979; Figure 1.5). The arrival of MESSENGER has permitted a greater understanding of the planet's magnetic field, indicating a dipole field offset from the spin axis by 0.8° (Anderson et al., 2012) and a dipole moment of ~ 190 nT-R_M^3 (which is calculated from the surface field strength and falls with the radius cubed, R_M is the radius of Mercury; Anderson et al., 2011, 2012).

Three hypotheses arise for the origin of Mercury's magnetic field; remnant magnetisation (e.g. Stephenson, 1976), a thermoelectric origin (Stevenson, 1987), or an active core dynamo (Ness et al., 1975). The strength of Mercury's field was measured to be 20 times larger than the interplanetary field of the solar system, which led Ness et al. (1974) to postulate that the magnetic field was due to some induction process at the surface, but is only 1/100 the size of the Earth's which Stevenson (1987) explained using a magnetic field driven by thermoelectric currents which result from temperature differences at the core-mantle boundary. A dynamo origin similar to that of the Earth's would place important constraints on the ther-

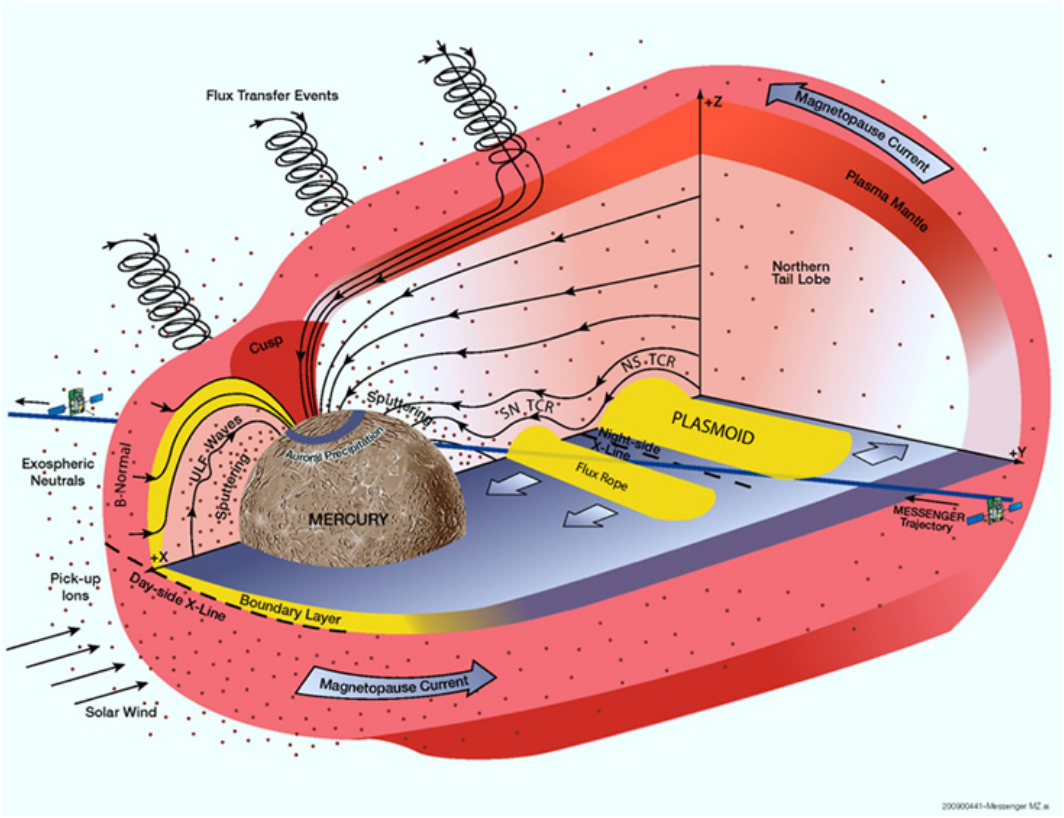

Figure 1.5: Mariner 10 discovered a permanent magnetic field surrounding the planet Mercury. Limited data from Mariner meant that full characterisation of this field would not be possible until the arrival of MESSENGER. Image credit: NASA/JPL (2013).

mal state and structure of the planet. A dynamo driven field requires a rotating convecting fluid, requiring part of the core to be molten. Post-Mariner 10 analysis of the surface properties of Mercury and the detection of a liquid layer in the planet seemed to back this option. However, some models have shed doubt that the magnetic field of Mercury is generated in a similar way to an Earth like dynamo, since a similar mechanism to the Earth would produce magnetic field strengths much larger than those observed (Vilim et al., 2010). Hence, other methods of explaining the weak observed magnetic field have been suggested (Vilim et al., 2010), including a deep dynamo in Mercury's interior (Christensen, 2006). Modelling by Christensen (2006) suggests a multiple layer model of the core of Mercury, with a stable sub-adiabatic layer at the top of core and a dynamo driven at depth within the planet by thermo-compositional convection resulting from the crystallisation of a solid inner core and the expulsion of sulphur. The strong field generated deep within the planet diffuses through the conducting stratified layer at the top of the core. In comparison wth convection, which is

a very efficient source of heat transfer and thus strong source of the magnetic field, conduction is relatively less efficient and will reduce the measured field strength of the magnetic field and therefore a stable conducting layer at the top of Mercury's core could explain the weak observed magnetic field of Mercury. Since the arrival of MESSENGER, a study by Cao et al. (2014) has been able to explain the quasi-stationary magnetic field of Mercury using uniformly distributed buoyancy sources within the liquid core. Sources of this type places constraints on core size, favouring a smaller inner core (Cao et al., 2014). Recent measurements of remnant magnetisation of Mercury's crust (from altitudes below 150 km) suggest that a dynamo driven magnetic field may have existed from early on in the planet's history, and the magnetisation measured was consistent with possible ancient field strengths similar to that of the Earth's (Johnson et al., 2015).

1.3 The Composition of Mercury's Core

1.3.1 Planetary Formation

Early models of planetary formation by Lewis (1972) suggested that in the region of Mercury's orbit, condensation will have ceased when the temperature reached $\sim$1400 K. At this temperature $CaTiO_3$, metallic Fe, and $MgSiO_3$ would have condensed, resulting in planetary bodies being highly enriched in Ca, Al, Ti and metallic Fe and Ni (Siegfried and Solomon, 1974); consequently, light elements, that may have a drastic effect on the behaviour of iron, such as sulphur, would not have condensed in the primordial solar nebula at the distance of Mercury's orbit. Although the equilibrium condensation models of Lewis (1972) predict only very small amounts of sulphur to be accreted in Mercury's interior, studies such as that of Stevenson et al. (1983) predict that radial mixing of the planet-forming materials within the primordial solar nebula could result in the incorporation of S through the accretion of S-bearing planetesimals (Schubert et al., 1988). Other formation scenarios have also been put forward which may explain the presence of sulphur and light elements in the interior of Mercury, such as a large impact early in its formation that stripped off the mantle layer (Figure 1.6; Harder, 2001).

However, this kind of formation scenario is problematic, as the planet has retained substantial moderately volatile elements such as potassium (Peplowski et al., 2011). An alternative scenario for Mercury's formation is the 'hit and run' model, in which multiple collisions

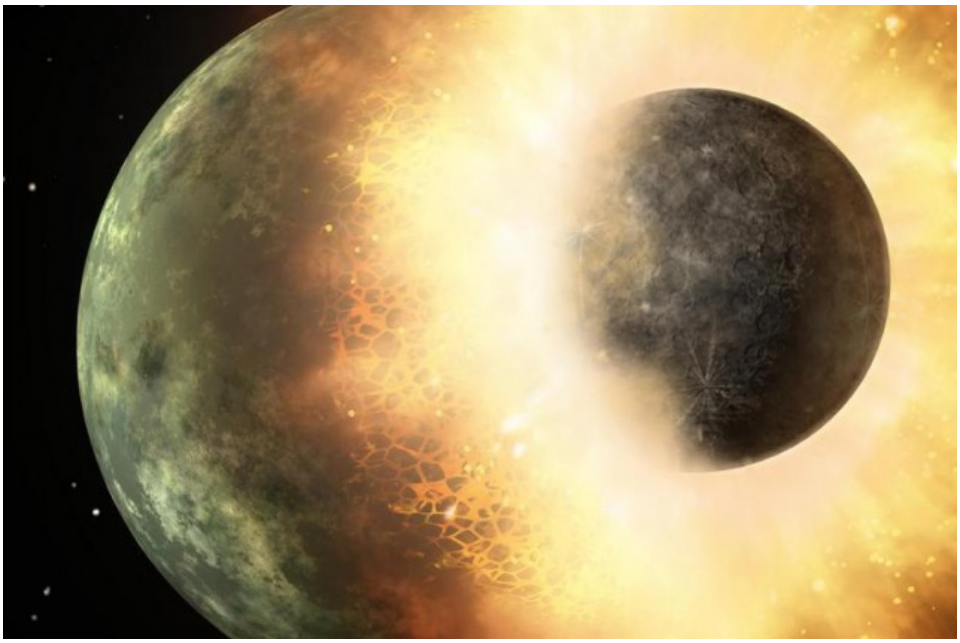

Figure 1.6: One previous theory of the formation of Mercury to explain the planet's high metal to silicate ratio is a giant impactor, however the abundances of potassium, thorium, and uranium on the surface of Mercury measured by the MESSENGER spacecraft may rule out the giant impact models of planetary formation. Image credit NASA/JPL/Caltech (2011).

can result in a Mercury-like planet (Asphaug and Reufer, 2014).

1.3.2 The Role of Sulphur in Mercury's Core

The detection of a liquid layer in Mercury's deep interior (among other features) rules out the existence of a pure iron core in Mercury. Thermochemical arguments suggest that if this was the case, the core of Mercury would be completely solid by present day and hence no molten region would remain (e.g. Solomon, 1976, core temperature $\sim$ 2100 K). In previous studies of the core of Mercury, and its core composition, the addition of sulphur has been favoured above other light elements. This is in part due to its cosmo-chemical abundance in the early solar system, and accretion of S-bearing planetesimals, but also due to its ability to drastically lower the melting temperature of iron, allowing it to remain molten to the present day.

The proportion of light elements may play a significant role in the formation of Mercury's core and the generation of its magnetic field. The ability of sulphur to dramatically lower the

melting curve may be fundamental in driving the magnetic field of Mercury and sustaining its liquid layer (Figure 1.7; Chen et al., 2008). Sulphur does indeed lower the melting temperature, but the observed multiple inflections in the melting curve (Figure 1.7) suggest core dynamics unlike those on Earth (Williams, 2009; Chen et al., 2008).

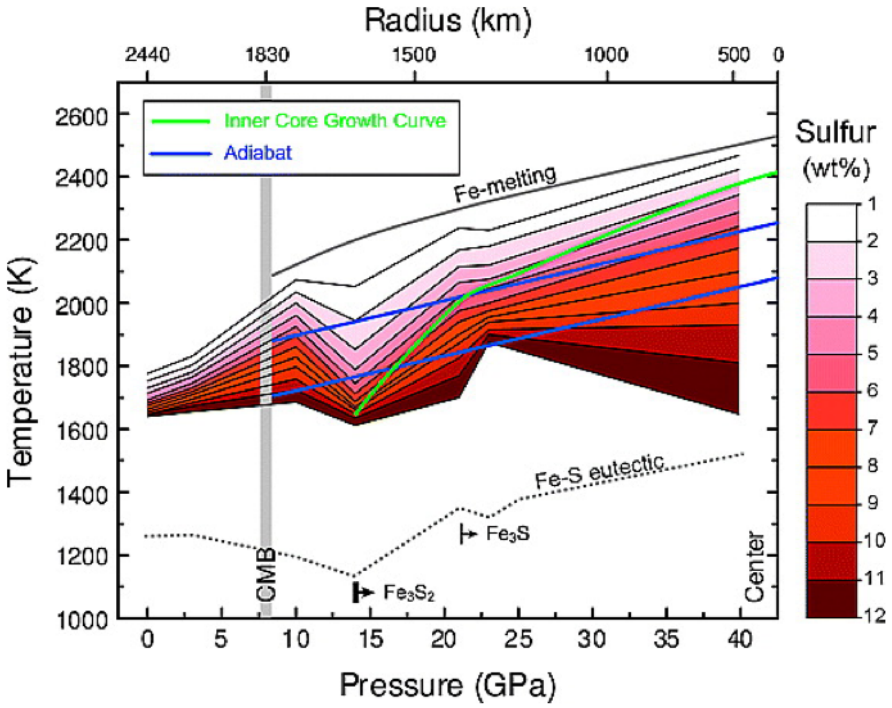

Figure 1.7: Melting curves measured by Chen et al. (2008) for a range of Fe-S alloys. With increasing sulphur enrichment the melting curve is increasingly depressed with respect to the pure iron melting curve. All Fe-S alloys measured include a peak at 10 GPa and two inflections (at 14 and 21 GPa) resulting in multiple crossings of the adiabat and consequently multiple crystallisation regions in Mercury. Figure from Chen et al. (2008).

One possibility is the 'snowing core' scenario, in which the iron solidifies at the top of the core and snows down to greater depths in the planet (Figure 1.8). Studies of Fe-S mixtures have suggested top-down 'snowing core' scenarios for Mercury's core (e.g. Williams, 2009; Chen et al., 2008), possibly in the form of a double snow state, with multiple crystallising regions (Figure 1.8). Similar scenarios have been suggested for the present core of Ganymede (Figure 1.8; Rückriemen et al., 2015; Chen et al., 2008) and future crystallisation of an inner core of Mars (Stewart et al., 2007). The 'snowing' core scenario could explain the weak observed magnetic field of Mercury, as it may drive a compositional dynamo deep inside the planet and also result in a stratified layer at the top of the core, which will have

further implications for the magnetic field, and structure of the planet (Chen et al., 2008; Dumberry and Rivoldini, 2015; Rückriemen et al., 2015; Christensen, 2006).

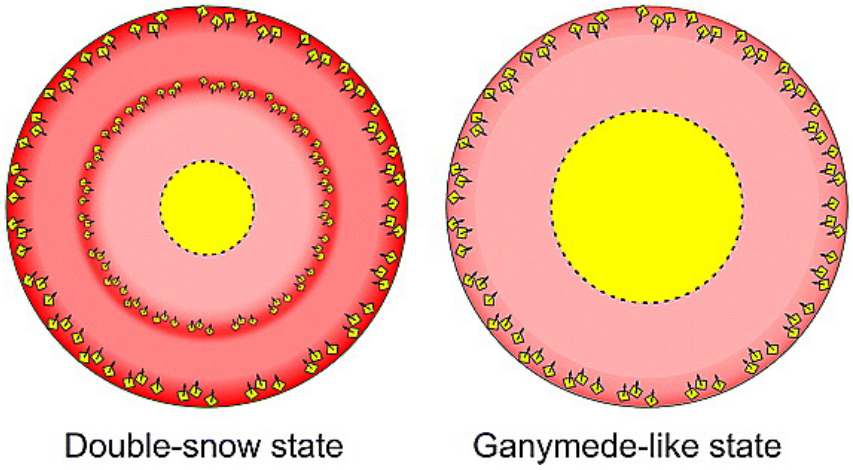

Figure 1.8: Schematic illustrations of the likely states of Mercury's core at the present time. In the double-snow state, the core consists of two distinct zones (red bands) where iron snow (yellow squares) forms, a thick liquid outer shell (pink) and a small solid inner core that is less than about 1200 km in radius (yellow). The iron snow sinking towards the centre (indicated by arrows) leads to a compositional gradient in the liquid, with sulphur enriched immediately above the snow boundaries (red) and depleted in the bottom layer (light pink). The middle layer (dark pink) has an intermediate sulphur concentration; it receives iron snow from above and sulphur-rich liquid from below. In the Ganymede-like state, the core has a single snow zone in a liquid outer shell, and a solid inner core. The radius of the inner core is determined by the core's sulphur content and temperature. Figure from Chen et al. (2008).

The sulphur content of the core is subject to strict limits placed by the geology of the planet's surface. Models by Schubert et al. (1988) suggest a very small amount of sulphur is required for a fluid outer core, but any less than 2 wt% would result in planetary contraction larger than observed on the surface. However more than 7 wt% would result in no core whatsoever. More recent work has placed further limitations, with models suggesting that at least 6.5 wt% of sulphur is need to agree with the contractional lobate scarps simultaneously with a core dynamo source for the magnetic field (Hauck II et al., 2004; Zuber et al., 2007). Further constraints could be made on the composition if it were shown that Mercury's magnetic field was unequivocally of dynamo origin. A dynamo origin of the magnetic field would imply that the liquid portion of the core is convecting, so a minimum amount of light element is needed to maintain a liquid core to the present day. As the inner core crystallises,

the outer liquid region would become more sulphur enriched, lowering the liquidus and as such slowing inner core growth (Stevenson et al., 1983; Schubert et al., 1988; Hauck II et al., 2004); too much sulphur initially inhibits inner core growth and thereby convection (Margot et al., 2007). Light elements in the core such as sulphur will have profound effects on the structure of the planet and the size of its core, as well as in the generation of its magnetic field. Modelling conducted by Rivoldini and Van Hoolst (2013) suggests Mercury has a core radius of 2004 +/- 39 km with an average core density of 7233 +/- 267 kg/m^3 and a sulphur fraction of 4.5 +/- 1.8 wt%. Rivoldini and Van Hoolst (2013) hypothesised these values based on two approaches; the first, an interior model which uses five mantle mineralogies, assumes a crust with a given density and thickness and two mantle temperatures (model details described in Rivoldini et al. (2009)). The second uses the density of the mantle, the thickness and density of the crust and the temperature of the core mantle boundary as parameters for the model. In both cases the core of Mercury is assumed to be composed of iron and sulphur only and the models then use the subsequent prediction of the temperature, pressure and concentration of sulphur in the core to predict the radius of the core. Furthermore, previous modelling by Rivoldini et al. (2009) suggest that with a sulphur fraction less that $\sim$5 wt% the planet could not have formed a solid inner core, as the melting temperature of Fe-FeS would be above the calculated core temperature.

However, sulphur is not the only likely component of Mercury's core. As described in Section 1.2.3, surface measurements of Mercury suggest a mixture of iron, sulphur and silicon in the planet's core; moreover, none of these models necessarily preclude the presence of other light elements such as H or C.

1.4 The Properties of Iron

1.4.1 Solid Iron and It's Melting Temperature

Iron has been studied not only for its role in alloys and steel, but also due to its important role throughout the solar system. As the heaviest element that can be readily created via nuclear fusion within the temperatures of star formation, and its small role in creating heavier elements via neutron capture, it is very abundant in the universe and is a building block for most planetary bodies in the solar system, from the core of a star to the cores of small planetesimals in their eccentric orbits. Iron is a large component of Mercury's core, and a

good understanding of this material is fundamental to investigating the state of Mercury's interior, but is also key to the investigation of the other small planetary bodies.

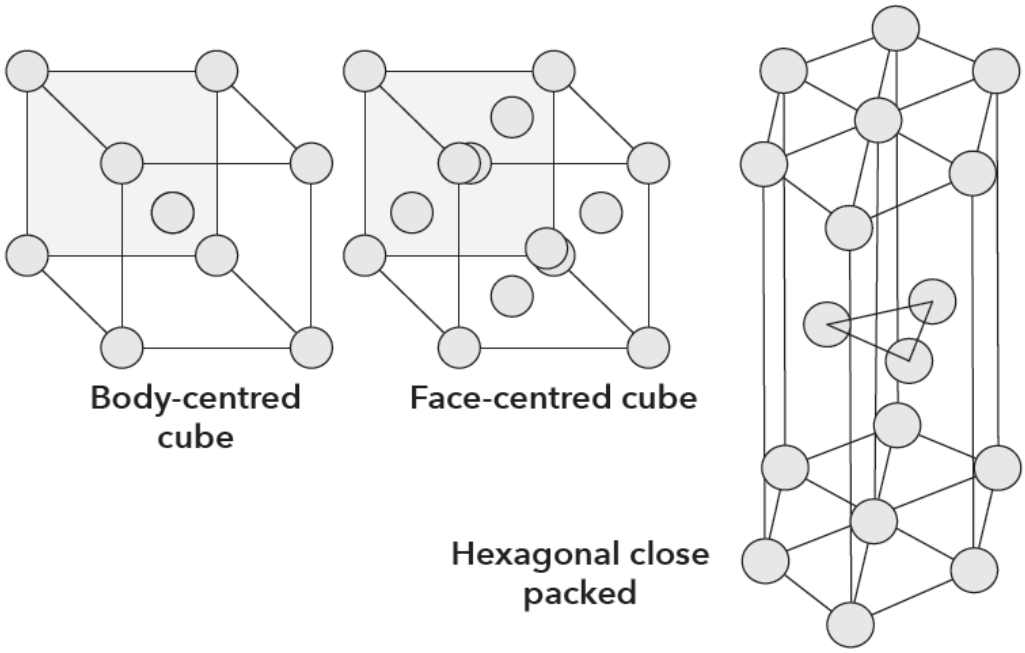

Figure 1.9: Examples of crystal structures of solid iron. In the body-centred cubic (bcc) structure, there is an atom at each corner of the unit cell (i.e. the corner atoms are shared among eight unit cells), and an identical atom in the centre. In the face-centred cubic (fcc) structure, there is an atom at each corner, and an atom at the centre of each face of the cube. The hexagonal close-packed structure has layers of close-packed atoms, 'A' and 'B', stacked in an ABAB sequence (the fcc structure can be viewed as a similar ABCABC stacking of close-packed layers). Solid iron transitions from a bcc structure to fcc structure at relatively low pressures but increasing temperature. At high temperatures and pressures, iron is in the hcp structure.

The phase diagram of iron consists of a body-centred-cubic (bcc) structured phase up to $\sim$12 GPa and below $\sim$1000 K, the low pressure bcc phase of iron is also referred to as ferrite iron, α. With increasing temperature iron transforms to the face-centred-cubic (fcc, also referred to as austenite, γ), or cubic-close-packed (ccp) phase, and then at low pressures back to bcc (δ), but with increasing pressure to the hexagonal-close-packed (hcp, ε-iron) phase (Figure 1.9; 1.10). The phase diagram of iron also features multiple triple points, with two in particular below 50 GPa and in the realm of Mercury's core conditions, a bcc-fcc-hcp (α-γ-ε) triple point at $\sim$ 8 GPa and 678 K (Klotz et al., 2008), and a bcc-fcc-liquid (δ- γ-liquid) triple point at 1990 K and 5.2 GPa (Bassett and Weathers, 1990).

Ab initio studies of the structure of iron at the extreme conditions of the Earth's core (360 GPa, $\sim$ 6000 K) found that the most stable phase appeared to be the hcp phase (Vočadlo et al., 2000), this was further confirmed using thermodynamic arguments (Vočadlo et al., 2003). Tateno et al. (2010) and Sakai et al. (2011) have independently used *in-situ* laser-heated diamond-anvil-cell techniques confirming that hcp is the stable phase of iron in the Earth's core (Figure 1.10). Good agreement was observed between early melting relation-

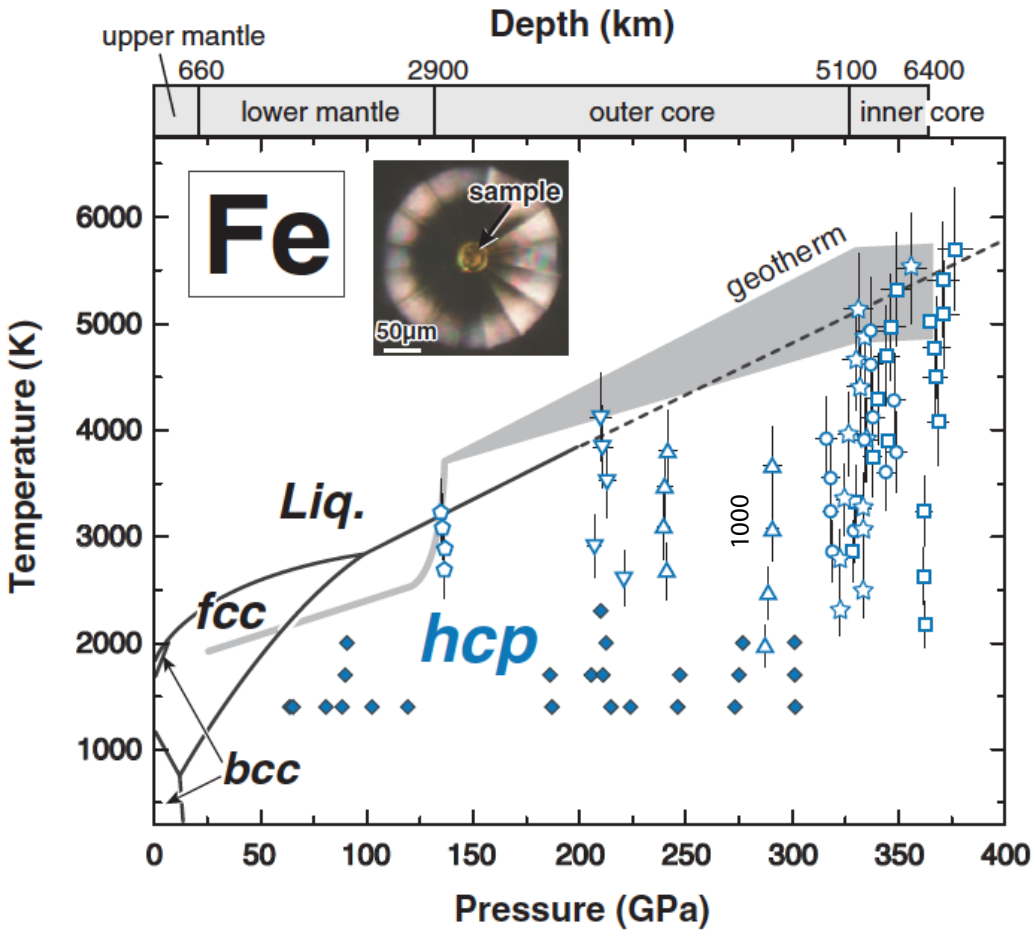

Figure 1.10: Phase diagram of Fe, including the geotherm of Earth. The high-temperature bcc (δ) and the low-temperature bcc phase (α) are shown. Also indicated is the fcc phase (also referred to as austenite, γ), the hcp phase (ε-iron) and the melting curve. From Tateno et al. (2010). Reprinted with permission from AAAS.

ships (e.g. Shen et al., 1993; Boehler, 1986; Liu and Bassett, 1975; Boehler, 1993) at low pressure, but when extrapolated to the much higher pressures of the Earth's core, predictions of the inner-core boundary temperature of the Earth (at $\sim$ 330 GPa) ranged anywhere from 5000 - 7000 K. Alongside the early diamond-anvil-cell experiments (e.g. Shen et al.,

1993; Boehler, 1993), shock wave experiments were used to attempt higher pressures closer to the extreme conditions of the Earth's core (Yoo et al., 1993; Nguyen and Holmes, 2004; Brown and McQueen, 1986). Shock wave experiments predicted a much higher melting temperature of iron than that found by Boehler (1993), albeit with large error bars (e.g. error range of 500 K, Brown and McQueen, 1986; Luo and Ahrens, 2004). *Ab initio* studies also predicted a higher melting temperature of iron, calculating temperatures around 6000 K (Alfè, 2009; Alfè et al., 2002b). Modern studies of the iron melting curve are reaching a consensus on the melting temperature of iron at ultra-high pressures. Anzellini et al. (2013) determined the melting curve between 50 and 200 GPa using static laser-heated diamond-anvil-cell techniques and synchrotron-based fast X-ray diffraction as the primary melting diagnostic. This produced a slope much closer to previous *ab initio* studies, and suggests a core-mantle boundary temperature of $\sim$ 6000 K (Figure 1.11). This study also indicated that the observed onset of rapid re-crystallisation coincided with the lower predicted melting temperatures e.g. Boehler, 1993. This suggests that the appearance of laser speckling used by these studies (e.g. Boehler, 1993) to indicate the onset of melting is sensitive to other behaviour, not just melting, and thus may possibly erroneously produce lower melting temperatures (Lord et al., 2014a,b). However, X-ray absorption measurements by Aquilanti et al. (2015) suggest iron melting temperatures consistent with the lower temperatures suggested by other studies (e.g Jackson et al., 2013; Boehler et al., 2008; Boehler, 1993). In contrast to the extreme conditions of Earth's core, at the relatively low pressures and temperatures of Mercury's deep interior (up to 36 GPa, Hauck et al., 2013), early studies along with modern work have produced good agreement. However as will be seen later in this work, although the temperatures are similar, the details of each melting curve may vary, dramatically affecting any conclusions this work may wish to draw. The addition of light elements to the iron system will change the melting temperature. As discussed in Section 1.3.2, sulphur can dramatically lower the melting temperature relative to pure iron alone (Chen et al., 2008, Figure 1.7). Small amounts of silicon can also lower the melting temperature compared to pure iron but to a smaller extent (Fischer et al., 2013); however large amounts of silicon mixed with iron have been found to increase the melting temperature (Lord et al., 2010; Fischer et al., 2013) reflecting the shape of the liquidus shown in Chapter five, Figure 5.1. This is similar to Morard et al. (2011) who investigated the Fe-Ni-Si ternary system and found an increase in the melting temperature of Fe-Si alloys with reducing Si

content (between 15 and 10 wt% Si), highlighting the complex nature of silicon inclusion in the iron system. A possible composition of the core of Mercury is a mixture of iron, sulphur and silicon, the implications of this ternary is discussed in Section 1.5.

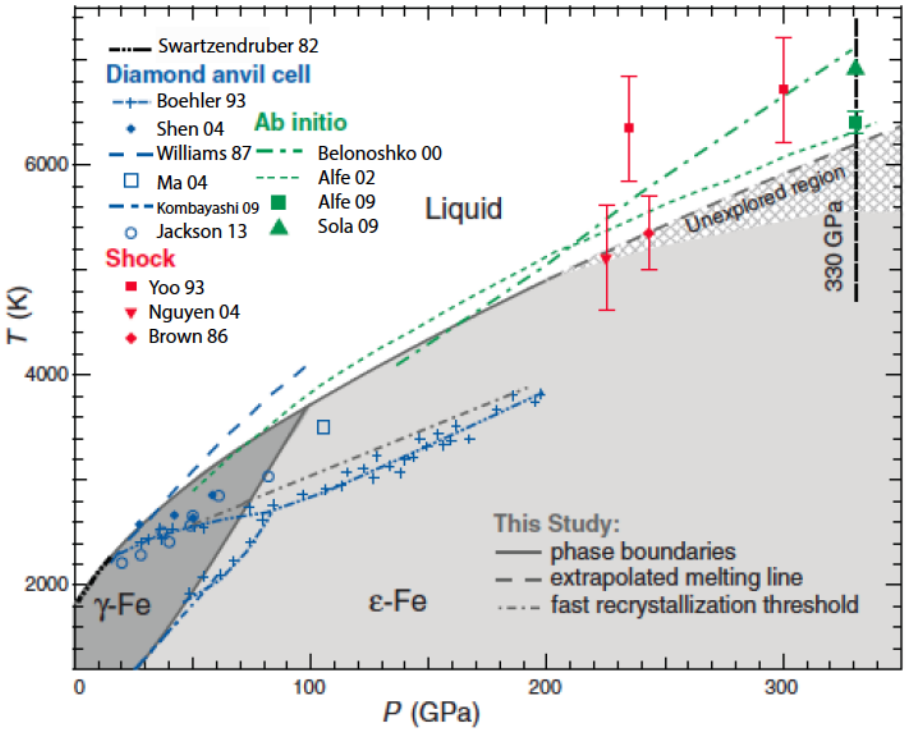

Figure 1.11: The phase diagram and melting curves of pure iron, including shock wave, diamond anvil cell and *ab initio* studies. Figure adapted from Anzellini et al., 2013. Reprinted with permission from AAAS.

1.4.2 Magnetic Changes In Iron

With increasing temperature and pressure, materials not only undergo structural changes, but also changes to the spin state of the material. At ambient conditions iron is ferromagnetic, but when the Curie temperature for iron ($\sim$ 1043 K) is exceeded, the spins become disordered and the material becomes paramagnetic, such that there is no measured overall magnetisation (Figure 1.12). Above the Curie temperature but at relatively low pressures and temperatures iron will be in the high spin regime as predicted by Hund's Rule, and due to the presence of unpaired spins, the individual atoms will retain a magnetic moment (but the sum of these would be zero; Speziale et al., 2005). With increasing pressure (and temperature) the atomic orbitals of iron collapse from the high spin to the low spin state.

This transition effectively quenches the magnetic moment of the atom, such that the magnetic moment per atom decreases to zero at a sufficiently high pressure (Chapter two, Figure 2.2). The high to low spin transition impacts not only on the magnetic state of a material, but also its physical properties, as the collapse of the magnetic moment effectively reduces the volume of the atom. This is one of the many reasons why this transition is crucial to understanding the detailed behaviour of a system, and the implications this may have on the properties of a planet.

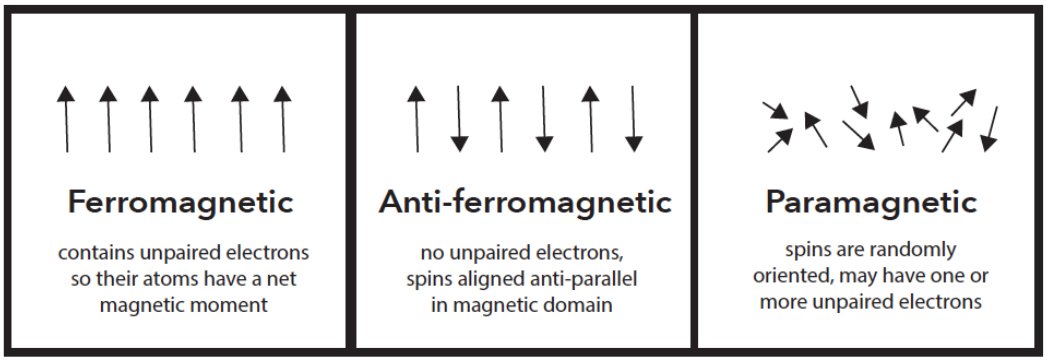

Figure 1.12: Orientation of spins in ferromagnetic, anti-ferromagnetic and paramagnetic materials (from left to right). Below the Curie temperature, iron is ferromagnetic, but at temperatures above the Curie temperature transitions to a paramagnetic material such that there is no net magnetic moment.

1.4.3 Liquid Iron

Above the melting temperature liquid iron also undergoes physical, energetic and possibly structural changes. *Ab initio* simulations of liquid iron have been performed by Vočadlo et al. (2003) and later by Ichikawa et al. (2014). These are in agreement for the evolution of the density, isothermal and adiabatic bulk modulus and Grüneisen parameter of liquid iron up to the conditions of the Earth's interior (e.g. Figure 1.13), although they differ in their predictions of the thermal expansion of liquid iron, which will be discussed in greater detail in Chapter 6. These studies performed *ab initio* calculations from 50 GPa upwards. For this reason, the calculations were non-spin polarised, essentially non-magnetic, as they were at sufficiently high temperature and pressure to be in the low spin regime. However, the low-pressure behaviour of liquid iron is relatively unconstrained and may undergo a transition from high to low spin. Experiments on the ambient pressure magnetic moment of liquid

iron using neutron diffraction at 1620°C (Waseda and Suzuki, 1970) and 1600°C (Weber et al., 1977, 1978) have found the magnetic moment of pure liquid iron to be 1.2 μ_B and 1.9 μ_B respectively. Thus, calculations within this range would need to be spin-polarised, and to fully consider the effect of magnetisation on the calculations and their predicted properties. Work by Sanloup et al. (2000) also suggests that there is a local-range structural change in liquid iron at $\sim$ 5 GPa. Sanloup et al. (2000) used high-energy synchrotron X-ray diffraction experiments on liquid iron, and revealed a structural change in the region of the γ- δ-Liquid triple point. Sanloup et al. (2000) found that the second- and third-neighbour shells in the radial distribution function shifted to shorter distances, changing in structure with increasing pressure. Conversely, using X-ray scattering in the diamond anvil cell, Shen et al. (2004) detected no structural changes along the melting curve of iron up to 58 GPa, and measured the structure of liquid iron to be a close-packed hard-sphere liquid.

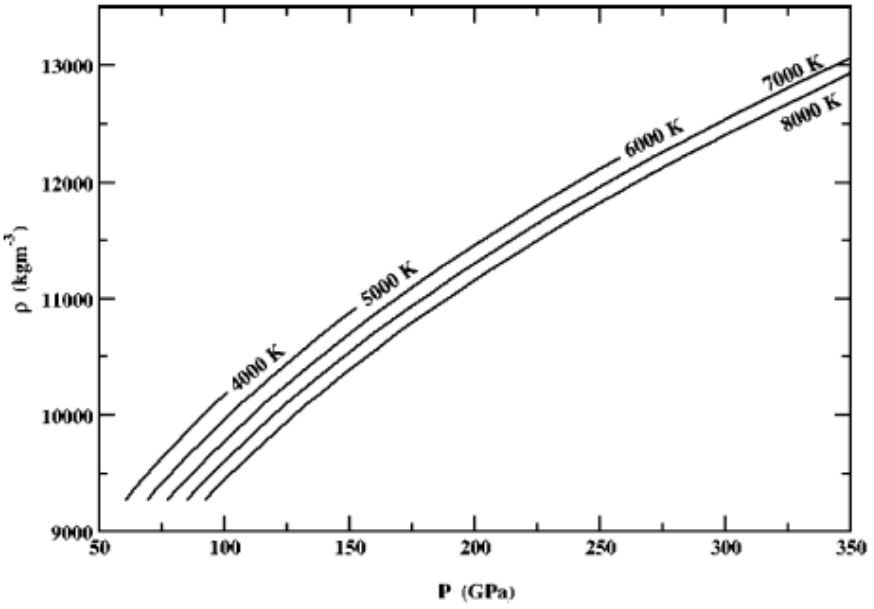

Figure 1.13: The density of pure liquid iron determined using non-magnetic *ab initio* calculations. Figure from Vočadlo et al. (2003). Reprinted from Physics of The Earth and Planetary Interiors, 140, L Vočadlo, D Alfè, M.J Gillan, D. G. Price, The properties of iron under core conditions from first principles calculations, 101 - 125, Copyright 2003, with permission from Elsevier.

1.5 An Fe-S-Si ternary in Mercury's Core

Fe-S-Si is subject to liquid immiscibility at pressures less than 15 GPa and $\sim$ 2000 °C for an alloy that is iron rich (Morard and Katsura, 2010; Sanloup and Fei, 2004; Siebert et al., 2004; Malavergne et al., 2007), which would result in a buoyancy segregation of S-rich liquids at the top of Mercury's core (Figure 1.14) and may also result in a iron snow type regime for the planet's core.

The amount of sulphur on the planet's surface will place important constraints on the sulphur content, and thereby the silicon content of the planet also. Work by Chabot et al. (2014) on the possible core composition ranges between 5-8 wt% Si at 5 wt% S, up to 3-7 wt% Si at $\sim$ 8 wt % S. It is possible that an Fe-S-Si core may explain the weak observed magnetic field of Mercury. Previous models consider an Fe rich Fe-S core, in which the iron will crystallise, such that FeS would provide a very effective compositionally driven dynamo. However, in the Fe-S-Si system silicon would not be excluded, and would partition into the liquid as well as the precipitating solid. The core-mantle boundary pressure of Mercury is $\sim$ 5.5 GPa (estimates range between 4 GPa and 7 GPa, Hauck et al., 2013), within the immiscible region of the Fe-S-Si ternary system (Morard and Katsura, 2010), but at the central core pressures of Mercury (36 GPa; Hauck et al., 2013) the liquid may be miscible. The miscible liquid region, upon encountering the immiscible region, may form a S rich layer at the top of the core, which may crystallise and form a stable stratified solid Fe-S layer (Smith et al., 2012; Chabot et al., 2014; Hauck et al., 2013). As the core crystallises the resulting liquid may become S-enriched, shifting the composition into the immiscible region, resulting in the whole core experiencing liquid immiscibility. The true effect of this on the evolution of the planet's core is challenging, as one could imagine a variety of ways in which the story of the planet's formation may occur in this case. Estimates of an Fe-Si-FeS mixture in Mercury's core by Knibbe and van Westrenen (2015) suggest an outer liquid core boundary between 1985 to 2090 km for high silicon and sulphur core contents or the presence of an FeS layer at the core-mantle boundary. However, Knibbe and van Westrenen (2015) additionally suggest that Fe-S may be unstable at the outer-core conditions of Mercury, and may be denser than the surrounding liquid, and hence, alternate mechanisms would be required to maintain an FeS layer at the top of the core.

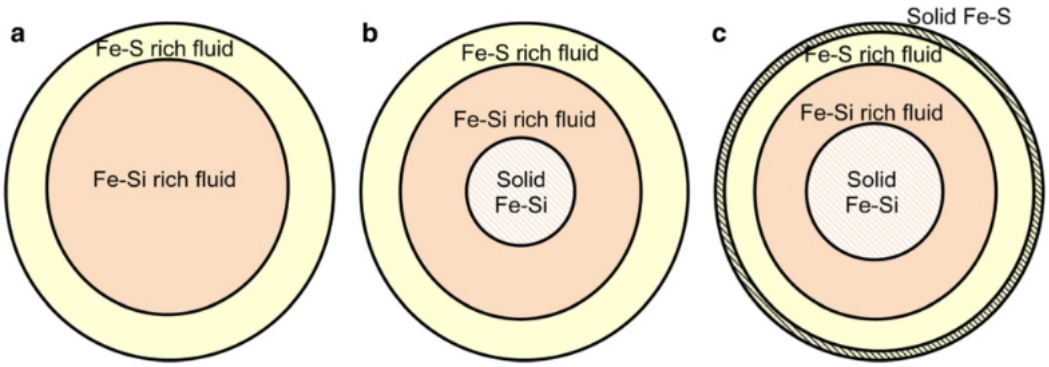

Figure 1.14: Cross Sections of possible layered structures of an Fe-S-Si core in Mercury, with decreasing temperature from a to c. Figure from Breuer et al. (2015) (http://creativecommons.org/licenses/by/4.0/).

1.6 Summary

This thesis will present *ab initio* molecular dynamics calculations on the equations of state and thermoelastic properties of pure liquid iron and a liquid iron, sulphur and silicon mixture. In addition, the melting behaviour of $Fe_{0.8}S_{0.1}Si_{0.1}$, a possible candidate for the composition of Mercury's core, has been determined experimentally in Chapter five. First principles methods have been used in Chapter six, seven, eight and nine to determine the equation of state, isothermal bulk modulus and to map the high to low spin transition of pure liquid iron and $Fe_{0.8}S_{0.1}Si_{0.1}$ at 2000, 3000 and 4000 K. The mean Grüneisen parameter and volumetric coefficient of thermal expansion have also been calculated for liquid Fe and $Fe_{0.8}S_{0.1}Si_{0.1}$ between 2000 - 4000 K. Additionally the calculated thermodynamic properties of Fe and $Fe_{0.8}S_{0.1}Si_{0.1}$ have been used to determine the adiabatic gradient of both materials, which are subsequently used alongside published melting curves of pure iron and the liquidus of $Fe_{0.8}S_{0.1}Si_{0.1}$ determined in Chapter five to model the evolution of Mercury's core. Predictions of physical properties made using accurate equations of state feed directly into models of planetary thermal evolution and the magnetic field, such that improved estimates can dramatically change the story of a planet and impact on our understanding of the evolution of our solar system through its comparative planetology. This chapter has provided the motivation and theoretical background to the study presented in this thesis. The proceeding chapters will detail the methods used to study the evolution, composition and structure of Mercury, the results, and consequently the conclusions that can be drawn.

Chapter 2

Computational Methods

This work aims to determine the physical and thermodynamic properties of pure liquid iron and a liquid iron-sulphur-silicon alloy (with the relative atomic abundance of 80:10:10 at% or alternatively 88:5.5:6.3 wt%). Measuring the behaviour of these liquids at the conditions relevant to interior of Mercury is difficult to achieve experimentally. Thus an alternate method has been used to study material behaviour: first principles, or *ab initio* calculations. *Ab initio* methods consider systems at an atomistic level, calculating the macroscopic properties of materials from their microscopic behaviour. This chapter describes the theoretical basis of *ab initio* calculations, followed by details of its use in this work.

2.1 The First Principles Computational Method

Ab initio simulations seek to calculate the properties of materials using a quantum mechanical approach, considering only the behaviour of the electrons and nuclei to determine the ground state energy and subsequently all the properties of interest for that material. However, the exact solution of quantum mechanical equations is impossible for complex systems of multiple electrons and nuclei, so, additionally, the use of density functional theory (DFT) has been employed. In this work, density functional theory has been implemented within the Vienna *Ab initio* Simulation Package (VASP; Kresse and Hafner, 1993, 1994; Kresse and Furthmüller, 1996a,b) using the projector augmented wave method (Blöchl, 1994; Kresse and Joubert, 1999) and a gradient corrected functional to approximate the exchange-correlation energy (see Section 2.1.3, Perdew et al., 1992, 1993).

This chapter will first describe the theory of *ab initio* calculations and the approximations

necessary to determine, as closely as possible, the true solution for the system. This will be followed by a detailed description of the running of VASP and the inputs required. Finally, a full methodology will be given for determining the properties of materials and the theory involved therein, this also includes an introduction to thermodynamic integration (more detail can be found in Chapter seven).

2.1.1 The Schrödinger Equation

A fundamental equation of quantum mechanics is the time independent non-relativistic Schrödinger wave equation, which describes fully the quantum mechanical behaviour of a dynamic system:

$$\hat{H}\Psi_i(\vec{x_1},\vec{x_2},...,\vec{x_N},\vec{R_1},\vec{R_2}...\vec{R_M}) = E_i\Psi_i(\vec{x_1},\vec{x_2},...,\vec{x_N},\vec{R_1},\vec{R_2}...\vec{R_M}) \tag{2.1}$$

In which Ψ_i is the wave-function of the i^{th} state, E_i represents the corresponding energy of the i^{th} state and $\hat{H}$ is the Hamiltonian for a system consisting of M nuclei and N electrons. The Hamiltonian of a system describes the interactions between the electrons and nuclei; for a system of M nuclei and N electrons it is given by:

$$\hat{H} = -\frac{1}{2}\sum_{i=1}^{N}\nabla_i^2 - \frac{1}{2}\sum_{A=1}^{M}\frac{1}{M_A}\nabla_A^2 - \sum_{i=1}^{N}\sum_{A=1}^{M}\frac{Z_A}{r_{iA}} + \sum_{i=1}^{N}\sum_{j>i}^{N}\frac{1}{r_{ij}} + \sum_{A=1}^{M}\sum_{B>A}^{M}\frac{Z_AZ_B}{R_{AB}} \tag{2.2}$$

The terms M_A and Z_A denote the nuclear mass and charge of nucleus A, similarly Z_B represents the charge of nucleus B (in Hartree atomic units). The labels i and j represent the electrons in the system. The spatial coordinates of the electrons, nuclei and distance between them are described by r_i, R_A and r_{iA} respectively. The first two terms of equation 2.2 describe the kinetic energy of the electrons and the kinetic energy of the nuclei. The remaining three terms represent the attractive electrostatic interaction between the nuclei and the electrons and the repulsive potential due to the electron-electron and nucleus-nucleus interactions.

The solution of the Schrödinger wave equation finds the total energy for any given system. In finding the total energy, the configuration can be varied and the minimum possible energy found, known as the ground state energy, from which many physical properties can be

calculated.

The Schrödinger equation can be solved exactly for one particle, but with increasing numbers of particles the complexity of the problem grows exponentially, rendering an N-body problem impossible to solve analytically. However simplifications can be made to aid in solving the N-body problem, the first of which is the Born-Oppenheimer approximation.

2.1.2 The Born-Oppenheimer Approximation

Due to their much greater mass, nuclei move much slower than electrons. The Born-Oppenheimer approximation suggests that the difference in speed is so great that the nuclei can be considered stationary in the reference frame of the electrons (Born and Oppenheimer, 1927). This significantly simplifies the problem as the electrons can then be considered to be moving in a field of fixed nuclei and consequently their nuclear kinetic energy is zero and their potential energy is constant. In this system the dynamics of the nuclei can be treated separately to the electrons, and thus, Schrödinger's equation can be solved for the electrons alone in a potential generated by the stationary nuclei. The electronic Hamiltonian ($\hat{H}_{elec}$) (eq. 2.2) is then reduced to (in Hartree atomic units);

$$\hat{H}_{elec} = -\frac{1}{2}\sum_{i=1}^{N}\nabla_i^2 - \sum_{i=1}^{N}\sum_{A=1}^{M}\frac{Z_A}{r_{iA}} + \sum_{i=1}^{N}\sum_{j>i}^{N}\frac{1}{r_{ij}} = \hat{T} + \hat{V}_{Ne} + \hat{V}_{ee} \tag{2.3}$$

and,

$$\hat{H}_{elec}\Psi_{elec} = E_{elec}\Psi_{elec} \tag{2.4}$$

in which $\hat{T}$ is the kinetic energy of the electrons, V_{Ne} and V_{ee} are the attractive electrostatic interactions between electrons and nuclei and the repulsive electrostatic interactions between electrons and electrons respectively. The terms E_{elec} and Ψ_{elec} are the electronic energy and wave function respectively. The total energy of the system is therefore simply the summation of the electronic energy, E_{elec}, and the constant nuclear repulsion term, E_{nuc}, i.e.

$$E_{tot} = E_{elec} + E_{nuc} \tag{2.5}$$

2.1.3 Correlation and Exchange

Schrödinger's equation can be solved exactly for a one electron only, i.e. in the case of hydrogen. When more than one electron is considered their motions will not be independent of each other, i.e. the resulting wave-function will not be a product of the individual wave-functions. The motions of multiple electrons will be correlated. The electrons must also follow the Pauli exclusion principle which states that in a single orbital you cannot have more than one electron in any given spin state and thus implies that the probability of finding two electrons within a volume element cannot change when their positions are interchanged, thus,

$$|\psi(\overrightarrow{r_1}, \overrightarrow{r_2})|^2 = |\psi(\overrightarrow{r_2}, \overrightarrow{r_1})|^2 \tag{2.6}$$

Therefore, to achieve this, the wave function needs to be anti-symmetric in the coordinates of the electrons and follow exchange symmetry, i.e. that when two electrons are interchanged the sign of the wave-function switches and from which the exchange energy arises. The difference between the true ground state energy and that calculated neglecting the exchange energy is called the correlation energy.

2.1.4 The Variational Principle

To solve the Schrödinger equation and find the true ground state of any system, the Variational principle is used, which states that the energy computed from any guessed wave function ψ is an upper bound to the true ground state energy E_0. The expectation value $E[\psi]$ is minimised with respect to all possible allowed N-electrons wave functions which gives the true ground state wave function ψ_0 and energy $E[\psi_0]$, i.e.,

$$E_0 = min_{\psi \to N} E[\psi] = min_{\Psi \to N} \langle \nabla | \hat{T} + \hat{V}_{Ne} + \hat{V}_{ee} | \psi \rangle \tag{2.7}$$

The Variational principle provides a method for determining the ground state energy and

wave function for any system of N electrons in a given nuclear potential, such that the ground state energy is simply a functional (function of a function) of the number of electrons N and the nuclear potential V_{ext}.

$$E_0 = E[N, V_{ext}] \tag{2.8}$$

Consequently the search for the ground state wave function can be formulated as a minimisation problem:

$$E_0 = min_{\psi} \langle \psi | \hat{H} | \psi \rangle \tag{2.9}$$

where the minimisation is over all normalised trial wave functions.

2.1.5 Hartree Theory

Thus far, independent electrons have been discussed within an external potential generated by the nuclei, but this has neglected the repulsion of the electrons. Hartree theory (1928) addresses this by replacing the insolvable many electron problem, with one of single electrons moving in an average potential. The Hartree potential is defined as:

$$V_i^H(r) = \sum_{j \neq i} \int \frac{|\psi_j(r')|^2}{|r - r'|} d\overrightarrow{r}' \tag{2.10}$$

The Hartree potential is different for each orbital, and therefore the orbitals are not orthogonal and must be solved self-consistently as the Hartree potential also depends on all other orbitals, ψ_j. Hartree theory does not produce an anti-symmetric wave function, and hence does not account for the exchange symmetry (described in 2.1.3), which is corrected in the Hartree-Fock scheme.

2.1.6 Hartree-Fock Theory

The Variational principle provides the method for solving the true ground state energy, however it requires the user to search through all possible wave functions to find which

minimises the total energy. Hartree-Fock theory (Fock, 1930) describes an educated guess to the structure of the wave function by assuming it to be an anti-symmetric product of functions (ψ_i) each of which depends on the coordinates of a single electron:

$$\Psi_{HF} = \frac{1}{\sqrt{N}} det[\psi_1 \psi_2 \psi_3 ... \psi_N] \tag{2.11}$$

where *det* indicates a matrix determinant, known as the Slater determinant. Hence, the Hartree-Fock wave function (Ψ_{HF}) can be substituted into the Schrödinger equation and an expression for the Hartree-Fock energy (E_{HF}) determined (E_{HF}, so distinguished from E_0 as it is not the true ground state since it does not account for correlation energy). This results in the following single particle Hamiltonian $\hat{h}_i$;

$$\hat{h}_i = -\frac{1}{2}\nabla^2 + V_{ext}(r) + V_i^H(r) + V_i^X(r) \tag{2.12}$$

where the first term, $-\frac{1}{2}\nabla^2$, refers to the kinetic energy, $V_{ext}(r)$ is the potential due to the nuclei, $V_i^H(r)$ is the Hartree potential (defined previously) and the final term ($V_i^X(r)$), is the exchange potential. Although the exchange energy is calculated exactly, the correlation energy is neglected.

The Hamiltonian is found via an iterative process where a trial wave function is formulated. This is used to build the trial Hamiltonian, and subsequently solving Schrödinger's equation to obtain the orbitals. These orbitals are then used as the input for the next iteration, and is repeated until self-consistency is reached, i.e., the input and output do not differ.

2.2 Density Functional Theory

Hartree-Fock methods are widely used to compute the properties of complex systems, but the method used in this work is density functional theory (DFT). Hartree-Fock treats exchange exactly but it neglects the correlation completely, whereas DFT includes approximations to both exchange and correlation and is more accurate for most condensed matter systems. Underpinning DFT is the assumption that the ground state properties of a many electron system are uniquely determined by an electron density that depends only on three

spatial coordinates (Hohenberg and Kohn, 1964).

2.2.1 Hohenberg and Kohn Theorems

Hohenberg and Kohn (1964) put forward mathematical proof of two theorems fundamental to DFT. The first is that the external potential is (to within a constant) a unique functional of the electron density. In turn the external potential then fixes the Hamiltonian, and, thus, the full N-body ground state is a unique functional of the electron density. As proof of this, consider two external potentials; $V_{ext}(\overrightarrow{r})$ and $V_{ext}(\overrightarrow{r}')$, which differ by more than a constant, but both give the same $\rho(r)$ for their ground state. This would result in two Hamiltonians ($\hat{H}$ and $\hat{H}'$), whose ground state energies would be equal, but whose normalised wave functions (Ψ and Ψ') would differ. If Schrödinger's equation is solved separately using each individual normalised wave function as a trial wave function, two ground state energies would be obtained, E_0 and E_0', and since Ψ' is not the ground state of $\hat{H}$ and vice versa, they can be described using the following inequalities (this assumes the ground states are non-degenerate but this same proof can also be shown to apply for degenerate scenarios also),

$$E_0 < E_0' + \int d^3r \left[V_{ext}(\overrightarrow{r}) - V_{ext}(\overrightarrow{r'}) \right] \rho(r) \tag{2.13}$$

$$E_0' < E_0 + \int d^3r \left[V_{ext}(\overrightarrow{r'}) - V_{ext}(\overrightarrow{r}) \right] \rho(r) \tag{2.14}$$

But if equations 2.13 and 2.14 are summed the result implies that $E_0 + E_0' < E_0 + E_0'$ which is contradictory. It follows then that there cannot be two different $V_{ext}(r)$ that give the same $\rho(r)$ as their ground state density. Therefore the density determines the number, external potential and all the properties of the ground state including the kinetic, potential and total energy ($T[\rho], V[\rho]$ and $E[\rho]$). The total energy can be written as the sum of these;

$$E[\rho] = E_{Ne}[\rho] + T[\rho] + E_{ee}[\rho] = \int \rho(r) V_{Ne}(r) dr + F_{HK}[\rho] \tag{2.15}$$

where $F_{HK}[\rho]$ is the Hohenberg Kohn functional defined as,

$$F_{HK}[\rho] = T[\rho] + E_{ee}[\rho] \tag{2.16}$$

and all other terms retain their meaning as described previously. The second of the two theorems tackles the issue of how to determine whether a density is the true ground state density. This is addressed by stating that the functional $F_{HK}[\rho]$ calculates the lowest energy if and only if the input density is the true ground state density, which is recognisable as the Variational principle (described in Section 2.1.4).

Therefore, by minimising the density, the ground state energy can be found. However, this hinges on knowing the form of the Hohenberg-Kohn functional, which alas remains a mystery. Hence, it is necessary to make approximations to this functional, starting with the Kohn-Sham equations (1965).

2.2.2 The Kohn-Sham Equations

Kohn and Sham (1965) proposed an approximation to the kinetic and electron-electron functions, collectively known as the Hohenberg-Kohn functional $F_{HK}[\rho]$, by replacing the original N-body problem by an auxiliary independent particle problem. In a similar way to the Hartree-Fock approximation Kohn and Sham use non-interacting electrons, known as Kohn-Sham electrons which are constructed such that their density is the same as that of the interacting electrons. Thus the effective Hamiltonian ($\hat{H}_{eff}$) is simply a sum of one-electron Hamiltonians;

$$\hat{H}_{eff} = \sum_{i=1}^{N_{el}} \hat{h}(\overrightarrow{r_i}) \tag{2.17}$$

This produces a Schrödinger like equation for each one-electron Hamilitonian:

$$\hat{h}(\overrightarrow{r_i})\psi_a(\overrightarrow{r_i}) = \varepsilon_a \psi_a(\overrightarrow{r_i}) \tag{2.18}$$

In which, ψ_a and ε_a are the Kohn-Sham eigenvalues and orbitals of a single electron. To find the ground state density of the system of non-interacting electrons, solve the Schrödinger equation in equation 2.18 and then fill up the lowest $\frac{1}{2}N$ states $\psi_n(\overrightarrow{r_i})$ (each with a spin-up and a spin-down electron),

$$\rho(\overrightarrow{r_n}) = 2\sum_{occ} |\psi_n(\overrightarrow{r_i})|^2 \tag{2.19}$$

Where the sum is over all the occupied states. The effective Hamiltonian is given by:

$$H_{eff}(\overrightarrow{r_n}) = -\frac{1}{2}\nabla^2 + v_{KS}(\overrightarrow{r_n}) \tag{2.20}$$

where v_{KS} is the effective Kohn-Sham potential:

$$v_{KS}(\overrightarrow{r_n}) = v_{ext}(\overrightarrow{r_n}) + v_H(\overrightarrow{r_n}) + v_{xc}(\overrightarrow{r_n}) \tag{2.21}$$

which is the sum of the external, Hartree and exchange-correlation potentials respectively. The Kohn-Sham potential depends on the electron density and therefore a self-consistent solution must be reached. Self-consistency is found iteratively by making an initial estimate of the electron density, solving the Kohn-Sham equation (eq. 2.18) and using eq. 2.19 to find the resulting density, if the resulting density does not match the initial density, then the initial density is changed and the process repeated until self consistency is reached. Finally, when the self-consistent ground-state density is found it can be used to compute the ground-state energy. The Kohn-Sham equations provide a method of computing much of the Hohenberg-Kohn functional and only leaves a much smaller term known as the exchange-correlation function needing to be approximated.

2.2.3 Exchange Correlation Function

One of the approximations to the exchange-correlation function is known as the Local Density Approximation, or LDA (introduced by Kohn and Sham, 1965; Perdew and Zunger, 1981). In LDA the exchange-correlation function is expressed as:

$$E_{XC}^{LDA}[n] = \int n(r)\varepsilon_{XC}(n(r))dr \tag{2.22}$$

where $\varepsilon_{XC}(n(r))$ is the energy per electron at the point r, which depends only on the density of the electrons at that point (more detail can be found in Gillan, 1997). Since $\varepsilon_{XC}(n(r))$

is a unique functional, it can be solved for the simpler system of the uniform electron gas. This approximation has been found to be widely successful, however it does not account for the full nature of the problem, as the exchange-correlation function ($E_{XC}[n]$) depends not only on the density at the point at which it is calculated but on the density everywhere in the system. The Generalised Gradient Approximation (GGA) attempts to account for this.

$$E_{XC}^{GGA}[n] = \int n(r)\varepsilon_{XC}^{GGA}(n(r);\nabla n(r))dr \tag{2.23}$$

GGA incorporates the non-local correlation effects into its approximation of $E_{XC}[n]$ by introducing a dependence on the gradient in the electron density in addition to the electron density at a singular point (Perdew, 1986; Perdew et al., 1992, 1993; Becke, 1988). Further corrections in addition to the GGA functional can be made, such as that of GGA+U, which includes an empirical correction to the energy (Jain et al., 2011). This work uses the PW91 GGA functional (Perdew et al., 1992, 1993)

2.3 Plane Wave Basis Sets

For practical purposes the wave function needs to be represented in a relatively straightforward way. To describe wave-functions Bloch's theorem provides a way of representing wave functions as a series of basis functions;

$$\psi_\mu(\overrightarrow{r}) = e^{i\overrightarrow{k}.\overrightarrow{r}}u_i(\overrightarrow{r}) \tag{2.24}$$

in which $e^{(i\overrightarrow{k}.\overrightarrow{r})}$ is the solution to Schrödinger's equation for a free particle, k are all the allowed wave vectors in the primitive cell of the reciprocal lattice, and $u_i(\overrightarrow{r})$ is the periodic term. The periodic term can be expanded as a linear sum of plane-waves with wave vectors that are reciprocal lattice vectors $\overrightarrow{G}$.

$$u_i(r) = \sum_{\overrightarrow{G}} c_{i,\overrightarrow{G}} e^{(i\overrightarrow{G}.\overrightarrow{r})} \tag{2.25}$$

Therefore each wave function can be expressed as a sum of basis functions, which are

themselves plane waves. The collection of basis functions that describe the wave function are known as a basis set.

$$u_i(r) = \sum_{\vec{G}} c_{i,\vec{k}+\vec{G}} e^{(i(\vec{k}+\vec{G}).\vec{r})} \tag{2.26}$$

This implies that to solve for an accurate wave function an infinite number of plane waves is needed. However, the coefficients for the plane waves $c_{(i,\vec{k}+\vec{G})}$ each have a kinetic energy:

$$\frac{\hbar^2}{2m}|\vec{k}+\vec{G}|^2 \tag{2.27}$$

Practically, an energy cut-off is imposed which determines the completeness of the basis set, i.e. at each k-point, only the plane waves that fulfil the following expression are included.

$$\frac{\hbar^2}{2m}|\vec{k}+\vec{G}|^2 < E_{cutoff} \tag{2.28}$$

The value of the cut-off energy is determined in this work using convergence testing and is described in Chapters 6, 7, 8 and 9.

2.4 Pseudopotentials

Bloch's theorem states that the electronic wave-functions can be expressed using a discrete set of plane waves, however a very large number of plane waves are required to map the tightly bound orbitals and to follow the rapid oscillations of the wave functions of the electrons in the core region (Figure 2.1). Hence an extremely large plane wave basis set would be needed to perform an all-electron calculation and consequently a large amount of computational time to calculate the electronic wave functions.

Pseudopotential theory (Cohen and Heine, 1970; Phillips, 1958) introduces a simplification to the complexity of the problem. The electrons closest to the nucleus have much higher kinetic energies than those further away. Thus, they play a smaller role in the behaviour of the system. This is exploited in the pseudopotential method by ignoring the dynamics of the core electrons and instead replacing this with an effective potential, a pseudopotential.

The pseudopotential is created to be identical to the all electron wave function outside the cut-off distance, r_c (Figure 2.1).

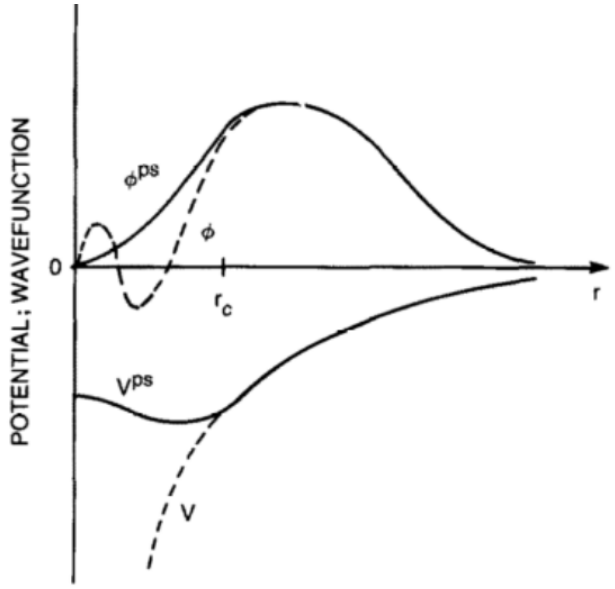

Figure 2.1: The Pseudopotential Method: the all electron potential V and orbital ϕ are altered to the pseudopotential V^{ps} and pseudo-orbital ϕ^{ps} inside the core radius r_c. Figure from Pickett (1989)[1].

2.4.1 Norm-Conserving to Ultra Soft Pseudopotentials

To accurately determine the exchange- correlation energy the pseudo wave-function and real wave-function must be identical outside of the core region (Figure 2.1) to ensure that both wave functions generate identical charge densities. This can be achieved by creating different potentials for each angular momentum component of the pseudopotential. This type of pseudopotential is called a non-local (as different angular momentum states have different effective potentials) norm-conserving (as they impose the condition that within the cut-off radius the norm of each pseudo-wave function is identical the corresponding all-electron wave function) pseudopotential. One of the major limitations in this type of pseudopotential is their high computational cost, as they require large plane wave basis sets for the transition metals and first row elements in the periodic table. The use of Ultra-soft pseudopotentials are a way of overcoming this. Ultra-soft potentials relax the norm-conserving constraint, allowing the pseudo-wave function to differ from the all electron

[1]Reprinted from Computer Physics Reports, 9, Warren E. Pickett, Pseudopotential methods in condensed matter applications, 115 - 197, Copyright 1989, with permission from Elsevier.

wave function inside the cut-off radius (Vanderbilt, 1990). This reduces the number of basis sets required, thereby reducing the overall computational cost but with little cost to accuracy.

2.5 Projector Augmented Wave Method (PAW)

The advantage of using pseudopotentials lies in it simplicity, however there are limitations. The price of this simplicity is that many elements such as the transition metals and rare Earth elements are computationally demanding to treat (Kresse and Joubert, 1999) and all the information on the charge density and wave function near the nucleus is lost (Blöchl et al., 2005). Augmented wave methods (introduced by Slater, 1937) are an alternative, which create basis functions from atom like wave functions in the atomic regions and functions that describe the bonding between them (Johannes et al., 2005). The projector augmented wave (PAW) method (Blöchl, 1994; Kresse and Joubert, 1999) combines the pseudopotential and augmented wave methods to create a unified electronic structure method.

The PAW method transforms physical wave functions onto auxiliary wave functions, resulting in smooth auxiliary wave functions which can be represented in a plane wave expansion, such that all the physical properties can be found from simply reconstructing the related true wave functions (Johannes et al., 2005). The advantages of the PAW method lies in that the full charge and spin density can be readily determined, which is extremely important when trying to understand hyperfine parameters which probe the electron density close to the nucleus.

2.6 k-point sampling

There exists an inherent symmetry to the crystal being simulated. This can be used in combination with Bloch's theorem to show that we need only calculate the electron states at a small number of k-points contained within the Brillouin zone. The number of atoms required to simulate the liquid iron and iron alloys in this work require large super cells of atoms, but since the volume of the Brillouin zone (BZ) is related to the volume of the super cell (i.e. the number of atoms involved in your calculation) Ω_{cell} by:

$$\Omega_{BZ} = \frac{(2\pi)^3}{\Omega_{cell}} \tag{2.29}$$

For an appreciably large system the Brillouin zone becomes very small, and hence only a few k-points are required to describe the variation across the Brillouin zone accurately. When calculating the properties of liquids, as has been done in this work, large systems sizes have been used and therefore only a single k-point is required, e.g. the gamma point at the centre of the Brillouin zone.

2.7 Vienna Ab-initio Simulation Package (VASP)

To solve Schrödinger's equation, even with the simplifications and approximations described, requires great computing power and software capable of achieving this. The calculations described throughout this work have been run using both the UCL HPC facility, GRACE@UCL and the UK national supercomputing service, ARCHER, as well as its former supercomputer HECToR. The software used in this work is VASP, the Vienna *Ab-initio* Simulation Package (Kresse and Hafner, 1993, 1994; Kresse and Furthmüller, 1996a,b). VASP is used in this work to perform *ab-initio* molecular dynamics simulations using the projector-augmented wave method to describe the electron-core interaction and plane wave basis sets. VASP calculates the exact instantaneous ground state and the PAW method has been used to reduce the number of plane waves required per atom.

VASP requires four basic input files; the INCAR, KPOINTS, POTCAR and POSCAR file. The POSCAR file describes both the atomic coordinates of the atom in the desired system and the volume of the cell. The POTCAR file contains all the information pertaining to the particular pseudopotential being used, which in this work is a GGA functional, PW91 (Perdew et al., 1992, 1993). The KPOINTS file determines the size of the k-point mesh and sampling of the Brillouin zone (the coordinates of a single k-point in this work). The INCAR file contains the instructions and parameters to be used in the calculation. These vary from the electronic temperature in the calculation to the type of energy minimisation algorithm used and the energy cut-off value. Also included in the INCAR file, particular to this type of study, are the instructions for molecular dynamics calculations including the desired time step and temperature.

2.8 Molecular Dynamics

In this work, to calculate the properties of liquids, molecular dynamics (MD) has been used. Instead of ensemble-averages, time-averaged quantities are calculated. The ergodic-hypothesis states that in the limit of infinitely long trajectories, the average does not depend on the initial conditions, and therefore the assumption can be made that both time- and ensemble-averaging yields the same result;

$$< A >_{ensemble} = < A >_{time} \tag{2.30}$$

MD simulations calculate the temporal behaviour of a system by breaking it down into discreet time steps and evaluating the equations of motion for the system and numerically integrating these. In VASP, the Velocity-Verlet algorithm is used to integrate Newton's equations of motions.

In Newtonian classical mechanics, a particle, initially at position $(\overrightarrow{r_0})$ and velocity $(\overrightarrow{v_0})$ and subject to a force $\overrightarrow{F}$ during time Δt, is moved to a new position $\overrightarrow{r}(t)$ according to the following relation:

$$\overrightarrow{r}(t) = \overrightarrow{r_0} + (\overrightarrow{v_0}\Delta t + \frac{1}{2}a\Delta t^2) \tag{2.31}$$

where the acceleration, $\overrightarrow{a} = \overrightarrow{F}/m$, is assumed constant during the time step Δt. If $r(t)$ is the current position and t is the increment, then the previous position is, $r(t-\Delta t)$ and the future position is, $r(t+\Delta t)$. These can be expanded using a Taylor series to find the future and past positions;

$$r(t+\Delta t) = r(t) + v(t)\Delta t + (1/2)a(t)\Delta t^2 + (1/6)b(t)\Delta t^3 + O(\Delta t^4) \tag{2.32}$$

$$r(t-\Delta t) = r(t) - v(t)\Delta t + (1/2)a(t)\Delta t^2 - (1/6)b(t)\Delta t^3 + O(\Delta t^4) \tag{2.33}$$

Adding the two expressions, then gives;

$$r(t+\Delta t) = 2r(t) - r(t-\Delta t) + a(t)\Delta t^2 + O(\Delta t^4) \tag{2.34}$$

This is the Velocity-Verlet algorithm, and provides a method for advancing the system forward in time provided the initial positions, velocities and procedure to calculate the forces are known.

Although the movement of atoms is treated classically, the forces acting on the atoms depend on the potential energy of the nuclei in the system and hence are determined quantum mechanically. The forces on the atoms are computed using the Hellman-Feynman theorem (Hellman, 1937; Feynman, 1939). The force on an ion i at position r_i can be found from the full derivative of the total energy, E,

$$F_i = -\frac{\delta E_{ext}}{\delta r_i} - \int n(r)\frac{\delta V_{ion}}{\delta r_i}dr - \int \frac{\delta E}{\delta n(r)}\frac{\delta n(r)}{\delta r_i}dr \tag{2.35}$$

where E_{ext} are all the external energies, and the final term, called the Variational force, vanishes when the wave functions are completely converged and the conditions of the Hellman-Feynman theorem are satisfied. Additional forces acting on the ions, such as Pulay forces which result from the derivative of the basis set with respect to atomic position (Pulay, 1969) are negligible as the basis sets used in this work are sufficiently large. The calculations described in this work are performed in the canonical ensemble, i.e. the number, N, volume, V and temperature, T, are fixed (also referred to as NVT calculations). To control the temperature in the simulation a thermostat algorithm is used, in this case the Nosé thermostat. Due to the nature of the calculation any value of interest is found as an average over simulation time. After each MD time step the atomic positions are written into a CONTCAR file, and as such can subsequently be used as the new POSCAR file to enable a direct continuation of the simulation.

2.8.1 The Nosé-Hoover Thermostat

The temperature of the simulation is controlled by the Nosé-Hoover thermostat and varies over simulation time. The Nosé-Hoover thermostat (Nosé, 1984) maintains constant temperature by adding two additional degrees of freedom to the system, and the use of a ficti-

tious heat bath. This work uses the Nosé algorithm such that the frequency of the temperature oscillation is controlled by the Nosé mass with a period of 40 time steps.

2.9 The Mean Squared Displacement and Radial Distribution Functions

This work uses two methods to analyse the state of the calculations, and their progression over simulation time. The first is the mean-squared displacement, (MSD), which is a measure of the deviation over time of the position of a particle to a reference position. The mean-square of the distance travelled by a particle following a random path is proportional to the time elapsed;

$$< r^2 >= 6Dt + C \tag{2.36}$$

In which $< r^2 >$ is the mean-square distance, t is the time and D and C are constants. The constant D is important as it defines the diffusion rate and is called the diffusion coefficient. The MSD is the averaged squared distance moved by the particles and so, if the system is in a liquid state, over long periods a continuous linear increase in MSD is observed with time (Chapter six, Figure 6.4).

The second method used in this work is the radial distribution function, $g(r)$. The radial distribution function of a system of particles describes how atomic density varies as a function of distance from a reference particle, and can be used to describe the distance between the nearest neighbours in the system;

$$g(r) = \frac{n(r)}{\rho 4\pi r^2 \Delta r} \tag{2.37}$$

In which $n(r)$ is the mean number of atoms, with mean atom density ρ, in a shell of width Δr, at a distance, r. In a liquid there will be an apparent peak at the position of the first nearest neighbour followed by a diffuse pattern. This is very distinctive of a liquid and serves as a secondary check of the state of the system (Chapter six, Figure 6.5).

2.10 The Blocking Method

MD simulations involve a series of time-steps, in which properties will fluctuate over time and the desired quantity is a time-averaged value, m . Thus, a measure of the error of the time-averaged value, m of a sample size, N, is the variance of the mean, $\sigma^2(m)$,

$$\sigma^2(m) = \frac{\langle m^2 \rangle - \langle m \rangle^2}{N} \tag{2.38}$$

This estimate of the variance is valid only for un-correlated sample sizes, whereas MD simulations involve a series of distinct but correlated time-steps. Therefore a different estimate of the error is required. The blocking method (Flyvbjerg and Petersen, 1989) provides this by calculating the variance, $\sigma^2(m)$, accounting for the correlation. The correlated calculations are broken down into blocks and the standard error of m is computed for each block. The block size is then increased, and with increasing block size, the error estimate approaches the true error.

2.11 Thermoelastic Properties

2.11.1 The Equation of State

VASP *ab-initio* molecular dynamics calculations determine the properties of a system at every time step. The calculated value then equilibrates over simulation time such that the average pressure, volume and temperature of the system can be determined with sufficiently long simulation time. From the volume of the system and some prior knowledge of the material being simulated (i.e. atomic mass, along with the number of atoms in the simulated system) the density can be readily determined. At a single temperature the pressure of a system at a series of volumes (set within the POSCAR file) can be calculated using the NVT ensemble in VASP and fitted to a finite 3rd order Eulerian strain expression, the Birch-Murnaghan 3rd Order equation of state (BM3EOS; Birch, 1947; Murnaghan, 1937), which in turn can be used to find additional important properties of a system. The isothermal BMEOS gives the following relationship between internal energy (the Helmholtz free energy) and volume;

$$F(V) = F_0 + \frac{9V_0K_0}{16}\left\{\left[\left(\frac{V_0}{V}\right)^{\frac{2}{3}} - 1\right]^3 K_0' + \left[\left(\frac{V_0}{V}\right)^{\frac{2}{3}} - 1\right]^2 \left[6 - 4\left(\frac{V_0}{V}\right)^{\frac{2}{3}}\right]\right\} \tag{2.39}$$

which can be related to the pressure using the following thermodynamic relation,

$$P = -\left(\frac{\partial F}{\partial V}\right)_T \tag{2.40}$$

thus producing the Birch-Murnaghan 3rd order equation of state;

$$P = \frac{3K_0}{2}\left[\left(\frac{V_0}{V}\right)^{\frac{7}{3}} - \left(\frac{V_0}{V}\right)^{\frac{5}{3}}\right]\left\{1 + \frac{3}{4}(K_0' - 4)\left[\left(\frac{V_0}{V}\right)^{\frac{2}{3}} - 1\right]\right\} \tag{2.41}$$

where P is the pressure, V_0 is the initial volume (usually taken as the volume at 0 GPa), V is the deformed volume (volume at pressure P), K_0 is the bulk modulus of the material at 0 GPa, and K_0' is the first derivative of bulk modulus evaluated at 0 GPa with respect to pressure (Poirier, 2000). Equation 2.41 is the expression fitted to the calculated pressures and volumes. Equation 2.41 can also be used to calculate the isothermal bulk modulus (or incompressibility), which is a measure of a material's resistance to uniform compression,

$$K_T = -V\left(\frac{dV}{dP}\right)_T \tag{2.42}$$

To calculate the thermodynamic properties of a system, the procedure described above can be repeated for a series of isotherms to produce a comprehensive picture of how the material behaves across a range of pressures and temperatures.

2.11.2 Coefficient of Thermal Expansion

When a system is subject to a change in temperature it will tend to change in volume also. This can be understood in terms of the movement of the atoms. When a material is heated the particles have more kinetic energy and therefore will maintain a greater average separation resulting in an expansion of the material due to the anharmonicity in the atomic

displacements. The volumetric coefficient of thermal expansion, α, is a measure of the fractional change in volume per degree change in temperature at a constant pressure;

$$\alpha = \frac{1}{V}\left(\frac{dV}{dT}\right)_P \tag{2.43}$$

which can be equally expressed as,

$$\alpha = \left(\frac{ln(V(T')/V(T))}{(T'-T)}\right)_P \tag{2.44}$$

in which V, T and P have their usual meaning and T' $>$ T. The BM3EOS can be calculated for a series of isotherms to calculate the volumetric coefficient of thermal expansion.

2.11.3 Grüneisen Parameter

The Grüneisen parameter is a dimensionless measure of how the temperature of a system will vary along an isentrope (reversible adiabat). Grüneisen (1912) described the microscopic definition of this parameter (γ_i) as the volume dependence of the i^{th} mode of vibration of the lattice (ω_i);

$$\gamma_i = -\frac{\delta ln\omega_i}{\delta lnV} \tag{2.45}$$

The sum of all γ_i throughout the first Brillouin zone leads to a macroscopic, sometimes referred to as the thermodynamic, definition of the Grüneisen parameter γ_{th}:

$$\gamma_{th} = \frac{\alpha V K_T}{C_V} \tag{2.46}$$

Each of the values necessary to compute the macroscopic Grüneisen parameter can be calculated from the methods described previously. An identical expression of γ is given by:

$$\gamma = V\left(\frac{dP}{dE}\right)_V \tag{2.47}$$

Where P is the pressure, V is the volume and E is the sum of the excess internal energy that arises from interactions, E_{XS} and the contribution due to the kinetic energy of the nuclei.

$$E = E_{XS} + \left(\frac{3}{2} N k_B T\right) \tag{2.48}$$

In which, N is the number of atoms, k_B the Boltzmann constant and T is the temperature of the calculation.

2.11.4 Adiabatic Temperature Gradient

The adiabatic temperature gradient describes how temperature changes with pressure within a planet. The adiabatic temperature gradient is given by;

$$\left(\frac{dT}{dP}\right)_S = \left(\frac{dV}{dS}\right)_P \tag{2.49}$$

in which S is the entropy, and all other terms have their usual meaning. This gives the following relation for the adiabatic gradient;

$$\left(\frac{dT}{dP}\right)_S = \left(\frac{\alpha V T}{C_P}\right) \tag{2.50}$$

In which $C_P = C_V(1 + \alpha\gamma T)$ is the constant pressure specific heat and all other terms are as previously described.

The adiabatic gradient can also be expressed using an alternate form, which has also been used in this work, which includes the adiabatic bulk modulus, given by,

$$K_S = K_T(1 + \alpha\gamma T) \tag{2.51}$$

Hence the adiabatic gradient can become:

$$\left(\frac{dT}{dP}\right)_S = \frac{\gamma T}{K_S} \tag{2.52}$$

The left hand side of the equation is the adiabatic change in temperature with pressure, hence we can use $dP = \rho g dz$ to obtain the adiabatic change with depth;

$$\left(\frac{dT}{dz}\right)_{adiabatic} = T\frac{\gamma g}{VK_S} \tag{2.53}$$

where g is the acceleration due to gravity and all other terms are as previously described.

2.12 Spin Crossover

This doctoral research focuses on the properties and behaviour of liquid metals and as such will need to consider their magnetic properties. As described in the first chapter liquid metals may (at low pressures and temperatures) undergo a high to low spin transition during which the magnitude of finite atomic moments on the individual atoms decreases to zero. This transition has important implications for the thermo-elastic properties of the material and thus must be considered fully. VASP *ab initio* calculations neglect magnetic entropy, a fundamental part of the Helmholtz free energy of the system, and so, to include this, free-energy minimisation and thermodynamic integration is used. There are two main types of free-energy, the Helmholtz free energy, F;

$$F = E - TS \tag{2.54}$$

and the Gibbs free energy, G,

$$G = F + PV \tag{2.55}$$

where P and V are the pressure and volume respectively, S is the entropy of the system and E the total internal energy. The Helmholtz free energy describes the maximum amount of work a system can achieve at constant volume and temperature, whilst the Gibbs free energy is the maximum amount of work at constant pressure and temperature. For a system with fixed temperature, number of atoms and volume, the Helmholtz free energy is a minimum for a system at equilibrium. Analogously, for a system of N atoms at constant pressure

and temperature, Gibbs free energy is a minimum. These two conditions can be derived from the second law of thermodynamics, which states, that for a closed system with energy E, volume V and number of particles N, the entropy is at a maximum when the system is in equilibrium. Vitally, as will be apparent in later sections, the Gibbs free energy can be used as a criterion for determining the most stable state from a series of possibilities, as, at constant pressure, temperature and number of atoms, the state with the lowest Gibbs free energy is the most stable.

2.12.1 Thermodynamic Integration

This magnetic entropy is dependant on the magnetic moment of the atoms, and acts negatively on the free energy of the system, such that it may stabilise larger finite local moments to higher pressures and temperatures.

This work relies on the use of thermodynamic integration to include magnetic entropy and determine the Gibbs free energy of four possible magnetic spins states for both pure liquid iron and $Fe_{0.8}S_{0.1}Si_{0.1}$ and hence, calculate the magnetic transition of both materials at the conditions of Mercury's core. In the following sections an introduction to the theory of thermodynamic integration will be put forward, a guide to its implementation and method can be found in Chapter seven.

The Helmholtz free energy that can be computed using "free" spin calculations is;

$$F = E - T(S_{el} + S_{vib} + S_{conf}) \tag{2.56}$$

In which the internal energy is denoted by E, temperature, T, and $S_{el}, S_{vib}, S_{conf}$ represent the electronic, vibrational and configurational entropies. In the canonical ensemble (which has been used here), the Helmholtz free energy can be calculated from the BM3EOS (equation 2.41) which is an expression of the relationship between the pressure and volume of the system, and using the thermodynamic identity expressed in equation 2.40.

The expression described in equation 2.56 is incomplete for a magnetic system, an additional term is required in the Helmholtz free energy, a magnetic entropic term, S_{mag};

$$F = E - T(S_{el} + S_{vib} + S_{conf} + S_{mag}) \tag{2.57}$$

In which all terms are as previously described and S_{mag} is equal to;

$$S_{mag} = k_B \sum_i ln(\mu_i + 1) \tag{2.58}$$

in which μ_i refers to the magnitude of the atomic moment. Thermodynamic integration was used to include the magnetic entropy, but this will not find the absolute Helmholtz free energy of a system, rather, a relative free energy to a reference state. In this work, the reference state has been chosen to be the low spin state (LS) of the materials. In the low spin state, each atom has a zero magnetic moment, i.e. the spins are orientated such that they cancel out (Figure 2.2).

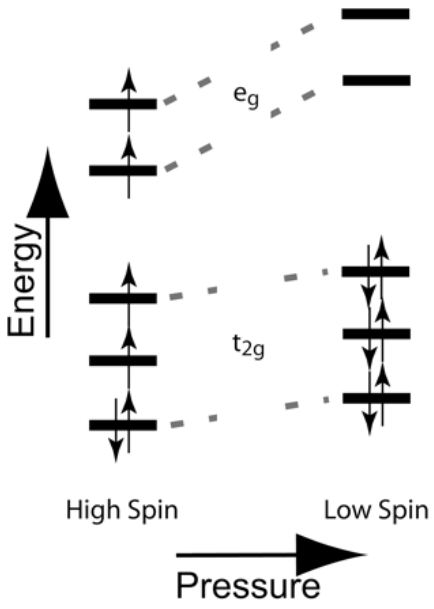

Figure 2.2: Distribution of electrons among *3d* orbitals for 6-fold coordinated Fe^{2+} in the high spin (left) and low spin (right) configurations. At low pressure iron is in the high-spin state, resulting in a magnetic moment on the atom caused by the presence of un-paired spins. With increasing pressure the energies of all the orbitals increases, thus iron transitions to the low spin configuration, with all electrons spin paired and therefore no magnetic moment. Image from Speziale et al. (2005). Copyright 2005 National Academy of Sciences, U.S.A.

The reference LS Helmholtz free energy is calculated using equation 2.39. However, to calculate the Helmholtz free energy of additional states with varying magnitudes of local atomic moment the Kirkwood coupling parameter method was used (Kirkwood, 1935). The Kirkwood coupling parameter method can be described by considering an N-particle system, with the potential energy function U. The potential energy function, U, is assumed to depend linearly on a coupling parameter, λ, such that for $\lambda = 0$, U equals the potential energy of the reference system, the low spin state, *LS*. At $\lambda = 1$, U equals the potential energy of the magnetic system in question (*MS*). The derivative of the Helmholtz free energy ($F(\lambda)$) with respect to λ can be written as an ensemble average for a system with potential energy U_λ:

$$\left(\frac{\partial F(\lambda)}{\partial \lambda}\right)_{N,V,T} = \left\langle \frac{\partial U(\lambda)}{\partial \lambda} \right\rangle_\lambda \tag{2.59}$$

The free energy difference between the LS and MS states can be obtained by integrating equation 2.59:

$$F(\lambda = 1) - F(\lambda = 0) = \int_{\lambda=0}^{\lambda=1} d\lambda \left\langle \frac{\partial U(\lambda)}{\partial \lambda} \right\rangle_\lambda \tag{2.60}$$

From the Helmholtz free energy, the Gibbs Free energy can be found (eq. 2.55) for each state. In this work the Gibbs free energies is then interpolated between five states, the LS, and four magnetic states of increasing magnetic moment per atom. The Gibbs free energy is then minimised to find the magnetic moment at each pressure (Figure 2.3).

From the magnetic transition of each material, the corresponding volume and energy relationships are found by interpolating between the volumes and energies of the original four magnetic states and the calculated magnetic state (Chapter seven). A full description of the method used to implement thermodynamic integration is given in Chapter seven.

2.13 Evolution of Planetary Cores

The adiabatic gradient is particularly useful as it can be used to investigate the evolution of planetary cores. As a planet evolves over time the planet cools and solidifies. Knowing the

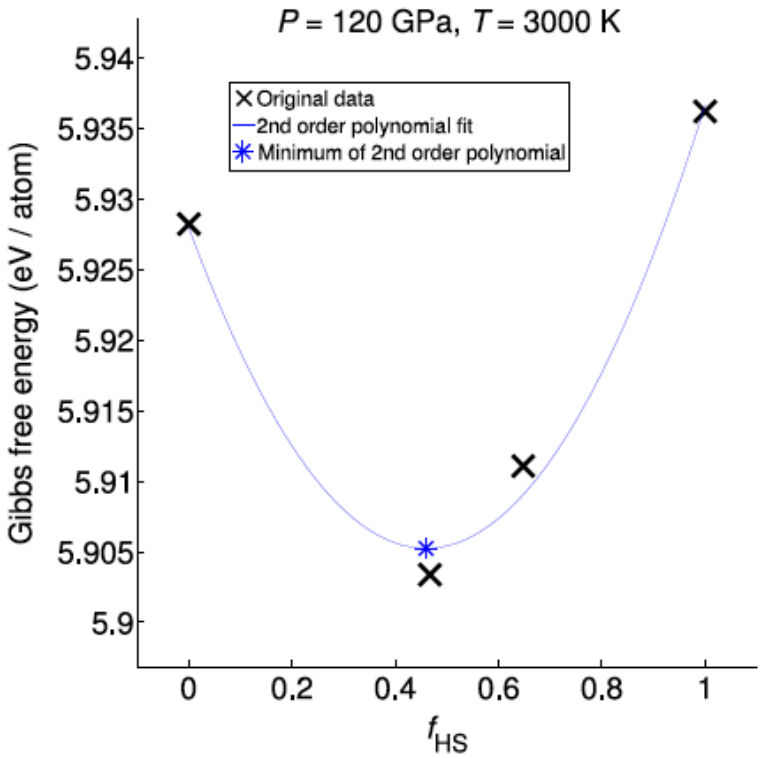

Figure 2.3: The stable magnetic state is found by comparing the Gibbs free energy of the four spin states and fitting a parabola between them. The minimum of the parabola then determines the value of the magnetic moment. Figure from (Holmström and Stixrude, 2015). The corresponding plot for this work is shown in Chapter seven. Reprinted figure with permission from E. Holmström and L. Stixrude, APS Physical Review Letters, 114, 117202, 2015. Copyright 2015 by the American Physical Society.

adiabatic gradient of a planet forming material and its melting curve leads to the crystallising behaviour of the material. As shown in Figure 2.4, if the adiabatic gradient is found to be shallower than the slope of the melting curve, then this results in a core that crystallises from the bottom up; this is the case for the Earth, where the inner core is crystallising from the outer core. However, if the adiabatic gradient is steeper than the slope of the melting curve then the core will crystallise from the top down, solidifying at lower pressures towards the surface and snowing down dense material to form a solid inner core. By determining the thermodynamic properties of liquid iron and liquid iron alloys relevant to the core of Mercury, the evolution of Mercury's core and possible crystallisation regime of Mercury's core can be determined.

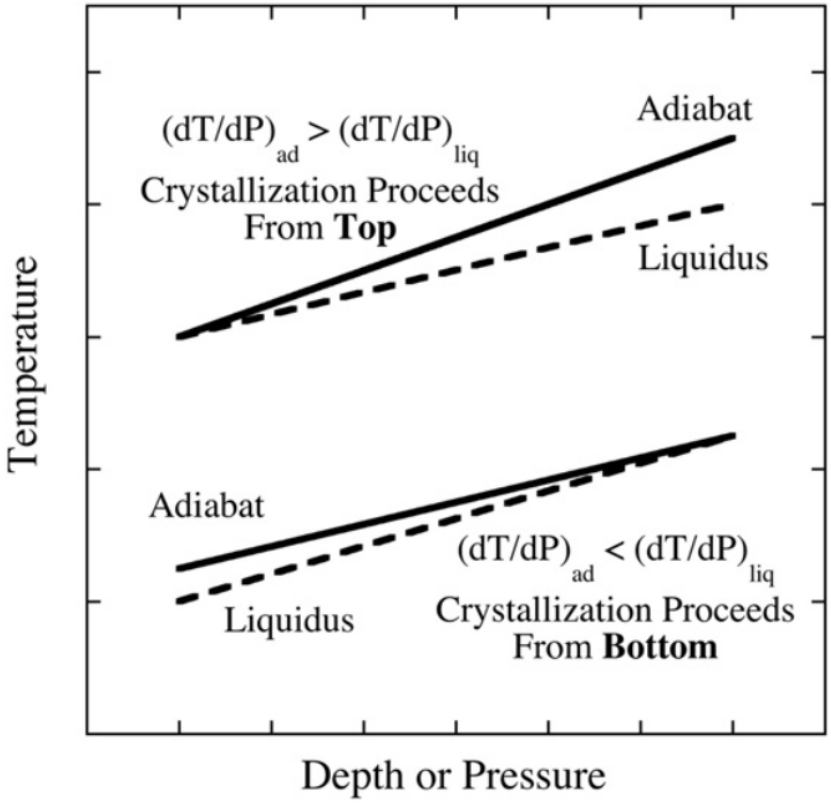

Figure 2.4: Description of the consequences of the relative slopes of the melting curve and adiabatic gradient of a material. In the above figure, the melting curve discussed in the text is referred to as the liquidus. The difference in these terms are simply that the melting curve refers to a single component material whereas liquidus refers to a multi-component material. In the context of this section, these can be thought of as referring to the same thing, the temperature at which a material melts. If the melting curve/liquidus is steeper than the adiabat then crystallisation will proceed from the bottom up, growing out from the inner core. If the opposite is true, and the melting curve is shallower than the adiabat, crystallisation will proceed from the top down, snowing down through the core. Reprinted from Earth and Planetary Science Letters, 284, Quentin Williams, Bottom-up versus top-down solidification of the cores of small solar system bodies: Constraints on paradoxical cores, 564 - 569, Copyright 2009, with permission from Elsevier.

2.14 Summary

This chapter has provided a theoretical background for the calculations performed in this thesis and detailed the methods required for the calculation of the equations of state, isothermal bulk modulus and magnetic transition of pure liquid iron (Chapters six and seven) and $Fe_{0.8}S_{0.1}Si_{0.1}$ (Chapters eight and nine) at 2000, 3000 and 4000 K, using both "free" spin calculations (Chapters six and eight) and thermodynamic integration (to include the effects of magnetic entropy; Chapters seven and nine). It has also detailed the calculation of the mean volumetric coefficient of thermal expansion and Grüneisen parameter for pure liquid iron and $Fe_{0.8}S_{0.1}Si_{0.1}$ between 2000 - 4000 K (Chapters six, seven, eight and nine). The following chapter will present the other half of the techniques used in this thesis and the methods required to investigate the melting behaviour of $Fe_{0.8}S_{0.1}Si_{0.1}$.

Chapter 3

Experimental Methods

This thesis presents a two-pronged approach to understanding the evolution and composition of Mercury's core. The first relies heavily on the use of *ab initio* computational methods (described in Chapter two). These can probe Mercury's core-forming materials on a fundamental level, giving direct access to their thermal and physical properties. However, as discussed in Chapter two, two forms of information are required to determine the crystallisation behaviour of a material: the adiabatic gradient (determined here using computational methods) and the slope of the liquidus determined from both this study and other experiments. The melting behaviour of a candidate Fe-S-Si alloy, $Fe_{0.8}S_{0.1}Si_{0.1}$, has been investigated experimentally using laser-heated diamond-anvil-cell (LH-DAC) techniques off-line at the University of Bristol (Chapter five). *In-situ* experiments were also performed at the Diamond Synchrotron Facility (Chapter five), but were ultimately unsuccessful. This chapter will describe the experimental analysis used in this work, including both off-line and *in-situ* melting methods, and explain the fundamental choices made in the methods of obtaining the liquidus of Fe-S-Si.

3.1 Diffraction Techniques

X-ray diffraction was used to investigate the melting behaviour of Fe-S-Si (Chapter five), as it can provide a definitive method for distinguishing solid from liquid materials by the loss of the sharp "Bragg reflections" from the solid phase. X-ray diffraction involves the diffraction or "reflection" of an incident beam by the sample being investigated. This section will briefly describe the theory of the diffraction technique, as well as the fundamental

principles upon which it is based, starting with Bragg's Law.

3.1.1 Bragg's Law

The production of a diffraction pattern is the result of an incident beam (X-rays in this work) that upon "reflection" produces a diffracted beam in which the X-rays, scattered by planes of atoms in the crystal, interfere constructively. If two reflected X-rays are coherent with a path difference of an integer number of wavelengths, n, then they will constructively interfere and produce a peak of diffracted intensity. This is most simply described using Bragg's Law (schematic of equation 3.1 given in Figure 3.1):

$$2dsin\theta = n\lambda \tag{3.1}$$

In which, d denotes the perpendicular distance between two adjacent planes, and can be described as a function of the Miller indices (hkl) of the appropriate lattice planes, i.e. for a simple cubic lattice with lattice vector a;

$$d_{hkl} = \frac{a}{\sqrt{h^2+k^2+l^2}} \tag{3.2}$$

As is visualised in Figure 3.1, if plane-wave X-rays are incident at an angle θ on a set of crystallographic lattice planes separated by a distance, d_{hkl}, the relative phase shift of the reflected wave is a function of the position of the atoms along the line perpendicular to the lattice planes. For example, in Figure 3.1 the phase shift of the reflected waves from the two darker atoms in the centre of the top and middle planes is equal to $2dsin\theta$ for any arbitrary value of θ. Constructive interference, however, will only occur if the phase shift, $2dsin\theta$, is a multiple of the wavelength λ, i.e. the set of hkl values satisfy Bragg's Law and produce a Bragg reflection. Each crystalline structure contains a unique set of d-spacings, and thus, if these can be indexed (i.e. the hkl values found), the sample can be identified and the sample's unit cell determined.

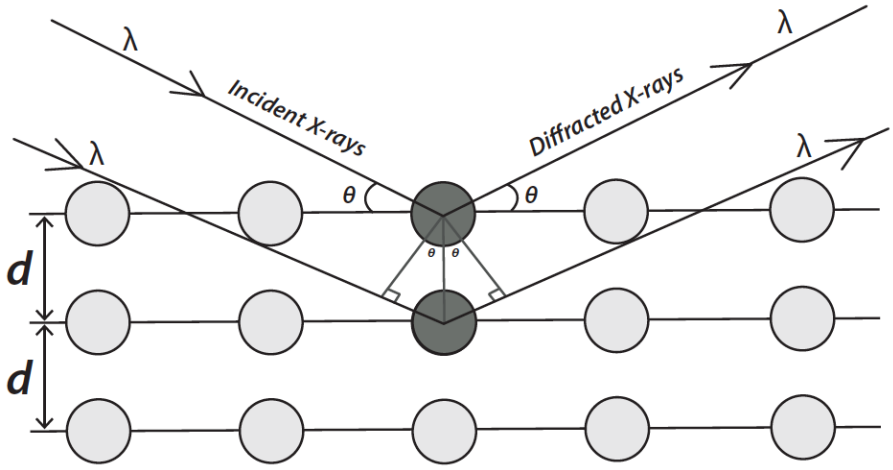

Figure 3.1: Visualisation of the Bragg Equation. Maximum scattered intensity is only observed when the phase shifts add to a multiple of the incident wavelength λ. Figure based on the Bragg diagram included in Birkholz et al. (2006).

3.1.2 Building A Diffraction Pattern

A single reflection angle, θ, will reveal the presence, or not, of a peak of intensity for a single set of lattice planes. Thus, in order to build a diffraction pattern, and systematically sample all various positions and possible lattice planes, one must sample a variety of different angles, or some other variant in Bragg's Law. A way of doing so is by varying the angle of the detector to the sample. When a plane, *hkl*, oriented in a single crystal satisfies the Bragg condition, the scattered radiation will be at a known angle, 2θ, with respect to the incident beam, such that placing a detector at this angle will be able to measure the intensity. Then, to image as many of the different lattice planes as possible, the detector and sample are moved, which will allow planes with a different set of Miller indices to satisfy the Bragg condition. This is the case for a single-crystal sample. However, this process can be simplified by, instead, using a polycrystalline powder. In this case, the sample can then be thought of as containing a very large number of small, randomly oriented single crystals such that for any reflection *hkl*, there will always be a finite number of planes oriented at the correct Bragg angle. However, when using a powdered sample, a single beam of reflected radiation becomes a cone of intensity, so, ideally, a cylindrical detector is required that measures the scattered radiation as a function of 2θ.

3.1.3 The Structure Factor

The structure factor is of fundamental importance when analysing a diffraction pattern as it provides a relationship between the intensity of the measured peaks, the position of the atoms in the unit cell and the atomic scattering factors (Figure 3.2).

$$F_{hkl} = \sum_{n=1}^{N} f_n exp[2\pi i(hx_n + ky_n + lz_n)] \tag{3.3}$$

In this expression, f_n denotes the atomic scattering factor of the n^{th} atom (which is the ratio of the amplitude of the X-rays scattered by this atom to that scattered by a single electron), x y and z are the fractional coordinates of the atom within the unit cell and h, k and l indicate the Miller indices of the lattice plane.

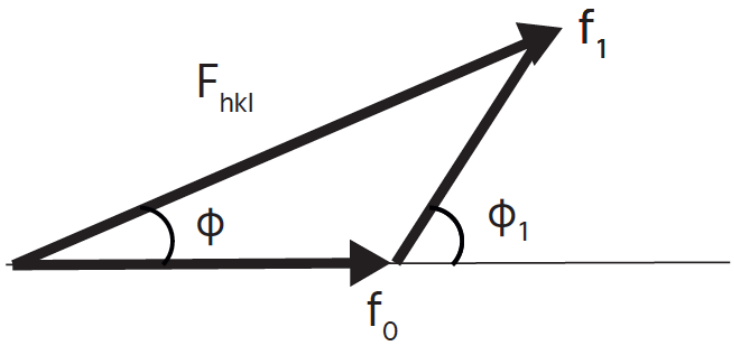

Figure 3.2: Vector diagram of the structure factor expression and the resultant wave scattered from two sets of atoms. The amplitudes of the waves are proportional to the atomic scattering factors f_0 and f_1. The phases differ by an angle ϕ_1. The resultant vector represents the two-atom structure factor with amplitude F_{hkl}. The offset in the positions of the two set of atoms introduces a net phase ϕ due to the phase difference. Figure recreated from the 'Structure factor' figure, Online Dictionary of Crystallography (IUCr) (2008).

3.2 Powder Diffraction

As described briefly in Section 3.1.2 there are many advantages to the use of a powdered sample rather than a single crystal. However, a powdered sample does have one significant disadvantage as it produces overlapping peaks. The Rietveld and Le Bail methods are ways

of distinguishing between peaks from different Bragg reflections.

3.2.1 Le Bail and the Rietveld Method

The Rietveld (1967) method relies on the diffraction peaks being of a known shape, and therefore the diffracted intensity from overlapping or partially overlapping peaks can be simply described as the sum of the contributions from the individual Bragg peaks. The peak position, intensity and shape in a given X-ray pattern are determined by a variety of factors from the experiment (e.g. beam characteristics or experimental set up) and the sample (e.g. fractional atomic coordinates and unit cell structure). In the Rietveld method (1967), a theoretical line profile is built using these parameters and refined using a least-squares refinement within an iterative process (Rietveld, 1969; e.g. Figure 3.3). The Le Bail method simplifies the use of the Rietveld method by removing the necessity to refine the structural factors. Instead, when fitting the powder diffraction pattern, this method obtains the initial intensities either from a Rietveld type calculation or by assuming all intensities are equal, after which the intensities of the peaks are then allowed to vary so as to obtain the best fit to the data. The advantage of the Le Bail method (Le Bail et al., 1988) is that it provides, in principle, the least-biased values for the unit-cell parameters as it is unaffected by factors such as preferred orientation in the sample.

The General Structure Analysis System (GSAS; Von Dreele and Larson, 1994) and EXPGUI the graphical user interface for GSAS (Toby, 2001), are software packages that fit structural models to X-ray and neutron diffraction data. They can be used for both single-crystal and powder diffraction data, and are capable of using both the Rietveld (shown in Figure 3.3) and Le Bail fitting methods.

3.2.2 Diffraction by Liquids

In a crystal there is long range order, such that single-crystal or powder diffraction from a solid sample will result in sharp Bragg peaks. However, liquid or amorphous samples only have short range order, and therefore, the resultant intensity from X-ray diffraction will be diffuse, producing broad “humps” rather than the sharp Bragg peaks characteristic of a crystalline sample (e.g. Figure 3.4). The appearance of diffuse Bragg peaks can therefore be used as a melting diagnostic, indicating the onset of melting in a sample. *In-situ* experiments

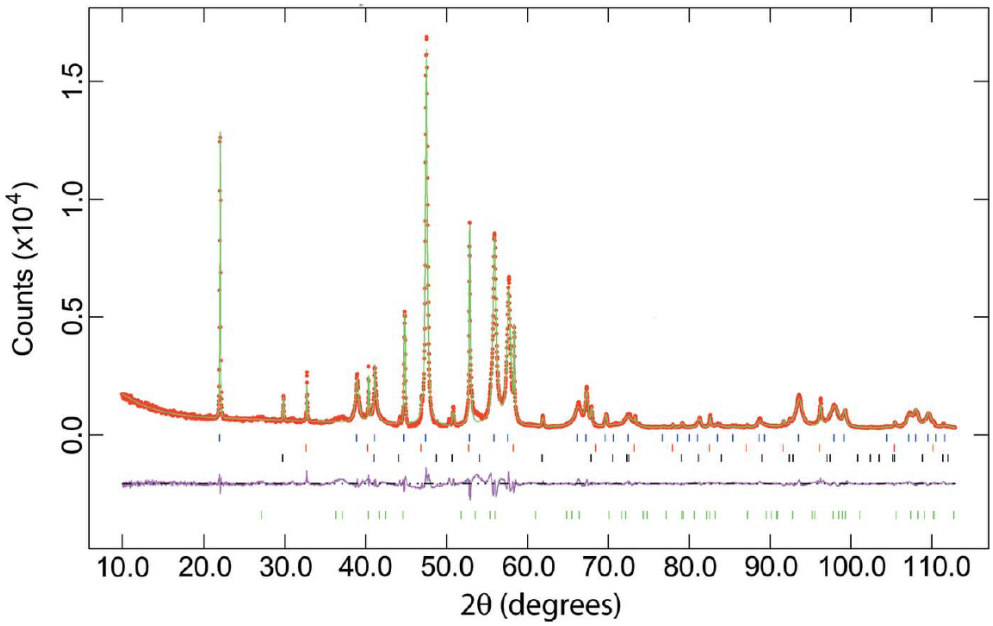

Figure 3.3: GSAS Rietveld refinement, in which the red crosses indicate the observed pattern, the green line marks the fitted pattern and the difference between these shown by the purple line underneath. Figure from Wood et al. (2013).

(e.g. Chapter five) use this as the primary criteria for identifying the melting temperature of material; X-ray diffraction patterns are obtained at set intervals with increasing temperature, such that the appearance of diffuse Bragg peaks indicate the melting temperature.

3.3 Generating High Pressures

Mercury's core reaches pressures of approximately 36 GPa (Hauck et al., 2013) and so this study has used Diamond-Anvil Cells (DACs) to study the behaviour of Fe-S-Si to 50 GPa. DACs are not the only method of obtaining high pressures experimentally, other experimental techniques include the Multi-Anvil Press (MAP) and Piston Cylinder (PC). The PC is one of the simplest methods of generating high pressure, which is produced by a piston pressing into a cylinder compressing a solid sample held in the assembly; it is typically capable of reaching pressures up to 6 GPa (Holloway and Wood, 1988). The MAP is used in Chapter four but only in an attempt to create the Fe-S-Si starting material for further compression in a DAC, and will be described in the next section.

Static compression is not the only technique to study materials at ultra-high pressure, as

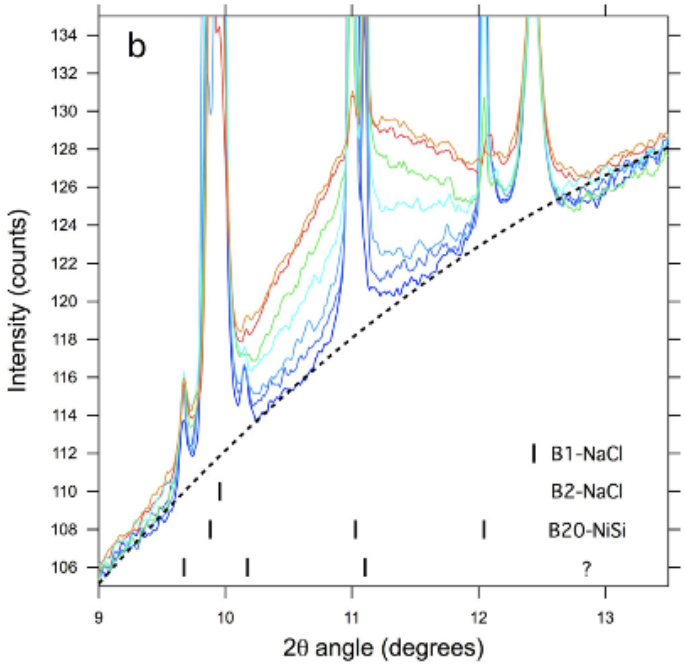

Figure 3.4: Diffraction from a liquid or amorphous sample will result in broad diffuse Bragg peaks, in stark contrast to the sharp Bragg peaks produced by a crystalline sample. Upon increasing temperature the sharp Bragg peaks of NiSi disperse into broader peaks (blue to red lines) which indicate that the sample has melted. Figure from Lord et al. (2014a)[1].

shock waves can provide extremely high pressures and temperatures, albeit on a very short timescale. Shock wave experiments use a projectile like set-up in which pressure is determined by the speed of the projectile and the relationship between the temperature, pressure and density of the material as defined by the material's unique Hugoniot curve. However, shock wave experiments commonly result in the loss of the sample and hence have not been used here.

3.3.1 The Multi-Anvil Press

Pressure is generated in the multi-anvil cell by compression in four or more directions, i.e., the tetrahedral set up with compression from four directions, the cubic set-up with six or the octahedral with eight. Pressure in the vessel is produced by hydraulic rams that drive pistons compressing the assembly. Modern designs of the MAP include two stages of anvils in the

[1]Reprinted from Physics of The Earth and Planetary Interiors, 233, Oliver T. Lord, Elizabeth T.H. Wann, Simon A. Hunt, Andrew M. Walker, James Santangeli, Michael J. Walter, David P. Dobson, Ian G. Wood, Lidunka Vočadlo, Guillaume Morard, Mohamed Mezouar, The NiSi melting curve to 70GPa, 13 - 23, Copyright 2014, with permission from Elsevier.

octahedral design, the first are hardened steel anvils, which then press onto the second set of eight tungsten carbide anvils, whose inner corners are truncated to create an octahedral space in the centre, within which the sample sits (Figure 3.5). X-ray diffraction is then possible on the pressurised sample by passing the X-ray beam through the gaps between the anvils.

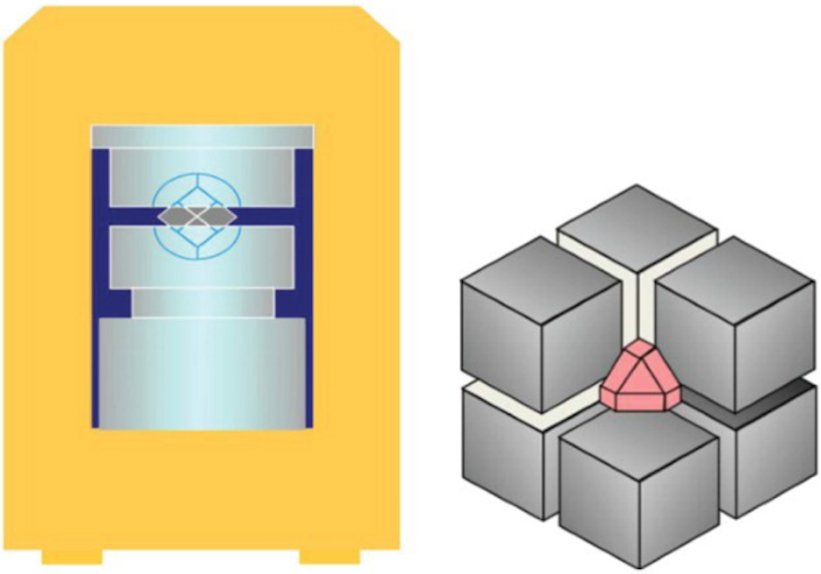

Figure 3.5: A diagram showing the truncated tungsten-carbide cubic anvils around the octahedral sample cell on the right, and on the left, the arrangement within the steel sphere inside the press. Figure from Liebermann (2011).

Multi-anvil cells can be used for pressures up to 25 GPa, but most commonly below 20 GPa, with the exception of sintered diamond-anvils with can reach up to 100 GPa . The samples placed within are usually easily recoverable and relatively large (e.g. on the order of millimetres). This is extremely useful for the production of starting materials (e.g. in Chapter four), and in experiments where the sample is needed for post processing e.g. looking at quench textures. However, the diffraction patterns obtained are complex and will include many patterns overlaid from the materials involved in the experimental assembly. This can make analysis challenging, as all these diffraction patterns need to be "removed" to reveal the desired properties of the sample. To both its benefit and detriment, the MAP can experience heavy deviatoric stresses. This is useful for studying the deformation behaviour of materials, but when hydrostatic stress is required, much care is needed to avoid such stresses. The conditions that can be achieved in the MAP match those of Mercury's

possible outer core pressures (approximately 5-8 GPa at the core-mantle boundary). However, the deep interior of the planet may reach up to 36 GPa (e.g. Hauck et al., 2013), which is only possible to obtain in a MAP using sintered diamond-anvils. These are typically less than 10mm in length (Irifune and T, 2010) and can reach pressures up to 100 GPa; however, this is a very expensive experimental technique. In this work, the MAP was used to manufacture the Fe-S-Si starting material, described in detail in Chapter four. However, the diamond-anvil cell (DAC) was used to achieve the conditions thought to be present in the centre of Mercury.

3.4 The Diamond-Anvil Cell

In a diamond-anvil cell, the sample, which is very small, is compressed between the truncated tips of two diamonds. In order to obtain a hydrostatic, or quasi-hydrostatic environment the sample is contained within a "gasket", generally a metal foil with a small hole drilled through it, and immersed in a pressure transmitting medium such a mixture of methanol-ethanol or, for higher pressures, an inert gas such as neon or helium (see Figure 3.6). This is a very powerful technique as a relatively small amount of force on the top of the two opposing diamonds can generate very large forces on the diamond culet, such that DACs are capable of generating pressures up to 360 GPa. Diamond is transparent to X-rays and has a very small unit-cell, which reduces the complexity involved with indexing the diffraction pattern. The advantages of the DAC set up lie in its simplicity, and that in most cases the diamonds are fully recoverable (although ultra-high pressures and temperatures may result in damage to the diamond), along with the experimental sample, allowing for post-processing and further analysis of the experiment. However, the sample sizes have to be very small, which can be challenging but advancing techniques including laser ablation have made the production of samples on this scale much more accessible.

There are in general two types of DAC, screw type and gas membrane type (Figure 3.7). Within each distinction there are various methods of generating pressure, but broadly speaking, gas membrane DACs create pressure by inflating a gas membrane behind the mount of one of the diamonds, forcing them together (Figure 3.7). Gas membrane methods are capable of precisely and remotely controlling the pressure of an experiment, but they can be difficult to set up and thus challenging to maintain. In contrast, screw type DACs create

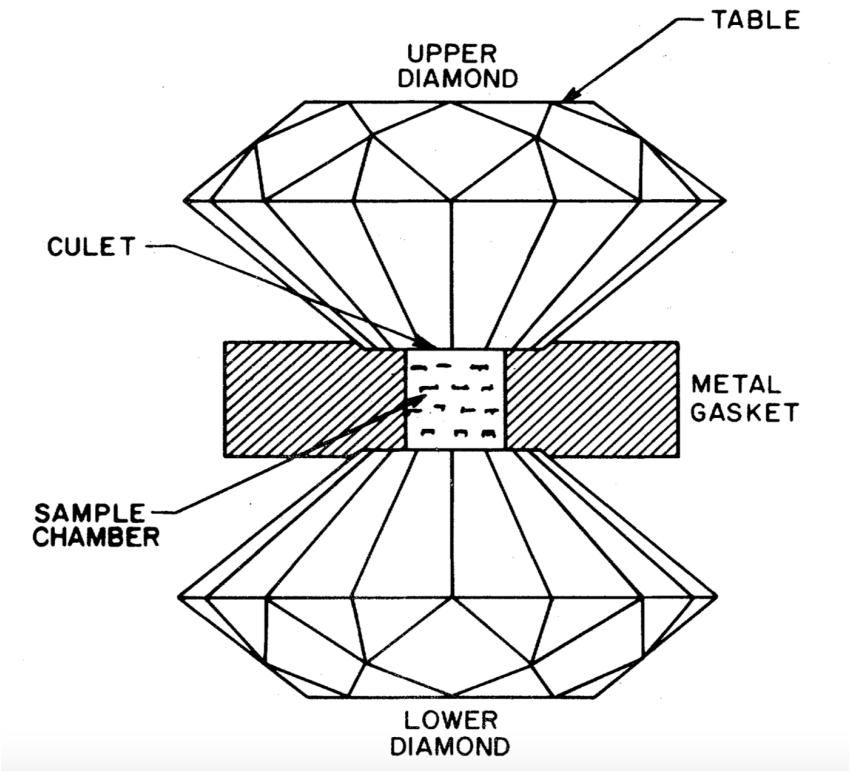

Figure 3.6: Schematic of the Diamond-Anvil Cell. Figure from Jayaraman (1983)[2].

pressure by the tightening of the screws that hold the two diamonds together, decreasing the distance between the diamond culets and increasing the pressure on the sample held between (e.g. shown in Figure 3.7). This work used the screw-type Princeton cell as screw type DACs are a relatively simpler design whilst also capable of providing a stable pressure over long periods of time.

3.4.1 Experimental Set-Up of a Diamond-Anvil Cell

The DACs used throughout this work are Princeton-type symmetric DACs. The diamonds mounted in the DACs had culet sizes that varied between 200 - 500 μm, depending on their use. The method of setting up the diamond-anvil cell is as follows:

1. Preparing the diamonds.

The diamonds are first cleaned and then checked thoroughly to ensure that they are aligned correctly with each other and set fully in the holder. The diamonds are cleaned under a

[2]Reprinted figure with permission from A. Jayaraman, Reviews of Modern Physics, 55, 65 - 108, 1983. Copyright 1983 by the American Physical Society.

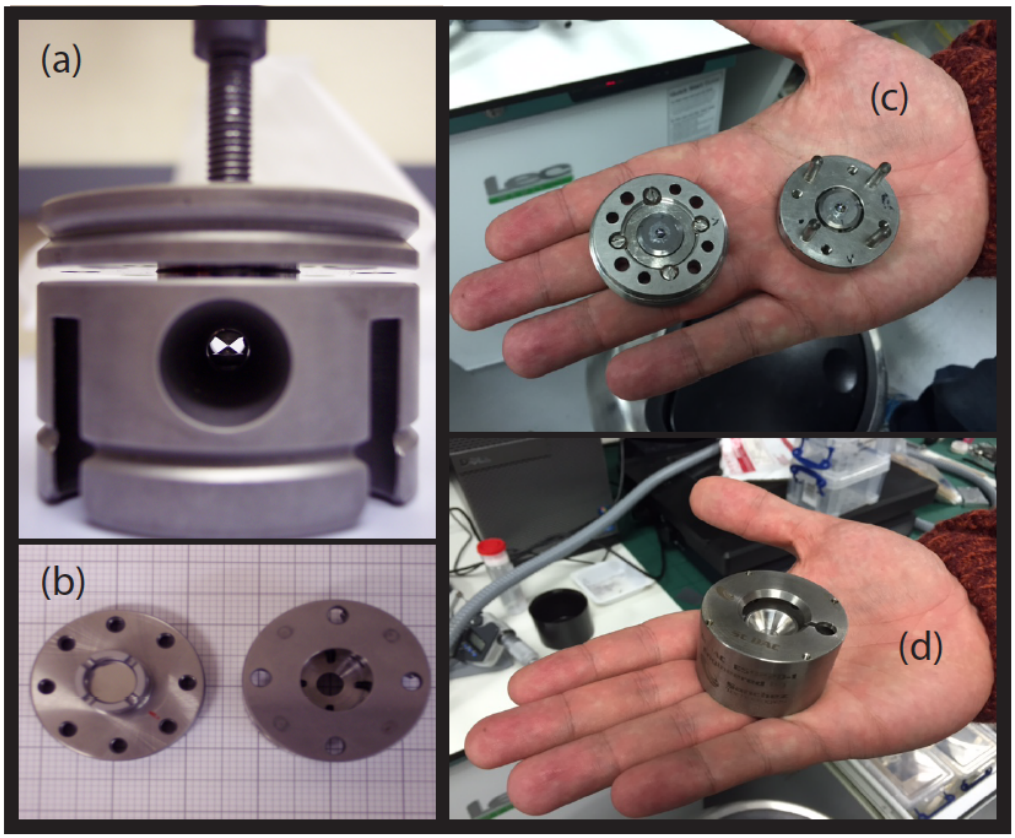

Figure 3.7: Examples of two ways of applying force in the diamond-anvil cell; on the left (a and b) are the symmetric screw-type DAC in which the pressure is generated by the tightening of screws. Figure 3.6 (a) depicts the Princeton symmetric screw-type DAC with the diamonds brought into close contact (the set screw can be seen in the top of the image). Figure 3.6 (b) shows the screw-type DAC in two pieces; the piston and the cylinder. On the right (c and d) is an example of a membrane driven diamond-anvil cell (this one in particular is from the I15 beam-line at the Diamond Light Source). Figure 3.6 (c) is a membrane driven DAC in two parts, the DAC is closed using the four screws depicted. Figure 3.6 (d) is an assembled membrane-driven DAC, including the capsule which would contain the membrane. Inflating the membrane generates force on the sample within the diamond anvil cell. Images (a) and (b) are courtesy of O. T. Lord, and (c)/(d) with thanks to S. Anzellini.

microscope using small thin strips of alumina "sand paper". These are pressed and dragged across the culet surface to remove and dislodge any dirt or remnant of a previous experiment. Any loose dirt is then cleaned under the microscope using cotton buds soaked in acetone. This process is repeated until the diamonds appear to be perfectly clean under the microscope. The diamond-anvil cell is then closed, and the culets brought into a close range, typically <1 μm distance between them, to ensure they are aligned correctly. If they are not, they can be moved in X and Y (i.e. side to side, not up and down) to improve the alignment. The parallelism of the diamonds can be checked by looking at the interference fringes, if there are many interference fringes the diamonds are sub-parallel and so new diamonds would need to be mounted or a more sophisticated cell is required. Correct alignments are crucial as, if not, this could result in a 'blow out', i.e. uneven pressure and the loss of the sample during the experiment, and could also result in significant damage to the diamonds.

2. Making and preparing the gasket.

In the DAC, gaskets are required to contain and hold the sample in place in the centre of the diamond culet. This work used both rhenium and stainless steel gaskets (both are initially 250 μm thick). The gasket is first cut to size to fit within the Princeton-type screw DAC and then indented (to approximately 40 μm thick) in order to sit flush in the assembly. First the gasket is cleaned, and four small measures of modelling clay are arranged around the bottom diamond (making sure not to get any on the diamond culet). Then the gasket is placed centred on the bottom diamond and secured into the clay. Once the gasket is secure and sitting on top of the bottom diamond (providing a layer between the top and bottom culet) the DAC is closed. A small amount of force, i.e. the squeezing of the closed DAC by hand, is enough pressure to partially indent the gasket. The DAC can then be opened and the gasket alignment marked with a pen or scratch to ensure a good sit when placed back in the DAC. At this point some ruby powder is added, which is used as a pressure calibration. The DAC is then re-closed and the screws inserted and closed. The DAC can then be tightened using Allen keys, until ruby spectra (see Section 3.4.2) indicates that the pressure inside the DAC is approximately 20 GPa for stainless steel, or 25 GPa for rhenium (to achieve 40 μm thickness), and sufficient to indent the gasket. The diamonds will then need to be cleaned again, using the same method as described in step one and the gaskets drilled. In this work

the automated UV (266 nm) laser ablation unit at the University of Bristol School of Earth Sciences has been used to drill the gaskets. A circular hole is drilled in the centre of the newly indented portion of the gasket, roughly one-third the diameter of the culet being used. Once drilled, the gasket can be cleaned thoroughly using a combination of an ultrasonic bath and a needle under the microscope to remove any dirt or burnt material. This results in a very clean sample chamber to hold and seat the sample in the centre of the culet.

3. Preparing the thermally insulating pressure medium.

Insulating material in the DAC is essential as it provides an encapsulating medium that ensures both hydrostatic pressure and thermal insulation in the sample chamber. The insulating pressure medium in this case is Al_20_3. Al_20_3 powder was loaded between two steel discs which were then loaded into a press and compressed to create thin sheets of approximately 10 -15 μm thickness. The thin sheets could then be loaded into the laser ablation unit at the University of Bristol School of Earth Sciences and cut to make 90 μm (approx) diameter discs. The insulating medium is form-fitting under compression, such that it prevents any open space in the sample chamber and ensures against distortion of the sample during the compression.

4. Preparing the sample.

Once the starting material has been produced (a detailed description of the production of the starting material is given in Chapter four) a thin foil is created using a hydraulic press and cut into small discs, approximately 40 μm in diameter under Argon gas using laser ablation. If a thinner foil is required, a small amount of material can be loaded between two diamond culets. In this method, a sufficient mound (under the microscope) of powdered sample is assembled and the DAC is closed slowly, ensuring the sample remains between the diamonds. The DAC is closed and compressed by hand and then opened, producing a thin foil.

5. Loading the Cell.

The DAC and gasket are prepared and cleaned and can be assembled. A small disc 10 -15 μm thick of insulating Al_20_3 cut into discs, 90 μm in diameter (approx.), is then placed and manipulated using a very thin needle in the sample chamber. On top of the insulating

medium a disc of Fe-S-Si is then placed, followed by a second Al_20_3 disc. Lastly, a small amount of ruby is placed on top of the second piece of insulating pressure media, off to one side, such that it does not coincide with the X-ray or laser path to the sample.

6. Closing the Cell.

The loaded cell is only partially closed initially and is heated for approximately an hour under argon gas to remove moisture and to avoid any chemical comtamination. After such time, the hot DAC can then be closed fully, cooled and tightened to the desired pressure.

3.4.2 Controlling The Pressure

In both the off-line and *in-situ* experiments (Chapter five) the pressure inside the DACs were controlled by the tightening of four screws that brought the diamond culets closer together, decreasing the volume between them and applying significant force onto the sample held between the two faces. Ruby fluorescence was used to determine the pressure inside the chamber as distinctive fluorescence peaks of ruby shift with increasing pressure (Figure 3.8). This pressure shift is very well calibrated (Forman et al., 1972; Mao et al., 1986) such that when pressuring the sample in the DAC the location of the ruby fluorescence peak could be measured and the pressure determined.

Another method of measuring pressure in the DAC is by Raman spectroscopy. Using the relationship between the Raman spectra of the diamonds with pressure, particularly the sharp high frequency edge of the Raman peak, which varies linearly with pressure, the pressure in the sample can be found. Raman spectroscopy introduces no foreign material within the sample chamber, however, the technique in comparison with that of Ruby florescence is challenging and so it may take time to get each pressure measurement. For ease of use and time efficiency, the ruby fluorescence technique has been used in this work.

3.4.3 Generating High Temperature

The off-line work described in Chapter five used the laser-heating system set up at the University of Bristol School of Earth Sciences, to heat the sample from both sides and measure the melting behaviour of $Fe_{0.8}S_{0.1}Si_{0.1}$ (a full description of this geometry is given in Lord et al. (2009); Figure 3.9). There is a both a camera and detector on both sides of

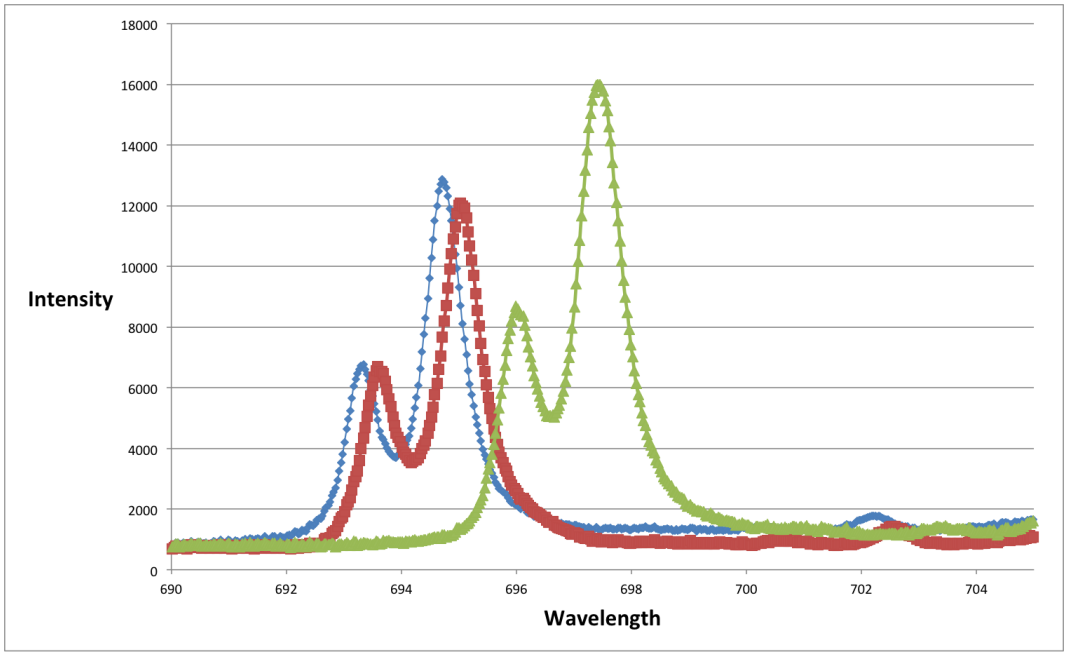

Figure 3.8: The characteristic fluorescence double peaks of ruby at three different pressures ranging from 0 - $\sim$ 9 GPa (blue to green respectively). The shift in position of the ruby peaks to longer wavelengths inside the diamond-anvil cell is used as a indication of the pressure of the sample chamber. Data courtesy of O. T Lord.

the DAC, and the first step is to ensure that the laser heating is aligned. This is achieved using the two cameras, which allow the user to image both sides of the sample and optically determine that the sample is being heated at the same spot on both sides.

Off-line, the temperature of the sample is determined from the thermal radiation emitted from the sample during the laser heating. The sample is treated as a grey body, i.e. its emissivity is independent of wavelength but is not equal to one, such that when comparing the intensities of thermal radiation at two different wavelengths, the emissivity cancels out. This was found by Heinz and Jeanloz (1987) and is fundamental to determining the temperature of a sample using spectro-radiometry. In practice a large number of wavelengths are sampled using a narrow slit to remove the noise in the data. The spectral intensity is then fitted using Wien's approximation to Planck's law.

$$J = ln(\varepsilon) - \frac{\omega}{T} \tag{3.4}$$

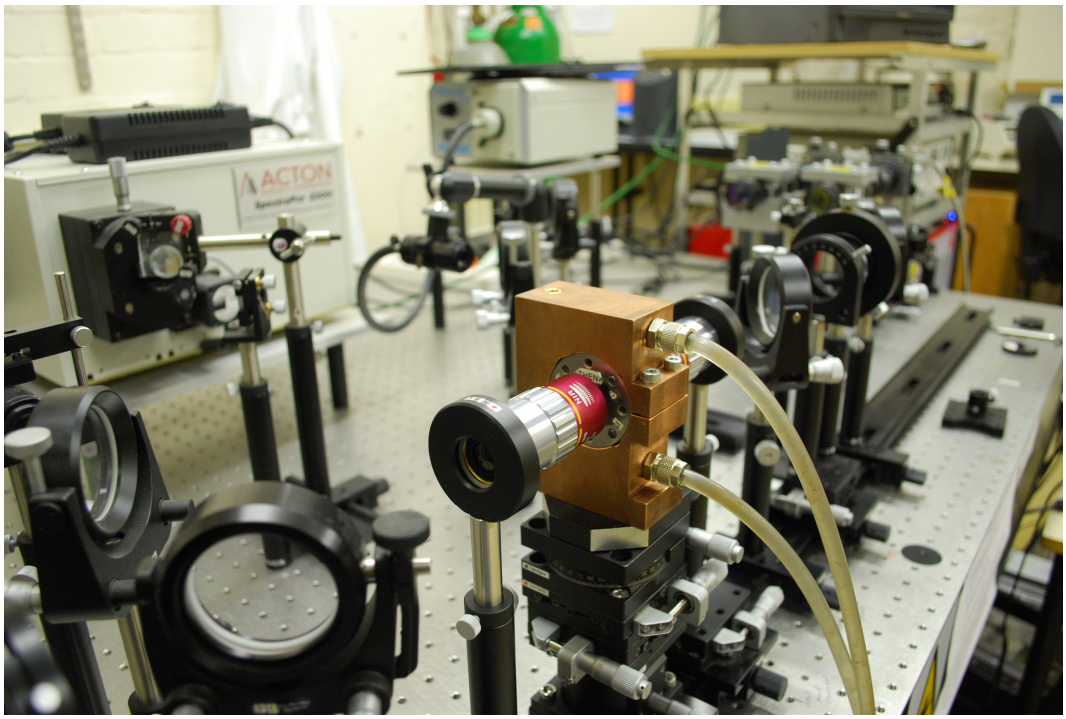

Figure 3.9: A diamond anvil cell inside a brass cooling block and mounted in the laser heating experimental set-up at the University of Bristol. Facing the DAC on both sides are objective lenses, these serve two purposes, the first is to focus the laser beam onto the sample, and secondly to collect the incandescent light emitted during the experiment. This experimental set up is used in Chapter five to study the (off-line) melting behaviour of $Fe_{0.8}S_{0.1}Si_{0.1}$. Image courtesy of O. T Lord.

where J is the normalised intensity, and ε the normalised wavelength. The temperature can then be controlled by varying the laser power. With increasing laser power, the temperature is increased until melting occurs, at which time the laser power- temperature curve forms a plateau. In DAC experiments the radial temperature gradients are very large (thousands of kelvin in the centre of the heated spot and close to room temperature at the edge), to minimise temperature gradients in the heated region beam shaping optics are used, which turns the gaussian temperature distribution to a 'top-hat' temperature distribution producing a relatively uniform temperature within this region. As discussed the wavelengths are samples using a narrow slit, which will measure temperatures across the whole heated region and across the temperature gradient also. When measuring the melting temperature, to correct for this the peak temperature is taken. To reduce the statistical error of the fit to Planck's Law (eq. 3.4) a 200 nm window is between 570 nm and 830 nm, depending on which gives

the lowest error. The entire 200 nm is then fitted, significantly reducing the statistical error to the order of a few kelvin. There are also axial gradients in the DAC, however in this work, thin opaque samples were used which absorb at the surface and in this case axial gradients are relatively small, plus in the off-line experiments, the melting temperature was measured at the surface where the sample is likely to start melting.

3.5 Measuring The Melting Temperature

Thus far in this work, references have been made to both the melting curve, and the liquidus temperatures of materials. The difference between these two terms are a result of the materials which they describe. A melting curve describes the melting temperature of a one-component material, e.g. pure iron (and hence its reference so far in the text), whereas a liquidus describes the melting temperature of a multi-component material. The distinctions arise due to the different natures of melt in the single and multi-component materials. In a multi-component material, the onset of melting is called the solidus, at such a point it is possible for only one phase to melt, with another remaining in the solid form, the liquidus defines the complete melting of the material (e.g see Chapter five, Figure 5.6) . There is no need for a such a distinction between the solidus and liquidus for a single component material, and thus the melting temperature can be referred to as the melting curve. In the off-line experiments presented in Chapter five the solidus and liquidus temperatures of $Fe_{0.8}S_{0.1}Si_{0.1}$ were identified by a change in slope of the laser power-temperature curve (solidus) and the following plateau (liquidus; following the method of Lord et al., 2009, 2014a; e.g. Figure 3.10).

The intention was to use the abrupt change in the laser power-temperature curve alongside the appearance of diffuse X-ray diffraction peaks (and disappearance of distinct Bragg peaks) during the *in-situ* laser-heated DAC experiments at the Diamond synchrotron light source. However, unfortunately the *in-situ* measurements were unsuccessful (further details can be found in Chapter five), and so an abrupt change in the laser power-temperature curve was the only criteria used. There are alternate methods of determining melt, such as the appearance of laser speckles, however these have been shown to be sensitive to other behaviour (Anzellini et al., 2013), not just melting, and hence may possibly erroneously produce lower melting temperatures (Lord et al., 2014a,b).

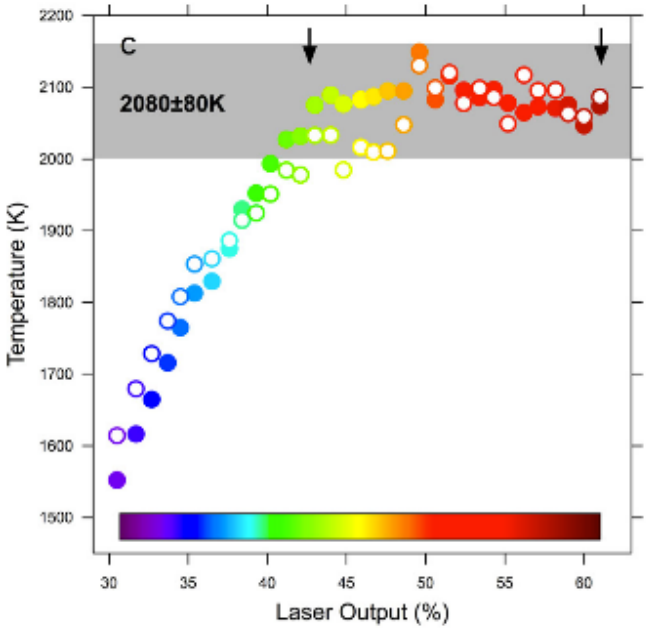

Figure 3.10: The plateau in the laser power- temperature curve was used to indicate melting. Figure from Lord et al. (2014a)[3].

3.6 Synchrotron Experiments

Chapter five describes the attempted Fe-S-Si melting experiments carried out at the Diamond facility at the STFC Rutherford Laboratory in Didcot, Oxford. Synchrotron X-ray sources are themselves particle accelerators, in which an X-ray beam is produced as electrons are accelerated in a curved path. Then insertion devices such as undulators or wigglers, are used to to achieve a narrow parallel beam. At I15, The Extreme Conditions beam-line at the Diamond Light Source (used in Chapter five) the insertion device used is a wiggler, which consists of many magnets that zigzag the electron beam, arranged to achieve constructive interference creating a brilliant, and very parallel, beam of radiation.

3.7 Summary

This chapter has described the experimental methods and equipment used to determine the melting behaviour of $Fe_{0.8}S_{0.1}Si_{0.1}$. In Chapter five, the DAC (Section 3.4) was used in

[3]Reprinted from Physics of The Earth and Planetary Interiors, 233, Oliver T. Lord, Elizabeth T.H. Wann, Simon A. Hunt, Andrew M. Walker, James Santangeli, Michael J. Walter, David P. Dobson, Ian G. Wood, Lidunka Vočadlo, Guillaume Morard, Mohamed Mezouar, The NiSi melting curve to 70GPa, 13 - 23, Copyright 2014, with permission from Elsevier.

off-line experiments at The University of Bristol School of Earth Sciences to investigate the solidus and liquidus temperatures of $Fe_{0.8}S_{0.1}Si_{0.1}$ (using the criteria described in Section 3.5). Also in Chapter five, *in-situ* experiments (Section 3.1) were carried out at the Diamond Light Source, Oxford, in an attempt to provide additional information on the melting behaviour.

Chapter 4

Sample Preparation

One of the tasks undertaken in this doctoral research is to determine the melting behaviour of $Fe_{0.8}S_{0.1}Si_{0.1}$ (relative atomic percentages). This was investigated using both off-line and *in-situ* diamond-anvil experiments; however before this could be carried out, the Fe-S-Si mixture needed to be manufactured. This chapter will detail the process used to create this mixture and the various alternative methods employed and tested before arriving at the final procedures. Firstly, the challenges expected in the creation of a homogenous mixture will be discussed, followed by the methods tested and finally a description of the refined methods used to create the Fe-S-Si starting material.

4.1 Fe-S-Si: A Challenging Ternary

Fe-S-Si, as described in Chapter one, could be fundamental to understanding the deep interior of the planet Mercury. The recent measurements of MESSENGER have placed constraints on the surface composition of Mercury, which suggest that the innermost planet formed under highly reduced conditions. In these circumstances silicon dissolves much more readily into iron, and as such there may be significant amounts of silicon in addition to sulphur in the core of Mercury. To understand the ramifications of this, research is needed to determine the behaviour of Fe-S-Si alloys at the conditions of Mercury's core.

Recent work on the Fe-S-Si ternary has revealed a very complicated behaviour, notably a large miscibility gap at pressures below 15 GPa (depending on relative abundance of silicon and sulphur; Morard and Katsura, 2010; Figure 4.1).

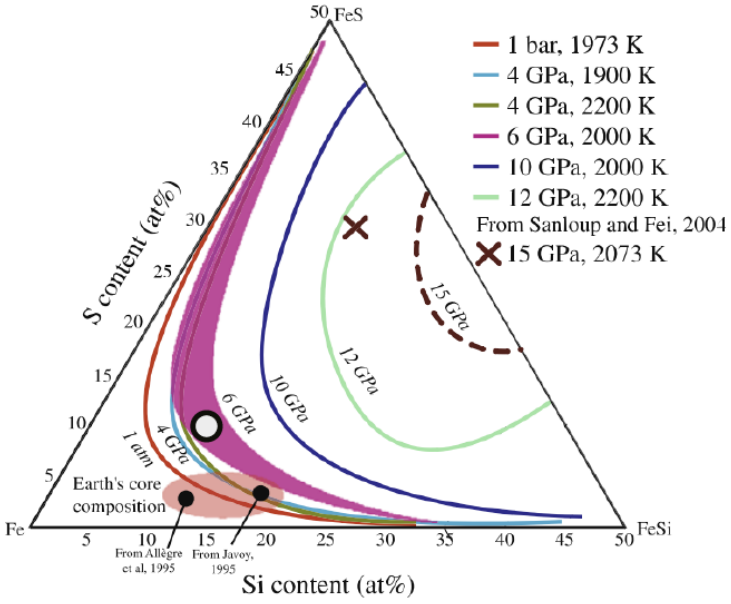

Figure 4.1: The evolving immiscible region of Fe-S-Si, the black circle indicates the $Fe_{0.8}S_{0.1}Si_{0.1}$ composition studied in this work, figure adapted from Morard and Katsura (2010)[1].

This study has attempted to simplify as much as possible the behaviour of the Fe-S-Si system whilst still providing a first look at the implications of the Fe-S-Si ternary for the core evolution and structure of Mercury. The composition chosen for study, $Fe_{0.8}S_{0.1}Si_{0.1}$ (relative at %), lies in the miscible region above approximately 6 GPa (Figure 4.1), thus remaining miscible throughout the core regions of Mercury (core-mantle boundary of Mercury is approximately 5.5 GPa; Hauck et al., 2013). This composition agrees with the modelling of Chabot et al. (2014) whose models of the core composition of Mercury, suggests a range of possible S and Si relative abundances (shown in Figure 4.2) that are consistent with the surface measurements of sulphur and low surface abundance of iron.

As the purpose of this study is to understand the ramifications of a Fe-S-Si ternary in the core of Mercury, ideally, the experiment will include only iron, silicon and sulphur. However, in practice this has proved to be very challenging, as both iron and iron-sulphur oxidise very rapidly. In addition to this, due to the nature of diamond-anvil experiments, the required sample size is very small, and so the materials need to be mixed on an extremely fine scale

[1]Reprinted from Geochimica et Cosmochimica Acta, 74, G. Morard,T. Katsura, Pressure - temperature cartography of Fe-S-Si immiscible system, 3659 -3667, Copyright 2010, with permission from Elsevier.

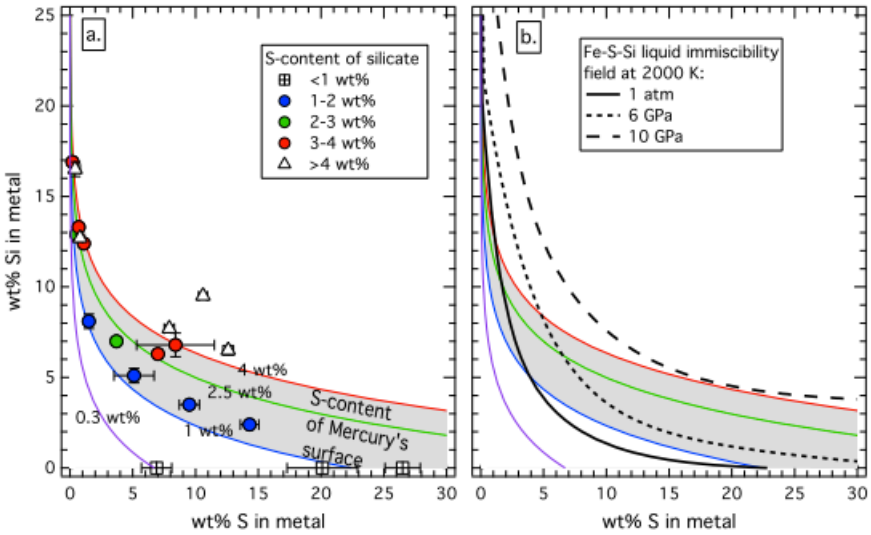

Figure 4.2: The possible sulphur and silicon abundances in Mercury's core constrained by the surface composition of Mercury taken from Chabot et al. (2014)[2](25wt% Si is approximately equal to 40 at% silicon and 30 wt% S is approximately equal to 43 at% sulphur).

to achieve homogeneity. Materials, when extremely small, may undergo behaviour possibly unlike that on the macro-scale. In particular, in this work, they were found to oxidise much more readily and incorporate large amounts of oxygen into the mixture. Large amounts of testing has been undertaken in the hope of eliminating as much oxygen as possible in this study, which will be described in the forthcoming sections.

4.2 Requirements for a DAC Melting Study

The aims and requirements of the diamond-anvil cell melting study, and thus for the resulting starting material were;

1. A mixture of iron, sulphur and silicon in their correct abundances on the scale needed for the diamond-anvil cell.

2. A homogeneous mixture of the materials in known amounts, such that the study can be repeated multiple times under the assumption that any sub-sample taken will have the same composition.

[2]Reprinted from Earth and Planetary Science Letters, 390, Nancy L. Chabot, E. Alex Wollack, Rachel L. Klima, Michelle E. Minitti, Experimental constraints on Mercury's core composition, 199 - 208, Copyright 2014, with permission from Elsevier.

3. A mixture containing only iron, sulphur and silicon.

4.3 Methods of Preparation

The ideal situation is to create a homogenous mixture on the scale of the diamond-anvil cell. The iron, sulphur and silicon were obtained as separate starting materials with differing grain sizes. The varying sizes of each component of the Fe-S-Si mixture were non-ideal and would likely not have resulted in a homogenous mixture if simply mixed in the correct abundance. Hence, the following methods were tested to not only mix the sample sufficiently, but to also grind and reduce the grain size of the mixture.

4.3.1 Pestle and Mortar

The first method tested for the preparation of the Fe-S-Si starting material used a mixture of elemental iron powder, FeSi and FeS, which were ground by hand in a pestle and mortar under ethanol. The sample ingredients were measured and added directly to an agate pestle and mortar along with a small amount of ethanol, enough to cover the sample. The mixture was then ground by hand in circular movements for approximately 20 minutes. The pestle and mortar grinds the material together whilst simultaneously mixing the material. The sample can be mixed for as long as needed to achieve the desired fineness of material, but in the first instance only a small amount of mixing was required. The pestle, mortar and wet ground sample were then placed under an infra-red lamp to accelerate the evaporation of the ethanol. Once the ethanol had evaporated entirely, the dry mixture could then be gathered and stored. The first attempt at creating a homogenous sub-micron scale mixture consisted of an initial short grind in the pestle and mortar followed by the use of a multi-anvil cell (MAP) to melt and quickly quench the sample in the hope of creating an entirely homogenous mixture.

4.3.2 The Multi Anvil Press

The first attempt to create the Fe-S-Si starting material used the MAP at the University of Bristol. The Fe-S-Si mixture was measured into the pestle and mortar and ground by hand for approximately 20 minutes, then put into the 14/8 Bristol cell design (2012) MAP assembly (Figure 4.3). The hexagonal boron nitride (hBN) capsule containing the sample

was centred both within the cell assembly and in the $LaCrO_3$.

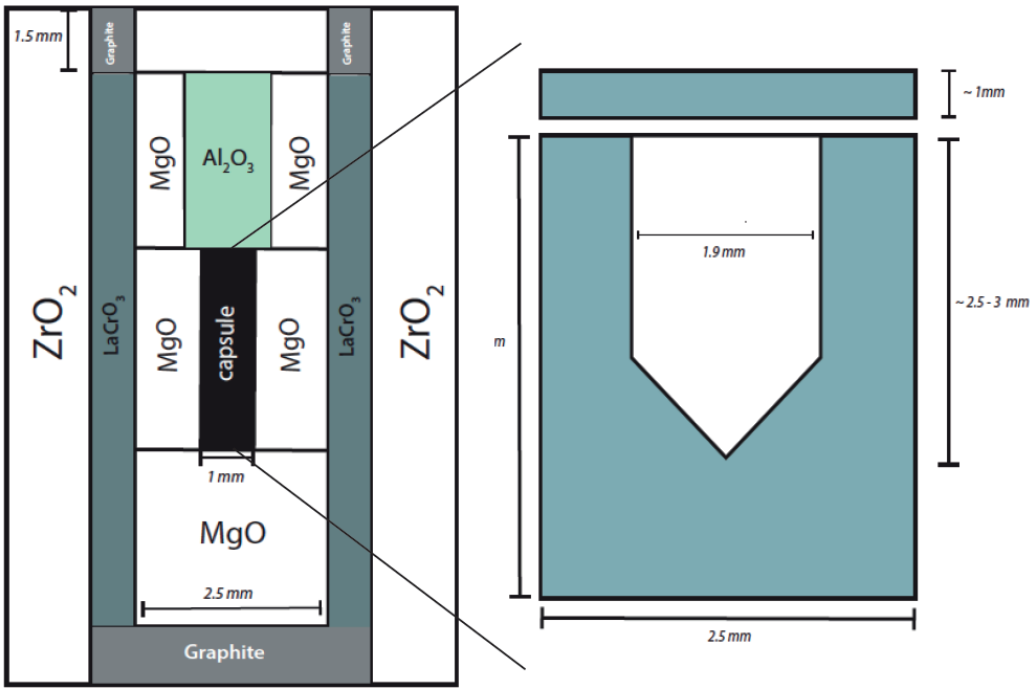

Figure 4.3: The 14/8 Bristol cell design (2012) MAP assembly.

The MAP was used in an attempt to create a homogeneous mixture of Fe-S-Si at pressures above the miscibility gap. The mixed powders would be melted in the MAP at pressure and quenched. Multiple attempts were made with the set-up shown in Figure 4.3, increasing the pressure to approximately 10 GPa (333 tonnes approx; above the 6 GPa threshold of immiscibility for this composition, Morard et al., 2010) and temperatures reaching 1750 °C. This temperature was held for approximately two minutes and then the sample was quenched. Upon quenching the resulting sample appeared to contain two distinct quenched liquids. The result of this experiment, when analysed using a hyper-probe electron probe micro-analyser with a field emission gun for an electron source (which will be referred to as the FEG probe), found a high proportion of lanthanum, which is believed to have originated from the $LaCrO_3$ furnace used in the experiments. The sample was recovered from a fully intact capsule with no obvious cracks or breakages, so it is possible that the hBN capsule used in the melting became very porous and resulted in the La diffusing through the capsule across the grain boundaries. Alternate set-ups including the use of an MgO capsule were subsequently considered, but due to the highly oxidising nature of Fe and FeS this was discarded as unlikely to be successful, hence efforts were turned to alternate ways of

grinding and mixing the sample, including using the pestle and mortar under liquid nitrogen.

4.3.3 Cryo-Grinding: Grinding Under Liquid Nitrogen

The grain size achievable using a pestle and mortar, even after an extended period of time grinding, remained in the multi-micron range, believed to be due to the smearing of the grains. The mixture, in particular the iron, is very soft and smeared in the grinding process. In an attempt to make the material much more brittle the mixture was cooled using liquid nitrogen. Firstly, the mixture was re-measured using the same elemental iron powder and FeS, but substituting an elemental nano-powder of silicon for the FeSi, producing a finer starting material. This was then put into the agate pestle and mortar and ground by hand under liquid nitrogen, rather than ethanol. The pestle itself was seated in a large foam container to keep it steady as well as to prevent the freezing of any materials that came into contact with it. The mixture was ground by hand for 60 minutes with samples taken at 20, 40 and the full 60 minutes. Each sample was pressed into a foil and analysed. Unfortunately, when analysed at each interval it was found that the grain size did not decrease with longer grinding time, and the grain size remained in excess of ten microns. It is not clear, however, whether this was due to the foil making process, and that the grain size was indeed smaller but when pressed spread to larger areas, but even if this is the case, the large grain size meant that such samples were unsuitable for the diamond-anvil cell. The drying process that followed the cryo-grinding also resulted in a large amount of oxidation, which would need to be prevented. This lead to the next iteration in the preparation of the starting material which was to more effectively grind the material using a planetary ball mill.

4.3.4 Planetary Ball Mill

A planetary ball mill (PBM) consists of a cylindrical container and lid containing a number of spherical agate balls. As the milling cylinder is rotated the balls move within the container grinding the sample (shown in Figure 4.4). When operating the planetary ball mill the following steps were taken:

1. The mill was thoroughly cleaned using ethanol and tissue, including the balls, the milling jar and lid. Within the lid careful attention was paid to the cleaning of the rubber O-rings to remove as much dirt and remnants of any previous experiment as possible.

2. A small of amount of iron-free sand was then added to the milling jar and the cleaned balls were added and lid reassembled and closed. This was then milled for two minutes. The sand helps to thoroughly clean the PBM and dislodge any dirt from the jar. The resulting sample size post grinding was very small, so to prevent any inhalation of any material, every time the jar was extracted from the PBM the lid was opened under an extraction hood. The sand was then removed and thrown away and the milling assembly cleaned once more as described in step one using tissue and ethanol.

3. The next step was to pre-contaminate the PBM. The cleaned milling jar, lid, balls and O-rings were reassembled and a small amount of experimental sample was added. The PBM was then run for two minutes. The mill was then cleaned for a third time, as described in step one, as well as disposing of the ground pre-contamination sample. The aim of this step was two fold, firstly to thoroughly clean the PBM for a third time and ensure as best as possible there is no material in the PBM that could contaminate the ground sample. The second was to ensure that even if there was remnant material in the PBM, it was the material wishing to be ground and hence will not contaminate the sample.

4. Once clean, the PBM was now ready for milling the Fe-S-Si powder mixture. The 5g charge (approximately as some was removed for pre-contamination) was then added to the mill and ground for 20 minutes in the first instance.

5. Once ground, the cleaning process was repeated using iron-free sand followed by cleaning using ethanol and tissue until the ball mill was clean.

The advantage of a PBM (Figure 4.4) over manual grinding lies primarily in the ability of the mill to continuously grind the sample for a long period of time, however, to effectively grind the sample a relatively large amount of material is needed. In this work 5g was measured out in the correct abundance to grind in the PBM, a far larger amount than would ever be needed for the diamond-anvil-cell. The reason for the large amount of material is that in the grinding process, the balls and container are coated in the ground mixture, so although as much is recovered as possible, there is significant loss of the sample. This lost material is assumed to be of the very well mixed sample and is thus expected to not affect the relative composition of the mixture.

To test the grinding and grain size with increasing grinding times, the mixture was ground

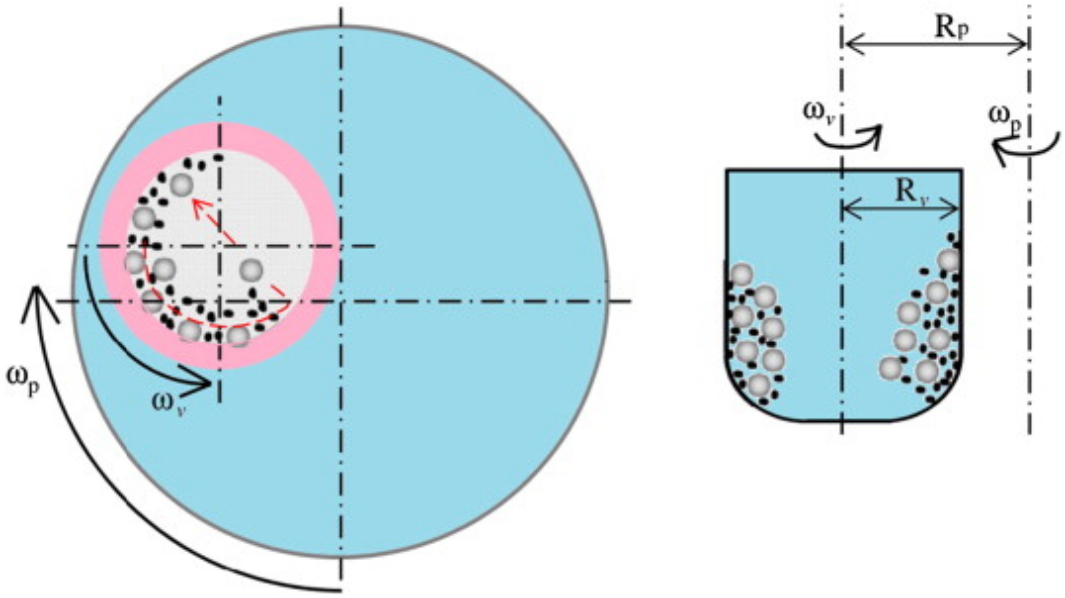

Figure 4.4: Schematic diagram of the planetary ball mill and vial, in which ω_p and ω_v indicate the angular velocity of the plate of the mill and one vial, and R_p and R_v the vectorial distances from the centre of the mill to the centre of the vial and the from centre of the vial to the radius of the vial, taken from Abdellahi et al. (2014)[3].

for a total of 120 minutes with samples taken at 20 minute intervals to analyse the reduction in size. The result of this initial analysis showed that the full two hours was required to reach the desired grain size. However, X-ray diffraction (XRD) analysis at UCL revealed a large amount of Fe_2SiO_4 and SiO_2 in the sample (Figure 4.5), which suggests that the sample was contaminated by the low iron sand, or may possibly indicate that a considerable amount of heat was generated in the energetic milling process. Unfortunately, this meant that the PBM was unsuitable for the production of the Fe-S-Si starting material, as it resulted in a material composition very different to the desired Fe-S-Si mixture.

The next step was to use another mechanical milling process, but one that did not produce as much heat as the PBM and was less likely to contaminate the mixture, which lead to the McCrone micronizing mill to grind in combination with the Wig-L bug high speed mixer to mix the sample.

[3]Reprinted from Powder Technology, 264, Majid Abdellahi, Maryam Bahmanpour, Marjan Bahmanpour, The use of artificial bee colony algorithm to speed up the nanopowders synthesis during high energy ball milling, 61 - 70, Copyright 2014, with permission from Elsevier.

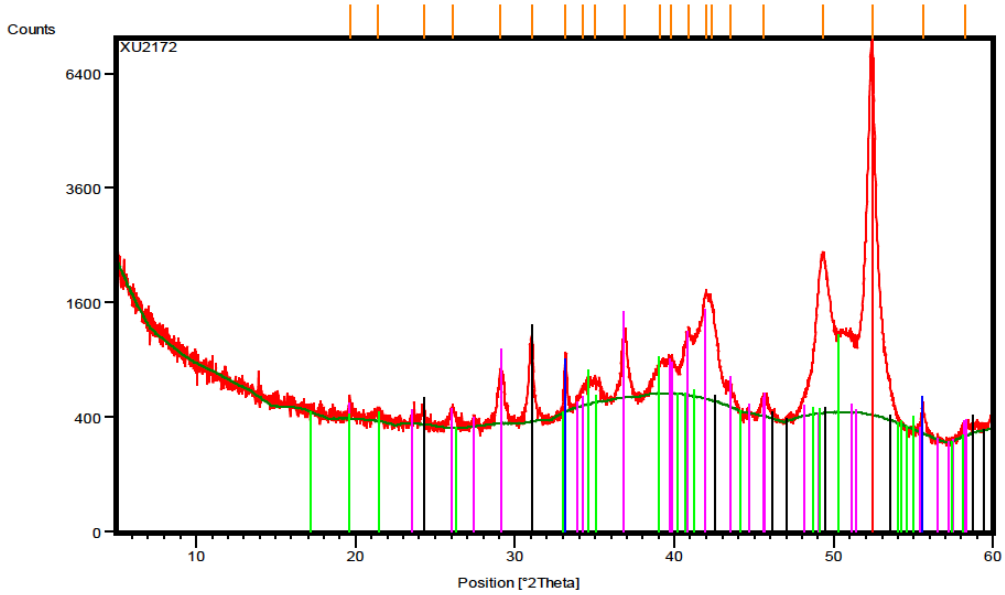

Figure 4.5: X-ray diffraction pattern of a planetary ball milled mixture of Fe-S-Si (experiment number XU2172, Co Kα_1 radiation, λ = 1.789 $\AA$); many of the peaks suggest the presence of Fe_2SiO_4 (pink lines) and SiO_2 (black lines) in the sample, likely as a result of the milling process. The peaks corresponding to iron are indicated by the red lines, blue lines mark the silicon peaks and green lines mark the peaks corresponding to troilite (FeS).

4.3.5 McCrone Micronizing Mill and Wig-L Bug

The next method tried in the succession of grinding techniques was the combination of the Wig-L bug and the McCrone micronizing Mill (shown in Figures 4.6 and 4.7). The Wig-L bug sample container consists of a plastic ball and a small plastic cylinder with a plastic lid (one millilitre capacity, shown in Figure 4.6). The assembly is fastened into the Wig-L bug machine, which effectively shakes the assembly rapidly for the required time. The ball sits with the sample and a small amount of ethanol inside the cylinder, which produces a slurry that is mixed by the movement of the ball over the course of the shake.

The McCrone micronizing mill acts in a similar way to the PBM and Wig-L Bug in that it is a cylindrical container containing a relatively free moving medium that moves in the grinding jar pulverising the sample and reducing its grain size. As shown in Figure 4.8 the micronizing mill sample container consists of a plastic cylindrical grinding jar and lid but instead of balls that can move in all directions in the jar (as was the case in the planetary

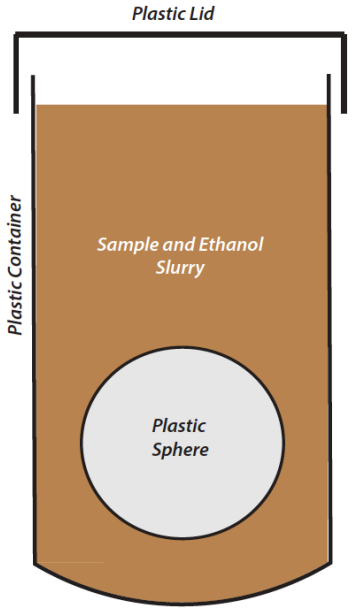

Figure 4.6: The components of the Wig-L Bug.

ball mill) the active grinding is achieved through agate pellets which are stacked in a 6 x 8 formation totalling 48 pellets. This is a less energetic grinding process than the PBM as the pellets move in one plane only, and only move a relatively small amount up and down in the jar. The McCrone micronizing mill benefits from having a smaller jar and smaller grinding pellets, which in-turn, permits smaller sample sizes in addition to the ability to continuously grind the sample over long periods of time.

The McCrone micronizing mill procedure was as follows:

1. Using tissue and ethanol, the capsule, lid, pouring lid and each individual pellet was thoroughly cleaned.

2. The clean pellets were then arranged in a 6 x 8 formation within the clean capsule (Figure 4.8). Then approximately 15 ml of ethanol was added to the capsule and the lid sealed on-top. Then began the 15:15 procedure, i.e. 15 ml of ethanol was milled for 15 seconds. The lid was then exchanged for the pouring lid and the ethanol decanted into a clean beaker and checked for clarity. If dirt remained, the 15:15 process was repeated until the ethanol ran clear.

3. The capsule was then pre-contaminated with a small amount of sample. The sample was

Figure 4.7: When operating the McCrone micronizing mill the length of shake is controlled using the clear dial on the top of the mill and switched on/off using the red switch. The McCrone milling capsule is held in the cylindrical holder on the face of the mill and secured using the metal clip.

accompanied with approximately 7 ml of ethanol and milled for approximately one minute. This mixture was then decanted (using the pouring lid) into a beaker.

4. The mixture could then be added to the micronizing mill (2 ml approx). If 'wet' grinding, this was accompanied with ethanol, whereas if milling 'dry' the capsule was dried after pre-contamination and then the sample alone was added for grinding.

5. Once the sufficient grinding time has passed, steps one and two were repeated until the mill was clean.

The McCrone mill was used in the first instance to grind FeS alone (as it had a relatively large grain size, -100 mesh), such that it could be added to the fine grained Si and Fe powders and then mixed using a Wig-L bug to create a finely ground homogeneous material. The FeS was milled using the McCrone micronizing mill and analysed using XRD at UCL. Two X-ray analyses were run, one with a short exposure ($\sim$ 750 seconds) and a second longer overnight exposure (17.22 hours; red and blue diffraction patterns in Figure 4.9 re-

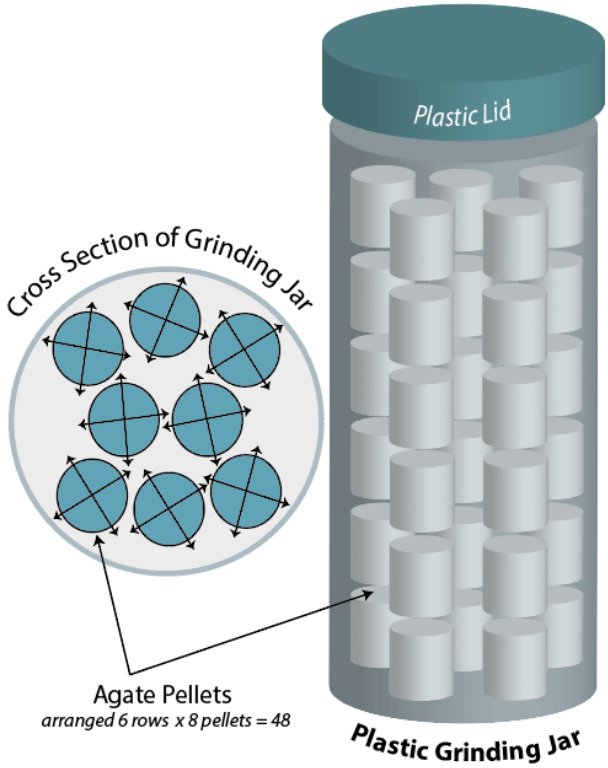

Figure 4.8: Grinding components of the McCrone Micronizing Mill.

spectively). All major peaks in the diffraction pattern (Figure 4.9) can be explained by an Fe or FeS (troilite) phase. The d-spacing of smaller peaks in the pattern appear to correspond to pyrrhotite (a different structure of FeS) with the exception of one broad peak ($2\theta \sim 25$ in Figure 4.9) in the longer exposure pattern, which suggests the presence of α-FeOOH (goethite). The α-FeOOH peak is not apparent in the shorter exposure, which may indicate that the sample oxidised overnight.

This highlighted the high susceptibility to oxidation of the FeS. Moving forward, two of the starting powders were changed to help prevent rapid oxidisation; the FeS was replaced by FeS_2, and the nano-powder of silicon was discarded in favour of a courser silicon powder (1 -5 micron grain size instead of < 100 nm). The first test involved the weighing of elemental powders of Fe, Si (grain size of 1 - 5 micron) and FeS_2 into a McCrone micronizing mill and running it 'wet', i.e. with the addition of ethanol. This was milled for a continuous 30 minutes and then decanted into a wide petri dish (to speed up evaporation) and left to dry. When this batch was analysed the grain size had remained large, approximately 10 microns and analysing the relative composition using a scanning electron microscope

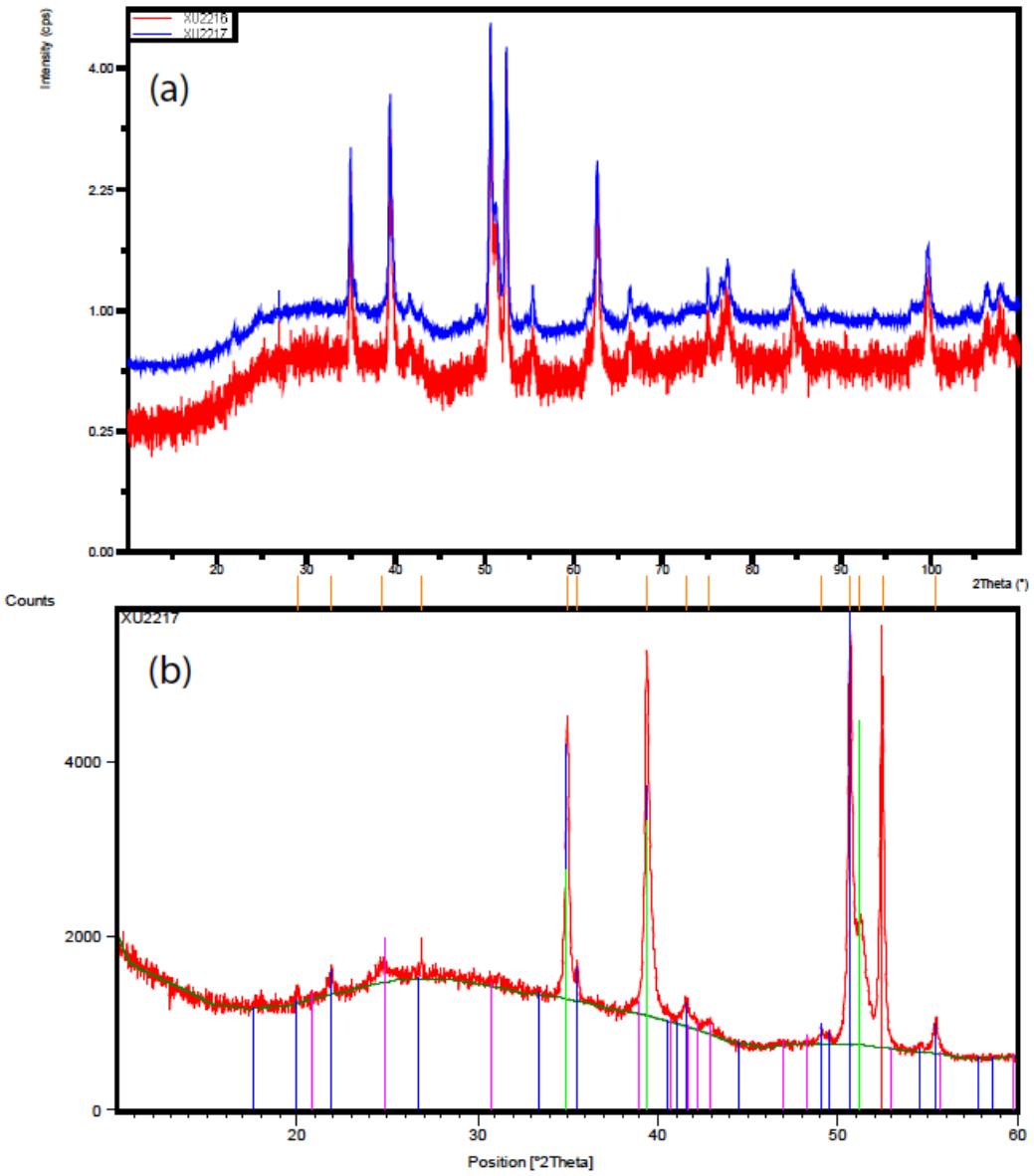

Figure 4.9: X-ray diffraction pattern of FeS measured at UCL (Co Kα_1 radiation, λ = 1.789 $\AA$; (a) red lines indicate peak intensities from a shorter exposure of 750 seconds, whereas the blue lines mark the peak measured intensities from a longer over-night exposure (17.22 hours; offset to highlight the differences between the two patterns). In both patterns the large peaks are explained by Fe and FeS (troilite) phases. Smaller peaks can be explained by the presence of a pyrrholite phase, with the exception of one broad peak at $2\theta \sim 25$ which suggests the presence of FeOOH and possible oxidisation of the sample. In figure (b) the longer 17 hour exposure is plotted only, Fe and FeS (troilite) phases are indictated by the red and blue markers respectively, other peaks are fitted to the presence of pyrrholite (green markers) and α-FeOOH (pink markers).

revealed approximately 5 wt% oxygen. Tests were subsequently run using pure iron, which was dry milled for a total of 45 minutes with samples taken every 15 minutes. Dry milling is exactly the same as 'wet' milling, but no ethanol is added to the system, and hence, no drying is needed. A sample taken from the 45-minute-milled pure iron was then put into the Wig-L bug for 30 minutes, followed by un-milled iron for 30 minutes. The resulting five samples of varying milling and mixing were then pressed into foils using a hydraulic press and tested for the presence of oxygen. A maximum concentration of approximately 2 wt% was found in the dry milled samples, so to further examine this, a second test was conducted using FeS_2 instead of pure iron. In this case approximately 2 ml of FeS_2 was milled in the McCrone for 30 minutes. After this time half the milled sample was mixed in the Wig-L bug and half kept dry. These were used to produce two foils and an additional foil was created from the FeS_2 directly from the container (as provided by the manufacturer, no milling or mixing). In all cases approximately 5 -6 wt% oxygen was found. The conclusion was drawn that dry milling the starting material in the McCrone micronizing mill was the best possible option. Additional steps were then added such that the sample was kept under vacuum throughout, except when being loaded or used to create the starting foils (to be loaded immediately after); the mixed materials ready for post experiment analysis were also kept under vacuum (see Section 4.4).

4.3.6 Magnetron Sputtering

In addition to the milling methods described thus far, an alternative production method was used called magnetron sputtering, which was implemented by Dr Oliver Lord at the University of Bristol. Magnetron sputtering is used to create a thin film of material by the process of "sputtering", i.e. ejecting material from a target onto a substrate. The magnetron sputtering machine creates a plasma, from which energetic ions (in this work these were argon ions) are accelerated into a source material (called a target), which consists of the material the user wishes to 'sputter'. The bombarded target consequently emits atoms which travel in straight lines and collide with the substrate and coalesce to form a thin film of material. Particular to magnetron sputtering, is the addition of a strong magnetic field close to the target. This confines the plasma to an area close to the target and helps to generate a stable plasma with a high density, this speeds up the sputtering process and is therefore less likely to introduce any impurities.

In this work, magnetron sputtering was used to create a thin film of Fe-S-Si. This was achieved by first 'sputtering' a layer of pure Fe onto an MgO substrate (which could then be used as one side of the thermally insulating pressure medium required for the DAC). A thin layer of pure Fe ($\sim$ 0.258 microns thick). This thin film of iron was then converted to FeS_2 (pyrite) by placing the iron coated MgO sheets into a pasteur pipette along with a "plug" of glass wool and 0.35 g of solid sulphur (shown in Figure 4.10).

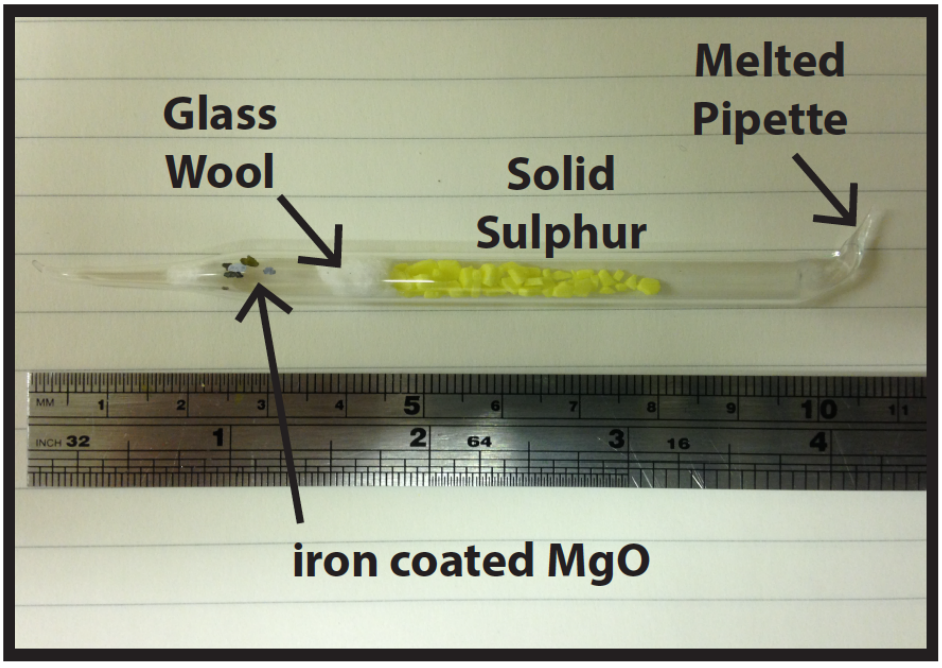

Figure 4.10: The experimental set up used to deposit FeS_2 onto an iron coated MgO substrate.

A tube was then connected to the end of the pipette, and argon gas pumped through the pipette whilst the narrow end was melted and sealed using a blow torch. Once sealed, the gas flow was switched off and the opposite end sealed in the same way. The gas flow needed to be stopped as the flow of argon gas could result in hot glass bubbles which may burst and ruin the ampoule. The finished ampoule was then placed into a box-furnace and ramped in temperature to 500°C at a rate of 350°C/hour with a 15 hour long dwell time at 350°C, before being removed from the oven and left to cool. The ampoule was then broken open to reveal MgO sheets coated in a thin film of pyrite. The ampoule method resulted in 0.00023 g of sulphur being deposited on the MgO substrate. This was then followed by a second 'sputtering' of $Fe_{0.83}Si_{0.17}$ (wt%; 1.812 microns thick), which gave a total mass of 0.00021 g of Si deposited. To correct the relative abundances of Fe, S and Si to create $Fe_{0.8}S_{0.1}Si_{0.1}$ (at%), a final layer of iron was sputtered (0.00205 g). This gave the total relative abundance

of $Fe_{0.7955}S_{0.1001}Si_{0.1044}$ (at%) (outlined in Table 4.1). A sample created using magnetron sputtering was analysed at I15, The Extreme Conditions beam-line at the Diamond Light Source in Oxford, using *in-situ* XRD (methodology can be found in Chapter three), which confirmed the presence of pyrite, amorphous iron and Fe-Si (in the bcc structure) (Figure 4.11). This suggested no contamination had occurred as a result of the sputtering method, and that the sample had not oxidised.

Table 4.1: Relative abundances of the starting material components produced by magnetron sputtering.

Element	Mass	wt %	at %
Fe	0.00320	87.86	79.55
S	0.00023	6.35	10.01
Si	0.00021	5.80	10.44

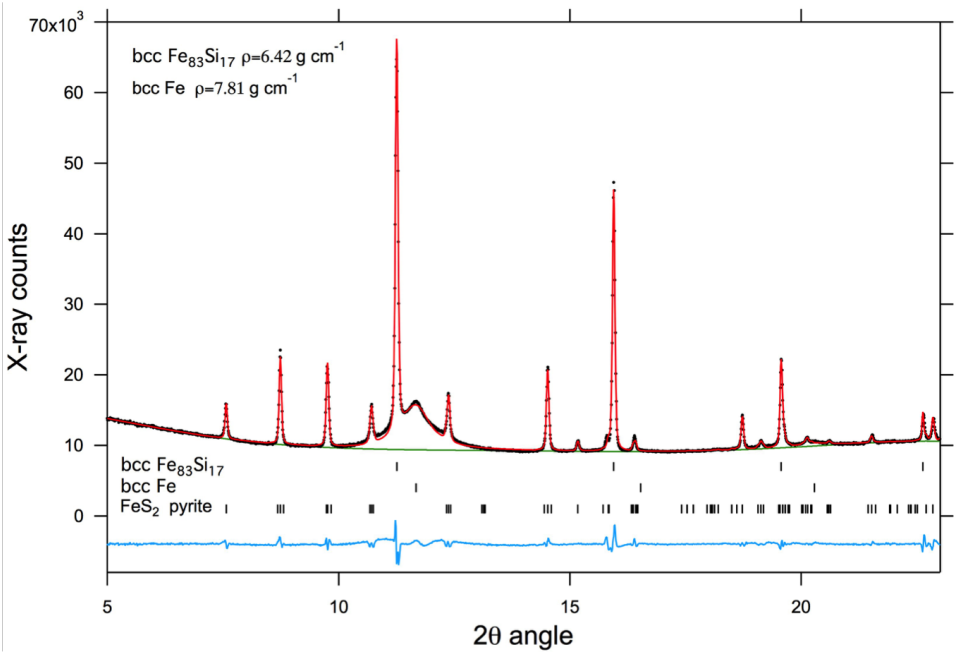

Figure 4.11: X-ray diffraction pattern of Fe-S-Si taken at the Diamond Light Source, Oxford (λ = 0.4133 $\AA$). The "bump" in the diffraction pattern suggests the presence of nearly amorphous iron, or possibly a very fine grained iron. The remaining peaks in the pattern can be fitted with the presence of pyrite (FeS_2), and a bcc structured Fe-Si suggesting that no oxidisation or contamination had occurred as a result of the magnetron sputtering method. Figure courtesy of O. T Lord.

4.4 Refined Method 1: Milling

The refined milling method used to create the Fe-S-Si starting materials used the McCrone micronizing mill and elemental powders of Fe ($<$ 10 micron), Si (grain size of 1 - 5 microns) and FeS_2 (-325 mesh). Each material was weighed out in the correct abundance directly into the McCrone capsule (no ethanol was used to wash the material into the chamber). The mixture was then milled dry for 30 minutes and emptied into a small vial, sealed and stored under vacuum. When required for a melting experiment, a small amount of powder was taken from the vial and pressed into a thin foil using either a hydraulic press or diamond-anvil-cell. This foil was then manipulated using a needle under a microscope and broken into sufficiently small pieces to be loaded into the DAC. The vial containing the powdered mixture was stored under vacuum as well as any resulting sample from a melting experiment. Dry milling along with the additional step of storing the sample under vacuum was used to suppress as best as possible the oxidisation of the starting material and fulfil the requirements laid out in Section 4.2.

4.5 Refined Method 2: Sputtering

The second refined method in the production of the Fe-S-Si starting material used magnetron sputtering. Rather than grinding the material, sputtering constructs samples on the atomic level such that it is capable of producing very thin films that are of very precise thickness. The first step in producing the $Fe_{0.8}S_{0.1}Si_{0.1}$ (at %) starting material was sputtering a layer of pure iron onto an MgO substrate (which was then subsequently used as one side of the thermally insulating medium required for the diamond-anvil-cell). The next step was to convert this into pyrite which required heating solid sulphur inside an ampoule (Section 4.3.6), which was then following by magnetron sputtering of $Fe_{0.83}Si_{0.17}$ (wt%). Finally, to achieve the correct relative abundance a final layer of pure iron was sputtered onto the thin film of Fe-S-Si. This was implemented by Dr Oliver Lord and was the preferred method of sample preparation as it produced a very precise, thin, homogeneous sample of Fe-S-Si.

4.6 Summary

This chapter has presented the steps taken to refine the methods used to create homogeneous, fine grained mixtures of $Fe_{0.8}S_{0.1}Si_{0.1}$. Two methods of preparation outlined in Sections 4.4 and 4.5 have been used in Chapter five to create the Fe-S-Si starting material. The first method used a McCrone micronizing mill (Figures 4.7 and 4.8) to dry mill a mixture of FeS_2, pure Fe powder and silicon powder, which was then stored under vacuum. The second method used magnetron sputtering to produce a thin film of Fe-S-Si on an MgO substrate.

Chapter 5

The Melting Behaviour of Fe-S-Si

The composition of Mercury's core remains a mystery. However, predictions of the likely composition can be made from the planet's properties and the external manifestations of the core. The high bulk density of Mercury suggests a planet highly enriched in metallic iron, but iron alone cannot explain the observed presence of liquid layers in its interior (Margot et al., 2007, 2012). Light elements such as sulphur and silicon can alter the liquidus of pure iron (Fischer et al., 2013; Lord et al., 2009; Chen et al., 2008) and therefore may play a role in maintaining Mercury's present day partially molten core, however, information on the properties of the Fe-S-Si ternary system at the conditions of Mercury's core are limited, in part due to the system's large miscibility gap below 15 GPa (Morard et al., 2008; Sanloup and Fei, 2004; Morard and Katsura, 2010). As is hypothesised for the Earth, it is also possible that other light elements such as carbon and hydrogen could be present in Mercury's core, but Fe-S-Si has been favoured by the community as it will provide a first order study of the planet's core composition and the implications of such for the core structure and evolution of Mercury.

The slope of the liquidus, alongside the adiabatic gradient can give insight into the core crystallisation regime and evolution of Mercury (Chapter 2, Section 2.13). One half of the information required, the liquidus, is detailed in this chapter, and the adiabatic gradient is described in Chapters eight and nine. Off-line experiments at the School of Earth Sciences, University of Bristol and *in-situ* experiments at the Diamond Light Source in Oxford were conducted to measure the liquidus and solidus relationships of Fe-S-Si (with the relative atomic percentages 80:10:10; $Fe_{0.8}S_{0.1}Si_{0.1}$).

A significant portion of time was spent refining the manufacturing method used to create a $Fe_{0.8}S_{0.1}Si_{0.1}$ starting material (Chapter 4). The initial experiments using a McCrone milled starting material (Chapter 4, Section 4.4) were then improved by using magnetron sputtering to create $Fe_{0.8}S_{0.1}Si_{0.1}$ as implemented by Dr Oliver Lord (Chapter 4, Section 4.5). These magnetron sputtered samples were then taken to be investigated on-line at the Diamond Light Source, but the experiments failed due to technical issues with the laser-heating set-up (Section 5.4), which are still not resolved (as of May 2016). Unfortunately, it was beyond the timescale of this doctoral research to repeat such experiments but Oliver Lord has conducted recent off-line experiments at the University of Bristol School of Earth Sciences which have been included in this chapter in order to find the liquidus and solidus relationships of $Fe_{0.8}S_{0.1}Si_{0.1}$.

5.1 Previous Experiments

In the experiments described in this chapter the dominant element is iron. The melting curve of iron has been investigated extensively, but there remains debate on the extreme melting temperatures of iron (discussed in more detail in Chapter 1). However, at the moderate pressures hypothesised for the deep interior of the planet Mercury (up to $\sim$ 36 GPa; Hauck et al., 2013), many studies of the melting curve of iron are in good agreement (e.g. Alfè et al., 2002b; Anzellini et al., 2013; Komabayashi et al., 2009; Chapter 1, Figure 1.11).

The addition of sulphur or silicon, or both, to the iron system changes the melting temperature (Chapter 1). Sulphur has been found to strongly depress the melting curve of iron (Chen et al., 2008; Chapter 1, Figure 1.7), whereas silicon has a more complicated relationship. Small amounts of Si have been shown to lower the melting curve of iron, although to a lesser extent than sulphur (Fischer et al., 2013; Figure 5.1), but large amounts of silicon, e.g. FeSi, may increase the melting temperature at pressures less than $\sim$ 100 GPa (Lord et al., 2009).

In this study a composition of Fe-S-Si with the relative atomic percentages 80:10:10 have been chosen as it lies in the miscible region of the Fe-S-Si ternary system for pressures exceeding $\sim$ 6 GPa (Morard and Katsura, 2010), and thus throughout the core pressures of Mercury. This composition is also consistent with the modelling of Chabot et al. (2014) which constrained the relative abundance of sulphur and silicon in Mercury's core using

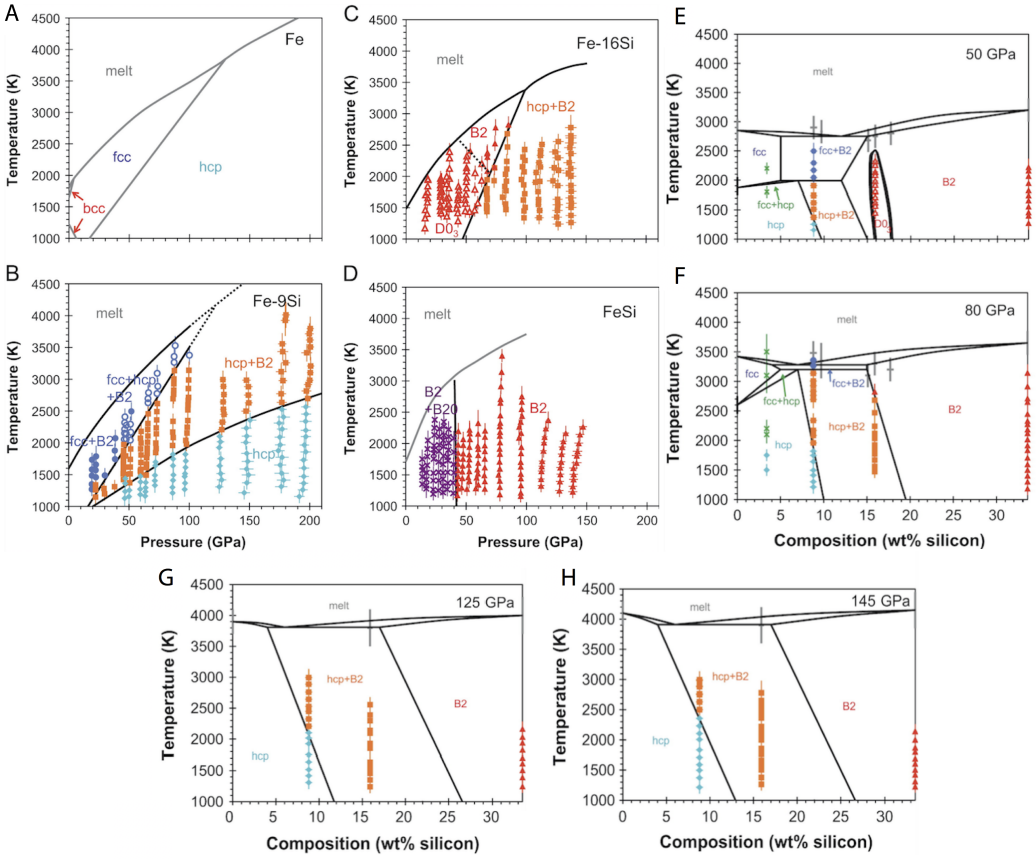

Figure 5.1: (A) Phase diagram of pure Fe from Fischer et al. (2013) which used the results of Komabayashi and Fei (2010) and Ma et al. (2004). (B) The Fischer et al. (2013) phase diagram of Fe-9Si. In which the filled blue circles indicate fcc+B2, open blue circles, metastable fcc+hcp+B2, orange squares represent hcp+B2 and teal diamonds, hcp. (C) Phase diagram of Fe-16Si from Fischer et al. (2012). Open red triangle is the $D0_3$ structure and filled red triangles indicate the B2 structure. (D) The Fischer et al. (2013) phase diagram of FeSi. Grey line represents the melting curve of Lord et al. (2010) and purple crosses represent B2+B20. Figures E, F, G and H are the composition-temperature phase diagrams in the Fe-FeSi system at varying pressures measured by Fischer et al. (2013). Symbols are as previously described with the additions of grey crosses to indicate melting points and green crosses to represent fcc+hcp. The black lines indicate estimated phase boundaries from the data points shown. In Figures E, F, G and H data is shown for Fe (Komabayashi and Fei, 2010; Ma et al., 2004); Fe-3.4Si (Asanuma et al., 2008); Fe-9Si (Fischer et al., 2013); Fe-10Si-5Ni and Fe-15Si-5Ni (Morard et al., 2011); Fe-16Si (Fischer et al., 2012); Fe-18Si (Asanuma et al., 2010); and FeSi (Fischer et al., 2013; Lord et al., 2010). Figures and caption taken from Fischer et al. (2013).

MESSENGER measurements of the planets surface composition.

Sanloup and Fei (2004) presented a liquidus curve for Fe-18.5wt% S- 8wt% Si, (a higher abundance of silicon and sulphur than studied here; Figure 5.2). Modelling of Mercury's core-mantle boundary (CMB) temperature ranges from 1850 - 2000 K (e.g. Rivoldini et al., 2009), and lies at a pressure of $\sim$ 5.5 GPa (Hauck et al., 2007, 2013). The results of Sanloup and Fei (2004) suggests that the addition of sulphur and silicon to iron will lower the melting curve with respect to pure iron, and extrapolating the liquidus curve implies that this composition would indeed remain liquid at the current modelled temperatures and pressures of Mercury's CMB, but in the form of two immiscible liquids (Figure 5.2). Shown in Figure 5.1 (E - H) are the composition-temperature phase diagrams in the Fe-FeSi system (Fischer et al., 2013), the difference between the solidus and liquidus relations is very small at all pressures shown, and thus it is likely the significant depression of the melting curve of an Fe-S-Si mixture is caused by the sulphur in the system.

Prior to the work presented in this chapter, there was no information on the liquidus of Fe-S-Si with a lower light element enrichment, and as such the liquidus curves of Sanloup and Fei (2004) for Fe-S-Si and the Anzellini et al. (2013) melting curve for pure iron will be used for comparison with the measured melting of $Fe_{0.8}S_{0.1}Si_{0.1}$ presented here.

5.2 Off-line Experimental Method

Off-line DAC melting experiments were carried out at the School of Earth Sciences, University of Bristol to measure the melting temperature of $Fe_{0.8}S_{0.1}Si_{0.1}$. Discontinuities in the temperature vs. laser power functions were used as an indicator of melting (Chapter 3, section 3.5; Figure 5.5) and the preparation and use of the diamond anvil cell followed the method described in Section 3.4.1, using Princeton-type symmetric DAC's with anvils containing 200 - 250 μm diameter culets.

The $Fe_{0.8}S_{0.1}Si_{0.1}$ starting material was manufactured in two ways, the first used a McCrone micronizing mill to mix and grind FeS_2, Fe and Si powders (Chapter 4, section 4.4). The $Fe_{0.8}S_{0.1}Si_{0.1}$ mixture was then compressed between the truncated tips of two diamonds with a large culet size of 500 μm. The resulting foil was then broken using a needle and a piece close to approximately 40 μm in diameter manipulated and placed between two

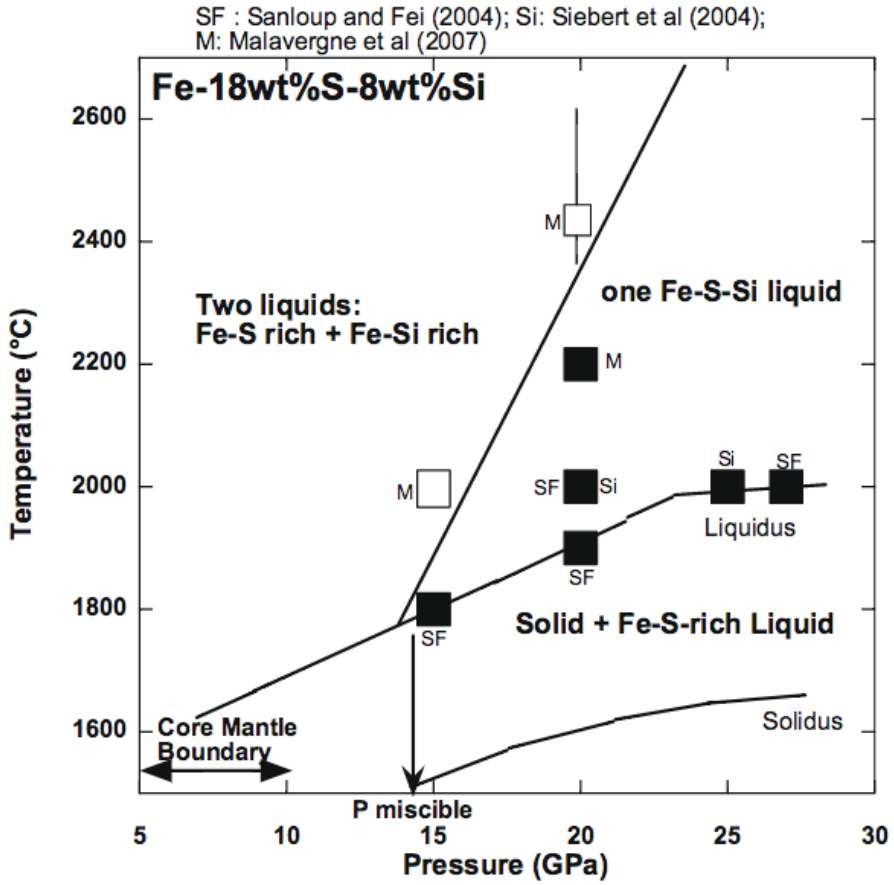

Figure 5.2: Melting relations in the Fe-S-Si system with $\sim$ 8 wt.% of Si and $\sim$ 18 wt.% of S, using a combination of the melting temperatures measured by Sanloup and Fei (2004) (SF), Siebert et al. (2004), (Si) and Malavergne et al. (2007) (M). Also indicated is the core boundary as well as the pressure where the miscibility gap closes. Figure taken from Malavergne et al. (2010)[1].

form fitting discs of Al_20_3 in the sample chamber within a drilled rhenium gasket (gasket preparation is outlined in Section 3.4.1, step 2).

The second method used to manufacture the $Fe_{0.8}S_{0.1}Si_{0.1}$ starting material used magnetron sputtering and a layering technique to achieve the correct composition (Chapter 4, section 4.5). A stainless steel gasket was used, and multiple samples were sandwiched between two MgO discs (the MgO discs are used as a thermally-insulating pressure-medium; Figure 5.3). Multiple samples in the same sample chamber meant that each "loading" of the DAC could

[1]Reprinted from Icarus, 206, Valérie Malavergne, Michael J. Toplis, Sophie Berthet, John Jones, Highly reducing conditions during core formation on Mercury: Implications for internal structure and the origin of a magnetic field, 199 - 209, Copyright 2010, with permission from Elsevier.

be used to conduct multiple melting experiments, significantly reducing the time taken to build a melting relationship.

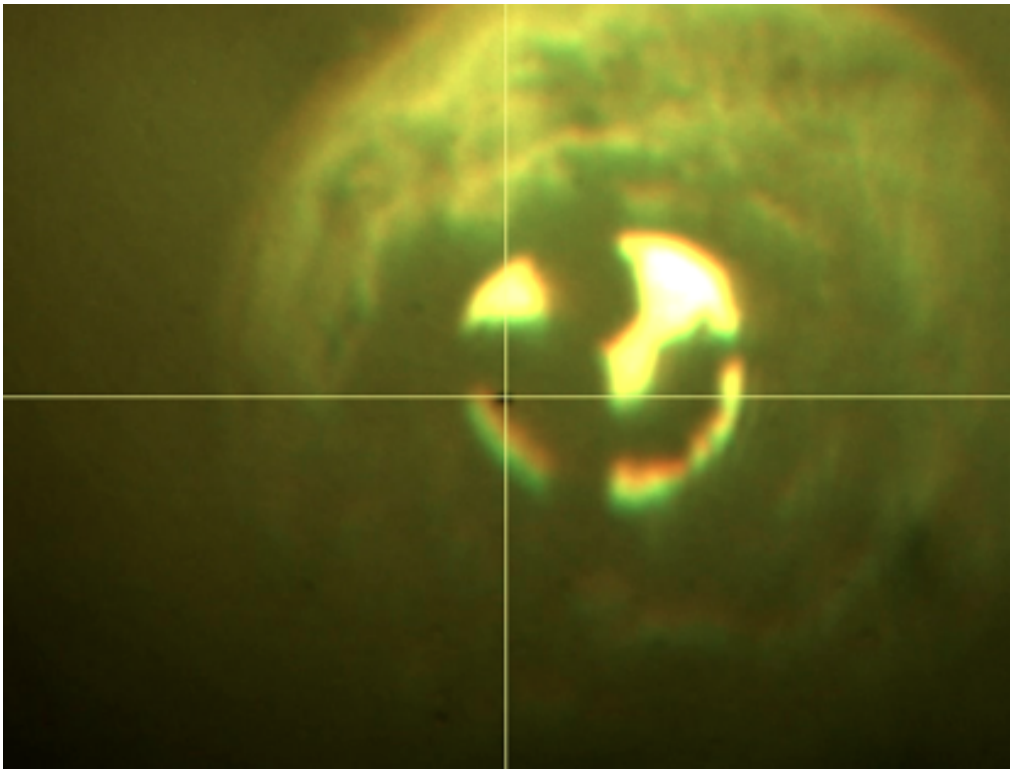

Figure 5.3: Example of a loaded DAC sample chamber including Fe-S-Si samples. Multiple pieces of Fe-S-Si (creating using the sputtering method, Chapter 4, Section 4.5) are placed onto an MgO disc into the sample chamber within a stainless steel gasket. A second piece of MgO (which acts as a thermally-insulating pressure medium) is placed on-top. This photo was taken at the I15 beam-line, Diamond Light Source, Oxford.

On top of the upper-most disc of MgO, ruby was added to the sample chamber, this enabled the measurement of pressure in the sample chamber (Chapter 3, Section 3.4.2). The pressure was monitored before and after heating and recorded post-heating. No correction has been made for the effects of thermal pressure in the experiments conducted using Al_20_3 as a pressure medium, however those using MgO have been corrected for thermal pressure based on the measured temperature and the known relationship between thermal pressure and pressure at room temperature when using MgO as a pressure medium and assuming there is a linear relation between thermal pressure and temperature (following Lord et al., 2014b).

Melting was achieved by a double-sided heating geometry, monitored on both sides by a detector and camera. The temperature of the sample was measured using both 1D and

2D spectro-radiometry independently. The 1D spectro-radiometry samples the temperature via a narrow slit and the spectra of the incandescent light generated by the heating of the sample, which is fitted to the Wien function (further details in Section. 3.4.3, and eq. 3.4). In 2D spectro-radiometry the entire heated spot is sampled. A single CCD camera is used to collect images of the laser-heated spot at four wavelengths (670, 700, 800 and 900 nm). Using spatial correlation the four individual images are combined, producing four intensity-wavelength data points for each pixel. In the same way as 1D spectro-radiometry, the temperature of each pixel is found by fitting to the Wien function, and can be used to generate a 2D heat map of the laser heated spot (Figure 5.4).

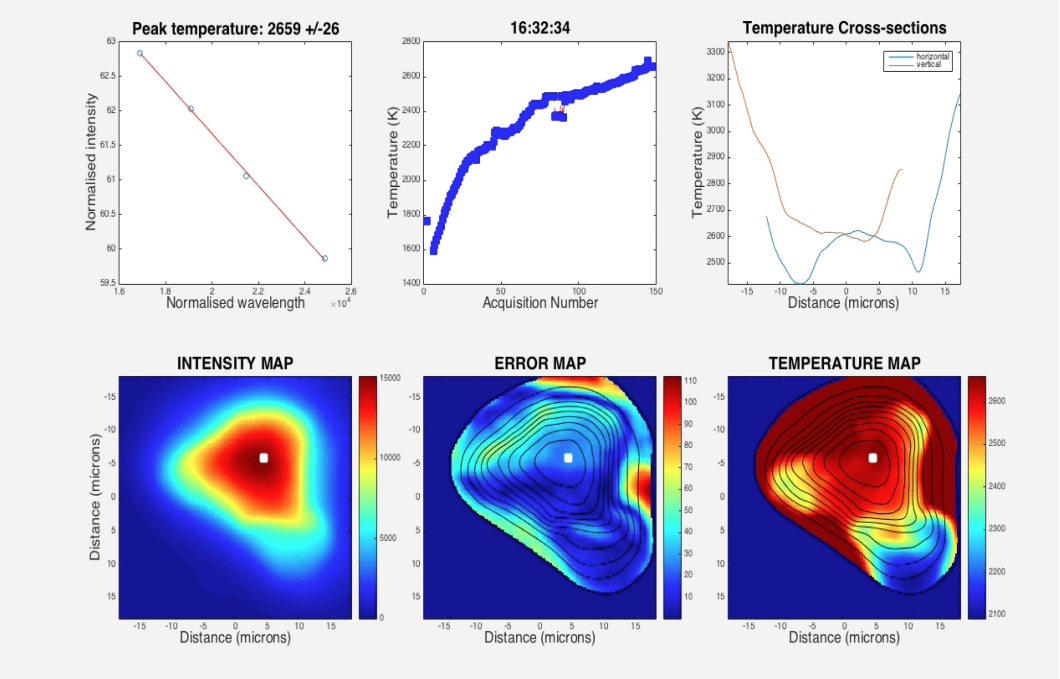

Figure 5.4: Snapshot of the 2D analysis used in these experiments, showing the 2D temperature map of Fe-S-Si creating using McCrone micronizing mill, at 44 GPa as well as the intensity of the radiation measured, and its associated error.

5.3 Off-line Melting Curve of Fe-S-Si

The melting temperatures and pressures of $Fe_{0.8}S_{0.1}Si_{0.1}$ are shown in Figure 5.6 and listed in Table 5.1. The standard deviation of the points in the plateau, from which the melting temperature is measured, is on the order of tens of kelvin, and the analytical error resulting from the fit to the Wien function is small ($<$10 K) (Chapter 3, section 3.4.3). Errors in the

measured melting temperature also arise from optical mis-alignment, chromatic aberration, temperature variations in the heated region as well as the wavelength dependence of the emissivity term, following Lord et al. (2014a), it is likely that these resulted in errors in the temperature measurement on the order of 100 K. The errors reported in Table 5.1 are a sum of this estimate and the statistical errors discussed, resulting in a total uncertainty on the order of $\pm$ 150 K (Table 5.1, Figure 5.6). A liquidus curve has been found by fitting the measured melting data (with exception of Table 5.1: EXPT 1) along with the measured melting temperatures of Fe-18.5wt% S- 8wt% Si from Sanloup and Fei (2004) (fitting to the midpoint between the brackets). EXPT 1 has not been included in the fitting as there has been no correction made for the thermal pressure during the experiment and therefore the melting pressure of EXPT 1 is approximated. Additionally, the exact composition of the $Fe_{0.8}S_{0.1}Si_{0.1}$ in EXPT 1 is uncertain, as the McCrone micronizing mill method (Chapter 4, Section 4.4) may have introduced some amount of oxygen into the material, whereas the composition of the starting material produced using the sputtering method (Chapter 4, Section 4.5) was measured *in-situ* at the Diamond Light Source, Oxford and was found to be consistent with a mixture of iron, sulphur and silicon alone, in the correct abundance (Chapter 4, Figure 4.11).

Table 5.1: Solidus and liquidus temperatures of $Fe_{0.8}S_{0.1}Si_{0.1}$; pressures ($P_{sol/liq}$) of the solidus and liquidus include a thermal correction. Also listed are the preparation methods used to manufacture the starting materials (Chapter 4, Sections 4.4 and 4.5).

EXPT	Sample Prep	P_{sol} (GPa)	Solidus (K)	P_{liq} (GPa)	Liquidus (K)
1	Milled	51.09	2172 $\pm$ 134	53.01	2679 $\pm$ 140
2 / EXP 123A	Sputtered	48.98	2737 $\pm$ 135	46.94	2206 $\pm$ 130
3 / EXP 123B	Sputtered	51.425	2720 $\pm$ 132	-	-
4 / EXP 124B	Sputtered	-	-	51.43	2720 $\pm$ 132

The temperature data were fitted to the Simon Glatzel equation (Simon and Glatzel, 1929):

$$T_m = T_{m0}\left(\frac{P_m}{A}+1\right)^{1/C} \tag{5.1}$$

In which, T_m is the melting temperature at pressure P_m, T_{m0} is the melting temperature at ambient pressure and A and C are fitting parameters.

To find the liquidus of $Fe_{0.8}S_{0.1}Si_{0.1}$, T_{m0} was fixed at 1573.15 K (estimated from Raghavan, 1988) and the fit found values of 31.081 GPa for A and 1.7426 for C. For the solidus relationship, T_{m0} was allowed to vary and fitted to be 1136.5 K, with A equal to 10.863 GPa, and C equal to 2.523 (listed in Table 5.2). The solidus and liquidus relationships are plotted in Figure 5.6. From the liquidus and solidus temperatures measured for $Fe_{0.8}S_{0.1}Si_{0.1}$, if Mercury's core was composed entirely of this composition, then the core would be molten at the conditions of top of Mercury's core (1850 -2000 K; e.g. Rivoldini et al., 2009 and 4 - 7 GPa, Hauck et al., 2013). To contain a solid inner core at the estimated pressures of the centre of Mercury's core ($\sim$ 36 GPa, Hauck et al., 2013) the temperatures would need to be below $\sim$ 2400 K, and thus have a shallow core adiabat. This is explored further in Chapter eight.

Table 5.2: Fitted parameters of the Simon Glatzel equation

	A (GPa)	C	T_{m0} (K)
Liquidus	31.081	1.7426	1573.15
Solidus	10.863	2.523	1136.5

5.4 In-situ Melting Experiments

In addition to the off-line experiments described thus far in this chapter, *in-situ* experiments were attempted at the Diamond Light Source, Oxford on the I15 'Extreme Conditions' beam-line. These experiments used the sputtered $Fe_{0.8}S_{0.1}Si_{0.1}$ starting material (Chapter 4, Section 4.5), Princeton-type symmetric DAC's and followed the same experimental set up as the off-line experiments discussed in the previous section.

A double-sided heating geometry has been put onto the Diamond Light Source I15 beam-line, and the intention was to heat the sample and take X-ray diffraction data from a small area within the heated spot, ensuring that the diffraction corresponded to the heated area. *In-situ* diffraction patterns were taken of the sample (Chapter 4, Figure 4.11) which confirmed the composition of the starting material created using the sputtering method (Chapter 4, Section 4.5), however, melting experiments were ultimately unsuccessful due to technical issues resulting from the laser-heating set-up on the beam-line which were still unresolved as of May 2016. Unfortunately the timescale involved with modifying the beam-line set-up

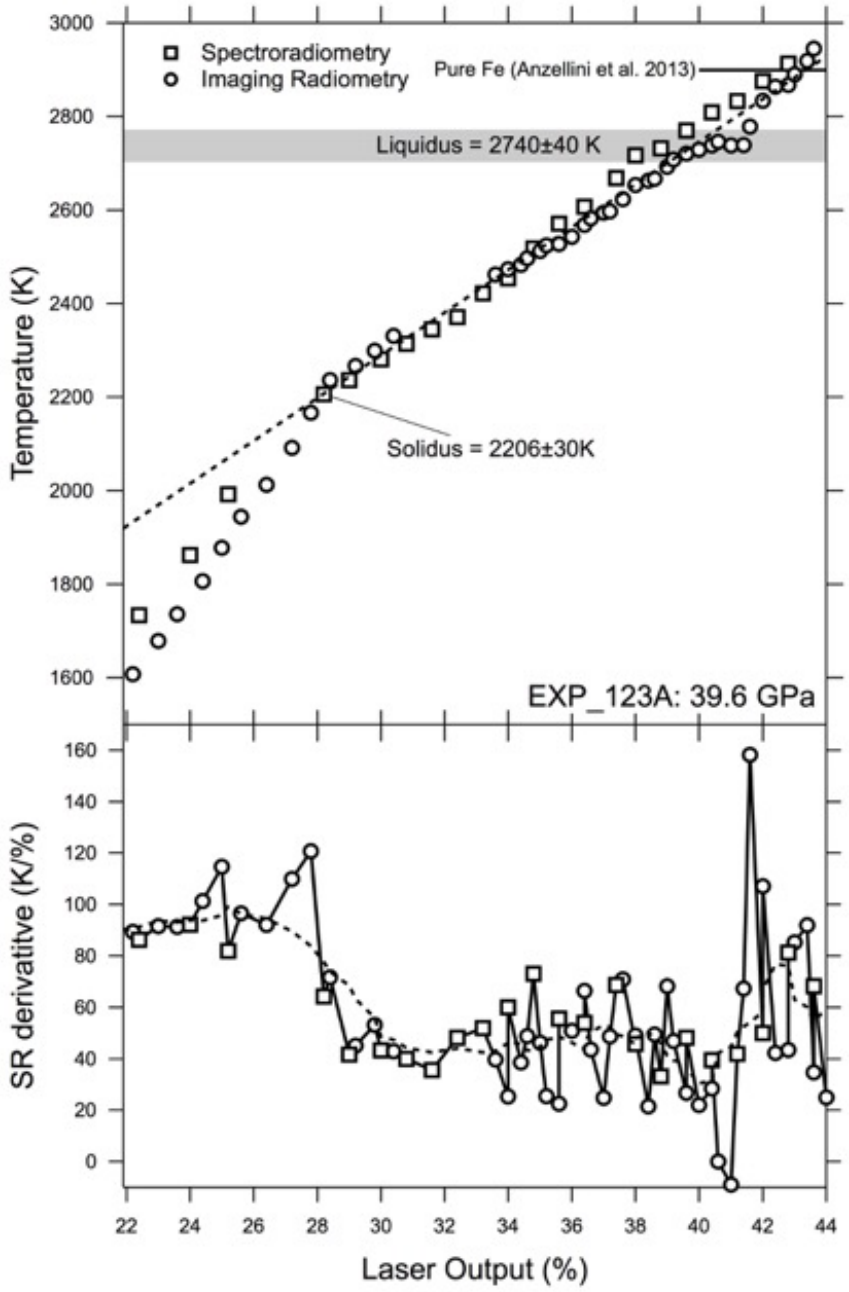

Figure 5.5: A typical laser power vs. temperature plot taken at 39.6 GPa, two changes in slope are observed, indicative of the solidus (2252 $\pm$ 30 K) and liquidus (2740 $\pm$ 40 K) temperatures. Both the 4-color mapping data (circles) and the spectro-radiometry (squares) agree there is a clear break in slope at low temperature possibly indicating the solidus, followed by a short plateau at high temperature indicating the location of the liquidus. The dashed line represents a 10-point boxcar smoothing of the data. The derivative is shown in the lower plot and the location of the liquidus is evident as the sudden decrease and rapid increase in the slope. Figure courtesy of O. T Lord.

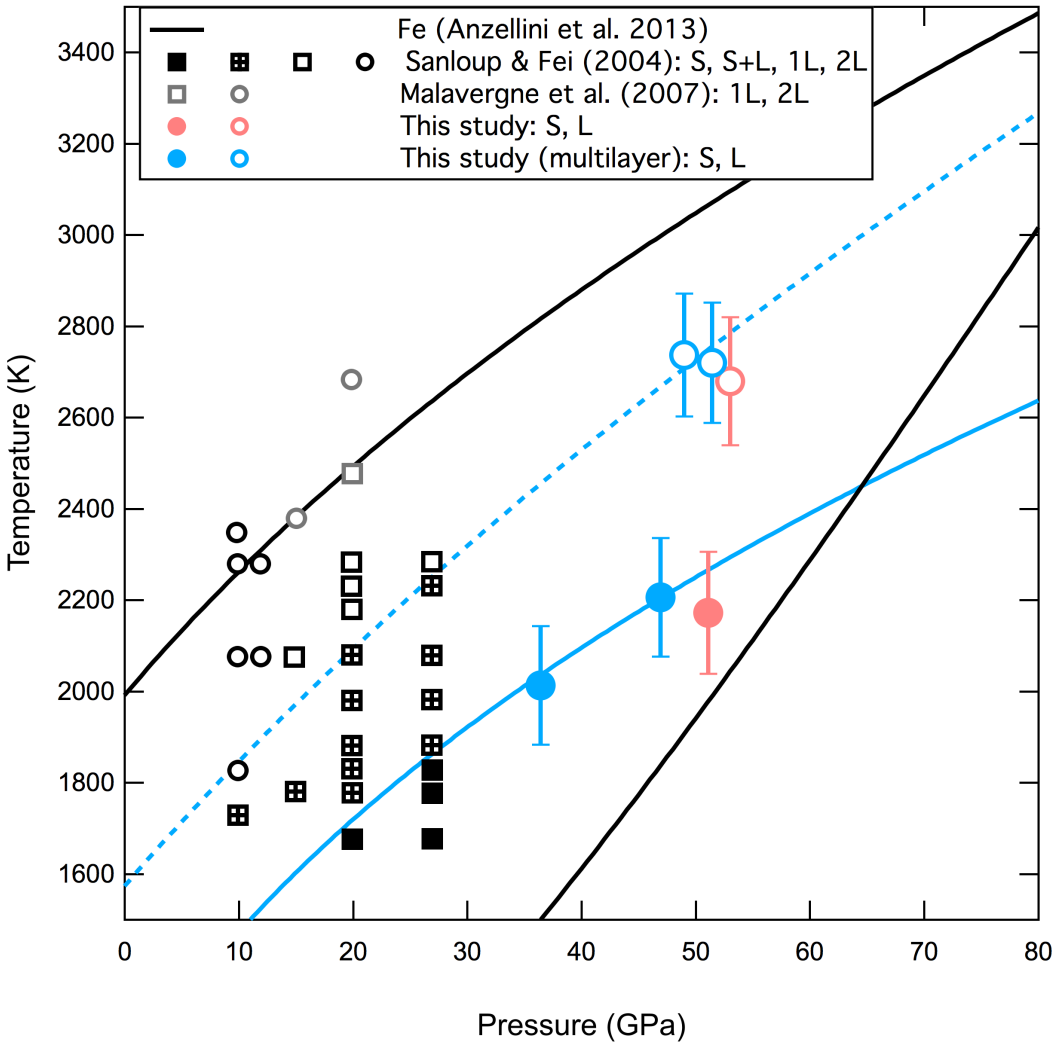

Figure 5.6: The experimental liquidus (shown with a blue dashed line) and solidus (solid blue line) of $Fe_{0.8}S_{0.1}Si_{0.1}$. The pure iron phase diagram as determined by Anzellini et al., 2013 is indicated by solid black lines, the top line is the melting curve of pure iron and the lower black solid line is the phase boundary between γ-Fe and ε-Fe. The data of Sanloup and Fei (2004) on Fe-18.5wt% S- 8wt% Si are indicated by black squares and circles; a filled black square represents a solid, a black square with a cross represents a solid+liquid run product, an empty square indicates one liquid, and a black circle two liquids. The results of Malavergne et al. (2007) are also shown, a grey square represents one liquid and a grey circle indicates two liquids. This study is represented by circles, a filled circle indicates the measured solidus temperature (solid line) and an empty circle indicates a liquidus temperature (dashed line). Experiments using a milled starting material (Table 5.1) are shown in pink, and those using a sputtered starting material are shown in blue. Error bars are also shown (Table 5.1) using capped lines in matching colours. The liquidus and solidus relationships are fitted to the Sanloup and Fei (2004) data and the blue circles (sputtered material). Figure courtesy of O. T Lord.

to measure the melting relationship was beyond the time-scale of this doctoral work.

5.5 Summary

Off-line experiments were conducted to measure the liquidus and solidus relationships of $Fe_{0.8}S_{0.1}Si_{0.1}$. *In-situ* measurements were also attempted at the Diamond Light Source but failed due to technical issues in the laser-heating set up. The liquidus was fitted using a combination of off-line experiments at the University of Bristol School of Earth Sciences and data from Sanloup and Fei (2004). Although Sanloup and Fei (2004) measured melting on a different composition of Fe-S-Si (18.5 wt% Si, 8 wt% S), the melting relations appear to coincide, and as such the assumption has been made that compositional differences have a negligible effect on the liquidus. In reality, this is likely not to be the case, and different compositions will result in different melting temperatures, however, the effect of this is unclear and further measurements are required to investigate the validity of this assumption. The liquidus and solidus relationships measured in this work suggest that if Mercury's core consisted of $Fe_{0.8}S_{0.1}Si_{0.1}$ alone, then at the conditions of the top of the present day core (1850 -2000 K; e.g. Rivoldini et al., 2009 and 4 - 7 GPa, Hauck et al., 2013), $Fe_{0.8}S_{0.1}Si_{0.1}$ would still be molten. These relationships also suggest that for Mercury to contain a solid inner core, the temperature at the centre of the planet would need to be less than $\sim$ 2400 K (Figure 5.6; $\sim$ 36 GPa, Hauck et al., 2013. The liquidus relationship determined in this study is used alongside the adiabatic gradient to investigate the crystallisation regime of a hypothetical $Fe_{0.8}S_{0.1}Si_{0.1}$ core of Mercury in Chapters eight and nine.

Chapter 6

The Thermoelastic Properties and Adiabatic Gradient of Pure Liquid Iron

6.1 Introduction

As the dominant element in the core of Mercury, the properties of iron are fundamentally important to understanding the deep interior of the innermost planet in the solar system. However, the properties of iron are important throughout the solar system and the results presented in this chapter are applicable to a range of small rocky bodies within the solar system including Ganymede and the Moon, and outside the solar system in the cores of sub-Earth size exoplanets (Chapter 1). This chapter further details the methods and gives the results of first principles molecular dynamics (FPMD) simulations used to calculate the equation of state and thermodynamic properties of pure liquid iron at 2000, 3000 and 4000 K (Figure 6.1).

The core of Mercury likely lies below 36 GPa (Hauck et al., 2013) and estimates of the core-mantle boundary (CMB) conditions range between 1850 - 2000 K (Rivoldini et al., 2009) and 4 - 7 GPa (Hauck et al., 2013). At these relatively low pressures pure liquid iron may undergo a high to low spin transition, which will not be captured by extrapolating previous work on non-magnetic Fe (e.g. Vočadlo et al., 2003; Ichikawa et al., 2014; see Section 1.4.3) to lower pressures. Magnetic NVT molecular dynamics calculations on pure liquid iron have been run at a range of temperatures and volumes corresponding to pressures up to 160 GPa (at 4000 K). Each isotherm is fitted to a third order Eulerian finite strain

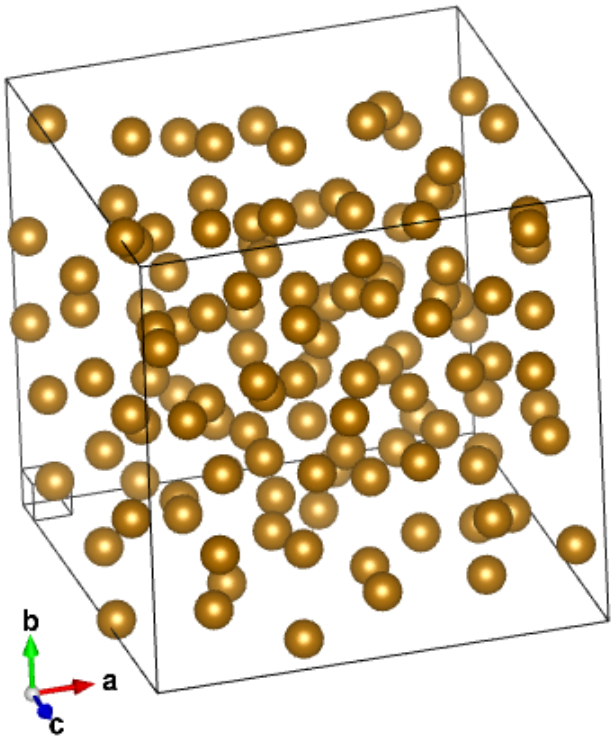

Figure 6.1: Snapshot of the first principles molecular dynamics simulation of pure iron, the 125 iron atoms are positioned randomly in the cell. The liquid state is confirmed using radial distribution functions and the mean-squared displacement of the atoms. Image created using the Visualization for Electronic and Structural Analysis Software, VESTA (Momma and Izumi, 2011).

expression, the Birch Murnaghan 3rd order equation of state (Birch, 1978; BM3EOS) and a combination of temperatures are used to calculate the thermal expansion and Grüneisen parameter of pure liquid Fe. These properties define the adiabatic gradient, which is used to suggest the crystallisation regime of a hypothetical pure Fe core. Additionally, radial distribution functions have been employed to investigate whether any structural changes occur under these conditions.

6.2 Calculations and Experiments on the Properties of Pure Liquid Iron

Constraining the changing properties of pure liquid iron with increasing pressures and temperatures can begin to reveal the conditions and structural changes at depth within a planet.

Due to its abundance in the solar system, and its role as a building block in the terrestrial planets, there consists a considerable volume of work published on the properties of iron. As detailed in the first chapter of this thesis, solid iron undergoes several structural changes with increased pressure and temperature, notably transforming from a body-centred cubic structure at low pressures to a hexagonal like structure at extreme pressures, and to a face-centred cubic (fcc) structure at high temperatures and low pressures. There is comparatively much less work in the literature on the properties of liquid iron. Sustaining a liquid experimentally is extremely difficult, whereas computer simulations make this type of study more accessible, albeit with their own unique challenges and at significant computing cost. The temperature at which iron melts when approaching the extreme conditions one would find at the centre of the Earth was historically a topic of debate (see Chapter one, Figure 1.11), however modern studies of the melting curve of iron now show excellent agreement between static (e.g. Anzellini et al., 2013), dynamic (e.g. Brown and McQueen, 1986) and *ab initio* results (Alfè et al., 2002b; Alfè, 2009).

The melting temperature of pure iron at 0 GPa is $\sim$ 1830 K, increasing to approximately 3730 K at 100 GPa (Anzellini et al., 2013). Hence, at the conditions of Mercury's core ($\sim$ 5.5 - 36 GPa) this would suggest an iron melting temperature of $\sim$ 2000 K at the outer core boundary increasing to approximately 2730 K at the planet's centre (estimated from Anzellini et al., 2013). However, as shall be seen in Section 6.10, the shape of the melting curves, even at these relatively modest conditions, becomes very important.

The question now turns to the behaviour of liquid iron at these pressures; as discussed, the structure of solid iron changes with increasing pressures and temperatures, but it may also continue to undergo changes in the liquid structure. From changes in the radial distribution function and the shape of the second nearest neighbour shell, determined by X-ray diffraction, Sanloup et al. (2000) have observed structural changes in liquid iron at 5 GPa, close to the solid iron triple point and the CMB pressure of Mercury, observing a transition from a body centred cubic (bcc) like structure to a bcc+fcc structure (shown in Figure 6.2), but these changes were not seen by Shen et al. (2004) who investigated the structure of liquid iron along the melting curve up to 58 GPa. This has been investigated here using radial distribution functions determined by first principles molecular dynamics (FPMD).

Thermodynamic and physical properties of pure liquid iron have been studied previously

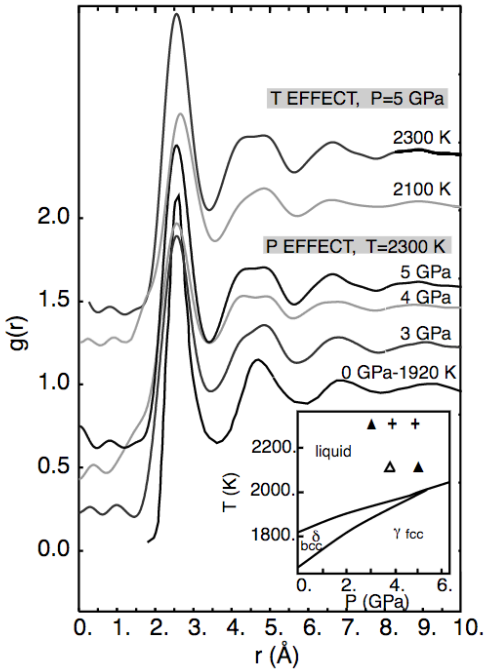

Figure 6.2: Structural changes in liquid iron observed in the radial distribution functions, figure from Sanloup et al. (2000). Pair correlation functions of liquid Fe at different *P-T* conditions including ambient pressure data from Yoo et al. (1995); Söderlind et al. (1996); Andrault et al. (1997); Steinle-Neumann et al. (1999) with an inset phase diagram of Fe at the experimental *P-T* conditions; the empty triangle corresponds to a partially bcc-like liquid, full triangles to bcc-like structured liquid and black cross to bcc+fcc.

using FPMD by two authors; Vočadlo et al., 2003 and Ichikawa et al., 2014. In both cases non-spin polarised calculations were performed at pressures and temperatures exceeding 50 GPa and 4000 K, far higher than the expected conditions of Mercury's deep interior. At the reduced conditions of Mercury's core pure liquid iron may undergo a high to low spin transition during which the absolute magnetic moment of each atom will decrease to zero. Experiments on the magnetic moment of pure liquid iron using neutron diffraction by Waseda and Suzuki, 1970 and Weber et al., 1978 have found the magnetic moment of pure liquid iron at 1873 K to approximately range between 1.2 μ_B and 1.9 μ_B respectively. This transition has a marked effect on the properties of liquid iron (see Figure 6.3) and as such fully spin polarised magnetic calculations were performed to capture this.

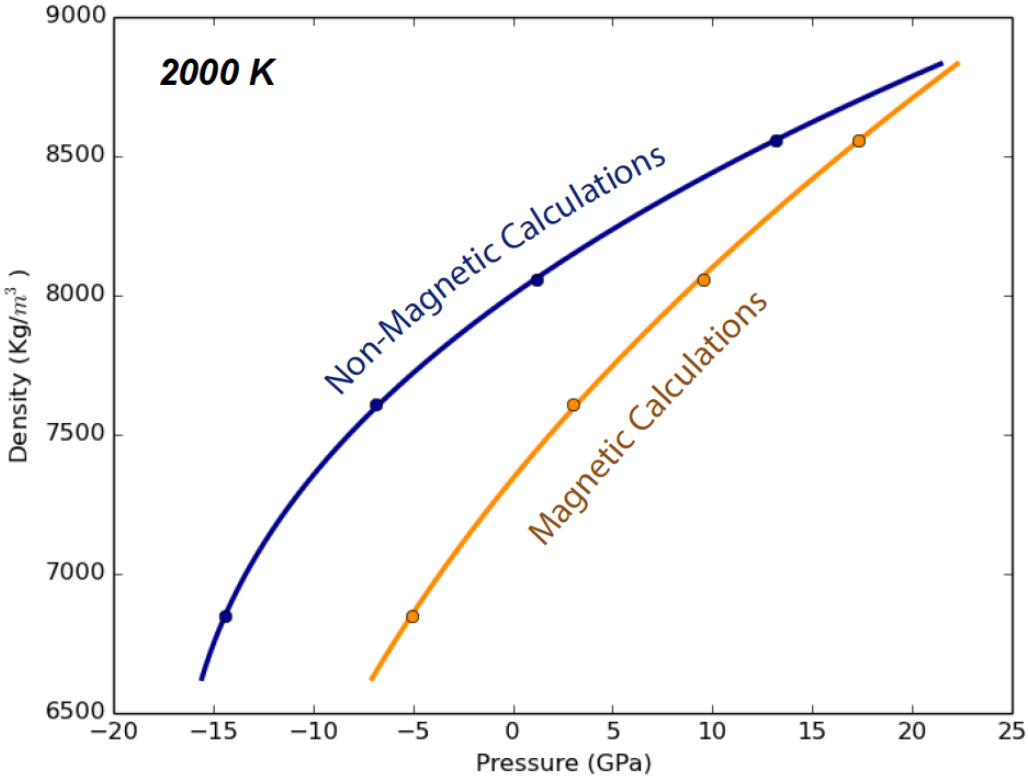

Figure 6.3: Density comparison between magnetic calculations (orange) and non-magnetic calculations (dark blue) for pure liquid iron at 2000 K.

6.3 Methods

First principles molecular dynamics (FPMD) calculations have been performed using the generalised gradient approximation with the PW91 enhancement factor (Perdew et al., 1992, 1993) to the solution of Density Functional Theory. PAW pseudopotentials (Blöchl, 1994; Kresse and Joubert, 1999) have been used to describe the core electrons which additionally treat the semi-core p states as valence electrons.

The simulations were conducted with a cell size of 125 atoms (Figure 6.1), initiated in a simple cubic structure and calculations performed at time steps of one femtosecond. A single k-point was used to sample the Brillouin zone located at $\frac{1}{4}, \frac{1}{4}, \frac{1}{4}$ (Baldereschi, 1973), which was found to better produce converged values of energy and pressure than gamma point sampling of the Brillouin zone. The cut-off energy was converged within the criterion of $\pm$ 5 meV resulting in an energy cut-off of 400 eV (Appendix A). The cubic structure was superheated to 10,000 K for a total of two picoseconds at a single volume to obtain an

initial liquid structure (confirmed by the mean-squared displacement and radial distribution functions, e.g. examples shown in Figures 6.4 and 6.5).

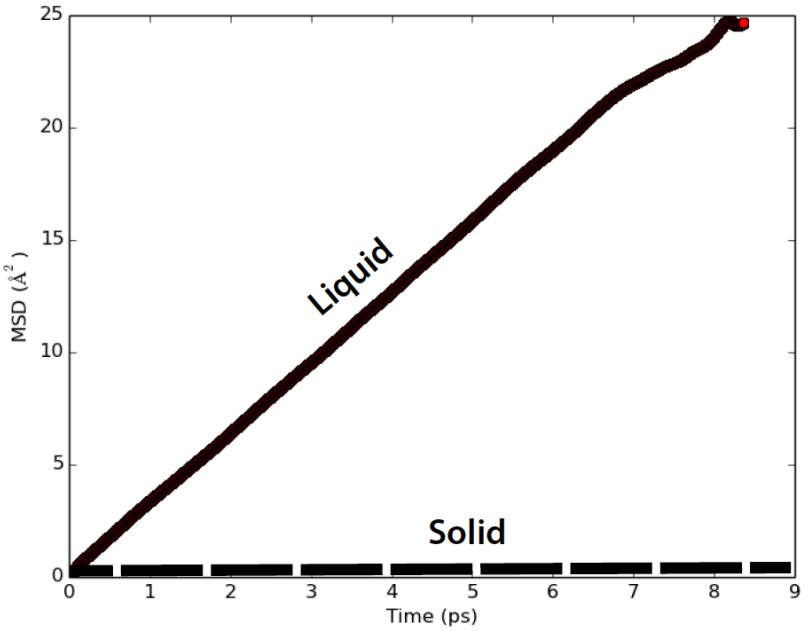

Figure 6.4: Mean squared displacement (MSD) is used to confirm the liquid state of pure liquid Fe in the FPMD calculations. A linear increase in MSD with simulation time is indicative of a liquid state (example of a pure liquid Fe simulation at -5 GPa shown in solid line), whilst a solid's MSD will stay constant (a hypothetical mean-squared displacement of a solid is shown using dashed line).

The superheated configuration was cooled independently to 2000, 3000 and 4000 K and compressed to a range of volumes corresponding to a pressure range of -5 GPa (expanded volume) to 160 GPa depending on temperature. The temperature in the calculation was controlled using the Nosé-Hoover thermostat (Nosé, 1984). The initial liquid configuration (resulting from the superheated calculation) was run for at least an additional two picoseconds to achieve equilibrium. Then finally, the FPMD were run for a minimum of four picoseconds at the desired volumes and temperatures to calculate the pressure and energy as an average over simulation time. Uncertainty in the time averaged values have been calculated using the blocking method (Flyvbjerg and Petersen, 1989) and was found to be less than 6 x 10^{-3} GPa in pressure and 0.1 meV in energy in all cases.

The calculations were run spin polarised and initiated with a finite atomic magnetic moment equal to +4 μ_B on each atom, totalling +500 μ_B for the 125 atom cell. This was found to

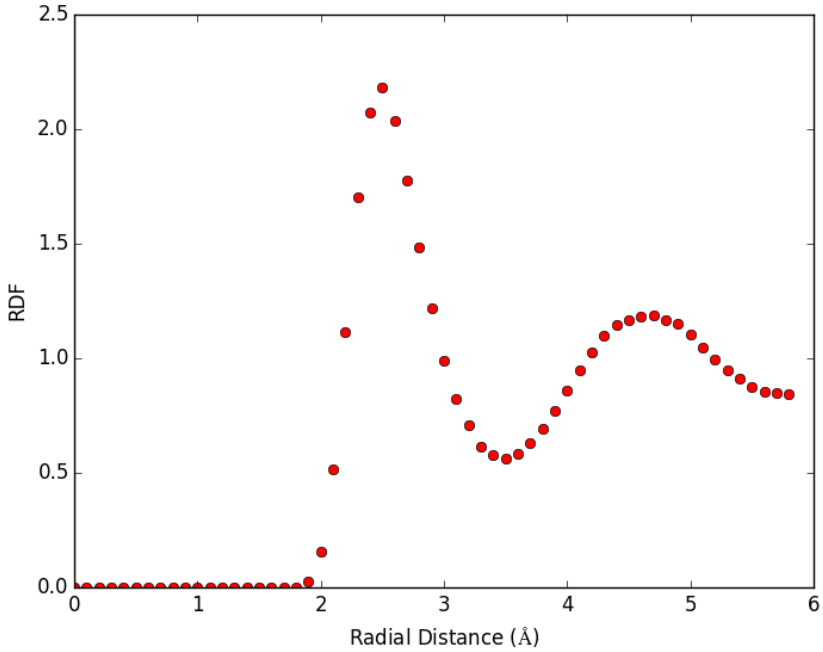

Figure 6.5: Radial distribution function (RDF) of pure liquid iron at -5 GPa. RDF's can be used to identify whether a simulation is liquid. The RDF of a liquid will be distinctive from a solid due its lack of successive peaks that would indicate long range order.

reduce to a zero overall magnetisation very quickly in the calculation, whilst (when outside the low spin state) maintaining a finite local moment on each atom, i.e. the simulation retained magnetic moments on the individual atoms but they were not ordered.

A consideration was also made to use a differing functional, namely GGA+U which includes an empirical correction to improve the estimate of the magnetic moment. This correction was implemented (U = 2.2 eV taken from Cococcioni and de Gironcoli, 2005), but it was found that GGA matched the experimental value of the magnetic moment (Waseda and Suzuki, 1970; Weber et al., 1978) better than that predicted by GGA+U (Figure 6.6). Hence, GGA (PW91) was used throughout the pure liquid Fe calculations as well as those described on Fe-S-Si in Chapter eight.

6.4 The High to Low Spin Transition

The calculations presented here were run using a spin-polarised magnetic system, initiated at a value of +4 μ_B per atom but allowed to freely equilibrate (i.e. "free" spin calculations).

The predicted magnetic transition from these calculations was found to be very gradual, with a 'high spin' magnitude of the magnetic moment per atom found to be 1.85 μ_B at 2000 K and 0 GPa, which gradually decreased to a value of $\sim$ 1.4 μ_B at 10 GPa (Figure 6.6). With increasing temperature the magnetic moment was found to decrease and more rapidly fall to zero. The higher-temperature 3000 and 4000 K calculations permitted the simulation of much higher pressures and as such the magnetic moment was simulated up to and including the predicted low spin state of this material, which occurred at $\sim$ 100 GPa.

Figure 6.6 includes the pressure ranges of the smaller terrestrial bodies (and rocky moons) in the solar system. Throughout all these, pure liquid iron is above the low spin state, i.e. there are finite atomic moments on each of the atoms. The system is in the paramagnetic state, which means that although there is a magnetic moment associated with the individual atoms, they are randomly oriented such that the magnetic moments cancel out over the material and there is no net magnetisation in the absence of an applied field. Spin polarised calculations performed here suggest that pure liquid iron would have an associated magnetic moment throughout the estimated core pressures of Mercury and thus may also have a large magnetic susceptibility which will have implications for the magnetic Reynolds number and the convective properties of the liquid and may be important in understanding the dynamo process in the planet (Frick et al., 2002). The associated finite local moments sustained in these calculations may also suggest some ferro-fluid like properties of liquid iron (e.g. Odenbach, 2004) and thus, magnetic calculations are required (as performed in this study) to accurately determine the properties and behaviour of pure liquid iron in the planet's deep interior.

However, VASP "free" spin calculations detailed in this chapter neglect the effect of magnetic entropy, which acts to increase the stability of magnetic phases. In order to include this effect, which may change or broaden the magnetic transition, free-energy minimisation via thermodynamic integration is used to accurately map the spin crossover, described in detail in the next chapter.

6.5 Structural Changes in Liquid Iron

There is debate on whether any structural changes occur in iron above the melting temperature, with Shen et al. (2004) observing no change in liquid iron structure along the

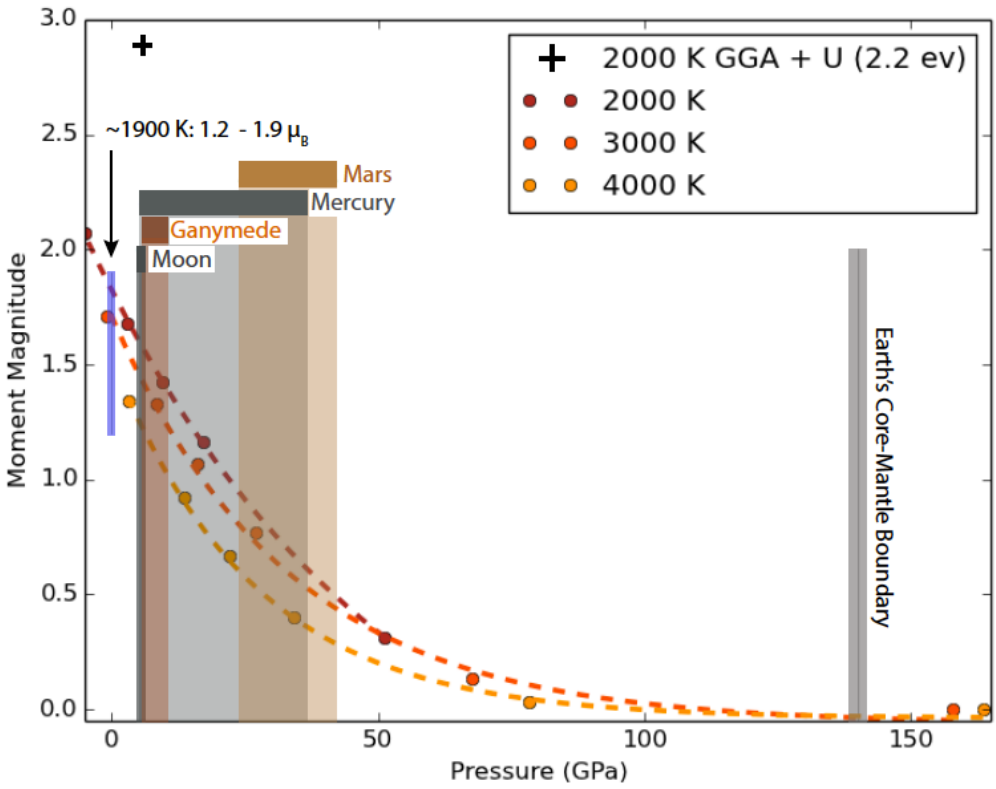

Figure 6.6: The magnetic transition of pure liquid iron at 2000, 3000 and 4000 K as predicted by magnetic first principles molecular dynamics calculations. The orange lines correspond to the 2000, 3000 and 4000 K isotherms (individual NVT calculations are represent by points), whilst the shaded bars indicate the approximate pressure ranges of the small bodies in the solar system and grey line represents the pressure of the Earth's core-mantle boundary. The pressures of Mercury's core are from Hauck et al. (2013), the pressures of Ganymede's core are from Rückriemen et al. (2015) and the pressures of the Moon and Mars' core are from Antonangeli et al. (2015). Also shown is the approximate value of the local finite moments at 2000 K using a GGA+U functional, this is much higher than that calculated using PW91 alone and far higher than the experimental range outlined in blue (1.2 - 1.9 μ_B; Waseda and Suzuki, 1970; Weber et al., 1978). Errors associated with the simulated magnetic moments are also shown but are smaller than the displayed point size.

melting curve in contrast with Sanloup et al. (2000) who found structural changes close to the iron-liquid triple point. Sanloup et al. (2000) detected structural changes in the iron liquid indicated by a shift in the second and third nearest neighbour shells in the radial distribution functions to shorter distances at 2300 K and 5 GPa (Figure 6.2). Radial distribution functions were calculated for the low pressure volumes at 2000 K simulated in this work, corresponding to pressures ranging from 0 - 17 GPa. A subtle change in the distinctly non-gaussian shape of the 2nd order neighbour shell has been calculated (Figure 6.7) and a small shift to shorter distances. The changing distance and shape of the 2nd order neighbour peak is similar to that reported in Sanloup et al. (2000) (Figure 6.2) and may suggest a good agreement between this work and their results and the onset of a structural change in the iron liquid. However, to resolve this shape further calculations would be required to distinguish the changes observed in the radial distribution function with pressure.

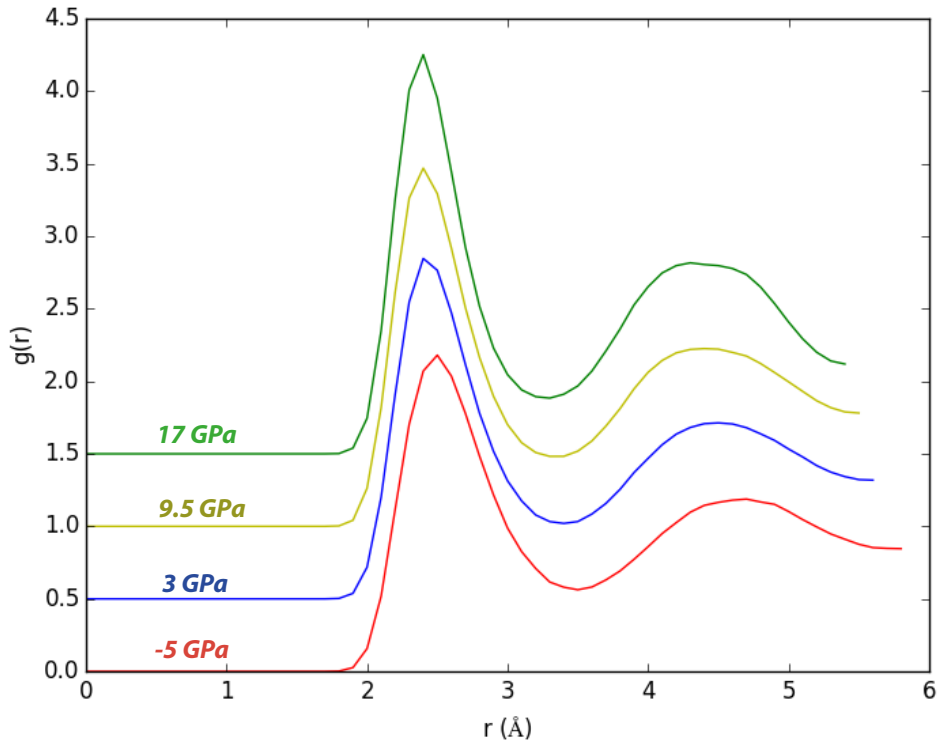

Figure 6.7: The first and second order neighbour shells in the radial distribution functions of pure liquid iron at 2000 K from -5 - 17 GPa (from red - green respectively) shifted by 0.5 in g(r) with respect to each other for clarity. A broad non-gaussian peak shape in observed in the 2nd nearest neighbour shell.

6.6 The Equation of State

In the canonical ensemble the volume of the calculation is specified and the pressure calculated as a function of simulation time. This produces the 'external pressure' simulated by VASP, but in order to find the total pressure the contribution due to the kinetic energy of the nuclei must be added:

$$P_{total} = P_{ext} + \left(\frac{Nk_BT}{V}\right) \tag{6.1}$$

In which P_{ext} is the measured property from VASP, k_B is the Boltzmann constant and T, the temperature of the calculation. The blocking method was used to find the error in the correlated time averaged values and combined using error propagation. The volumes and corresponding total pressures are given in Table 6.1.

Table 6.1: Volumes and calculated pressures of pure liquid iron at 2000, 3000 and 4000 K, [1] indicates non-liquid calculations, and [2] indicates calculations which were truncated to exclude vitrified portions of the simulation.

Temperature (K)	Density (kg/m^3)	Total Pressure (GPa)	Error ($\pm$ GPa)
2000	6846.9566	-5.0535	0.0012
	7607.7295	2.9897	0.0007
	8055.2430	9.5396	0.0010
	8558.6957	17.3025	0.0042
	9781.3666	51.3267	0.0041
	11411.5943 [1]	139.2101	0.0004
3000	6846.9566	-0.7810	0.0015
	7607.7295	8.5269	0.0006
	8055.2430	16.2104	0.0007
	8558.6957	27.1836	0.0008
	9781.3666	67.6029	0.0015
	1411.5943 [2]	157.9320	0.0055
4000	6846.9566	3.1477	0.0010
	7607.7295	13.6133	0.0011
	8055.2430	22.0628	0.0012
	8558.6957	34.2985	0.0014
	9781.3666	78.3329	0.0010
	1411.5943	163.5301	0.0023

The time averaged pressures and volumes were fitted to a third order Eulerian finite strain

expression, the Birch Murnaghan 3rd order equation of state (BM3EOS) using the EoSFit code (Angel et al., 2014; Table 6.2). At each temperature six canonical calculations were performed corresponding to volumes ranging between 13.54 - 8.13 $\AA^3$/atom (Table 6.1), however at the lower temperatures (2000, 3000 K), smaller volumes or partial runs had to be excluded as they were suspected to have undergone vitrification, revealed by the mean-squared displacement. At low temperatures and high pressures the linear relationship between the mean-squared displacement and simulation time, indicative of a liquid, was found to stall (Figure 6.8). This suggested that the simulation had transformed from a liquid into a glass like structure and consequently only those simulations that were considered liquid according to both their mean-squared displacement and radial distribution function were used in the analysis.

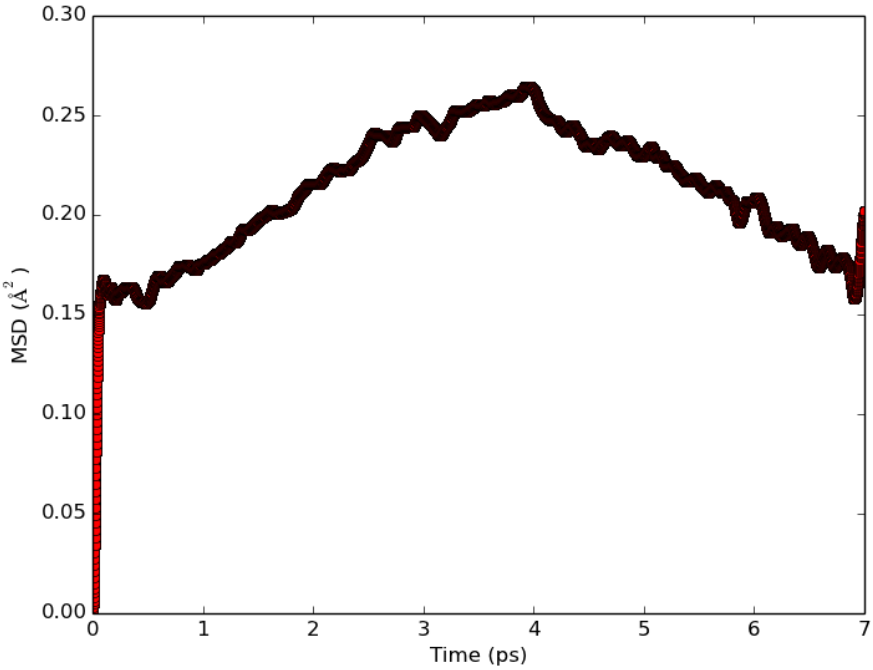

Figure 6.8: Mean squared displacement (MSD) is used to confirm the liquid state of pure liquid Fe in the FPMD calculations. A linear increase in MSD with simulation time is indicative of a liquid state (e.g. Figure 6.4). The truncated trend between MSD and simulation time shown here suggests that this calculation had vitrified, i.e. turned from a liquid into a glass like structure.

In Figure 6.9 the equations of state of each isotherm are plotted alongside the results of Vočadlo et al., 2003 and Ichikawa et al., 2014 for their lowest temperature 4000 K (all cal-

Table 6.2: Fitted parameters of the Birch Murnaghan 3rd order equation of state

Temperature (K)	V_0 ($\AA^3$)	ρ_0 (kg/m^3)	K_0 (GPa)	K'
2000	12.56(9)	7360	78(9)	6.1(8)
3000	13.40(18)	6920	65(13)	6.6(10)
4000	14.3(4)	6485	48(17)	7.1(15)

culations exceed 50 GPa). Very good agreement in the calculated density at 4000 K has been found, coinciding with small magnetic moments on the atoms in the simulations (Section 6.4). The density of liquid iron has been calculated here to be 7385 kg/m^3 at 0 GPa and 2000 K, which is higher than previous experimental measurements at ambient pressure and 2000 K that range from $\sim$ 6800 - 6950 kg/m^3 (Williams, 2009). This is also greater than that previously used by Riner et al. (2008) to model Mercury's internal structure, which used a liquid iron density of 7019 kg/m^3 for 1 bar and 1811 K (determined by Anderson and Ahrens, 1994). The considerably higher density of liquid iron calculated here could be a result of the magnetic transition predicted therein. The magnetic entropy of the system has not been included in the minimisation routine and thus the simulations described here will calculate a lower magnetic moment as a result of its absence. A larger magnetic moment will increase the volume of the atom and thus decrease the density and therefore could be the cause of the discrepancy (Figure 6.9). To resolve the difference between the density calculated here and the experimental measurements of the density of liquid iron, the magnetic entropy needs to be included, which is presented in Chapter 7.

Calculations performed at 2000 K additionally suggest that at 5 GPa (approximate conditions of Mercury's CMB e.g Rivoldini et al., 2009; Hauck et al., 2013) the density of liquid iron will be $\sim$ 7798 kg/m^3 (Table 6.3), and would increase to $\sim$ 9304 kg/m^3 at 36 GPa (the modelled pressure of Mercury's core, Hauck et al., 2013).

6.7 The Isothermal Bulk Modulus

A fit to the BM3EOS can be used to determine the isothermal bulk modulus of a material. The 'pvcal' function in the EoSFit code (Angel et al., 2014) was used to calculate the pressures and volumes along with the isothermal bulk modulus from the BM3EOS fit (shown in Figure 6.10).

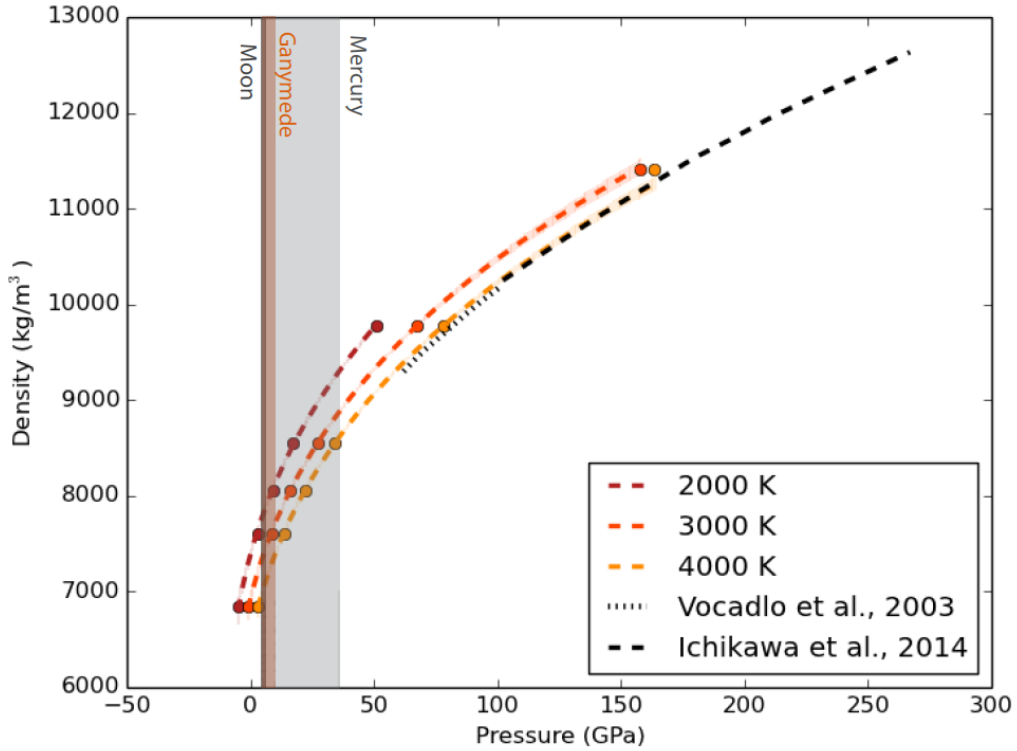

Figure 6.9: The fitted equation of state for pure liquid iron at 2000, 3000 and 4000 K (increasing lighter solid orange lines respectively. *Ab initio* calculations of Vočadlo et al. (2003) and Ichikawa et al. (2014) are shown as dashed lines in black. Errors are indicated by capped lines but are smaller than the point size shown. The modelled core pressures of Mercury are indicated by the shaded region, 5.5 - 36 GPa (Hauck et al., 2013). The pressures of Ganymede's core are from Rückriemen et al. (2015) and the pressure range of the core of the Moon is from Antonangeli et al. (2015).

This work agrees very well with the studies of Ichikawa et al. (2014) and Vočadlo et al. (2003) and all studies suggest an almost linear increase in bulk modulus with pressure, and an increasing bulk modulus with decreasing temperature (Figure 6.10).

6.8 The Thermal Expansion of Pure Liquid Iron

As described in Chapter two, Section 2.11 the thermal expansion of a material describes how the volume changes with temperature. To determine the thermal expansion, one requires constant pressure across the isotherms rather than constant volume which has been implemented here. This challenge is over-come using the BM3EOS. Using the fitted parameters for each isotherm the volume can be found at any specified pressure (using an iterative

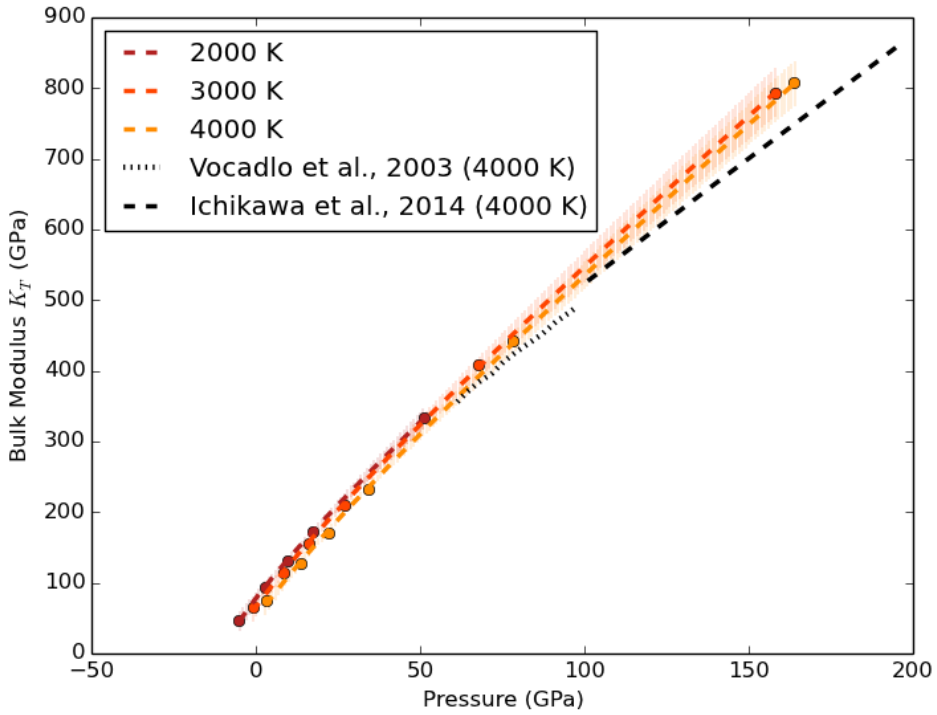

Figure 6.10: The calculated bulk modulus against pressure of the 2000, 3000 and 4000 K isotherms are shown in lighter orange lines respectively. The lines correspond to the fitted results of the BM3EOS and the points indicate the NVT calculations. Errors as a result of the fit to the BM3EOS are indicated by shaded lines. The results of Ichikawa et al. (2014) and Vočadlo et al. (2003) are shown in thick and thin dashed lines respectively.

solving process). The 'pvcal' module within the EoSFit code (Angel et al., 2014) calculates the volumes for a series of pressures. Those of the highest temperature (4000 K) and lowest temperature (2000 K) were used to calculate the mean thermal expansivity of pure liquid iron from 2000 to 4000 K as described in Chapter 2 (Figure 6.11). To investigate the change in thermal expansivity with temperature the same method was used to calculate the mean thermal expansivity between 2000 - 3000 K and 3000 - 4000 K also shown in Figure 6.11.

The thermal expansion predicted using this method suggests a markedly steep decrease in thermal expansion with respect to pressure (Figure 6.11). The thermal expansion calculated in this work appears consistent with that calculated by Ichikawa et al. (2014) and Vočadlo et al. (2003) but much lower than the measured ambient-pressure thermal expansivities of liquid iron. Experimentally the thermal expansivities of liquid iron have been found to

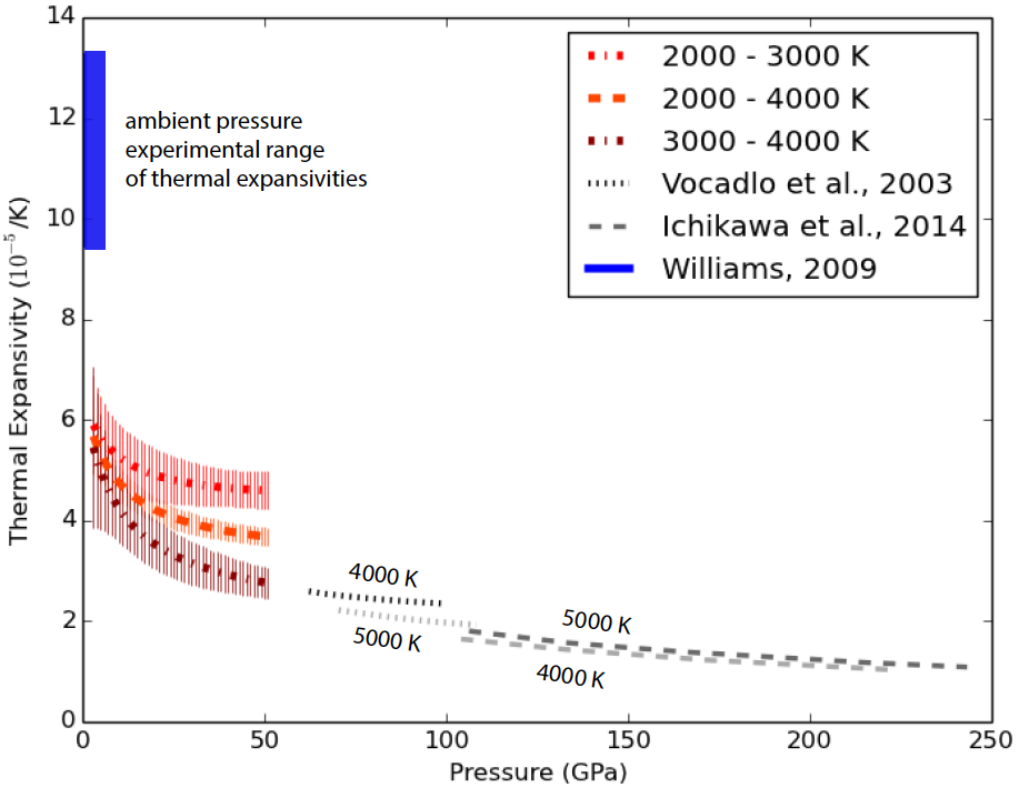

Figure 6.11: Thermal Expansion of pure liquid iron at 3000 K (dashed orange line), errors as a result of the BM3EOS fit (from which the volumes are derived) are indicated by capped lines. The results of Ichikawa et al. (2014) and Vočadlo et al. (2003) are shown by thick and thin grey dashed lines respectively.

range approximately between 9.2 -13.2 x $10^{-}5$ /K, although a comprehensive review of the literature by Assael et al. (2006) recommends the higher measured thermal expansion of 13.2 x $10^{-}5$ /K which is relatively constant with temperature up to 2500 K (Figure 6.11, Williams, 2009). It is possible that a partial cause of the discrepancy results from the fitting of the BM3EOS, as a small change to this fit could translate to a large change in the calculated thermal expansion. However, as discussed in Section 6.6 a significant cause of the low calculated thermal expansion could result from neglecting the magnetic entropy in the minimisation routine. The inclusion of the magnetic entropy will extend the stability of larger finite local moments to higher pressures. An increased local moment will result in a larger volume and thus may impact the thermal expansion. This is explored in Chapter 7. The change in temperature (ΔT = 2000 K) used in the thermal expansion calculation is large and thus tests were carried out with a much smaller ΔT equal to 100 K (e.g. calculations

performed at 2950 and 3050 K to determine the mean thermal expansion between 2950 and 3050 K). However an issue arises if two values with their associated errors are very close, as in such a scenario the relationship between them can not be accurately constrained. Subsequently, the smaller ΔT calculations were discarded in favour of the three isotherms (2000, 3000 and 4000 K) described to calculate the mean thermal expansivity between 2000 and 4000 K, 3000 - 4000 K and 2000 - 3000 K.

In Figure 6.11 the thermal expansivity decreases with increasing temperature, this is unusual but is consistent with the results of Vočadlo et al. (2003) also shown in Figure 6.11.

6.9 The Grüneisen Parameter

The Grüneisen parameter determines the change in temperature along a isentrope and plays a vital role in understanding the thermodynamics of a planet's interior. This work has used the description of γ as outlined in equation 2.47 in Chapter two, Section 2.11.3;

$$\gamma = V\left(\frac{dP}{dE}\right)_V \tag{6.2}$$

where P is the pressure, V is the volume and E is the sum of the excess internal energy that arises from interactions, E_{XS}, and the contribution due to the kinetic energy of the nuclei;

$$E_{int} = E_{XS} + \left(\frac{3Nk_BT}{2}\right) \tag{6.3}$$

In which, N is the number of atoms, k_B the Boltzmann constant and T is the temperature of the calculation.

This determined the mean change in pressure with respect to energy $\left(\frac{dP}{dE}\right)$ between 2000 and 4000 K for pure liquid iron, which was then multiplied by the volume. The errors in the Grüneisen parameter were calculated using a combination of the blocking method (described in Chapter two, Section 2.10) and error propagation (see Figure 6.12).

A steep increase in the Grüneisen parameter with pressure has been found which contradicts the relatively flat relationships found by Vočadlo et al. (2003) (also plotted in Figure 6.12)

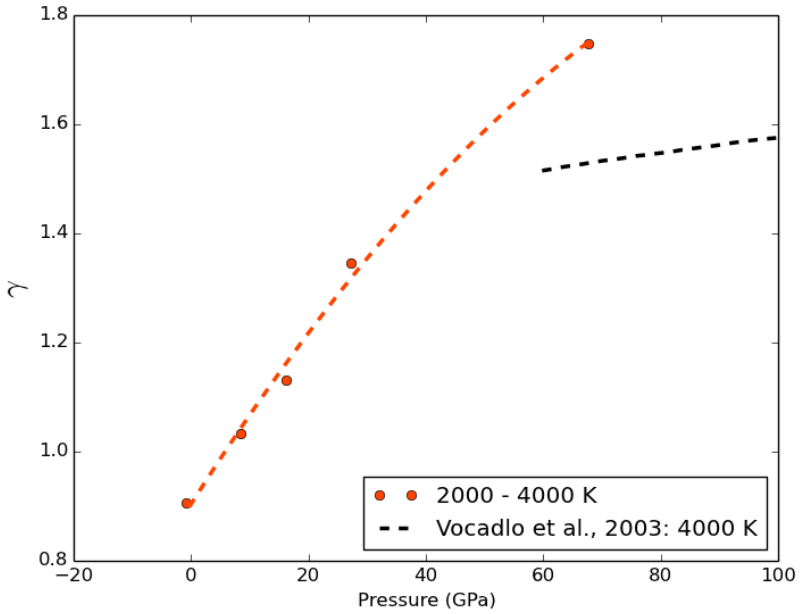

Figure 6.12: Mean Grüneisen parameter of pure liquid iron between 2000 - 4000 K (dashed orange line). The points represent the calculated NVT points, and error bars are also shown, however these are smaller than the displayed point size. Also shown by the dashed black line are the results of Vočadlo et al., 2003 using *ab initio* calculations on liquid iron at 4000 K.

and Ichikawa et al. (2014) but has also been found for silicate liquids (Stixrude and Karki, 2005). It is possible that with increasing pressure the Grüneisen parameter's relationship with pressure changes and flattens as was observed in subsequent studies of the properties of silicate liquids (e.g. Stixrude et al., 2009) and has also been found in Chapter eight.

6.10 The Adiabatic Gradient: Crystallisation of Mercury's Core

The adiabatic gradient, in combination with the slope of the liquidus can determine the crystallisation behaviour of a material and, vitally, this can be used to study the evolution of a planet's interior. If the slope of the liquidus is shallower than the adiabatic gradient then the crystallisation will occur first at lower pressures, resulting in crystallisation of a planet's core from the top-down (Figure 6.13B). If the opposite is true, and the slope of the liquidus is found to be steeper than the adiabatic gradient then the core will crystallise from

the bottom-up, naturally growing out from the centre of the planet, as is thought to be the regime forming the Earth's solid inner core (Figure 6.13A).

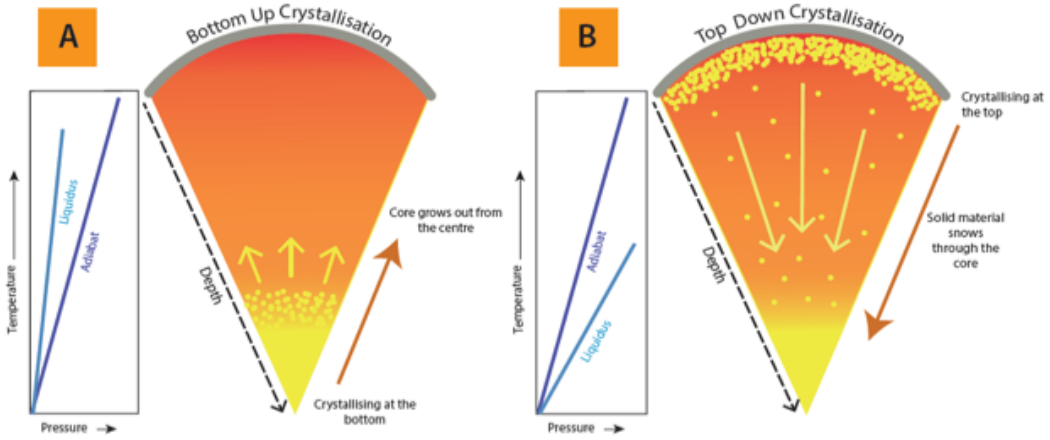

Figure 6.13: Schematic describing the consequences of the relative slopes of the adiabatic gradient and liquidus for the evolution of planetary cores. (A) If the liquidus is steeper than the adiabatic gradient, crystallisation will proceed from the bottom-up. (B) Top down crystallisation as a result of the liquidus slope being shallower than the adiabatic gradient.

The adiabatic gradient of pure liquid iron can be calculated as outlined in Chapter two, Section 2.11.4 using the following expression;

$$\left(\frac{dT}{dP}\right)_S = \frac{\gamma T}{K_S} \tag{6.4}$$

in which γ is the Grüneisen parameter, T is the temperature of the calculation (3000 K in this case) and K_S, the adiabatic bulk modulus which can be found using the isothermal bulk modulus K_T, temperature, T and the thermal expansion α:

$$K_S = K_T(1 + \alpha\gamma T) \tag{6.5}$$

This results in the following expression for the adiabatic gradient:

$$\left(\frac{dT}{dP}\right)_S = \frac{\gamma T}{K_T(1+\alpha\gamma T)} \tag{6.6}$$

Each of the above properties have been calculated in the previous sections and were used to calculate the adiabatic gradient of pure liquid iron at 3000 K.

The slope of the melting curve of pure iron has been studied in great detail and the various measurements agree fairly well on the melting temperatures at relatively low pressures. However, the fine detail and shape of the melting curves, and the derivative of the curves differ. For this reason, two relationships were compared against the adiabatic gradient, the melting curve of Anzellini et al. (2013) and the melting curve of Shen et al., 1998 (Figure 6.14). Both the Shen et al. (1998) and Anzellini et al. (2013) melting curves of iron were measured using *in-situ* X-ray diffraction, however the curve of Anzellini et al. (2013) also included the low-pressure iron phase diagram of Swartzendruber (1982) in the fitted relationship.

The "free" spin adiabatic gradient of pure liquid iron lies entirely beneath the gradient of the melting curve of Anzellini et al. (2013) which suggests bottom-up crystallisation throughout the core pressures of Mercury (as illustrated in Figure 6.13A). However, when the adiabatic gradient is compared against the slope of the melting curve of Shen et al. (1998) a very different picture appears. The adiabatic gradient is found to be steeper than the Shen et al. (1998) melting curve at the pressures of Mercury's core mantle boundary, but with increasing pressures, transitions to a shallower relationship (than the melting curve) and then a steeper relationship. This could result in a much more complex core crystallisation regime for the deep interior of Mercury and possibly result in multiple crystallisation zones within the planet (e.g. Figure 6.15).

In this scenario where the adiabatic gradient crosses the slope of the melting curve, as the planet cools, the relationship between the geotherm (for simplicity, this can be thought of as the adiabatic gradient of the planet, although this isn't strictly true) and the liquidus may be very complex. In the early stages of the planets formation the interior will be very hot and entirely molten (Figure 6.15a), during this stage the interior of the planet will be vigorously convecting and the temperature profile will be adiabatic. The temperature profile of the planet may differ from the liquid adiabat if either the temperature falls below the liquidus (as

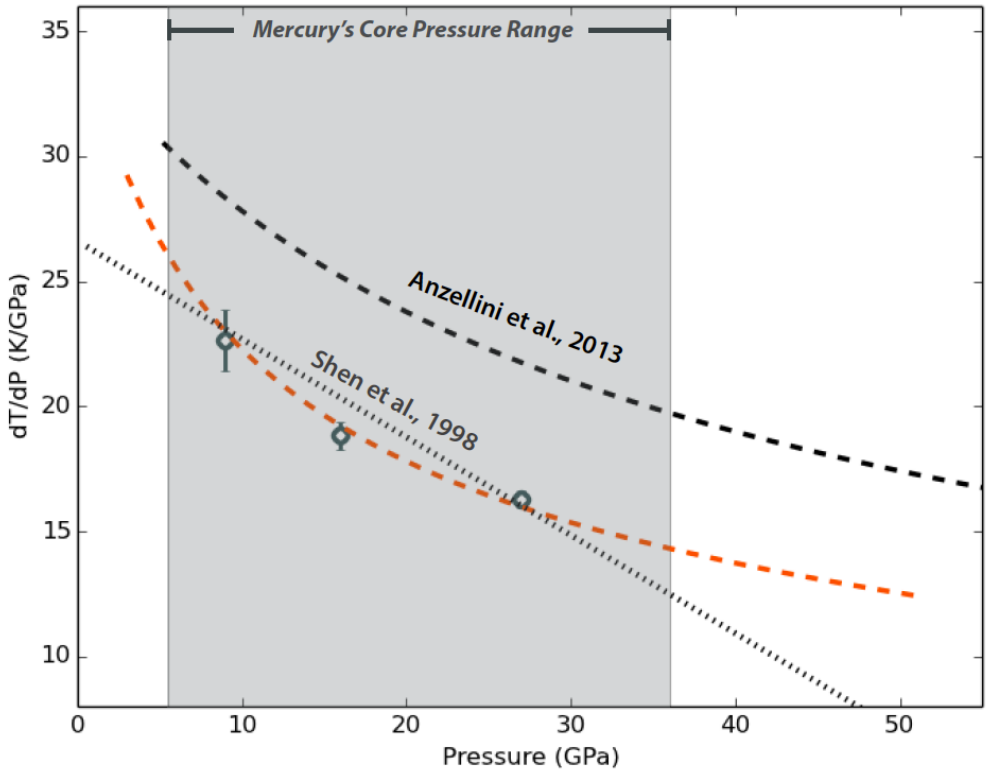

Figure 6.14: The comparison between the adiabatic gradient of pure liquid iron at 3000 K calculated using the fitted relationships in Sections 6.6 - 6.9 (shown in orange) and the gradients of published iron melting curves. Black circles indicate VASP canonical calculations and errors are represented for each of the NVT calculations using capped lines. The dashed grey and black lines describe the slopes of the melting curves of Shen et al. (1998) and Anzellini et al. (2013) respectively.

a result of the latent heat of fusion) or if any non-convective mass transfer takes place, e.g. iron snow. Both of these are likely to occur in Mercury's core. For example for the results shown in Figure 6.14, over time, as the planet cools and the temperature of the outer core falls below the liquidus, the conditions will evolve into a "snowing core" regime (Figure 6.15b). The release of latent heat due to crystallisation at the top of the core will move the temperature profile away from adiabatic, and will pin the geotherm to the melting curve in regions where the adiabat is cooler than the melting curve, while solid crystallised material will sink and redissolve once it reaches the depth where the geotherm exceeds the melting curve, further cooling the deep core. The sinking iron snow would then also change the temperature profile at depth within the core. As the core continues to cool, the deep adiabat, which is shallower than the melting curve, will cross at the base of the core resulting in

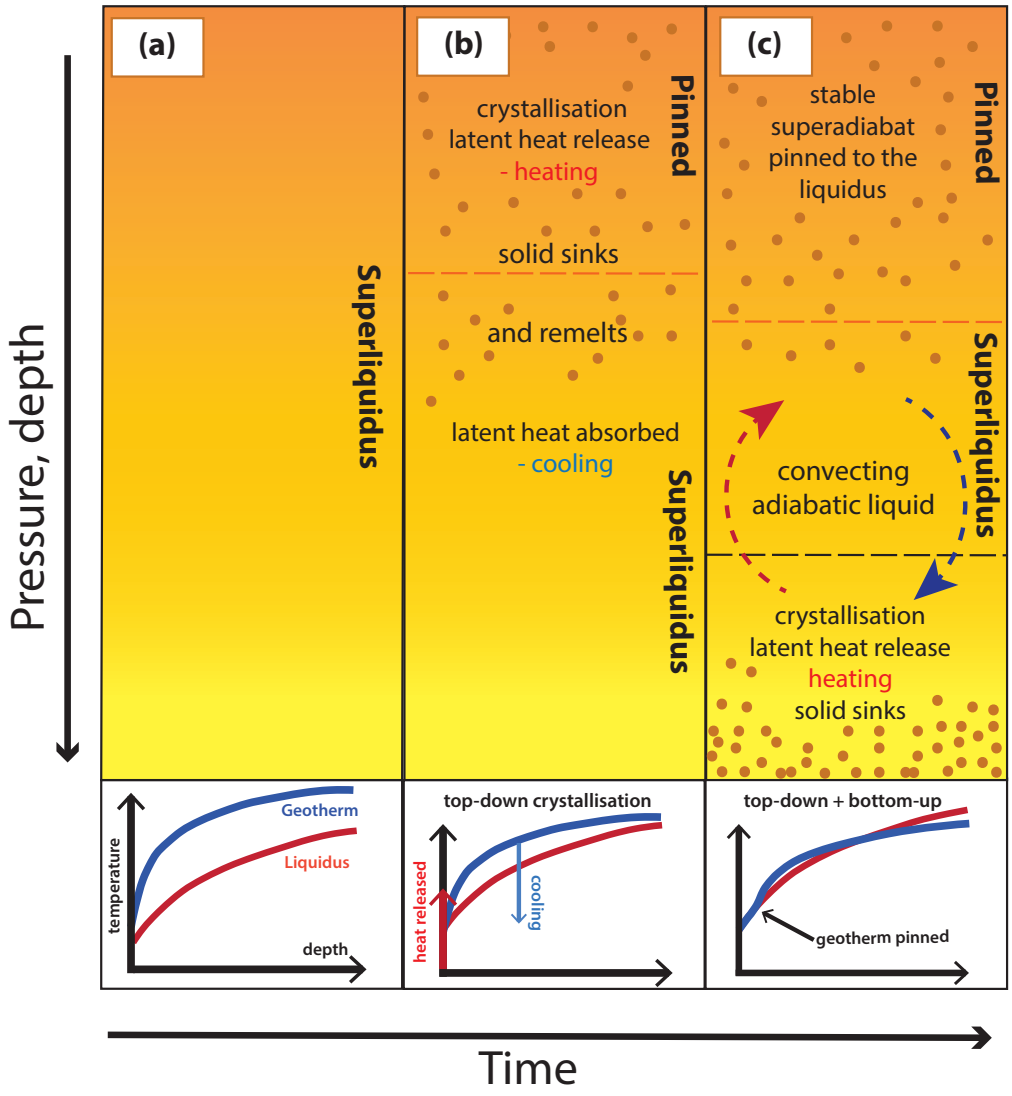

Figure 6.15: Possible consequences of a mixture of crystallisation scenarios, including a combinations of bottom-up and top-down evolutionary regimes.

(a) Early in the planet's formation the interior is very hot and entirely molten.

(b) Over time, as the planet cools the adiabat, due its shape, will cross the liquidus at low pressures first. Crystallisation will occur at low pressures at the top of core evolving into a "snowing" core regime.

(c) The re-melting of the solid at depth will continue to cool the deep core such that the adiabat of this region will cross the liquidus at the base of the core resulting in basal crystallisation. The latent heat produced by crystallisation will be removed by convection and settle stably, forming a central 'mushy' zone and an inner core, in addition to an upper snow zone in the outermost core.

basal crystallisation, shown in Figure 6.15c. In this scenario, released latent heat will be removed by convection and settle stably to form a central mushy zone and eventually, an inner core, all whilst maintaining an upper snow zone with a stable subadiabatic geotherm in the outermost core.

The adiabatic gradient can be used to calculate the temperature at depth within the planet. Current estimates of the CMB temperature of Mercury lie in the approximate range of 1850 - 2000 K (e.g. Rivoldini et al., 2009), extrapolating the adiabatic gradient determined in this work to the core pressures of Mercury ($\sim$ 36 GPa, Hauck et al., 2013), suggests that the temperature at the centre of a hypothetical liquid iron Mercurian core would range between $\sim$ 2576 - 2726 K (corresponding to the range of estimated CMB temperatures, 1850 - 2000 K).

However as mentioned in previous sections, the magnetic entropy has not been included in the free-energy minimisation routine used to calculate the adiabatic gradient and properties upon which it is based. The magnetic entropy may broaden the magnetic transition or increase the stability of the larger finite magnetic moments to higher pressures and thus will likely produce a different equation of state of pure liquid iron. The close relationship between the gradients of the iron melting curves and calculated adiabatic gradient suggests that any small change in this could result in an entirely different evolutionary scenario for Mercury's core. Free-energy minimisation techniques have been used in Chapter seven to include the magnetic entropy and re-calculate the adiabatic gradient of pure liquid iron.

6.11 Summary

This chapter has outlined the results of first principles molecular dynamics calculations on liquid iron at pressures ranging from -5 to 160 GPa and at 2000, 3000 and 4000 K. A series of volumes were calculated at each isotherm which determined the equation of state for pure liquid iron at each temperature. As a consequence of this fit, the isothermal bulk modulus was calculated, and multiple temperatures were used to determine the mean Grüneisen parameter and thermal expansion of pure liquid iron between 2000 - 4000 K (a summary of the thermodynamic properties are listed in Table 6.3 for the approximate conditions of Mercury's CMB). These properties define the adiabatic gradient and were used to calculate the evolutionary scenario for a pure iron core in Mercury, suggesting either bottom-up (when

compared against Anzellini et al., 2013) or a more complex crystallisation regime. The calculations suggest that within Mercury's core, pure liquid iron will be in an intermediate spin state, undergoing a gradual spin transition. Overall, good agreement has been found with previous work on pure liquid iron, although further work is needed to explain differences in thermal expansion and Grüneisen parameter. The broad 2nd neighbour peak shape in the low pressure radial distribution functions of liquid iron appears to agree with the measured 2nd nearest neighbour peak measured by Sanloup et al. (2000) and may indicate structural changes in liquid iron at high pressure. The calculations presented in this chapter have not included the effect of magnetic entropy, a fundamental part of the Helmholtz free energy of a magnetic system. The magnetic entropy may impact the magnetic transition of pure liquid iron as well as have implications for the physical and thermodynamic properties of the material. Any small change to the close relationship between the adiabatic gradient and slope of the melting curve presented in Figure 6.14 may have implications for the hypothetical evolution of a pure iron Mercurian core, and thus it is important that the influence of magnetic entropy is included. Following on from the work described in this chapter, Chapter seven describes the use of free energy minimisation to include magnetic entropy and calculates the effect this has on the properties of pure liquid iron.

Table 6.3: Properties of liquid iron at 2000, 3000 and 4000 K at the approximate pressure of Mercury's CMB ($\sim$ 5 GPa) and centre of the core ($\sim$ 36 GPa). The Grüneisen parameter and thermal expansivity are mean values between 2000 - 4000 K.

T *(K)*	P *(GPa)*	ρ *(kg/m^3)*	γ	α *(10^{-5}/K)*	K_T *(GPa)*
2000	5	7798	-	-	107.0
3000	5	7369	0.99	5.32	96.2
4000	5	7011	-	-	80.61
2000	36	9304	-	-	262.8
3000	36	8878	1.43	3.84	257.3
4000	36	8615	-	-	243.7

Chapter 7

The Magnetic Transition and Thermoelastic Properties of Pure Liquid Iron Using Thermodynamic Integration

7.1 Introduction

Chapter six details magnetic "free" spin *ab initio* molecular dynamics calculations of the thermoelastic properties of pure liquid iron and indicates that liquid iron undergoes a gradual high to low spin transition up to pressures of 90 GPa (at 4000 K). However, the results of Chapter six are missing one vital piece of the puzzle; the magnetic entropy. The magnetic entropy is a fundamental part of the Helmholtz free energy of a magnetic system and acts to reduce the free energy of magnetic states, which may extend the stability of magnetic spin states (outside of the low spin) to higher pressures (Chapter two, Section 2.12.1, eq 2.57). The calculations in Chapter six have not captured this, thus the effect this may have on the pressure - volume relationship for pure liquid iron is currently unknown. A very sensitive relationship has been predicted between the slope of the melting curve of pure iron and its adiabatic gradient (Chapter six). Therefore, it is important to understand the implications of including the magnetic entropy and accurately constraining the adiabatic gradient, as any small change may alter the suggested evolutionary scenario of a hypothetical pure iron Mercurian core.

In this chapter the high to low spin transition and thermodynamic properties of pure liquid iron have been found using *ab initio* molecular dynamics calculations and a free-energy

minimisation routine to include the effects of magnetic entropy.

7.2 Calculation Details

First principles molecular dynamics (FPMD) calculations have again been performed using the generalised gradient approximation with the PW91 enhancement factor (Perdew et al., 1992, 1993) to the solution of Density Functional Theory. PAW pseudopotentials (Blöchl, 1994; Kresse and Joubert, 1999) have been used to describe the core electrons which additionally treat the semi-core p states as valence electrons. The same cell size (125 atoms) and converged values of energy cutoff (400 eV) and Brillouin zone sampling (one k-point located at $\frac{1}{4}, \frac{1}{4}, \frac{1}{4}$ from Baldereschi, 1973) were used throughout as described in the previous chapter to maintain consistency across the calculations (Chapter 6, Section 6.3). The same superheating technique as described in Chapter 6 was used to produce the starting configuration for all the non-magnetic and spin-polarised calculations presented in this chapter, in which the initial cubic structure was superheated to 10,000 K at a single volume and cooled and pressured to produces varying volumes at each temperature. The calculations run with a constrained total magnetisation were superheated at each individual volume.

7.3 Helmholtz Free Energy

The magnetic entropy is a fundamental component of the Helmholtz free energy equation and hence may impact the magnetic transition and thermoelastic properties of liquid iron calculated in Chapter six. The Helmholtz free energy is equal to;

$$F(V,T,f) = E(V,T,f) - T(S_{el}(V,T,f) + S_{vib}(V,T,f) + S_{conf}(V,T,f) + S_{mag}(V,T,f)) \tag{7.1}$$

in which, E is the internal energy, V is the volume, f is the magnitude of the atomic moment, T is the temperature which is multiplied by a linear sum of the electronic, vibrational, configurational and magnetic entropies ($S_{el}, S_{vib}, S_{conf}$ and S_{mag}).

This study has used first principles methods and the perturbative approach to thermodynamic integration to study the spin crossover (Chapter 2, Section 2.12) in pure liquid iron

at temperatures ranging from 2000 - 4000 K and pressures from 0 - 80 GPa. This section details the step-by-step outline of the method used to calculate the effect of this magnetic entropy.

7.3.1 Equations of State at Constant Moment Magnitude

The first step in calculating the magnetic transition of pure liquid iron is to compute the equations of state of two possible magnetic states; the low spin state, LS, in which the local moment of each atom is equal to zero and a magnetic state with a large moment magnitude, MS3, in which the atomic moment is equal to three Bohr magnetons.

Calculation Details

The equations of state of the highest magnetic state (MS3) and lowest (LS) have been calculated using *ab initio* molecular dynamics NVT simulations on 125 atom super cells of pure liquid iron. The LS simulations were run non-magnetically, and the MS3 calculations run spin polarised with a constrained total magnetisation of the cell set to +375 μ_B, i.e. + 3 $\mu_B/atom$, which over the course of the simulation equilibrated to 2.9 $\mu_B/atom$. The difference in the two values, 2.9 $\mu_B/atom$ and 3 $\mu_B/atom$, are a result of how the atomic magnetic moments are computed. The finite local moment per atom is calculated by projecting the spin density onto nuclear-centred atomic like orbitals, and hence, may be smaller than the total magnetisation of the cell divided by the number of atoms. In an effort to be consistent across all magnetic calculations the projected atomic moments (e.g. 2.9 $\mu_B/atom$) were used throughout.

Five volumes were calculated at each temperature of the MS3 calculations ranging from 14.9 - 10.83 $\AA^3$/atom. The simulations were run for a minimum of six picoseconds, with the initial two picoseconds removed as calibration time (details of each volume and their associated values and errors are given in Appendix B). The molecular dynamics simulations produced time averaged computed 'external' pressures and energies for each calculation. 'External' pressure was not the final pressure required however, as it does not include the pressure due to the kinetic energy of the nuclei, hence this was added in post-processing to produce the total pressure of the calculation (e.g. Chapter 6, Section 6.6).

EOS of the Highest and Lowest Moments

At each temperature (2000, 3000 and 4000 K) the total pressures and volumes of the MS3 and LS states were fitted to a third order Eulerian finite strain expression, the Birch Murnaghan 3rd order equation of state (Birch, 1978; Chapter 2, equation 2.41; BM3EOS) using EoSFit (Angel et al., 2014; Figure 7.1, Table 7.1). The results shown in Figure 7.1 describe the important effect of magnetism: MS3 has a much larger volume at all pressures (e.g. $\sim$ 15 % difference at 20 GPa and 3000 K).

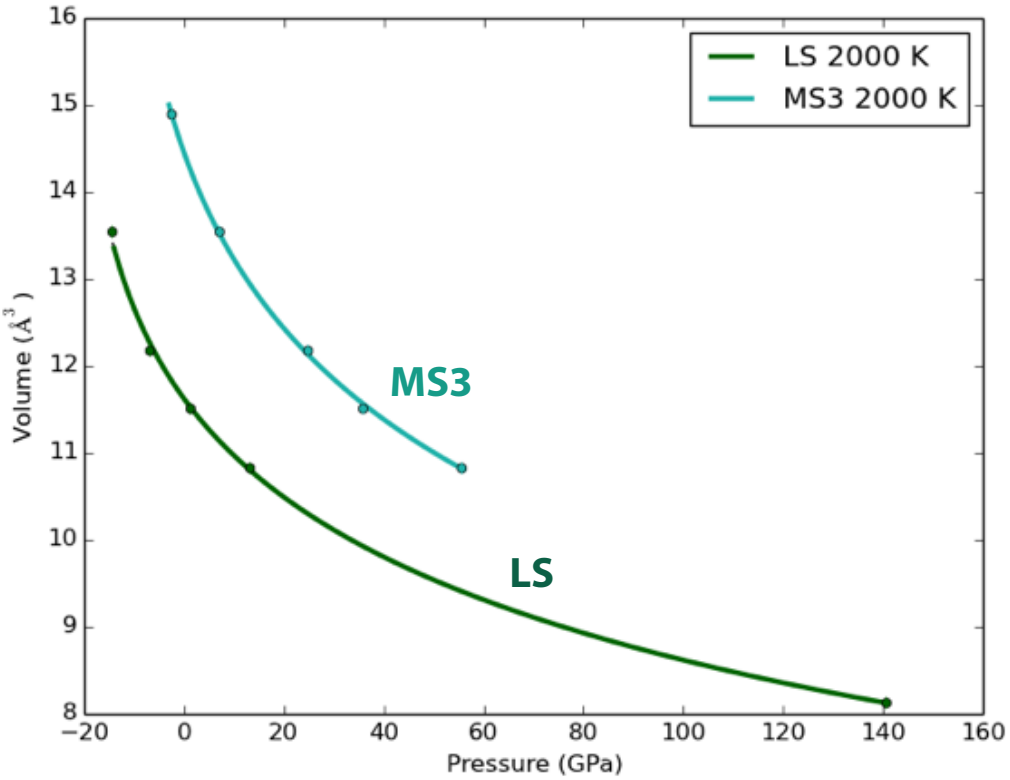

Figure 7.1: The equations of states for the highest spin (MS3) and low spin states of pure liquid iron at 2000 K. The highest magnetic spin (MS3) state is represented in light green and the low spin (LS) in dark green. The solid line represents the fit and the points correspond to the individual molecular dynamics calculations.

Intermediate Moment Equations of State

The canonical "free" spin calculations described in Chapter six have been used to create the three intermediate constant spin equations of state (corresponding to the spin states; MS0, MS1 and MS2) following the method of Holmström and Stixrude (2015) (Figure 7.2).

Three volumes (12.19 $\AA^3$/atom, 11.51 $\AA^3$/atom and 10.84 $\AA^3$/atom volume) were taken at each temperature, which at 2000 K, corresponded to magnetic moments equal to 1.7 μ_B (MS2), 1.4 μ_B (MS1) and 1.2 μ_B (MS0). Each equation of state was then constructed using a volume fraction, g_v,

$$g_v^{MS} = \frac{V(P_0)_{MS} - V(P_0)_{LS}}{V(P_0)_{MS3} - V(P_0)_{LS}} \tag{7.2}$$

In which, $V(P_0)_{MS}$ represents the volume of the magnetic state (MS, either MS0, MS1 or MS2), $V(P_0)_{MS3}$ is the volume of the MS3 state and $V(P_0)_{LS}$ is the volume of the LS state at pressure, P_0. The volume of the MS0, MS1 and MS2 phases could then be found for any other pressure, P', using the expression (illustrated in Figure 7.2);

$$V_{MS}(P') = V_{LS}(P') + g_V^{MS}[V_{MS3}(P') - V_{LS}(P')] \tag{7.3}$$

Once the volumes were assembled for each MS state, these were fitted to a BM3EOS (Table 7.1).

Five equations of state were found for each temperature corresponding to five magnitudes of finite local moment on the individual atoms (e.g. shown in Figure 7.3 for the 2000 K isotherm; Table 7.1).

7.3.2 The Helmholtz Free Energy of Each State

Helmholtz Free Energy of The Reference State

The constant F_0 in Chapter 2, equation 2.39 was unknown, so the free energy of any state could not be known absolutely, only relative to the LS state. The free energy of the LS state was calculated from the *P-V* BM3EOS fit by integrating the thermodynamic expression in Chapter 2, equation 2.40;

$$F_{LS}(V,T,0) = F(V_0,T,0) - \int_{V_0}^{V} P(V,T,0)dV \tag{7.4}$$

in which V and T are the volume and temperature and V_0 is the volume at zero pressure.

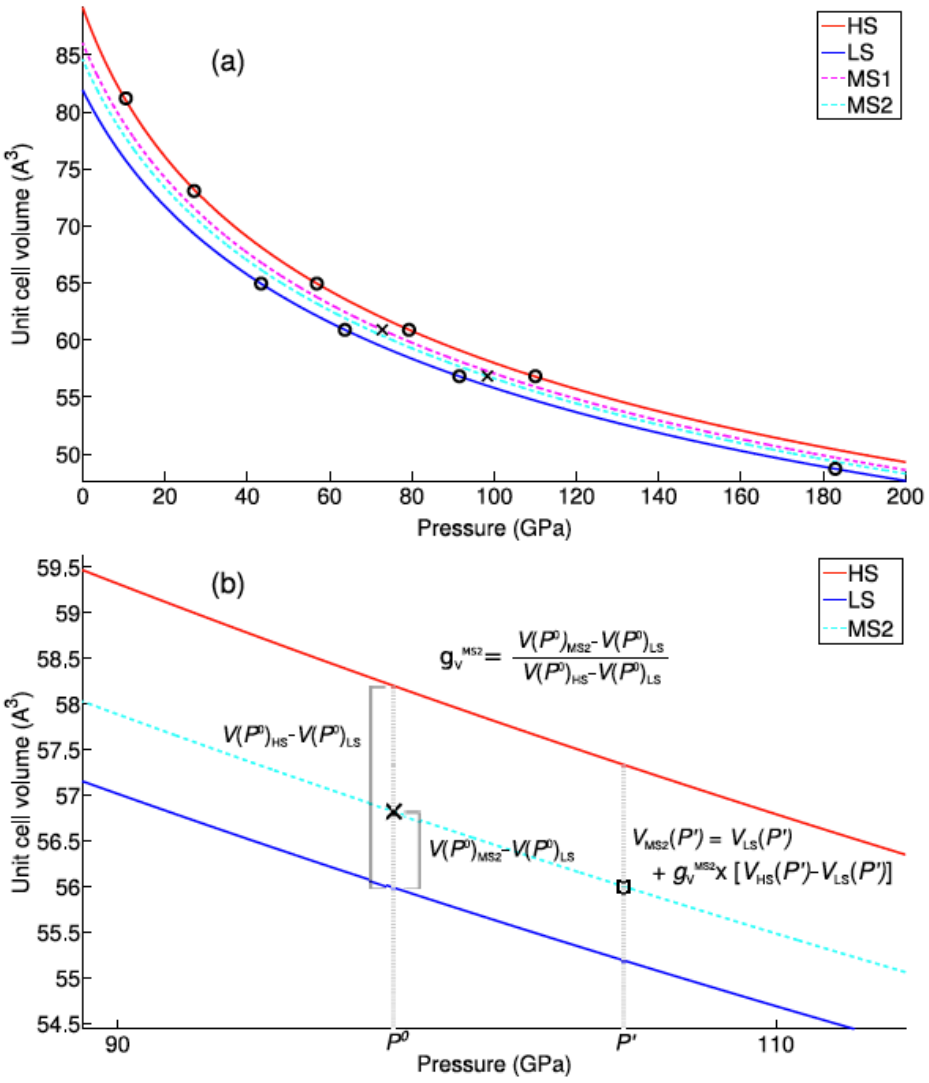

Figure 7.2: Method of finding the intermediate spin equations of state using the highest spin (HS) and low spin (LS) fitted equations of state. Figure courtesy of E. Holmström.

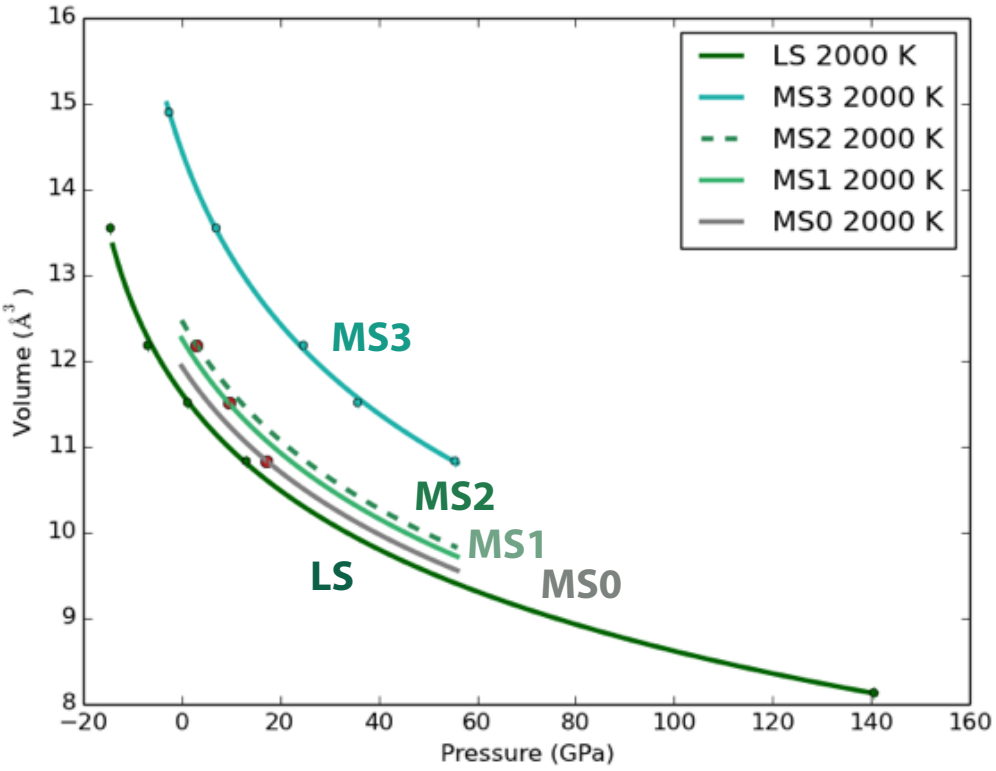

Figure 7.3: Equations of state of the low spin (LS) (dark green solid line), highest spin state calculated (MS3) (light green solid line) and three middling spin states at 2000 K (MS2, MS1, MS0 ; dashed dark green, light green and grey lines respectively). The intermediate simulations used to calculate the three intermediate spin states from Chapter six are indicated by red points.

The Difference in Free Energy

The difference in free energy, ΔF, between each magnetic state (MS) and the LS state was calculated using the Kirkwood switching scheme and thermodynamic integration. Thermodynamic integration was performed between each MS state and the LS reference state at the integration volume (V_i, which varied for each MS state) across a parameter lambda, λ, (which ranged between 0 and 1);

$$\Delta F_{MS/LS} = \int_0^1 d\lambda \langle E_{MS} - E_{LS} \rangle_\lambda \tag{7.5}$$

This was calculated as the area under a straight line with two end constraints at $\lambda = 0$ and

Table 7.1: Fitted parameters of the Birch Murnaghan 3rd order equation of state: LS, MS0, MS1, MS2 and MS3

T (K)	Name	Moment Magnitude ($\mu_B/atom$)	V_0 ($\AA^3$/atom)	K_0 (GPa)	K'
2000	MS3	2.93	14.45	89.24	5.27
	MS2	1.69	12.47	121.30	5.53
	MS1	1.44	12.26	126.71	5.53
	MS0	1.17	11.94	136.32	5.51
	LS	0.00	11.62	147.51	5.47
3000	MS3	2.92	15.50	72.02	5.13
	MS2	1.34	12.42	104.16	5.29
	MS1	1.08	12.87	108.06	5.28
	MS0	0.78	12.71	111.96	5.27
	LS	0.00	12.42	119.64	5.23
4000	MS3	2.91	16.67	53.64	5.37
	MS2	0.93	13.68	87.94	5.07
	MS1	0.67	13.53	90.91	5.03
	MS0	0.40	13.44	92.84	5.00
	LS	0.00	13.29	96.00	4.96

λ = 1;

$$\Delta E_{\lambda=0} = (E_{MS})_{LS} - (E_{LS})_{LS} \tag{7.6}$$

$$\Delta E_{\lambda=1} = (E_{LS})_{MS} - (E_{MS})_{MS} \tag{7.7}$$

where $(E_{MS})_{LS}$ is the MS energy projected onto the LS trajectory and $(E_{LS})_{MS}$ is the LS energy projected onto the MS trajectory. The $(E_{MS})_{MS}$ and $(E_{LS})_{LS}$ terms represent the time averaged free energies of the MS and LS states respectively.

Adiabatic switching was used within the Kirkwood coupling scheme (Kirkwood, 1935) to calculate $(E_{MS})_{LS}$ and $(E_{LS})_{MS}$. To calculate $(E_{LS})_{MS}$, for example, the trajectory of the MS molecular dynamics calculation was split into a large number of individual calculations (e.g. each femto-second). The positions of the atoms at each femtosecond from a portion of the

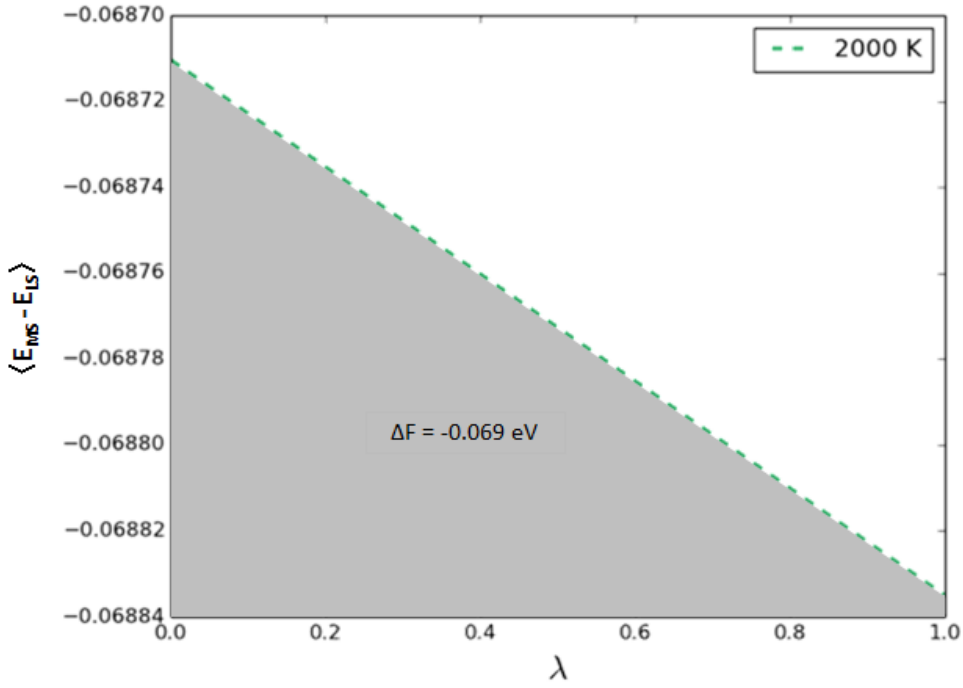

Figure 7.4: Shown is the change in free energy between the MS1 state and the LS state at 2000 K. The change in free energy is found as the area under the red dashed line constructed using up to three constraints. The first two are $\langle E_{MS} - E_{LS} \rangle_{\lambda}$ at $\lambda = 0$ and $\lambda = 1$, the third is the gradient at $\lambda = 1$.

calibrated region of the original NVT molecular dynamics calculation was then rerun, but forced into the opposing magnetic state, e.g. for $(E_{LS})_{MS3}$ the MS3 trajectory was forced into the LS state at each step. This was run for a minimum of 4000 femtoseconds (i.e. 4000 individual calculations) to produce the time averaged energy of the MS3 spin state projected on the LS state, $(E_{LS})_{MS3}$. Derived from thermodynamic perturbation theory, the fluctuations in the molecular dynamics calculation additionally determined the gradient at $\lambda = 1$, e.g. for $\lambda = 1$ of the MS3 spin state;

$$\frac{\langle (E_{MS3} - E_{LS})^2 \rangle_{\lambda=1} - \langle (E_{MS3} - E_{LS}) \rangle_{\lambda=1}^2}{2k_B T} = -\frac{1}{2} \frac{d \langle E_{MS3} - E_{LS} \rangle_{\lambda=1}}{d\lambda} \tag{7.8}$$

Therefore, the value is constrained at $\lambda = 1$ and $\lambda = 0$ and the gradient is constrained at $\lambda = 1$. In the MS3-LS integration all three constraints are used to find ΔF as the area under a 2^{nd} order polynomial (Table 7.2). This was compared with the free energy difference

determined using only two constraints (Table 7.2), and two constraints were found to be sufficient. Thus, only two constraints were used to find ΔF of the MS0, MS1 and MS2 spin states (Table 7.2).

Table 7.2: Δ F relative to the LS state: using three constraints (MS3) and two constraints (MS2, MS1, MS0) at 2000 K

T (K)	Name	Moment ($\mu_B/atom$)	ΔF (2nd Order)	ΔF (λ = 1 + Grad)
2000	MS3	2.93	0.14	0.09
	MS2	1.69	-	-0.12
	MS1	1.44	-	-0.07
	MS0	1.17	-	-0.07
3000	MS3	2.92	0.29	0.24
	MS2	1.34	-	-0.06
	MS1	1.08	-	-0.04
	MS0	0.78	-	-0.01
4000	MS3	2.90	0.44	0.39
	MS2	0.93	-	-0.03
	MS1	0.67	-	-0.01
	MS0	0.40	-	-0.01

The Helmholtz Free Energy of the Magnetic States

The Helmholtz free energy of each state at V_i is;

$$F(V_i,T,f) = F_{LS}(V_i,T,0) + \Delta F_{TI}(V_i,T,f) - TS_{mag}(V_i,T,f) \tag{7.9}$$

In which F is the Helmholtz free energy, V_i is the integration volume, T is the temperature and f the magnetic moment. The term, $F_{LS}(V_i,T,0)$, represents the free energy of the LS state at the integration volume, and $\Delta F_{TI}(V_i,T,f)$ indicates the difference in free energy between the LS state and the magnetic state. This also includes the magnetic entropy term, $S_{mag}(V_i,T,f)$, which is defined;

$$S_{mag}(V_i,T,f) = -k_B \sum_i \ln(\mu_i + 1) \tag{7.10}$$

In which, μ_i is the magnitude of the local atomic moment and k_B is the Boltzmann constant. The free energy of every other volume (V) was then found using the thermodynamic expression in Chapter 2, equation 2.40;

$$F(V,T,f) = F(V_i,T,f) - \int_{V_i}^{V} P(V,T,f)dV - TS_{mag}(V_i,T,f) \tag{7.11}$$

i.e.,

$$F(V,T,f) = F(V_i,T,f) + [F_{BM}(V,T,f) - F_{BM}(V_i,T,f)] - TS_{mag}(V_i,T,f) \tag{7.12}$$

Where all terms are as previously described.

7.3.3 Gibbs Free Energy

The Gibbs free energy was calculated for each of the magnetic phases using the following expression;

$$G(P,T,f) = F(V,T,f) + VP(V,T,f) \tag{7.13}$$

in which, F is the Helmholtz free energy, P is the pressure and V is the volume. At intervals of 1 GPa, the Gibbs free energies of the four magnetic states (MS3, MS2, MS1, MS0 and LS) were fitted to a parabola, the minimum of which determined the preferred magnitude of the local moments on each atom (Figure 7.5). This was repeated for each pressure and temperature thus calculating the magnetic transition of pure liquid iron at 2000, 3000 and 4000 K (Figure 7.6).

7.4 The Magnetic Transition of Pure Liquid Iron

Presented in Figure 7.6 are the magnetic transitions at 2000, 3000 and 4000 K of pure liquid iron. Compared to the magnetic transition predicted using "free" spin polarised *ab initio* calculations in Chapter six, the spin crossover calculated using thermodynamic integration predicts a higher magnetic moment for all temperatures and pressures studied. The low spin state has not been predicted for any of the temperatures, and therefore the finite local moments on the individual atoms have been predicted to higher pressures than calculated in

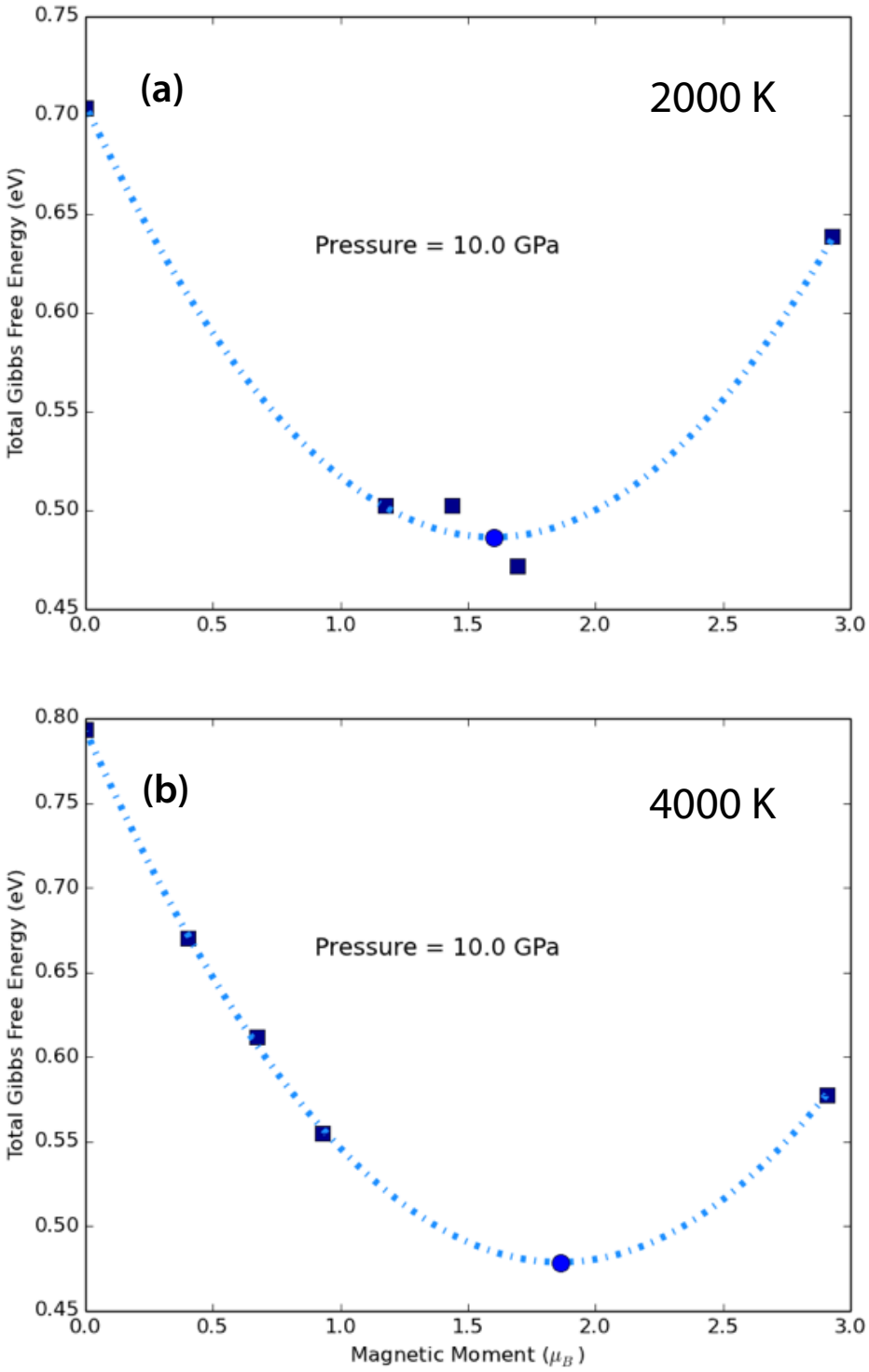

Figure 7.5: Gibbs Free Energy at 10 GPa and 2000 (a) and 4000 K (b) for the MS3, MS2, MS1, MS0 and LS moment magnitudes (blue squares). The minimum of the fitted parabola (dashed line) indicates the preferred magnitude of the local moment (blue circle).

Chapter six, and much above the predicted central pressure of Mercury ($\sim$ 36 GPa, Hauck et al., 2013). As a result of including the magnetic entropy, the trend between magnetic transition and temperature has completely reversed, i.e. in Chapter six, Figure 6.6, at increasing temperatures the magnetic moment decreased, however, in Figure 7.6, the magnitude of the atomic moment increases with temperature transition. In the following section the magnetic transition is used to determine the thermodynamic properties of pure liquid iron, and investigate the impact the inclusion of magnetic entropy has on the thermo-elastic properties of the material.

7.5 Thermoelastic Properties

So far in this chapter, part of the spin crossover in pure liquid iron has been calculated, but the question remains how this translates to the physical properties of the material. The following sections will detail the subsequent calculations of the thermodynamic and physical properties of pure liquid iron using the refined magnitude of the atomic moments presented in Section 7.4.

7.5.1 The Equation of State

At each pressure, P, the volumes corresponding to each spin state were collated to find a relationship between volume and magnetic moment at constant pressure (Figure 7.7). The magnetic moment at pressure, P, was found using the relationship found in Section 7.4 (Figure 7.6), and the corresponding volume recorded.

This was repeated for each pressure and temperature and fitted to the BM3EOS (Birch, 1978) to find the equation of state of pure liquid iron at 2000, 3000 and 4000 K (Figure 7.8, Table 7.3). As predicted in the previous chapter the inclusion of the magnetic entropy has decreased the calculated density of liquid iron at all pressures and temperatures. A significant decrease in density has been calculated, e.g. at 2000 K and 0 GPa, "free" spin calculations suggest a liquid iron density of 7385 kg/m^3 (corresponding to a volume of 12.56 $\AA^3$), and with the magnetic entropy included this has decreased to 7164 kg/m^3 (12.97 $\AA^3$), a 3% change in value. The refined density presented in this chapter remains larger than the preferred experimental value of 6900 kg/m^3 (Williams, 2009), differing by 4%. The difference in density between experimental values and that calculated here is similar

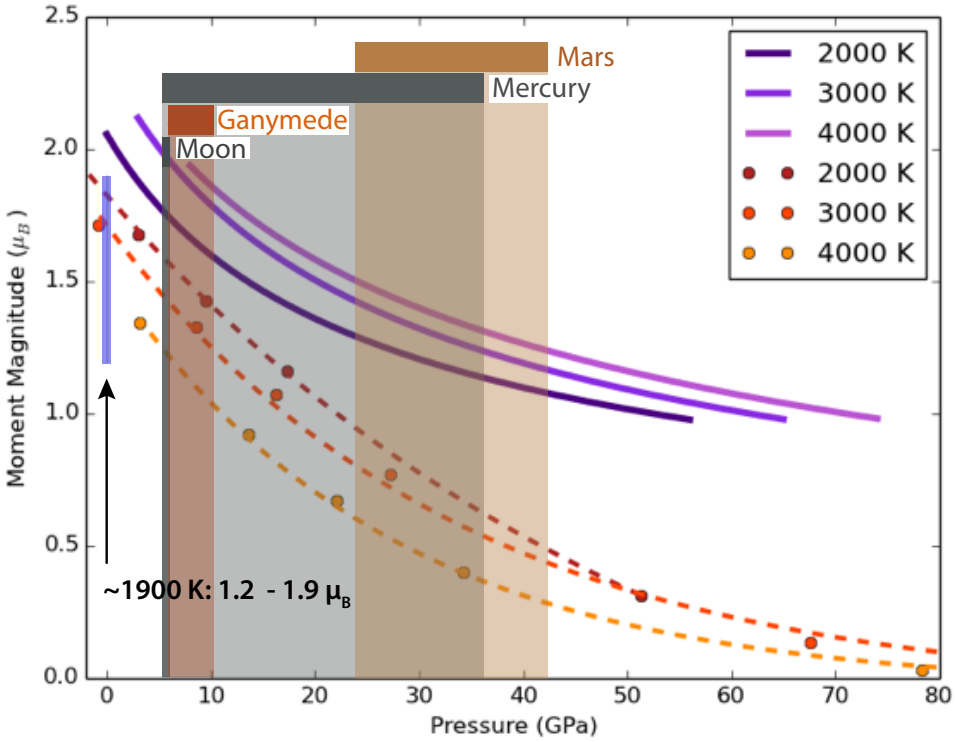

Figure 7.6: The spin crossover in pure liquid iron at 2000, 3000 and 4000 K (dark to light purple solid lines respectively). The fitted magnetic transition is shown using the solid purple lines alongside the corresponding results of Chapter six using "free" spin calculations (shown using dashed lines with the individual calculations outlined using points). Error bars associated with the "free" spin calculations are indicated using capped lines (smaller than the marker size shown). Also shown are shaded bars which indicate the approximate pressure ranges of the small bodies in the solar system. The pressures of Mercury's core are from Hauck et al. (2013), the pressures of Ganymede's core are from Rückriemen et al. (2015) and the pressures of the Moon and Mars' core are from Antonangeli et al. (2015). The experimental range of values for the atomic moment of liquid iron are outlined in blue (1.2 - 1.9 μ_B; Waseda and Suzuki, 1970; Weber et al., 1978)

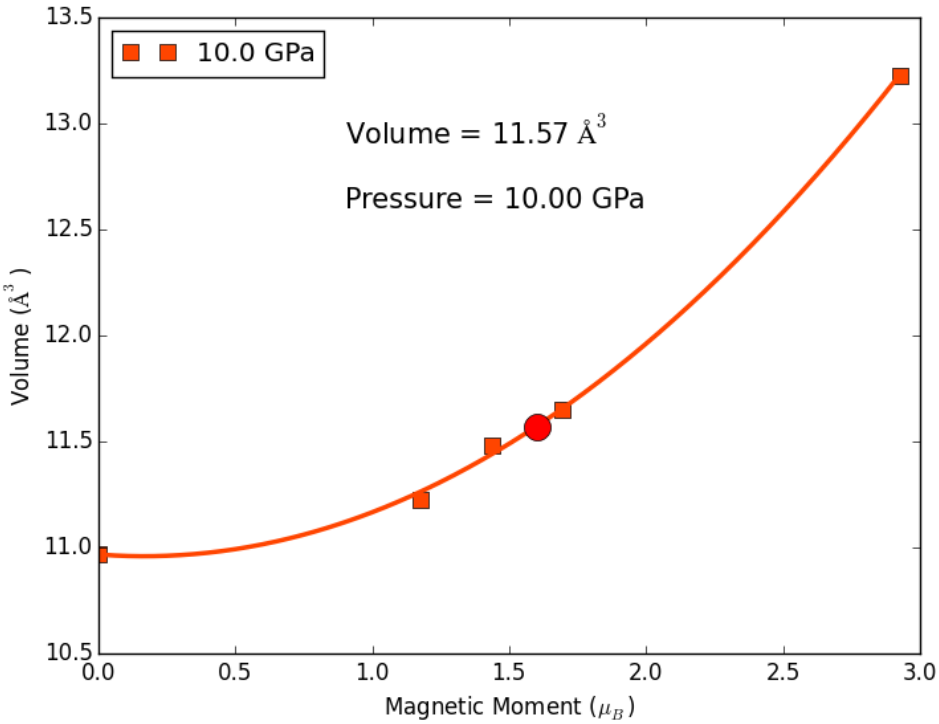

Figure 7.7: Method of finding the volume at each pressure using the corresponding volumes for each of the five spin states (MS0, MS1, MS2, MS3 and LS, indicated by orange squares). A parabola is fitted to the five spin states, and the volume corresponding to the correct magnetic moment for this pressure recorded, shown by the red circle at 10 GPa and 2000 K.

to that found in GGA calculations of bcc iron (3%, Stixrude et al., 1994) and therefore it is likely that the remaining discrepancy in the density has resulted from the uncertainty in the exchange-correlation functional (GGA). It may also be due to errors in the experiments or it may be a result of the parabolic assumption made to describe the Gibbs free energy in Section 7.3.3. If the values differ from the parabolic assumption then it is possible that the calculations presented here under-predict the magnitude of the local atomic moments and thus predicts a smaller volume. To resolve this, further calculations would be needed at different magnitudes of local moments to provide further constraints on the minimum Gibbs free energy at each pressure, however this was not possible within the timeframe of this work.

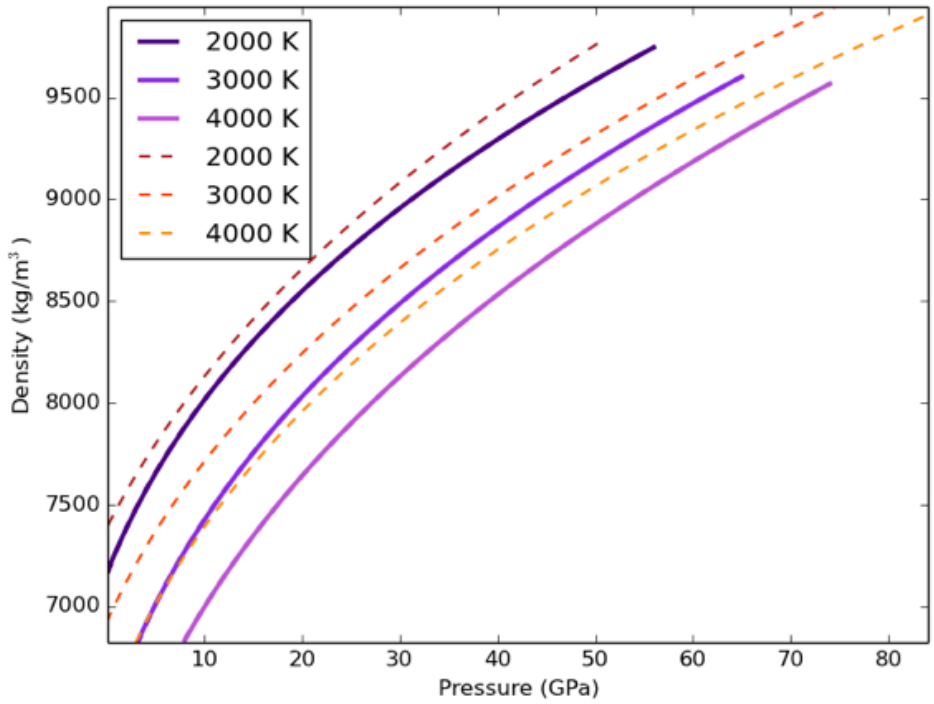

Figure 7.8: The equations of state of pure liquid iron at 2000, 3000 and 4000 K (from dark to light purple). Filled circles indicate the pressures and volumes calculated from the magnetic transition, the line represents the fit to the Birch Murnaghan 3rd order equation of state. Also shown are the results of Chapter six, "free" spin calculations of the density of pure liquid iron (orange dashed lines, dark to light from 2000 - 4000 K).

Table 7.3: Fitted parameters of the Birch Murnaghan 3rd order equation of state at 2000, 3000, 4000 K

T (K)	V_0 ($\AA^3$/atom)	K_0 (GPa)	K'
2000	12.97	55.31	8.41
3000	38.66	38.66	7.54
4000	15.63	36.31	6.25

7.5.2 The Bulk Modulus and Thermal Expansion

The bulk modulus of pure liquid iron was calculated using the analytical derivative of the BM3EOS $P(V)$ expression (e.g. Ita and Stixrude, 1992; Figure 7.9). A small change in the isothermal bulk modulus was observed for all temperatures relative to the "free" spin cal-

culations in Chapter six (Figure 7.9), such that it suggests that although the value and trend of the magnetic moment with pressure changes dramatically, the shape of the relationship between pressure and volume is not significantly affected.

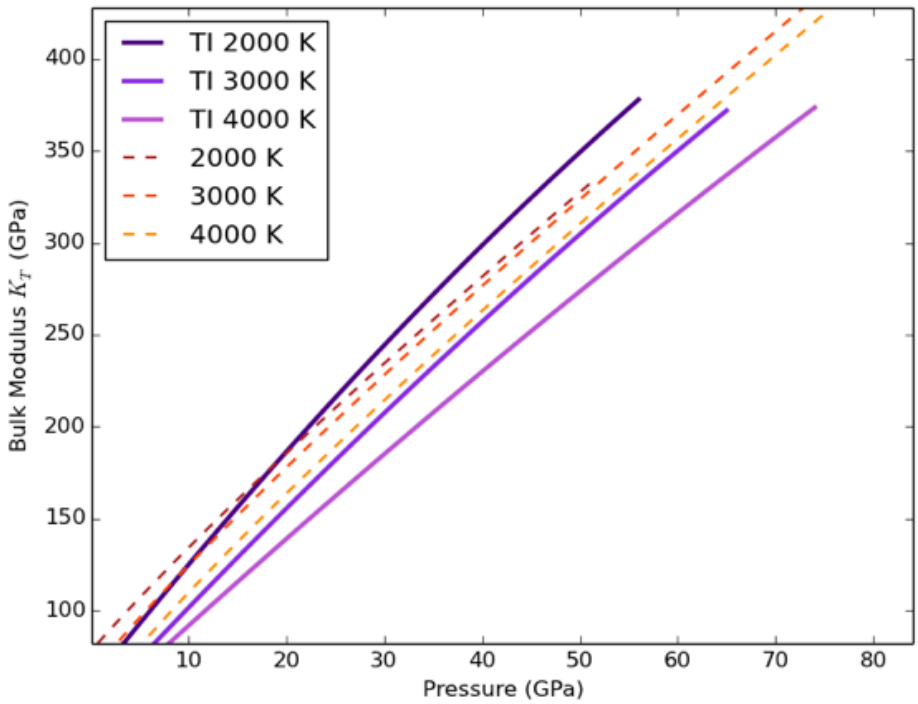

Figure 7.9: The isothermal bulk modulus of pure liquid iron computed using thermodynamic integration at 2000, 3000 and 4000 K (from dark to light purple respectively) compared to the results of Chapter six, using "free" spin magnetic calculations (indicated by orange dashed lines).

The mean thermal expansion between 2000 and 4000 K is found using equation 2.44 (Chapter two, Section 2.11.2):

$$\alpha = \left(\frac{ln(V(T')/V(T))}{(T'-T)} \right)_P \tag{7.14}$$

in which V, T and P have their usual meaning and T' $>$ T.

In Chapter six, "free" mixed spin calculation suggests an initial steep decrease in thermal expansivity which flattens out at approximately 20 GPa (Figure 6.11), conversely, thermodynamic integration calculates a more gradual decrease in thermal expansion throughout the

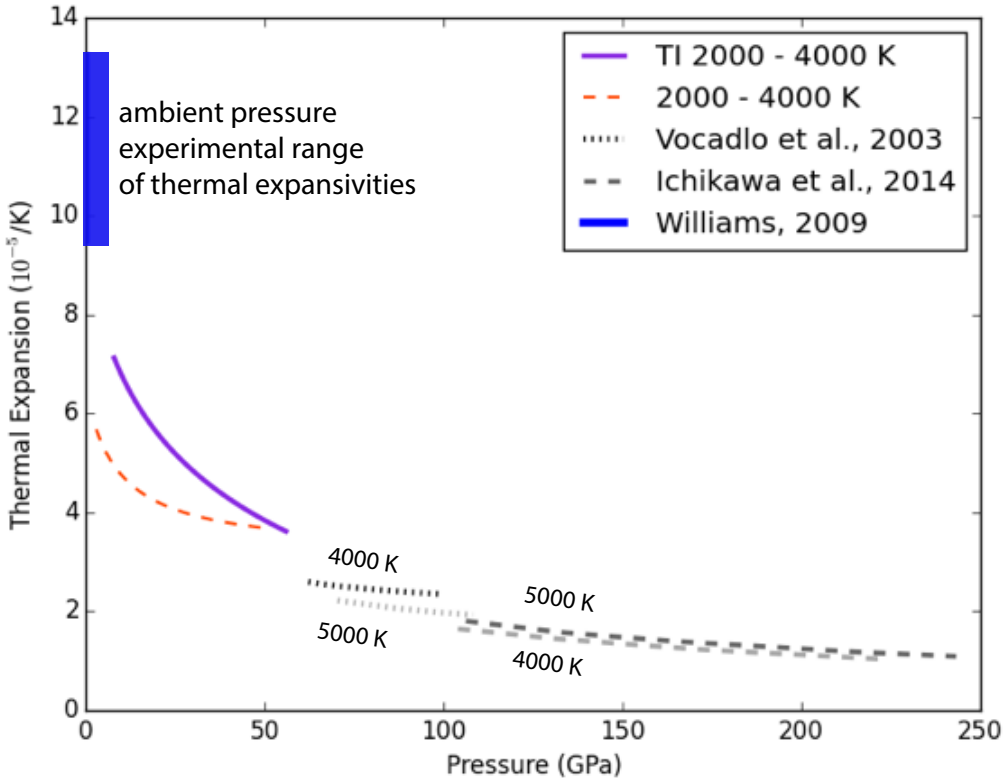

Figure 7.10: The mean thermal expansion of pure liquid iron between 2000 and 4000 K computed using the refined magnetic transition determined using free energy minimisation (purple solid line). Also shown are the result of "free" spin calculations of pure liquid iron (dashed orange line) and the results of Vočadlo et al. (2003) and Ichikawa et al. (2014) (4000 and 5000 K, black and grey dashed lines). The range of experimentally measured thermal expansivities of pure liquid are indicated by a blue bar (Williams, 2009).

entire simulated pressure range (Figure 7.10). The thermal expansion calculated from thermodynamic integration is higher than that predicted in Chapter six, as a result of the changes to the magnetic transitions of each temperature, and their effect on the volume of pure liquid iron. The magnetic transitions described in Section 7.4 were altered not only in their pressure dependance, but also in temperature. The high to low spin transition predicted is very gradual across all temperatures, such that at 2000 K this matches the gradual decrease predicted in Chapter six, whereas "free" spin calculations suggested a much steeper decline for 4000 K in comparison with that calculated using thermodynamic integration. Therefore the inclusion of magnetic entropy has changed the relationship between volume and temperature, and have therefore calculated an increased coefficient of thermal expansion than

that calculated in Chapter six.

Although increased relative to Chapter six, the calculated thermal expansion of pure liquid iron does not match the experimental measurements of thermal expansion which range between 9.2 - 13.2 x 10^{-5} /K (Williams, 2009; Figure 7.10). The cause of this is again unclear, but as described in Section 7.5.1 this could be a result of the parabolic assumption made to the Gibbs free energy in Section 7.3.3, or errors in the experiments. If the magnitude of the local atomic moment is underestimated for one temperature, or by different amounts at each temperature then this could result in a smaller thermal expansion calculated and may result in the discrepancy shown here.

7.5.3 The Grüneisen Parameter

As a result of the methods described in the previous section, the magnetic transition and volume-pressure relationship has been found for pure liquid iron, including the influence of magnetic entropy. However, in doing so, information on the excess internal energy (that arises from interactions), determined as part of the VASP minimisation routine, has been lost. To calculate the excess internal energy a similar method as presented in Section 7.5.2 was used. At each volume, V, the excess internal energy of the highest spin (MS3), LS, and some intermediary spin state (found in Chapter six) was used to find a relationship between excess internal energy and magnetic moment. The BM3EOS fit for each isotherm was used to find the pressure, $P(V,T,f)$, at volume, V, and then used to find the correct magnitude of the local moment (f) at said pressure (from the transition calculated in Section 7.4). The magnetic moment at pressure, $P(V,T,f)$ was then used to find the corresponding excess internal energy that arises from interactions at volume, V (Figure 7.11).

The excess internal energy for each volume was added to the contribution due to the kinetic energy of the nuclei (see Section 6.9, equation 6.3) to produce the total internal energy. Using the BM3EOS fits and Chapter two, equation 2.47 the mean Grüneisen parameter between 2000 and 4000 K was calculated for each volume (Figure 7.12). In Figure 7.12 an initial sharp increase in Grüneisen parameter with pressure is calculated, which flattens out to a shallower, possibly linear relationship, this has also been observed for liquid $MgSiO_3$ (Stixrude and Karki, 2005; De Koker and Stixrude, 2009).

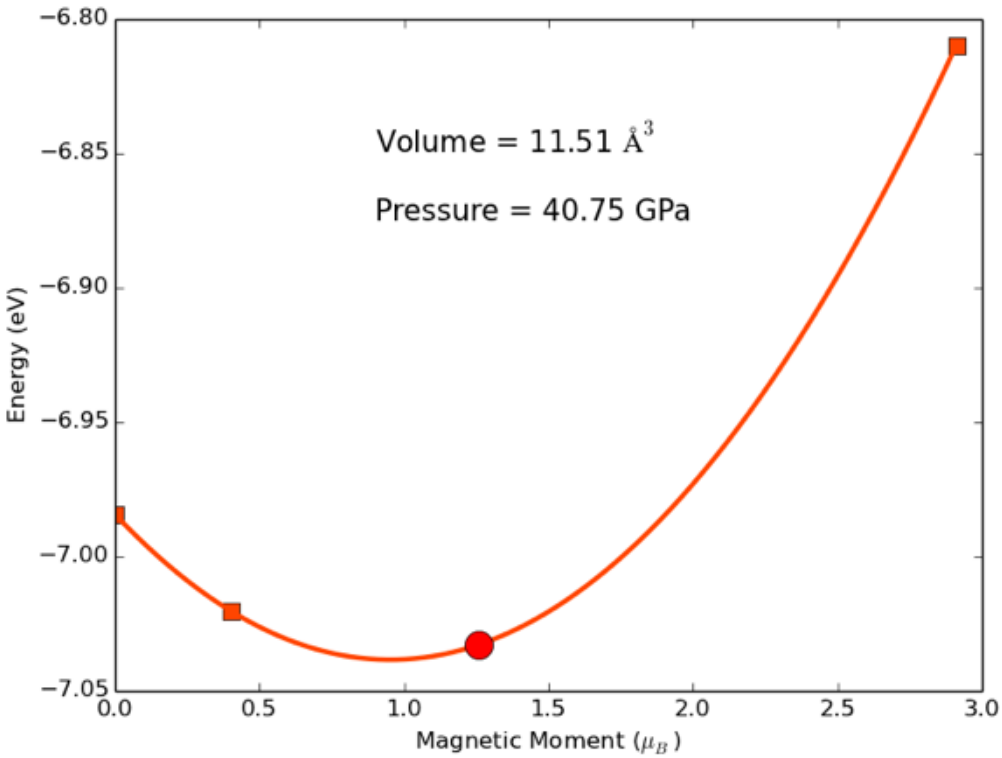

Figure 7.11: Method of finding the excess internal energy from interactions at each pressure using the corresponding excess internal energy for the MS3, LS, and an intermediate magnetic state (indicated by orange squares). A parabola is fitted to the three spin states, and the excess internal energy at the correct magnetic moment for this volume is recorded, indicated by the red circle at 11.5 $\AA^3$/atom (41 GPa) at 4000 K.

7.6 The Adiabatic Gradient

Using the isothermal bulk modulus, and mean values of the Grüneisen parameter and thermal expansion between 2000 and 4000 K the adiabatic gradient of pure liquid iron has been calculated at 3000 K (Figure 7.13). The adiabatic gradient is higher than that found using "free" spin calculations in Chapter six, and suggests a complicated crystallisation regime for a hypothetical iron core of Mercury.

The calculated adiabatic gradient suggests a transition between a top down and bottom up crystallisation regime at a higher pressure than predicted previously in Chapter six. The relative slopes of the adiabatic gradient and the melting curve of Anzellini et al. (2013)

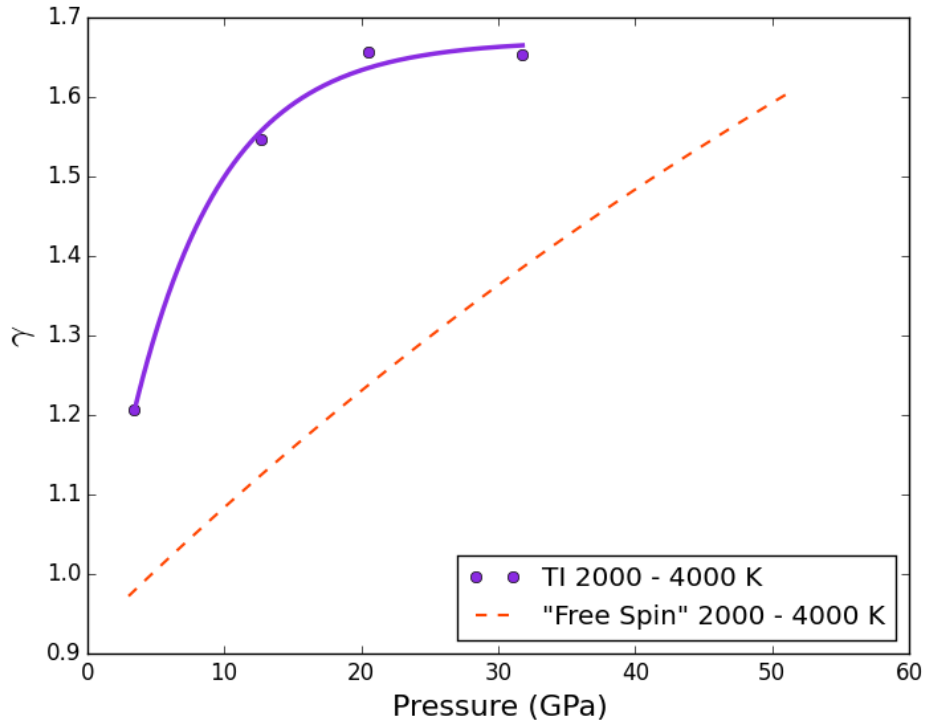

Figure 7.12: The mean Grüneisen parameter of pure liquid iron between 2000 - 4000 K computed using thermodynamic integration. The line indicates an exponential fit to the calculated Grüneisen parameter at four volumes (represented by filled circles). The orange dashed line represents the mean Grüneisen parameter between 2000 - 4000 K calculated for pure liquid iron using "free" spin calculations (Chapter six).

suggest a complicated evolutionary scenario for a pure iron Mercurian core containing multiple crystallising regions (e.g. Section 6.10, Figure 6.15). Whereas, the adiabatic gradient in relation to the slope of Shen et al. (1998), could suggest total top-down crystallisation of a pure iron core. The modelled temperatures of Mercury's core-mantle boundary range between 1850 -2000 K (following Rivoldini et al., 2009, the adiabatic gradient calculated in this chapter therefore suggests that a pure iron Mercurian core could reach between 2877 - 3027 K at the planet's centre ($\sim$ 36 GPa, Hauck et al., 2013).

7.7 Summary

This chapter has investigated the high to low spin transition of pure liquid iron at 2000, 3000 and 4000 K using thermodynamic integration to include the influence of magnetic

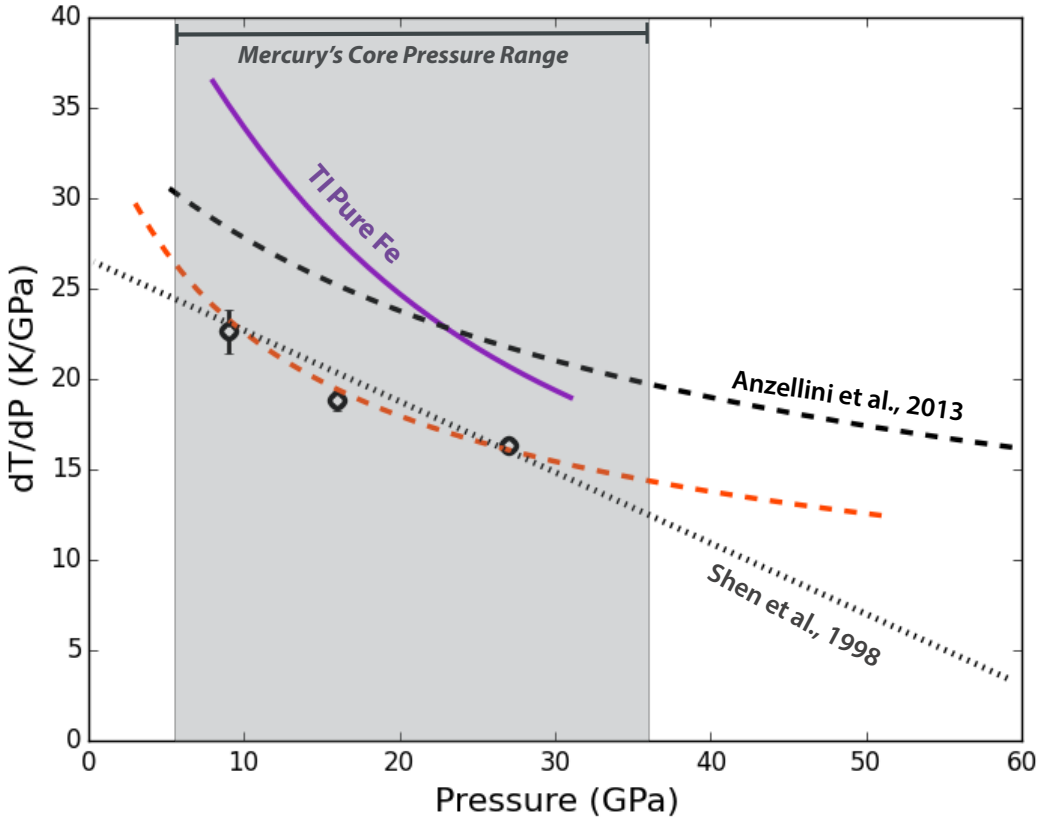

Figure 7.13: The adiabatic gradient of pure liquid iron at 3000 K computed using the refined magnetic transition (shown by the solid purple line). This is compared alongside the adiabatic gradient determined using "free" spin magnetic calculations (Chapter six; dashed orange line, the orange points indicate the individual VASP calculations) and the melting curves of Anzellini et al. (2013) (shown in the thick black dashed line) and Shen et al. (1998) (thin grey dashed line).

entropy. With respect to the "free" spin calculations of Chapter six, the magnitude of the local atomic moments of pure liquid iron have been found to increase at all pressures and temperatures. In contrast with the results of Chapter six, the calculated magnetic transition becomes broader with increasing temperature, consistent with studies of the spin crossover in solid ferropericlase (Holmström and Stixrude, 2015). In all cases the low spin state of pure liquid iron was not predicted within the pressure range calculated, suggesting that at 4000 K, the low spin states lies at pressures much higher than 80 GPa. The equations of state and isothermal bulk modulus of pure liquid iron have been calculated at 2000, 3000 and 4000 K and the mean coefficient of thermal expansion and Grüneisen parameter calculated between 2000 and 4000 K. These were used to calculate the adiabatic gradient

of pure liquid iron at the conditions of Mercury's core and has been found to be higher than that predicted in Chapter six. In comparison with the melting curve of Anzellini et al. (2013) the calculated adiabatic gradient suggests a complicated crystallisation regime for a hypothetical pure iron core in Mercury with multiple crystallising regions. However, conversely, when compared against Shen et al. (1998), an entirely top-down crystallisation regime is predicted, highlighting the importance in the fine detail of the melting curves. This chapter has also shown the influence of the magnetic entropy term in the Helmholtz free energy. The inclusion of magnetic entropy has increased the stability of the magnetic phases to higher pressures across all calculations, and significantly broadened the transition at higher temperatures. Including the magnetic entropy has resulted in a higher predicted adiabatic gradient of pure liquid iron and a different crystallising regime for a hypothetical pure iron core of Mercury. The pressures reached encompass the entire core pressure range of Mercury, but pure liquid iron is also important in the cores of larger terrestrial planets such as the Earth, Mars and sub-Earth size exoplanets. This study reaches deep into the core of Mars but further calculations would allow the study of a hypothetical pure iron Martian core and its evolution over time as well as the early evolution of the Earth's core.

Chapter 8

The Thermoelastic Properties and Adiabatic Gradient of Fe-S-Si

8.1 Introduction

The observed high density of Mercury suggests it is predominantly made of iron, but thermal history considerations dictate that a pure iron or iron-nickel Mercurian core would have solidified by the present day (e.g. Cassen et al., 1976; Schubert et al., 1988) and therefore cannot explain the ground-based observations of a liquid layer within the planet (Margot et al., 2007). In this chapter, the method tested and used in Chapter six to investigate the behaviour of pure liquid iron has been applied to a more likely composition to exist in Mercury's deep interior, that of an Fe-S-Si mixture (Chapter 1). This chapter presents calculations of the thermo-elastic properties of a matching composition to that studied in Chapter 5 with the relative abundances of 80 at% Fe, 10 at% Si, and 10 at% S. A hypothesised iron-rich, Fe-S-Si mixture for the composition of Mercury's core has arisen as a result of many factors including the high metallic content of Mercury's core, the cosmo-chemical abundance of sulphur, the observed liquid layers in the planets interior and the reduced conditions inferred for the planets formation from the low iron content of Mercury's surface (Chapter 1). This composition in particular, $Fe_{0.8}S_{0.1}Si_{0.1}$, has been chosen as a starting point to discover the potential implications an Fe-S-Si mixture may have on the core evolution of Mercury, as it agrees with the core compositions suggested by the modelling of Chabot et al., 2014, whilst also lying in the miscible region of the phase diagram at the pressures of Mercury's core (Morard and Katsura, 2010; Chapter 4). While this chapter

will focus on the core of Mercury, it is also possible that Fe-S-Si may be important in understanding other small rocky bodies in the solar system, e.g. Mars and may also apply to the study of sub-Earth size exoplanets.

First principles molecular dynamics (FPMD) calculations have been run to determine the equations of state and thermodynamic properties of $Fe_{0.8}S_{0.1}Si_{0.1}$ at three temperatures, 2000, 3000 and 4000 K and pressures ranging from -3 to 140 GPa (Table 8.1). In Chapter six magnetic calculations were performed in order to capture the high to low spin transition; similar calculations have been performed here. The iron in the Fe-S-Si mixture may undergo a spin transition and hence, all calculations have been run spin-polarised to capture this and any effects it may have on the behaviour of the material.

8.2 FPMD Calculations on Fe-S-Si

To calculate the thermoelastic properties of $Fe_{0.8}S_{0.1}Si_{0.1}$, FPMD calculations have been run at five volumes across three isotherms (2000, 3000 and 4000 K; Table 8.1) using the generalised gradient approximation to the solution of density functional theory with the PW91 enhancement factor (Perdew et al., 1992, 1993). PAW pseudopotentials (Blöchl, 1994; Kresse and Joubert, 1999) were used to model the core electrons and in particular the iron semi-core p states as valence electrons. The volumes calculated were constant across all the isotherms and are described in Table 8.1, alongside the calculated total pressures (which is the sum of the 'external' pressure calculated by VASP and contribution due to the kinetic energy of the nuclei).

The calculations had a cell size of 150 atoms, corresponding to 120 iron, 15 silicon and 15 sulphur atoms. The initial structure was simple cubic (grown to the dimensions of 5 x 5 x 6 using PHON, Alfè, 2009), with the positions of the sulphur and silicon atoms chosen at random. A snapshot from within the equilibrated region of the calculation (Figure 8.1) alongside the radial distribution function (Appendix E) both indicate that the silicon and sulphur did not group or cluster during the course of the simulation.

At extremely high pressures, liquids that are metastable in first-principles calculations may undergo vitrification, i.e a transition to a glass like structure (e.g. Chapter 6, Figure 6.8). Due to the uncertain nature of the melting temperature of $Fe_{0.8}S_{0.1}Si_{0.1}$ when this study

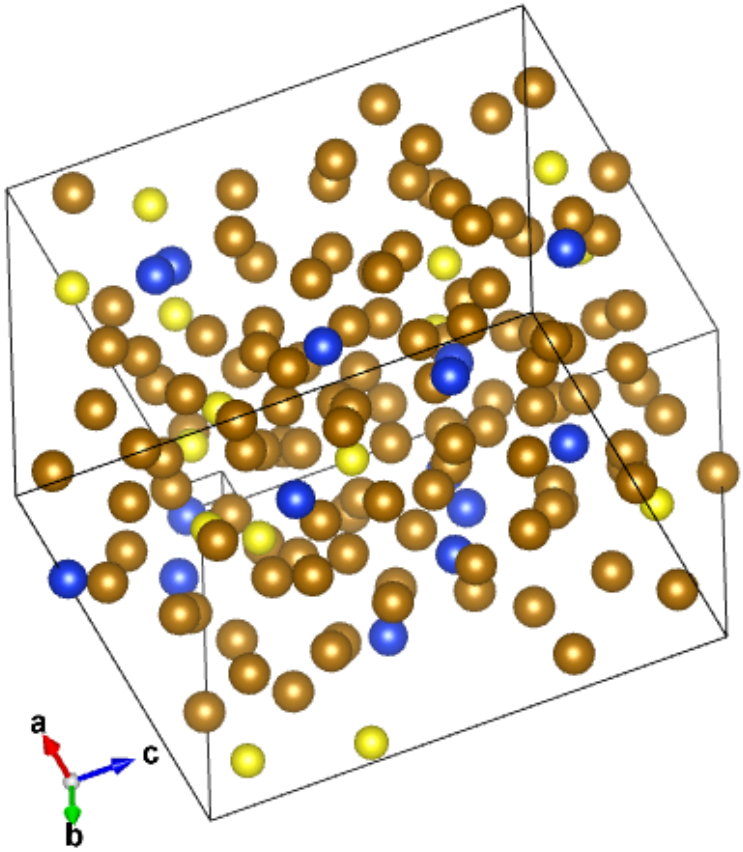

Figure 8.1: The initial randomised cubic structure used in the FPMD calculations of Fe-S-Si is superheated to 10,000 K for greater than 1.5 ps and cooled to the desired temperature (4000 K in the above image). Snapshot shown here is at 4000 K taken within the equilibrated region of the simulation. Image created using the Visualization for Electronic and Structural Analysis Software, VESTA (Momma and Izumi, 2011).

was undertaken a different starting procedure was used than has been described in Chapter six. In Chapter six, the simulation was superheated to 10,000 K for two picoseconds at a single volume, then cooled and pressurised to produce the volumes ranging between 13.54 - 8.13 $\AA^3$/atom and temperatures between 2000 - 4000 K. Instead, in this case, in an attempt to avoid solidification, five separate starting configurations were produced by superheating five volumes (ranging between 14.14 - 8.48 $\AA^3$/atom) individually to 10,000 K for a minimum of 1.5 picoseconds (confirmed using the radial distribution function and mean-squared displacements; Chapters two and six) .

Each volume was then cooled to 2000, 3000 and 4000 K to produce three isothermal equa-

tions of state. As described earlier in this work, the temperature in the calculation was controlled using the Nosé-Hoover thermostat (Nosé, 1984), and performed using time steps of one femtosecond. As before, a single k-point was used to sample the Brillouin zone located at $\frac{1}{4}, \frac{1}{4}, \frac{1}{4}$ (Baldereschi, 1973), which was again found to better produce converged values of energy and pressure (obtained using a 2 x 2 x 2 k-point grid) than gamma point sampling of the Brillouin zone. The cut-off energy was converged within a criterion of $\pm$ 5 meV/atom resulting in an energy cut-off of 400 eV (Appendix A). The simulations were then run for at least an additional two picoseconds in addition to the superheating to achieve equilibrium at the desired temperatures. Then, finally, the FPMD were run for a minimum of four picoseconds at the desired volumes and temperatures to calculate the pressure and energy as an average over simulation time. Uncertainty in the calculated values was determined using the blocking method (see Chapter two, Section 2.10) and was found to be less than 0.01 GPa in pressure and 0.6 meV in energy.

The calculations were run spin polarised, initiated with a finite atomic magnetic moment equal to +4 μ_B/atom for the iron atoms and 0 μ_B/atom for the sulphur and silicon, totalling a net magnetisation of +480 μ_B for the super-cell. Unlike the pure iron calculations (presented in Chapter six), the net magnetisation of the supercell did not reduce to zero over the course of the calculation. Tests were run using a short simulation (200 femtoseconds) on the effect of differing starting configurations, e.g. initialising a paramagnetic structure with no overall total magnetic moment from the outset, and within error ($\pm$ 0.01 μ_B, 0.2 meV and 0.5 GPa) no effect on the other properties of the system was found.

The radial distribution functions were also calculated for each pressure at 2000 K (Appendix E, Figure E.2) to investigate any possible structural changes in the $Fe_{0.8}S_{0.1}Si_{0.1}$ liquid, as were calculated for pure liquid iron in Chapter 6. The 2nd nearest neighbour peak in the Fe-Fe interactions were found to shift to shorter distances as well as change to a distinctly non-gaussian shape with increasing pressure (Appendix E, Figure E.2). This may suggest a structural change in the liquid with increasing pressure, however the current calculations would need to be extended to longer simulation times to reduce the noise in the calculated g(r), and additional calculations are needed to identify the pressure conditions at which this structural change occurs, which were outside the time-scale of this work.

8.3 Spin Transition in Fe-S-Si

The iron magnetic spin transition in $Fe_{0.8}S_{0.1}Si_{0.1}$ presented here has been found to be gradual and systematically higher in pressure than pure liquid iron at the same conditions. The magnitude of the atomic moments has also been calculated to be higher than pure iron at the same conditions (Figure 8.2). The peak height at the Fermi level is larger for Fe-S-Si, and therefore, following the Stoner criterion, additionally suggests a larger moment magnitude than pure liquid iron (Appendix C). The highest local moment was calculated to be 2.2 $\mu_B/atom$ at 2000 K and the lowest pressure, which gradually decreased to zero at 120 GPa (Figure 8.2). The gradual decrease in magnetic moment was not found to vary significantly with temperature, albeit at a lower initial value. A transition to low spin is calculated at $\sim$ 120 GPa for all temperatures studied (Figure 8.2). This is far higher than the central pressure of Mercury (approximately 36 GPa; Hauck et al., 2013 and therefore suggests that Fe-S-Si would remain in an intermediary spin state throughout the planet's interior, which may have significant implications for the core and the generation of the planet's magnetic field. It also suggests that like pure liquid iron, Fe-S-Si may also have a large magnetic susceptibility which will have important implications for a dynamo driven magnetic field in Mercury (Frick et al., 2002). Also shown in Figure 8.2 are the core pressures of the Moon, Ganymede and Mars, and in all cases the calculations suggest that $Fe_{0.8}S_{0.1}Si_{0.1}$ would remain outside the low-spin state.

As described in Chapter six and seven, the true nature of the magnetic transition in Fe-S-Si has not been captured fully in these simulations, as VASP "free" spin magnetic calculations neglect magnetic entropy, which will tend to underestimate the size of the finite local moments of the atoms (e.g. shown in Chapter seven). This is rectified in the following chapter, which uses free-energy minimisation to include the magnetic entropy and investigate the effect this has on the magnetic transition as well as the thermodynamic and physical properties of $Fe_{0.8}S_{0.1}Si_{0.1}$.

8.4 The Equation of State

Calculations were made at five volumes at each temperature (2000, 3000 and 4000 K) that were kept constant across all the isotherms. Each isothermal set of volumes and their corresponding pressures were then fitted to a third order Birch Murnaghan equation of state

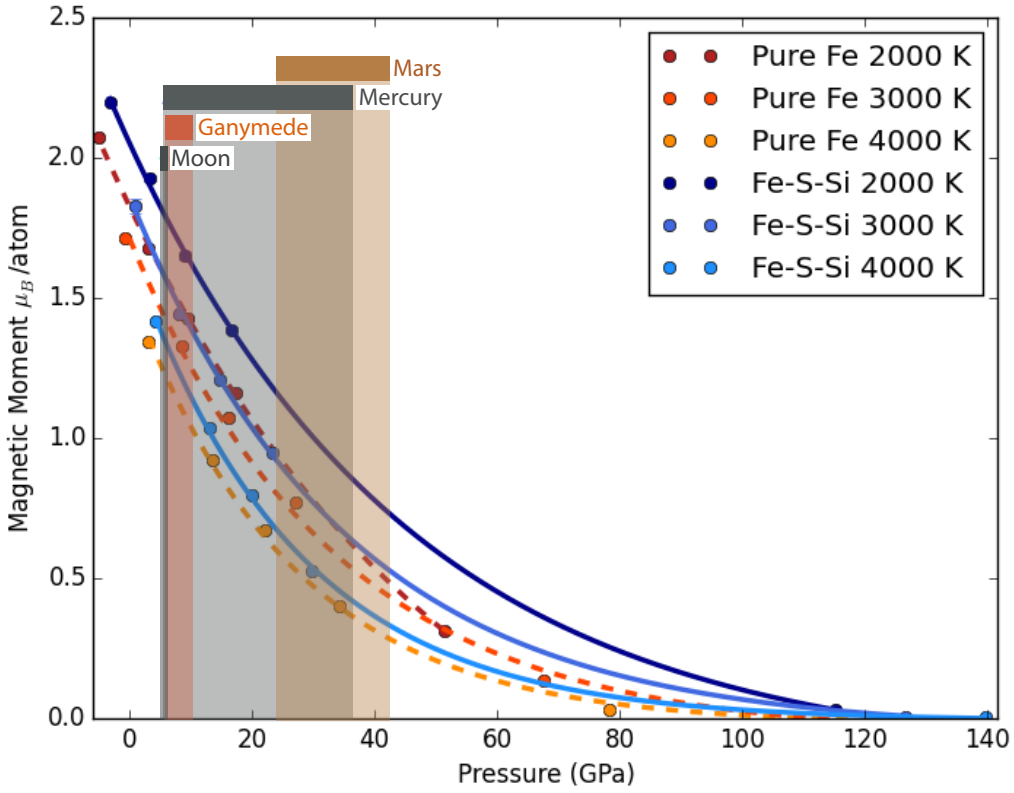

Figure 8.2: Spin crossover of Fe-S-Si (solid blue lines) alongside similar calculations on pure liquid Fe (dashed orange lines; Chapter six) at 2000, 3000 and 4000 K. Shaded bars indicate the approximate pressure ranges of the small bodies in the solar system. At all pressures studied, both pure Fe and $Fe_{0.8}S_{0.1}Si_{0.1}$ are outside of the low spin state, which suggests that both Fe-S-Si and pure iron liquids would retain a finite local moment throughout the pressures of Mercury, Ganymede, Mars and the Moon. The addition of silicon and sulphur to the pure iron system has been found to increase the relative iron local moments at all temperatures and pressures. The pressures of Mercury's core are from Hauck et al. (2013), the pressures of Ganymede's core are from Rückriemen et al. (2015) and the pressures of the Moon and Mars' core are from Antonangeli et al. (2015).

(Birch, 1978; BM3EOS) using the EOSFit code (Angel et al., 2014; Table 8.2, Figure 8.3).

Table 8.1: The densities, volumes and pressures computed from *ab initio* molecular dynamics calculations of Fe-S-Si.

Temperature (K)	Density (kg/m^3)	Total Pressure (GPa)	Error ($\pm$ GPa)
2000	5952.0213	-3.2359	0.0024
	6613.3571	3.2453	0.0028
	7002.3781	8.9577	0.0022
	7440.0266	16.6116	0.0033
	9920.0355	115.3095	0.0036
3000	5952.0213	0.8375	0.0032
	6613.3571	8.1569	0.0035
	7002.3781	14.7794	0.0036
	7440.0266	23.3876	0.0022
	9920.0355	126.7441	0.0083
4000	5952.0213	4.3290	0.0022
	6613.3571	12.9805	0.0027
	7002.3781	19.8685	0.0029
	7440.0266	29.7271	0.0039
	9920.0355	139.6716	0.0053

Table 8.2: Fitted parameters of the Birch Murnaghan 3rd order equation of state

Temperature (K)	V_0 ($Å^3$/atom)	ρ_0 (kg/m^3)	K_0 (GPa)	K'
2000	13.30(14)	6329	62(9)	6.6(7)
3000	14.4(3)	5845	44(12)	6.7(10)
4000	15.6(7)	5396	31(15)	7.1(15)

As one would expect, the density of Fe-S-Si is markedly decreased with respect to pure liquid iron, such that at the approximate conditions of the Mercury's core mantle boundary (CMB, 2000 K, 5 GPa; Rivoldini and Van Hoolst, 2013; Rivoldini et al., 2009; Hauck et al., 2007, 2013) the density of $Fe_{0.8}S_{0.1}Si_{0.1}$ would be 6757 kg/m^3, approximately 13% less dense than pure liquid iron (Chapter six, Section 6.6). However, as described in Chapter six and seven, it is likely that the density calculated here is an overestimate of the true density of $Fe_{0.8}S_{0.1}Si_{0.1}$ resulting from neglecting the magnetic entropy in the minimisation routine. The inclusion of the magnetic entropy is likely to increase the size of the finite local moments on the atoms, and thus increase the volume also, decreasing the density. This is explored further in Chapter nine.

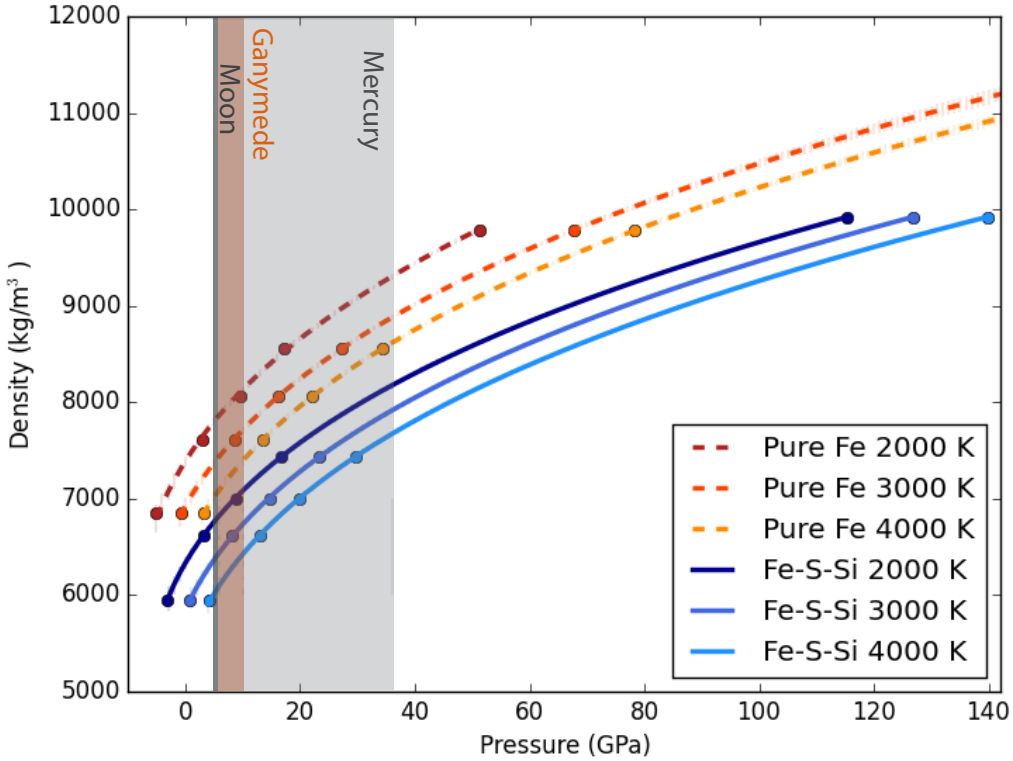

Figure 8.3: The equations of state for Fe-S-Si (shades of blue) and pure Fe (shades of orange) at 2000, 3000 and 4000 K. Fe-S-Si is markedly less dense than pure Fe at the same conditions. Fits are shown with solid lines for Fe-S-Si and dashed lines for pure Fe, with lighter colours indicating increasing temperature, individual NVT calculations are shown using points. Errors are also shown on this plot using capped lines but are within the marker size shown. The pressure range of Mercury's core is indicated by the shaded region (Hauck et al., 2013), along with the pressures of Ganymede's core from Rückriemen et al. (2015) and the pressures of the Moon's core from Antonangeli et al. (2015).

8.5 The Isothermal Bulk Modulus

The isothermal bulk modulus is determined directly from the fit to the BM3EOS. The 'pv-cal' function within EoSFit (Angel et al., 2014) solves the BM3EOS iteratively for a range of pressures and was used to calculate the isothermal bulk modulus shown in Figure 8.4 for $Fe_{0.8}S_{0.1}Si_{0.1}$ at 2000, 3000 and 4000 K.

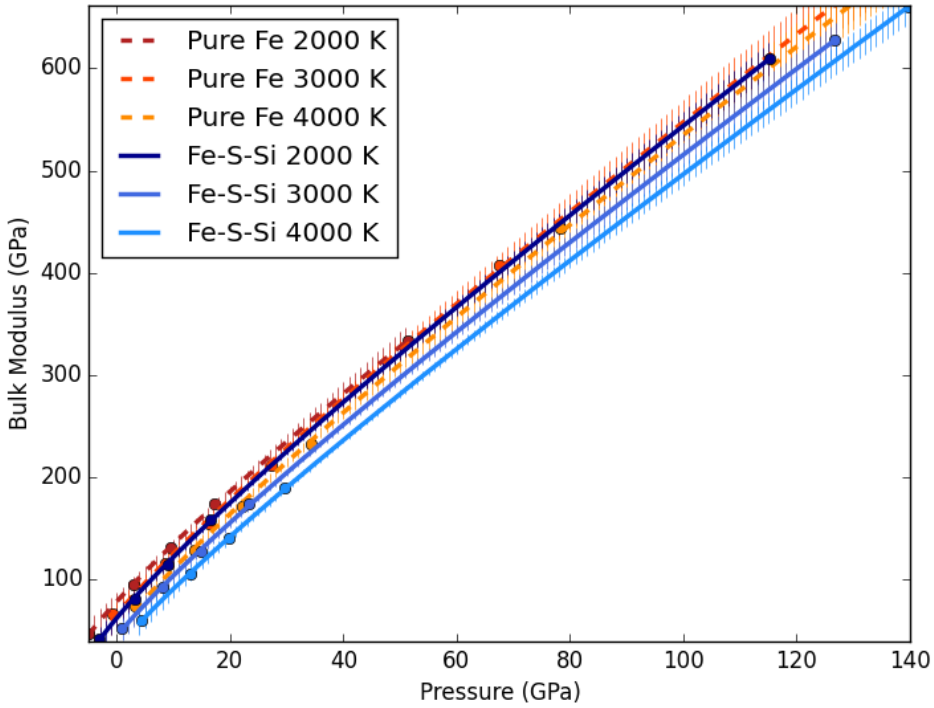

Figure 8.4: The isothermal bulk modulus for Fe-S-Si (shades of blue) and pure Fe (shades of orange) at 2000, 3000 and 4000 K. Calculations suggest Fe-S-Si has a lower incompressibility in comparison with pure Fe at the same conditions. Fits from the BM3EOS are shown with solid lines for Fe-S-Si and dashed lines for pure Fe, with lighter colours indicating increasing temperature, individual VASP NVT calculations are shown using points and errors as a result of the fit to the BM3EOS are indicated by shaded lines.

The isothermal bulk modulus of Fe-S-Si has been found to be similar in magnitude to that of pure iron, suggesting the addition of sulphur and silicon has not dramatically changed the compressibility of the material. In Chapter six the isothermal bulk modulus was found to follow a linear trend with respect to pressure, which agreed very well with previous modelling results of Vočadlo et al. (2003) and Ichikawa et al. (2014), the same has been

found here (shown in Figure 8.4).

8.6 Thermal Expansion

In the same manner as described in Chapter six, the highest temperature (4000 K) and lowest temperature (2000 K) isotherms have been used to determine the mean thermal expansion of $Fe_{0.8}S_{0.1}Si_{0.1}$ between 2000 and 4000 K (Figure 8.5a) using the following expression (Chapter 2):

$$\alpha = \left(\frac{ln(V(T')/V(T))}{T' - T} \right)_P \tag{8.1}$$

in which V is the volume, T is the temperature and P is the pressure, and T' $>$ T. To investigate the change in thermal expansivity with temperature the same method was used to calculate the mean thermal expansivity between 2000 - 3000 K and 3000 - 4000 K (shown in Figure 8.5). At low pressure the thermal expansion decreases with temperature but switches at $\sim$ 50 GPa to a regime in which thermal expansion increases with temperature. However, the size of the error bars (also included in Figure 8.5) encompasses a large range and therefore the fine detail of the thermal expansivities is uncertain. Further calculations are required to extend the molecular dynamics simulations to longer times and reduce the statistical error, as a large portion of the error associated with the thermal expansivity is a result of the BM3EOS fit from which the volumes are derived. The thermal expansion calculated here is low in comparison with experimental measurements of the thermal expansion of pure Fe liquids which range between 9.2 - 13.2 x 10^{-5} /K (Williams, 2009) but is higher than the thermal expansion calculated for pure liquid iron in Chapter six at low pressure (Figure 8.5). The increased thermal expansion reported here may be a result of the sulphur in the system, as previous studies of Fe-S systems report larger expansivities than measured in pure liquid iron (Williams, 2009). In Chapter seven the inclusion of the magnetic entropy increases the calculated thermal expansion of liquid iron and it is likely that the same will happen here. The calculations described thus far in this chapter have not accounted for the magnetic entropy of the system and thus will tend to underestimate the magnitude of the finite local moments, and therefore, underestimate the volume. The thermal expansion depends on the volume of the system, and the change in volume with pressure and therefore

a small change in these may result in a large change in the calculated thermal expansion. This is explored in detail in Chapter nine.

8.7 The Grüneisen Parameter

The Grüneisen parameter, γ, has been calculated as outlined in equation 2.47 in Chapter two, Section 2.11.3, as a result of VASP FPMD calculations. At each volume, the difference between the pressure at 2000 and 4000 K is divided by the corresponding difference in the internal energy of the systems (for more details see Chapter 6, Section 6.9). This calculated the mean gradient in the pressure with respect to energy for Fe-S-Si between 2000 and 4000 K, which was then multiplied by the volume to find the Grüneisen parameter (Figure 8.6).

A steep dependence of the Grüneisen parameter with pressure has been found, followed by a possible flattening of this trend. This is contradictory to the work of Vočadlo et al. (2003) and Ichikawa et al. (2014), which at high pressure have both found a relatively flat relationship of the Grüneisen parameter of pure iron with pressure, however the 'flat' region predicted in this work appears at high pressure and may coincide with their work (e.g. the results of Vočadlo et al. (2003) are shown in Figure 8.6). An initial steep increase is consistent with liquid $MgSiO_3$ (Stixrude and Karki, 2005), and the subsequent flattening of the Grüneisen parameter has also been observed in other studies of silicate liquids at very high pressure (e.g. Stixrude et al., 2009).

8.8 The Adiabatic Gradient and Mercury's Core Evolution

Estimates of the CMB temperature (T_{CMB}) of Mercury range between 1850 - 2000 K (e.g. Rivoldini et al., 2009). At the core pressures of Mercury the adiabatic gradient calculated here suggests that the temperature at the centre of a Mercurian $Fe_{0.8}S_{0.1}Si_{0.1}$ core ($\sim$ 36 GPa, Hauck et al., 2013) could range between $\sim$ 2658 K (T_{CMB} = 1850 K) and 2808 K (T_{CMB} = 2000 K).

The adiabatic gradient of $Fe_{0.8}S_{0.1}Si_{0.1}$ has been calculated up to 115 GPa (Figure 8.7). In Figure 8.8 the adiabatic gradient calculated using the thermoelastic properties determined throughout this chapter are plotted alongside that of pure liquid iron (from Chapter six), the slopes of the pure iron melting curves (Shen et al., 1998; Anzellini et al., 2013) and

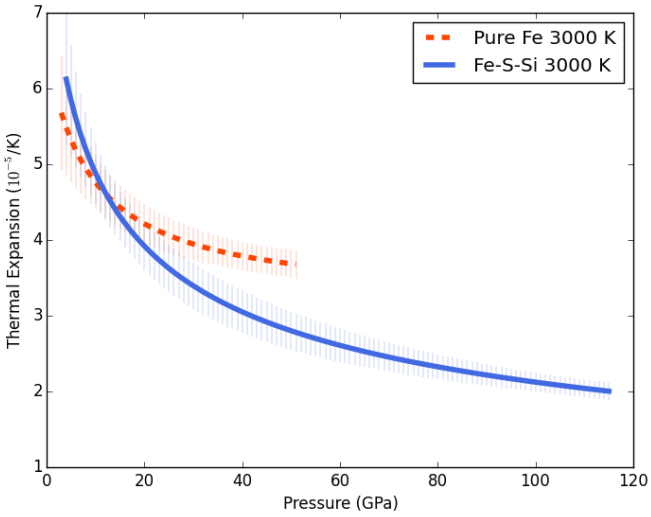

(a) The mean thermal expansion of Fe-S-Si (solid blue) and pure Fe (dashed orange) between 2000 - 4000 K

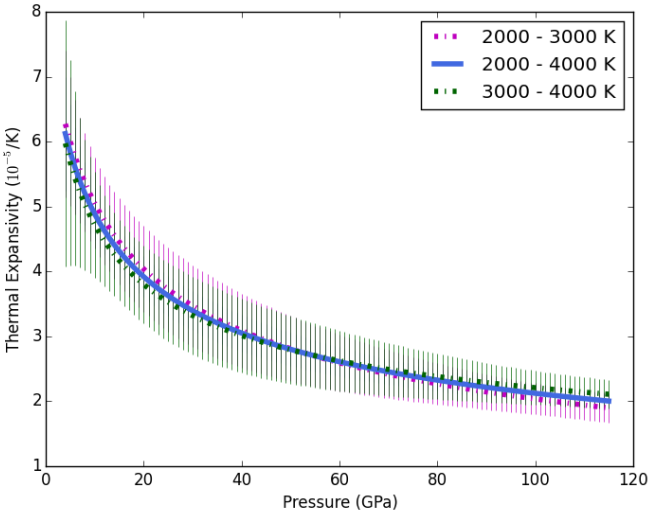

(b) The mean thermal expansion of Fe-S-Si between 2000 - 3000 K, 2000 - 4000 K and 3000 - 4000 K

Figure 8.5: (a) The mean thermal expansion for Fe-S-Si (solid blue) and pure Fe (dashed orange) between 2000 - 4000 K. Calculations suggest a similar magnitude of thermal expansion for both Fe-S-Si and pure Fe at low pressures but with a more rapid decrease in thermal expansivity in Fe-S-Si with increasing pressure. Fits are shown with solid lines for Fe-S-Si and dashed lines for pure Fe and errors as a result of the BM3EOS fitting (from which the volumes are derived) are represented by shaded lines.

(b) Mean thermal expansion of Fe-S-Si between 2000 - 4000 K (blue solid line), 2000 - 3000 K (pink dashed line) and 3000 - 4000 K (green dashed line). In all cases errors are indicated by shaded lines. The errors of each temperature overlap considerably and thus the fine detail is unclear.

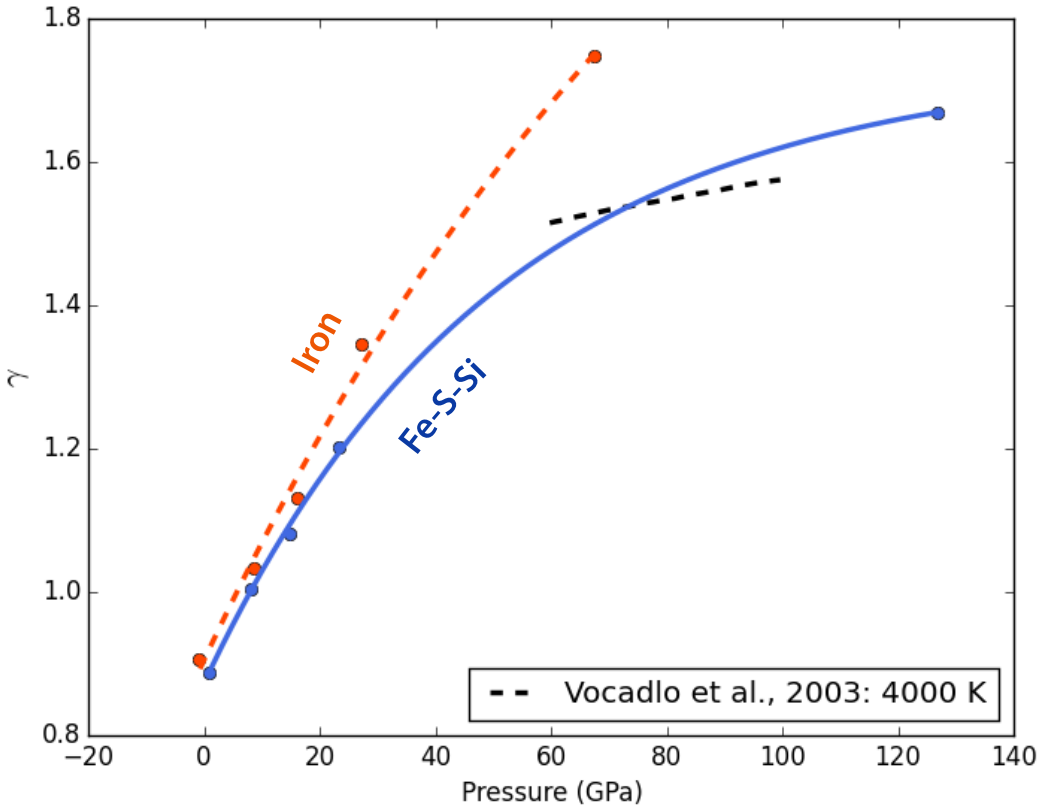

Figure 8.6: The mean Grüneisen parameter for Fe-S-Si (solid blue) and pure Fe (dashed orange) between 2000 - 4000 K, also shown are the results of Vočadlo et al. (2003) for pure iron at 4000 K. Calculations suggest a similar magnitude of Grüneisen Parameter for both Fe-S-Si and pure Fe at low pressures but with increasing pressure the Grüneisen Parameter of Fe-S-Si flattens and diverges away from the pure Fe relationship. Fits are shown with a solid line for Fe-S-Si and dashed lines for pure Fe.

crucially, the slope of melting curve of the same composition ($Fe_{0.8}S_{0.1}Si_{0.1}$) determined in Chapter five (hereafter referred to as the Fe-S-Si melting curve). The slope of the melting curve of Fe-S-Si (from Chapter 5) is similar to that of pure iron, but has been found to be marginally shallower at low pressures, but steeper upon increasing pressure. This is in contrast to the shallower slopes suggested for FeS alloys (Chen et al., 2008), however, various Fe-Si alloys have been found to have similar melting curves to iron (e.g. Fischer et al., 2013; Lord et al., 2010), and in general (except at points of inflection), the liquidus of FeS is also steeper than pure iron which may suggest similarity between these studies and the slope of the Fe-S-Si liquidus found here. At low pressures the adiabatic gradient of $Fe_{0.8}S_{0.1}Si_{0.1}$ has been found to be higher than the adiabatic gradient of pure liquid iron,

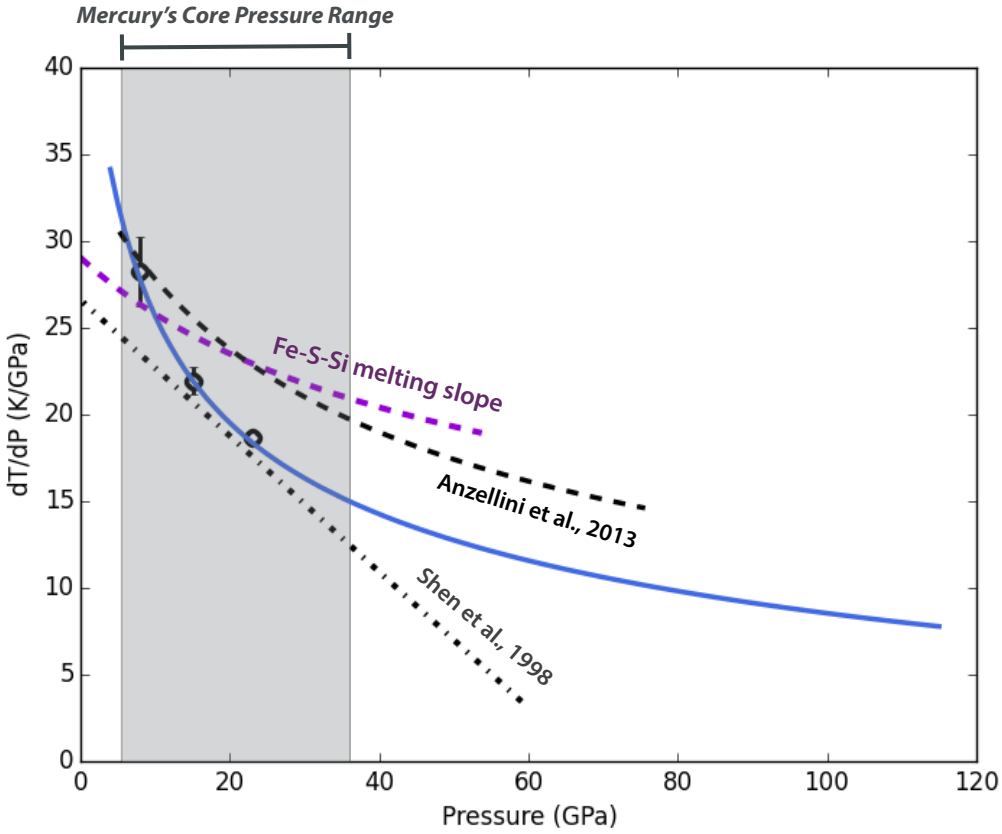

Figure 8.7: The calculated adiabatic gradient of $Fe_{0.8}S_{0.1}Si_{0.1}$ shown in blue. Independent calculations using the original NVT calculations (but using the fitted thermal expansion at the NVT pressures) are indicated by black circles, and errors by capped black lines. The dashed grey and and black lines indicate the slopes of the melting curves of Shen et al. (1998) and Anzellini et al. (2013) respectively. The smaller dashed magenta line indicates the slope of the $Fe_{0.8}S_{0.1}Si_{0.1}$ melting curve determined experimentally in Chapter five.

but the results suggest that approaching 50 GPa the two curves become very similar.

At low pressures the adiabatic gradient is steeper than the slope of the Fe-S-Si melting curve (Figure 8.7, 8.8), suggesting a 'top-down' crystallisation regime at the top of the core (see Chapter six, Figure 6.13B). With increasing pressure the relationship between the adiabatic gradient and slope of the Fe-S-Si melting curve switches, and the adiabatic gradient has the shallower trend. The adiabatic gradient then remains the shallower relationship throughout the core pressures of Mercury. A transition between two crystallising regimes within the core pressure range may produce a complex evolutionary history of the core with multiple

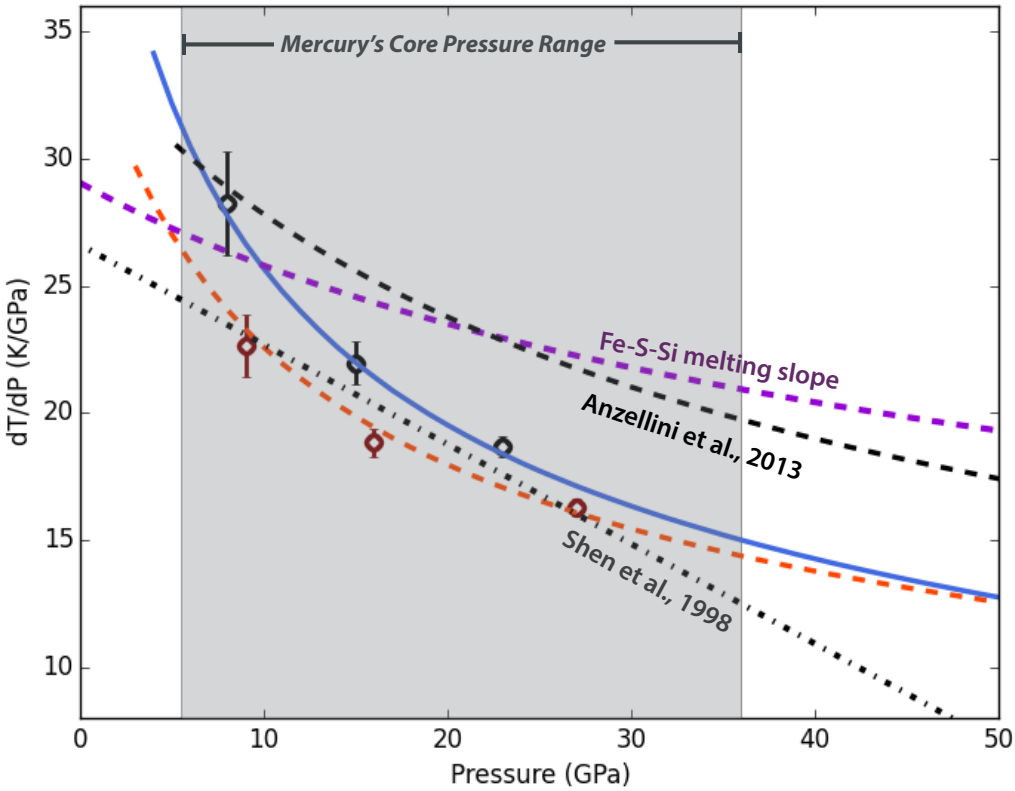

Figure 8.8: The comparison between the adiabatic gradient of pure liquid iron at 3000 K (shown in orange) and the adiabatic gradient of $Fe_{0.8}S_{0.1}Si_{0.1}$ shown in blue. In both cases circles indicate VASP NVT calculations (black is Fe-S-Si and dark red pure Fe) and the fit is indicated by the line. Errors are shown for each of the NVT calculations using capped lines. The dashed grey and and black lines indicate the slopes of the melting curves of Shen et al. (1998) and Anzellini et al. (2013) respectively for pure iron. The smaller dashed magenta line indicates the slope of the $Fe_{0.8}S_{0.1}Si_{0.1}$ melting curve determined experimentally in Chapter five.

crystallisation zones, as described in Chapter six Section 6.10 and Figure 6.15. However, another factor that could play a role in the planet's formation is the relative difference in steepness of the curves. At low pressures (in the top down regime, Figure 8.8) the gradient of the Fe-S-Si melting curve is relatively close to the adiabatic gradient, but with increasing pressure (moving into the bottom-up regime) the gradients increasingly differ, with the adiabatic gradient becoming increasingly shallower relative to the gradient of the melting curve. This could result in the high pressure adiabat, upon cooling, crossing the liquidus first, i.e. initialising bottom-up crystallisation and forming a solid inner core from the centre outwards (Figure 8.10). *Ab initio* calculations of the partition coefficients of silicon and sulphur indicates values close to one (Alfè et al., 2002a). However, Morard et al. (2014) suggests that silicon is relatively incompatible with solid iron, as is sulphur, but possibly to a lesser extent. It is possible then, that the silicon and sulphur will preferentially partition into the melt and thus, create a primarily solid iron inner core and over time enrich the remaining liquid at shallower depths in silicon and sulphur (Figure 8.9).

At the low pressures of the top of Mercury's core and due to the miscibility gap in Fe-S-Si (Morard and Katsura, 2010), the liquid Fe-S-Si may then move into the immiscible region of the phase diagram and form two distinct liquids. Fe-S is less dense than Fe-Si and thus will form a stably stratified liquid layer at the top of the core, whilst the Fe-Si may tend to mix back into the Fe-S-Si mixture (Figure 8.10).

A stably stratified layer at the top of Mercury's core has implications for the planet's magnetic field and may explain the observed weak magnetic field strength (e.g. Christensen, 2006). If the Fe-S layer is a conducting layer, then the magnetic field generated by compositional convection at depth (due to the crystallisation of a solid inner core) would need to diffuse through this layer reducing the measured field strength. However, conversely, if the liquid layer of Fe-S was convecting at the top of the core this may result in a more complicated effect on the magnetic field strength and behaviour, e.g. if they were producing magnetic fields of the opposite polarity etc (Figure 8.11). But, as with Chapters six and seven, it is important to first resolve the difference the inclusion of magnetic entropy may produce and the effect this may have on the adiabatic gradient, as this could change the predicted crystallisation regime entirely; this is explored in Chapter nine.

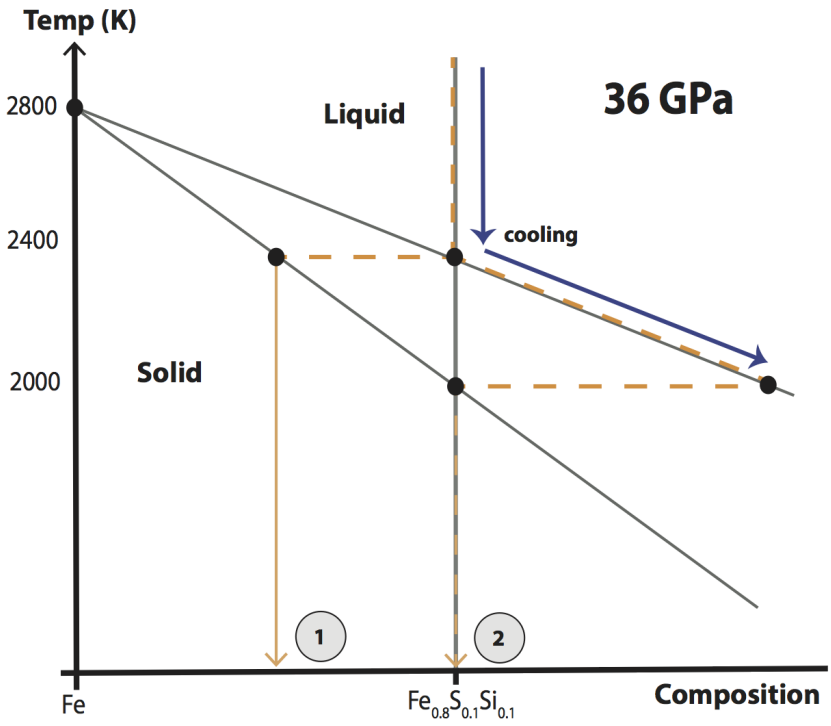

Figure 8.9: A schematic describing the composition of the crystallising material at depth within a hypothetical $Fe_{0.8}S_{0.1}Si_{0.1}$ core. Grey lines indicate the approximate liquidus and solidus relations measured in Chapter five and the path of the crystallising solid outlined in orange. As the planet cools and crosses the liquidus the $Fe_{0.8}S_{0.1}Si_{0.1}$ liquid will begin to crystallise. The first composition to crystallise will be iron enriched relative to the original composition (1). As the planet continues to cool the composition of the liquid will travel down the liquidus curve until it has sufficiently cooled to cross the solidus curve and the original $Fe_{0.8}S_{0.1}Si_{0.1}$ will crystallise (2).

8.9 Summary

This chapter has described the results of first-principles, molecular dynamics spin polarised calculations at 2000, 3000 and 4000 K. The spin transition of $Fe_{0.8}S_{0.1}Si_{0.1}$ has been mapped from -3 to 140 GPa, which suggests that this material would stay outside the low spin state throughout Mercury's core. The equation of state and isothermal bulk modulus of $Fe_{0.8}S_{0.1}Si_{0.1}$ has been calculated at three temperatures, 2000, 3000 and 4000 K and the thermal expansion and Grüneisen parameter as a mean value between 2000 - 4000 K (a summary of the thermodynamic properties are listed in Table 8.3 for the conditions of Mercury's core). In combination, these thermodynamic properties have been used to investigate

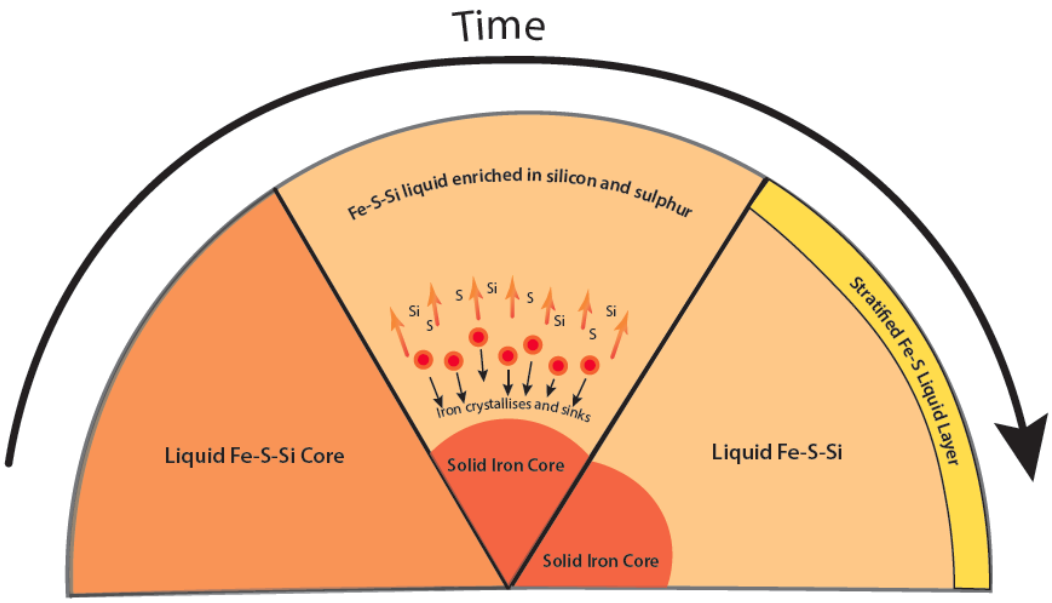

Figure 8.10: From left to right are the broad steps in the evolution of a Mercurian Fe-S-Si core. Initially, soon after planet formation, the entire core will be molten which upon cooling, due to the relative shape of the adiabat and liquidus of Fe-S-Si will crystallise from the centre outwards. As the crystallisation continues, the solid iron core will be result in the remaining Fe-S-Si liquid becoming increasingly enriched in sulphur and silicon. Due to the immiscibility gap in Fe-S-Si, the Fe-S-Si mixture will become two liquids and due to the buoyant nature of of Fe-S will form a stably stratified Fe-S liquid layer at the top of the core.

the core evolution of Mercury via the adiabatic gradient of Fe-S-Si and its relation with the melting curve determined experimentally in Chapter five. The relationship between these two trends suggest that if Mercury's core consisted of Fe-S-Si (with the relative atomic abundances of 80:10:10) then the evolution of its solid inner core would be complex. Previous models of Mercury's internal structure (Riner et al., 2008; Hauck et al., 2013; Rivoldini and Van Hoolst, 2013) combined the properties of each independent component. The properties calculated in this chapter may provide better constraints on the behaviour of Fe-S-Si and therefore may have significant implications for the planet's core size, shape and structure. However, in order to accurately constrain the physical and thermodynamic properties of Fe-S-Si the magnetic entropy must be considered. The magnetic entropy has not been included in the calculations described in this chapter but may have a significant effect on the properties of Fe-S-Si as shown for iron in Chapter seven. This is addressed in the following

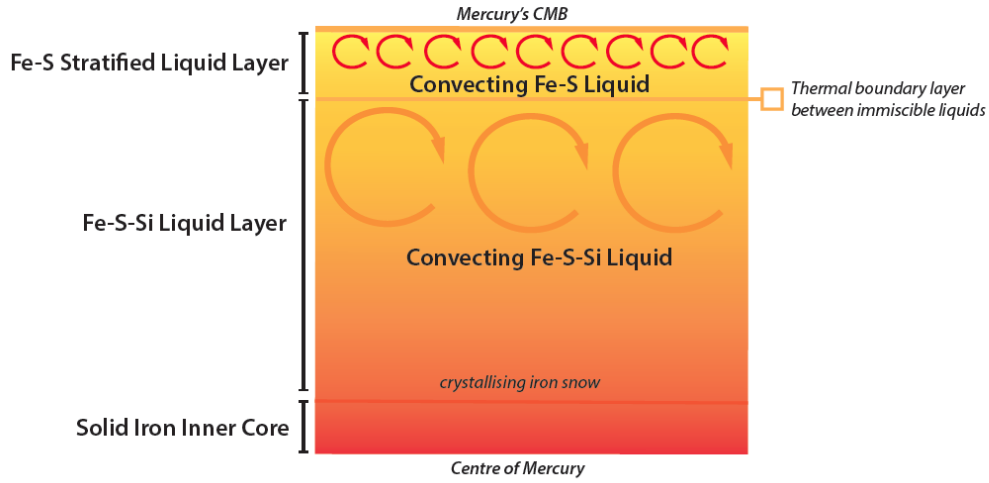

Figure 8.11: If the stably stratified liquid layer at the top of Mercury's core is convecting it may have implications for the surface magnetic field strength.

chapter which details the use of free-energy minimisation and thermodynamic integration to find the magnetic transition, physical and thermodynamic properties of $Fe_{0.8}S_{0.1}Si_{0.1}$.

Table 8.3: Properties of liquid $Fe_{0.8}S_{0.1}Si_{0.1}$ at 2000, 3000 and 4000 K at the approximate pressure of Mercury's CMB ($\sim$ 5 GPa) and centre of the core ($\sim$ 36 GPa).

T *(K)*	P *(GPa)*	ρ (kg/m^3)	γ	α $(10^{-5}/K)$	K_T *(GPa)*
2000	5	6756.94	-	-	92.86
3000	5	6363.27	0.95	5.84	75.21
4000	5	6011.97	-	-	62.53
2000	36	8174.24	-	-	254.00
3000	36	7914.68	1.32	3.17	232.50
4000	36	7671.39	-	-	217.60

Chapter 9

The Thermodynamic Properties of Fe-S-Si using Thermodynamic Integration

9.1 Introduction

The previous chapter details magnetic "free" spin *ab initio* molecular dynamics calculations on a Fe-S-Si mixture with the relative atomic abundance (80:10:10) and suggests a gradual spin transition over a broad pressure range of 120 GPa, far beyond the central pressure of Mercury (36 GPa, Hauck et al., 2013). The adiabatic gradient of $Fe_{0.8}S_{0.1}Si_{0.1}$ in relation to the gradient of the liquidus (measured in Chapter five) suggests a complicated evolution of Mercury's core with a 'bottom-up' crystallisation regime and a stratified liquid Fe-S layer at the top of the core. However, the calculations performed in Chapter eight do not include the influence of magnetic entropy. In Chapter seven it was found that including the magnetic entropy resulted in a higher adiabatic gradient and a different prediction of the evolution of Mercury's core and it was, therefore, imperative that the same procedure was followed for Fe-S-Si.

In this chapter the spin crossover and thermodynamic properties of $Fe_{0.8}S_{0.1}Si_{0.1}$ have been found up to 25 GPa and between 2000 - 4000 K using free energy minimisation and thermodynamic integration following closely the method described in Chapter seven.

9.2 Calculation Details

The first principles molecular dynamics simulations performed in this chapter follow the set-up described in Chapter 8, Section 8.2 (i.e. GGA, PW91). The same cell size (150 atoms), converged values of energy cutoff (400 eV) and Brillouin zone sampling (one k-point located at $\frac{1}{4}, \frac{1}{4}, \frac{1}{4}$ from Baldereschi, 1973) were also used throughout to maintain consistency across the calculations (Chapter 8, Section 8.2).

The starting configurations consisted of simple cubic super-cells of 120 iron, 15 sulphur and 15 silicon atoms distributed randomly within the cell. The initial structure was superheated for two picoseconds at each volume independently (as outlined in Chapter eight). Five volumes were calculated at each temperature of the highest moment magnitude (MS3) ranging from 15.6 - 11.31 $\AA^3$/atom. Five volumes were also simulated for the LS state at each temperature between 14.14 - 8.49 $\AA^3$/atom. The simulations were run for a minimum of six picoseconds, with the initial two picoseconds removed as calibration time (details of each volume and their associated values and errors are given in Appendix B). This produced time averaged computed 'external' pressures and energies for each calculation. 'External' pressure was not the final pressure required however, as the 'external' pressure calculated by VASP did not include the kinetic energy contribution from the nuclei, hence this was added in the post-processing to produce the total pressure of the calculation (Chapter 6, Section 6.6; Appendix B).

9.3 The Magnetic Transition of Fe-S-Si

The magnetic transition of Fe-S-Si has been determined using first principles methods and the perturbative approach to thermodynamic integration. The Gibbs free energy of a series of moment magnitudes have been calculated and the free energy minimised to find the equilibrium magnetic moment.

9.3.1 Equations of State

A total of five magnetic states were studied, the low spin state, LS (in which the magnitude of the local atomic moment is zero), and four magnetic states of increasing moment magnitude per atom, MS0, MS1, MS2 and MS3. As in the case of pure Fe, the equations of state of

the LS state and largest moment magnitude, MS3 were calculated using *ab initio* molecular dynamics calculations on a canonical ensemble of 150 atom super cells (120 iron, 15 silicon and 15 sulphur). The LS simulations were run non-magnetically, and the MS3 calculations run spin polarised with a constrained total magnetisation of the cell equal to +360 μ_B, i.e. +3 μ_B/iron atom, which over the course of the simulation equilibrated to $\sim$ 2.86 $\mu_B/atom$ (Table 9.1). At each temperature (2000, 3000 and 4000 K) the total pressures and volumes of the MS3 and LS states were then fitted to a Birch Murnaghan 3rd order equation of state[1] (Chapter 2, equation 2.41; Birch, 1978; BM3EOS) using the EoSFit software (Angel et al., 2014; Figure 9.1). Figure 9.1 highlights the importance of including the correct magnetic moment in the simulations, e.g. the volumetric difference of $\sim$ 14 % between the MS3 and LS states at 3000 K and 20 GPa.

The canonical "free" spin calculations described in Chapter eight have been used to create the three intermediate equations of state (MS0, MS1 and MS2) following the method of Holmström and Stixrude (2015) and outlined in Chapter 7, Section 7.3.1. Thus, five equations of state were found for each temperature corresponding to five atomic moment magnitudes (Figure 9.2, Table 9.1).

9.3.2 The Thermodynamic Integration of Three Magnetic Phases

The free energy of the LS state was calculated from the fitted parameters of the BM3EOS, however the constant F_0 (Chapter 2, equation 2.39) was unknown and therefore the free energy of the magnetic MS0, MS1, MS2 and MS3 states were calculated relative to the LS (reference) state (F_0 of the LS state was taken to be equal to zero). Adiabatic switching was used within the Kirkwood coupling scheme (Kirkwood, 1935) along with thermodynamic integration to calculate the change in free energy relative to the LS state as the area under the straight line across a parameter lamdba as outlined in Chapter seven, Section 7.3.2. The adiabatic switching simulations were run for a minimum of four picoseconds (from within the equilibrated region of the MS3, MS2, MS1, MS0 and LS calculations) which corresponded to four thousand individual calculations. The simulations provided constraints at $\lambda = 0$ and $\lambda = 1$, and the fluctuations in the molecular dynamics calculation additionally

[1]Except at 2000 K, in which the lowest pressure calculation (corresponding to 14.14 $Å^3$/atom) was not used in the fitting of the LS BM3EOS as it suggested a large expanded-volume (for pressures see Appendix B).

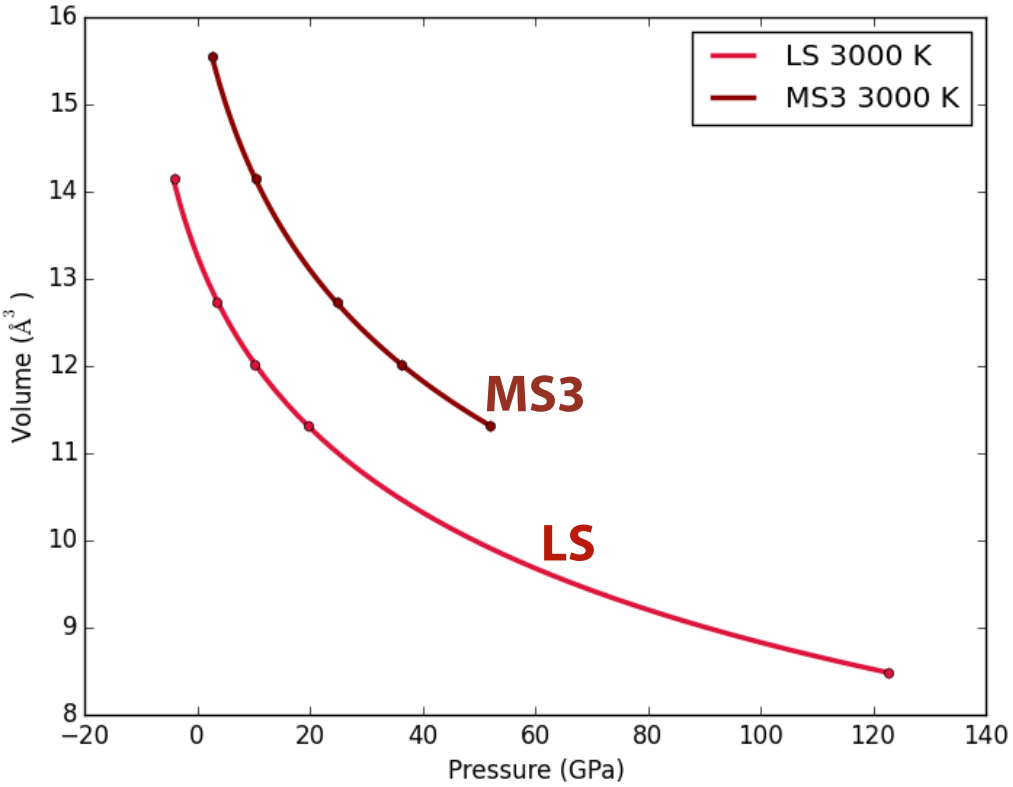

Figure 9.1: The equations of states for the high spin and low spin states of $Fe_{0.8}S_{0.1}Si_{0.1}$ at 3000 K. The highest magnetic spin (MS3) state is represented in dark red, and the low spin (LS) in bright red. The solid lines represent the fit and the points correspond to the individual calculations. Error bars are indicated by capped lines. Other temperatures can be found in Appendix B.

determined the gradient at $\lambda = 1$, e.g. for $\lambda = 1$ of the MS3 spin state (Chapter 7, Section 7.3.2). In the MS3-LS integration all three constraints are used to find ΔF as the area under a second order polynomial (Table 9.2). This was compared with the free energy difference determined using only two constraints (Table 9.2), and two constraints were found to be sufficient. Thus, only two constraints were used to find ΔF of the MS0, MS1 and MS2 moment magnitude calculations (Table 9.2).

9.3.3 Helmholtz Free Energy

The Helmholtz free energy of each state at the integration volume, V_i, was found using the expression described in Chapter 7, equation 7.9, and from this, the free energy of all other volumes calculated using the fitted parameters of the BM3EOS, equation 7.11 (Chapter 7,

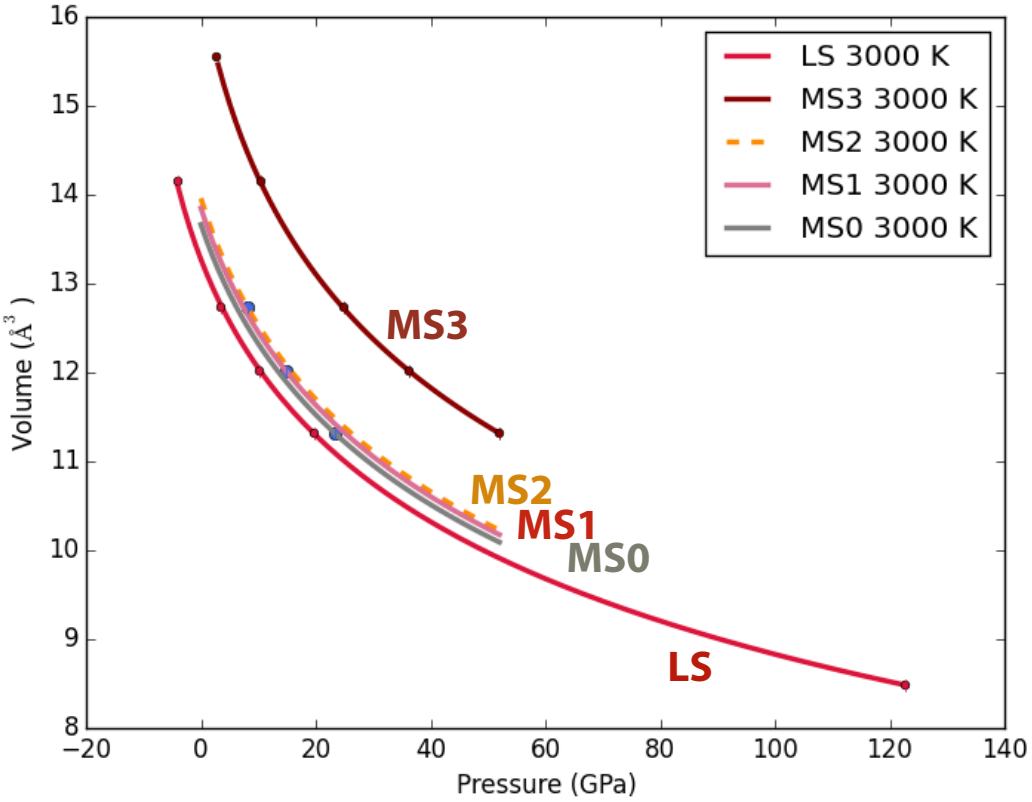

Figure 9.2: Equations of state of the low spin (LS) (red), highest spin state calculated (MS3) (dark red) and two middling spin states at 3000 K (MS2, MS1; light and dark red dashed lines respectively). Blue points indicate calculations from Chapter 8 used to calculate the two intermediate equations of state. Other temperatures are listed in Table 9.1.

Section 7.3.2).

9.3.4 Gibbs Free Energy and Free Energy Minimisation

The Gibbs free energy was calculated for each of the magnetic phases at 1 GPa intervals. In Chapter seven, at each pressure, the Gibbs free energies of the five states (MS3, MS2, MS1, MS0 and LS) were fitted to a parabola, the minimum of which determined the preferred magnitude of the atomic moment (Chapter 7, Figure 7.5; Figure 9.3). However, at lower temperatures (e.g. 2000 K), the calculated Gibbs free energies diverged from the parabolic assumption and this approximation may have, therefore, under-estimated the magnitude of the moment. In Figure 9.3a, the five Gibbs free energies have been fitted to both a second and third order polynomial (Figure 9.3). In Figure 9.3a, at 2000 K the third order fit suggests a much higher local moment magnitude than that suggested by a parabolic fit, whereas in

Table 9.1: Fitted parameters of the Birch Murnaghan 3rd order equation of state: LS, MS0, MS1, MS2 and MS3

T (K)	Name	Mag Moment ($\mu_B/atom$)	V_0 ($Å^3$/atom)	K_0 (GPa)	K'
2000	MS3	2.87	15.02	63.30	6.40
	MS2	1.94	13.17	84.91	6.37
	MS1	1.67	13.02	87.61	6.35
	MS0	1.40	13.01	88.93	6.20
	LS	0.00	12.80	91.80	6.30
3000	MS3	2.85	16.34	45.81	6.30
	MS2	1.46	13.95	68.16	5.84
	MS1	1.22	13.84	69.70	5.81
	MS0	0.95	13.66	72.45	5.74
	LS	0.00	13.27	78.97	5.59
4000	MS3	2.84	18.45	23.89	7.20
	MS2	1.04	14.81	55.60	5.76
	MS1	0.80	14.61	58.88	5.64
	MS0	0.53	14.45	61.66	5.55
	LS	0.00	14.27	65.14	5.45

Figure 9.3b at 4000 K the second order relationship appears to fit very well. It is possible that the deviation at 2000 K is a result of the 'noise' in the calculations, i.e. the errors that have resulted from the fitting procedures performed throughout the study, but, with the current results, a parabolic fit has been used to find the magnitude of the local moment, as a third order relationship appears to overfit the results. In order to correct these results and more closely fit the Gibbs free energy, an extra constraint on the curve would be required to improve the second order relationship, or confirm the third order fit to the calculations, however this was outside the timeframe of this study.

9.3.5 Magnetic Transition of Fe-S-Si

Throughout the calculations presented in this chapter, the low spin state has not been predicted for any of the temperatures, and therefore the spin crossover in Fe-S-Si has been predicted to reach higher pressures than calculated in Chapter eight, and much above the predicted central pressure of Mercury ($\sim$ 36 GPa, Hauck et al., 2013). As a result of in-

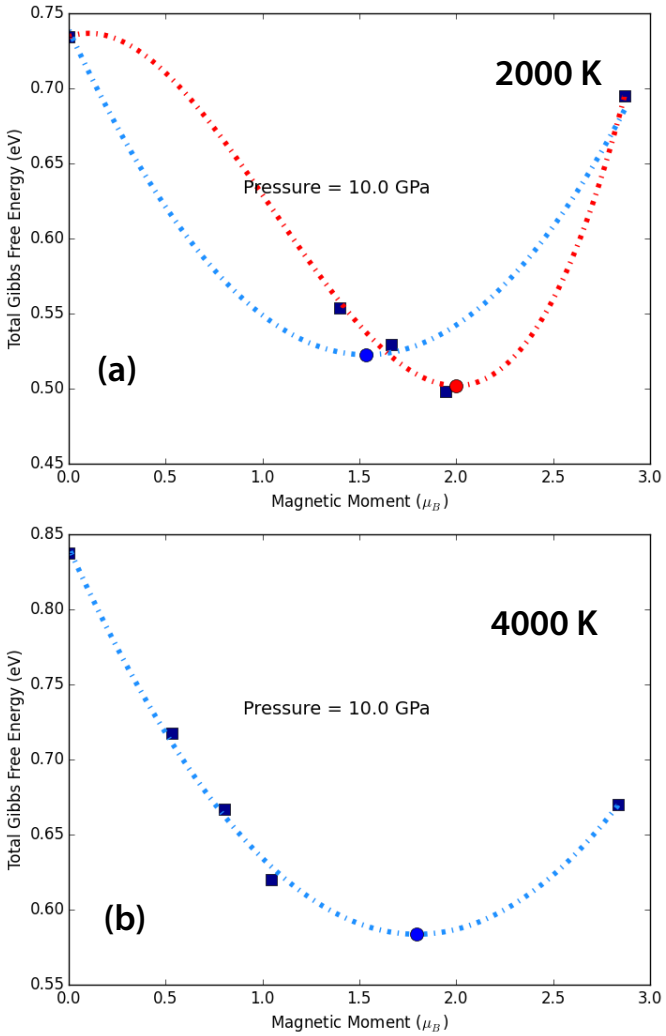

Figure 9.3: Gibbs Free Energy at 10 GPa and 2000 K and 4000 K. The Gibbs free energies of the MS3, MS2, MS1, MS0 and LS moment magnitudes are indicated by blue squares. In (a) at 2000 K, both a second and third order polynomial fit are shown (blue and red dashed lines respectively). The minimum of the fitted parabola (dashed blue line) indicates the preferred mean magnitude of the magnetic moment (blue circle) and the minimum of the third order polynomial is indicated with a red circle. It appears as though the parabolic assumption underestimates the magnitude of the local moment, however a third order fit probably over-fits the results and may produce systematically larger local moments. This is in contrast to the scenario shown in (b) which is also at 10 GPa, but at 4000 K where the parabolic assumption fits very well. Errors shown are a lower bound on the estimated size of the error bar thought to be associated with these calculations; but it is possible that these are much larger than shown and thus may also be a cause of the deviation from the parabolic assumption.

Table 9.2: Δ F relative to the LS state: MS3, MS2, MS1, MS0 (2000 K) using three constraints (MS3) and two constraints (MS2, MS1, MS0)

T (K)	Name	Moment ($\mu_B/atom$)	ΔF (2nd Order)	ΔF (λ = 1 + Grad)
2000	MS3	2.87	0.10	0.04
	MS2	1.94	-	-0.14
	MS1	1.67	-	-0.09
	MS0	1.40	-	-0.06
3000	MS3	2.85	0.21	0.17
	MS2	1.46	-	-0.06
	MS1	1.22	-	-0.04
	MS0	0.95	-	-0.04
4000	MS3	2.84	0.33	0.29
	MS2	1.04	-	-0.03
	MS1	0.80	-	-0.02
	MS0	0.53	-	-0.01

cluding the magnetic entropy, the trend between the magnetic transition and temperature has completely reversed, i.e. in Chapter eight, at increasing temperatures, the magnitude of the local moment decreased, however, in Figure 9.4d, the higher temperature 3000 and 4000 K isotherms suggest a slightly higher magnitude of the local moment, although this may be caused by the deviation in the Gibbs free energies at low temperature in the calculations. In Chapter eight the transition is steeper at 4000 K, and becomes broader at lower temperatures. In Figure 9.4 the broadness of the transition is similar at each temperature and does not appear to significantly differ with increasing temperature. The broad magnetic transition and increase in magnetic moment with increasing temperature of liquid Fe-S-Si is similar to that calculated for pure liquid iron in Chapter 7 (see Appendix D, Figure D.1). In the following section the magnetic transition is used to determine the thermodynamic properties of Fe-S-Si, and investigate the impact the inclusion of magnetic entropy has on the adiabatic gradient.

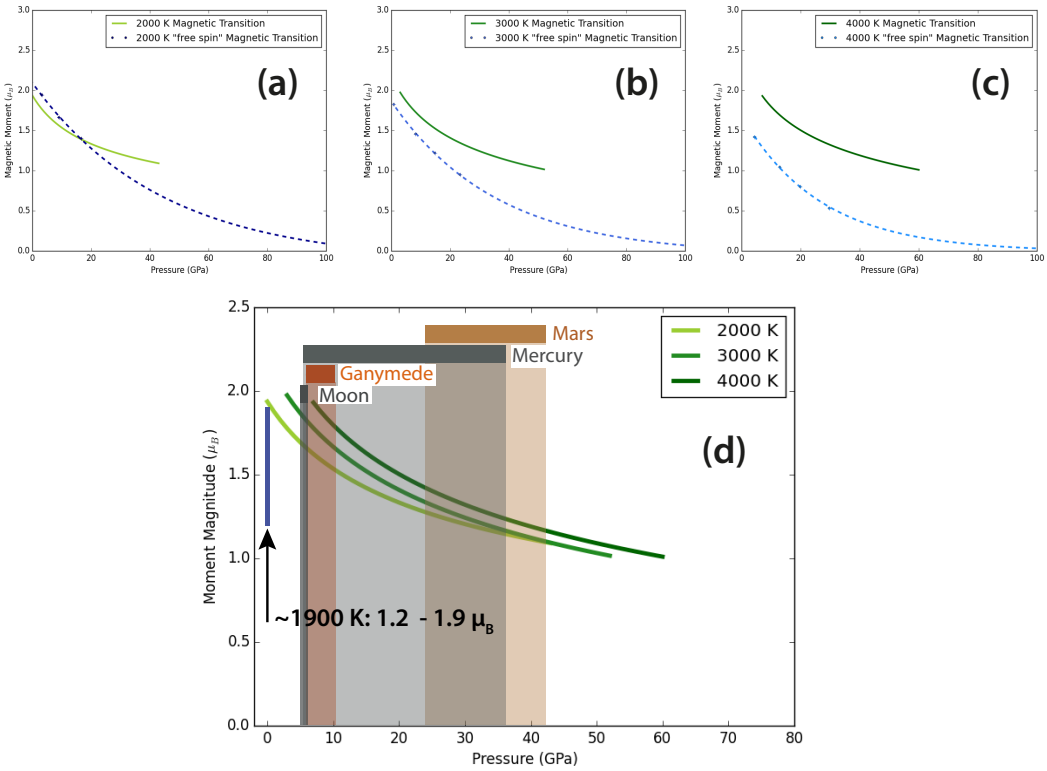

Figure 9.4: The high to low spin transition of $Fe_{0.8}S_{0.1}Si_{0.1}$ found using free energy minimisation, (a) 2000 K, (b) 3000 K, (c) 4000 K and (d) all temperatures. The fitted magnetic transition is shown using the solid green line, to compare the results of Chapter six using "free" spin mixed spin calculations are also shown (blue dashed line with the individual calculations and errors outlined using blue points and capped lines).

9.4 Thermoelastic Properties of Fe-S-Si

9.4.1 The Equation of State

Following the method presented in Chapter seven, at each pressure the volumes corresponding to each spin state (LS, MS0, MS1, MS2 and MS3) were collated to find a relationship between volume and magnetic moment at constant pressure (e.g. Chapter 7, Figure 7.7). The magnetic moment at each pressure was found using the magnetic transition (Figure 9.4), and the corresponding volume recorded. This was repeated for each pressure and temperature and fitted to a BM3EOS to find the equation of state of $Fe_{0.8}S_{0.1}Si_{0.1}$ at 2000, 3000 and 4000 K (Figure 9.5, Table 9.3).

At all pressures and temperatures, the calculated density of $Fe_{0.8}S_{0.1}Si_{0.1}$ is markedly less

than the calculated density of pure liquid iron (Chapter 7; Appendix D, Figure D.2). The calculated density of $Fe_{0.8}S_{0.1}Si_{0.1}$ has decreased relative to the "free" spin calculations (Chapter eight) at 3000 and 4000 K. However, at 2000 K including the magnetic entropy has had the opposite effect and the density has increased (at 5 GPa and 2000 K, "free spin" calculations predict a density of 6757 kg/m^2 whereas in the present chapter the density is 6795 kg/m^2). It is possible that the difference between the two 2000 K equations of state are within error of the density calculated via thermodynamic integration as it has resulted from a series of fits. As described in previous sections, this is also another possible side-effect of the deviation from the parabolic assumption used in Section 9.3.4, as it may have underestimated the magnitude of the atomic moments and thus predicted a smaller volume (and therefore higher density). To investigate this, a further constraint on the parabolic fit to the Gibbs free energy is required, although unfortunately this was outside of the timescale of this work.

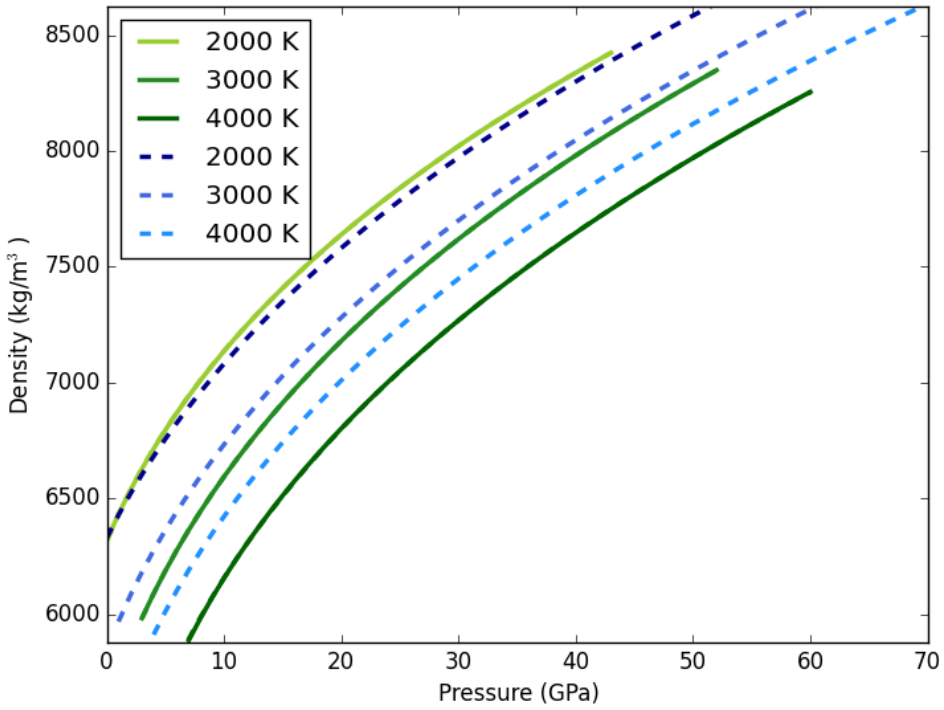

Figure 9.5: The equations of state of $Fe_{0.8}S_{0.1}Si_{0.1}$ at 2000, 3000 and 4000 K (from light to dark green). Dashed blue lines indicates the "free" spin simulations from Chapter eight from 2000 - 4000 K (light to dark blue). The density calculated inclusive of magnetic entropy has decreased relative to Chapter eight at 3000 and 4000 K, but increased at 2000 K.

Table 9.3: Fe-S-Si fitted parameters of the Birch Murnaghan 3rd order equation of state at 2000, 3000, 4000 K

T (K)	V_0 ($\AA^3$/atom)	K_0 (GPa)	K'
2000	13.33	50.43	8.13
3000	15.09	33.71	7.05
4000	17.37	17.08	7.95

9.4.2 The Bulk Modulus and Thermal Expansion

The bulk modulus of $Fe_{0.8}S_{0.1}Si_{0.1}$ was calculated using the analytical derivative of the BM3EOS $P(V)$ expression (e.g. Ita and Stixrude, 1992; Figure 9.6). At 3000 and 4000 K the isothermal bulk moduli calculated including the magnetic entropic term have decreased relative to the "free" spin calculations in Chapter eight (Figure 8.4). Conversely, at 2000 K, the bulk modulus is decreased at low pressures, but is higher than predicted by "free" spin calculations at higher pressures (Figure 9.6). However, at all pressures and temperatures the isothermal bulk moduli are smaller than that calculated for pure liquid iron at the same conditions (Chapter 7; Appendix D, Figure D.3). The isothermal bulk modulus is calculated using the fit to the BM3EOS, and as discussed earlier in this chapter, it is possible that the volumes predicted are underestimated at 2000 K due to the divergence from the parabolic assumption. It is also possible that the divergence from the parabolic assumption is not constant at all pressures which will also impact the bulk modulus trend shown.

The thermal expansion was calculated using equation 2.44 (Chapter two, Section 2.11.2). Figure 9.7 shows two calculations of the mean thermal expansion of $Fe_{0.8}S_{0.1}Si_{0.1}$ between 2000 and 4000 K, firstly using "free" spin calculations (in blue), and secondly calculated using thermodynamic integration (in green). In comparison with the results of Chapter eight, including the magnetic entropy stabilised a larger magnitude of the local moment to higher pressures and has resulted in an increased thermal expansion. The differences between mean thermal expansion calculated in this chapter and that simulated in Chapter eight may be a result of the changes to the magnetic transitions of each temperature, and their effect on the volume of Fe-S-Si. At low pressure, the thermal expansion reported here is larger than calculated for pure liquid iron in Chapter seven (see Appendix D, Figure D.4),

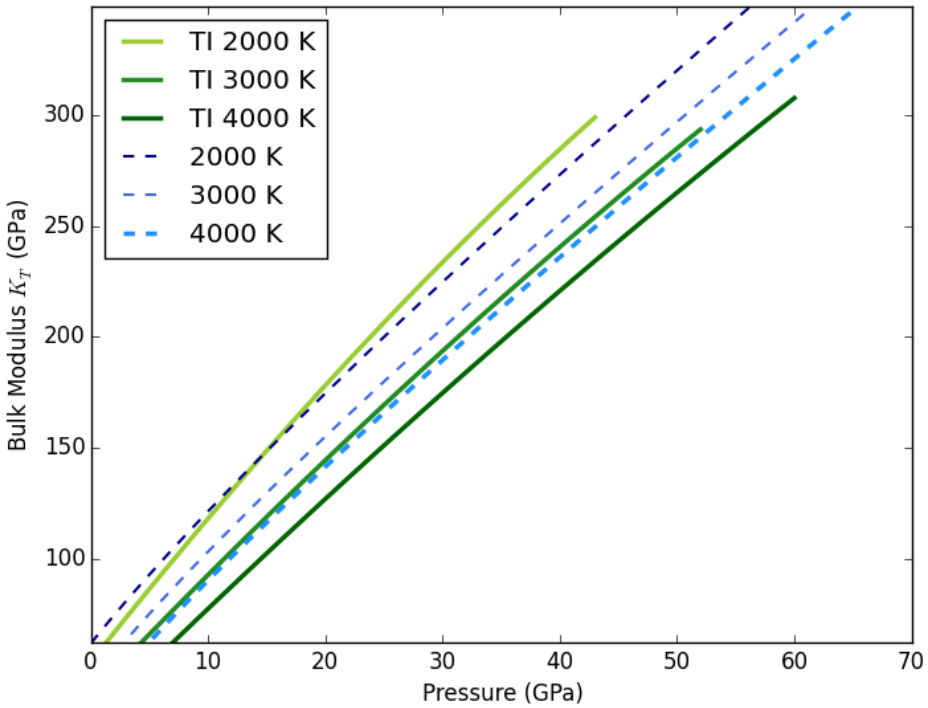

Figure 9.6: The isothermal bulk modulus of Fe-S-Si computed using thermodynamic integration at 2000, 3000 and 4000 K (from light to dark green respectively) compared to the results of Chapter eight, using "free" spin magnetic calculations (indicated by blue dashed lines).

this may be a result of the sulphur in the system as previous studies of liquid Fe-S systems report larger expansivities than measured in pure liquid iron (Williams, 2009).

9.4.3 The Grüneisen Parameter

The Grüneisen parameter has been calculated using the expression defined in Chapter two, equation 2.47. As a result of the methods described in the previous section, the magnetic transition and volume-pressure relationship has been found but in doing so, information on the excess internal energy (that arises from interactions), determined as part of the VASP minimisation routine, has been lost. To calculate the excess internal energy at each volume, the excess internal energy of the largest moment magnitude (MS3), the lowest, LS, and some intermediary magnitude (found in Chapter eight) were used to find a relationship between excess internal energy and the magnitude of the atomic moment. The BM3EOS fit for each isotherm was used to find the pressure, $P(V,T,f)$, at volume, V, and then used to find the

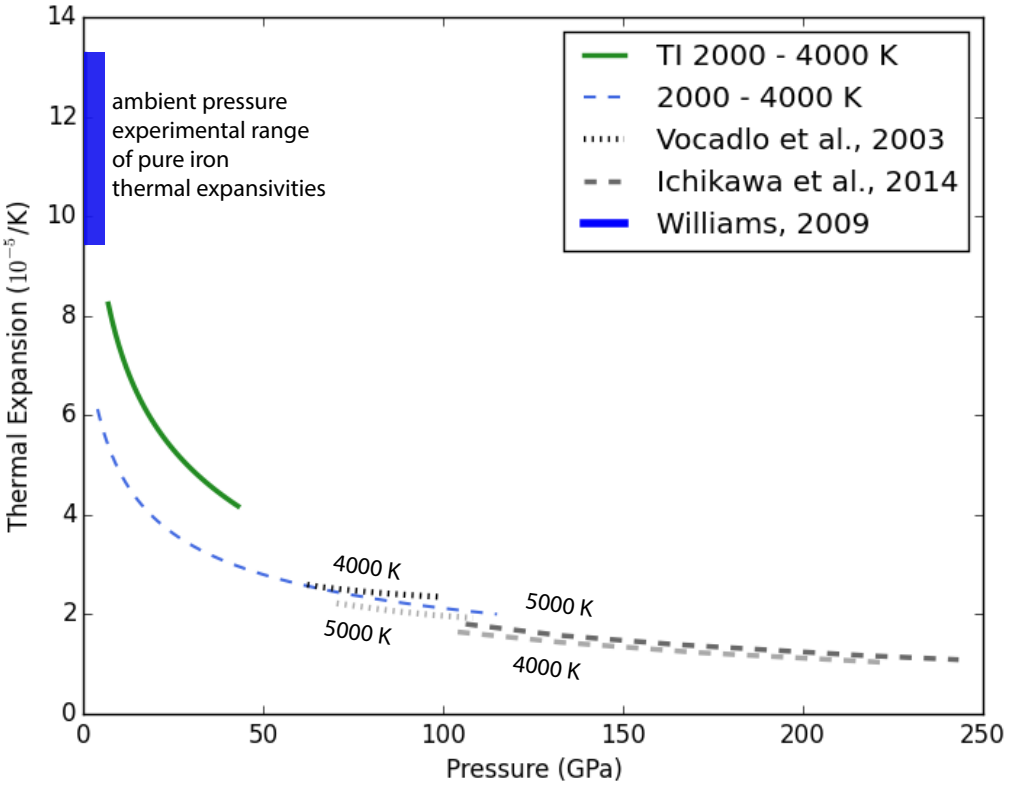

Figure 9.7: The mean thermal expansion between 2000 - 4000 K of Fe-S-Si (green) computed using the refined spin crossover determined using thermodynamic integration. Also shown is the mean thermal expansion between 2000 - 4000 K calculated using "free" spin calculations detailed in Chapter eight (blue). The blue bar indicates the experimental measurements of pure iron thermal expansion from Williams, 2009. The *ab initio* calculations of the thermal expansion of pure liquid iron by Vočadlo et al. (2003) and Ichikawa et al. (2014) are shown by grey and black dashed lines.

correct magnetic moment at said pressure (from the transition calculated in Section 9.3.5). The magnetic moment at pressure, $P(V,T,f)$ was then used to find the corresponding excess internal energy at volume, V.

The excess internal energy for each volume was added to the contribution from the kinetic energy of the nuclei (Chapter 2, equation 2.48) to produce the total internal energy. Using the BM3EOS fits and equation 2.47 (Chapter two) the Grüneisen parameter was calculated for each volume at 3000 K (Figure 9.8). In Chapter 8, Figure 8.6 an initial sharp increase in Grüneisen parameter with pressure is calculated, which flattens out to a shallower, possibly linear relationship, in this chapter, the same initial sharp increase has been calculated, how-

ever the pressure is restricted relative to the results of Chapter eight and thus whether this subsequently flattens is unclear. The magnitude of the Grüneisen parameter calculated here is similar to that calculated for pure liquid iron in Chapter 7 (see Appendix D, Figure D.5), however pure liquid iron appears to plateau at a lower pressure than calculated for Fe-S-Si.

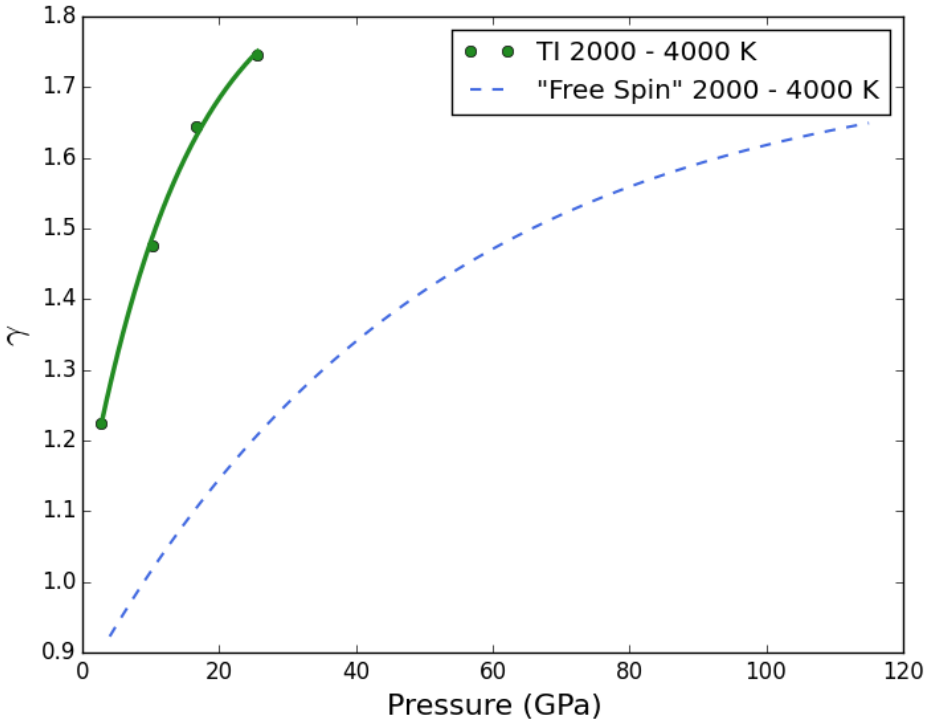

Figure 9.8: The mean Grüneisen parameter of Fe-S-Si between 2000 and 4000 K computed using thermodynamic integration. The line indicates an exponential fit to the calculated Grüneisen parameter at four volumes (represented by filled circles). The solid line indicates the mean Grüneisen parameter and the blue dashed line represents the mean Grüneisen parameter calculated using "free" spin calculations (Chapter eight).

9.5 The Adiabatic Gradient

Using the isothermal bulk modulus at 3000 K and the mean Grüneisen parameter and thermal expansion between 2000 - 4000 K, the adiabatic gradient of $Fe_{0.8}S_{0.1}Si_{0.1}$ has been calculated at 3000 K (Figure 9.9). The adiabatic gradient is higher than that found using "free" spin calculations in Chapter eight and higher than calculated for pure liquid iron in Chapter 7 (see Appendix D, Figure D.6), and may suggest a hypothetical layered Fe-S-Si core of Mercury.

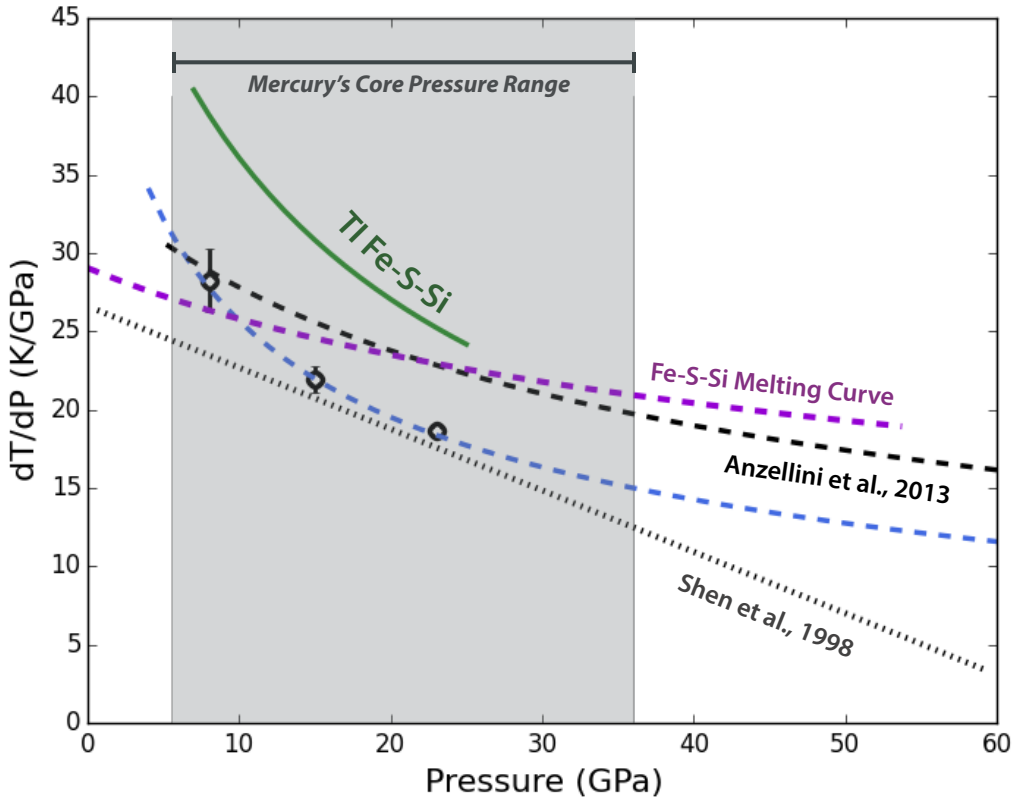

Figure 9.9: The adiabatic gradient of $Fe_{0.8}S_{0.1}Si_{0.1}$ at 3000 K computed using the refined spin crossover (shown by the solid green line). This is compared alongside the adiabatic gradient determined using "free" spin magnetic calculations (Chapter eight; dashed blue line, the black points indicate the individual VASP calculations) and the melting curves of Anzellini et al. (2013) (shown in the thick black dashed line) and Shen et al. (1998) (thin grey dashed line) are also shown alongside the gradient of the Fe-S-Si melting curve measured experimentally in Chapter five (dashed purple line).

The adiabatic gradient calculated via thermodynamic integration suggests a transition between a top-down and a bottom-up crystallisation regime at a higher pressure than predicted previously in Chapter eight. The relative slopes of the adiabatic gradient and Fe-S-Si melting curve in Chapter eight suggested a complicated evolutionary scenario for Mercury's core containing multiple crystallising regions. In contrast to Chapter eight, however, here, the relative shape of the adiabatic gradient of Fe-S-Si and the Fe-S-Si melting curve would result in top-down crystallisation of a hypothetical Fe-S-Si core. Using the modelled temperatures of the core-mantle boundary of Mercury from Rivoldini et al. (2009) which range between 1850 - 2000 K (which also fall within the range of temperatures used by Hauck

et al., 2007), the adiabatic gradient predicted in this chapter would result in temperature estimates for the centre of the core ranging from 2960 - 3110 K and consequently (from the experimental melting curve in Chapter five) still molten.

9.6 Summary

This chapter has calculated the magnetic transition of $Fe_{0.8}S_{0.1}Si_{0.1}$ using free energy minimisation and thermodynamic integration to include the magnetic entropic term into the Helmholtz free energy of the system. The resulting magnetic transition predicts a higher magnitude of the local magnetic moment at all pressures and temperatures and consequently impacts upon all the predicted thermo-elastic properties of Fe-S-Si relative to the results of Chapter eight. The density of Fe-S-Si calculated here relative to the "free" spin calculations in the previous chapter has decreased, suggesting that if Mercury's core consisted of a $Fe_{0.8}S_{0.1}Si_{0.1}$ alloy the density at the core-mantle boundary (i.e. $\sim$ 5 GPa, Hauck et al., 2013) at 2000 K would be 6795 kg/m^3. The magnetic transition calculated in this chapter at 2000, 3000 and 4000 K alongside the "free" energy calculations detailed in Chapter eight have been used to calculate the density and bulk modulus of Fe-S-Si at 2000, 3000 and 4000 K and the mean thermal expansion and Grüneisen parameter between 2000 and 4000 K. These were all combined to find the adiabatic gradient of Fe-S-Si at 3000 K at the conditions of Mercury's core. In comparison with the slope of the melting curve measured experimentally in Chapter five, the adiabatic gradient suggests top-down crystallisation of Mercury's core. In the top-down regime the core adiabat crosses the liquidus at low pressures, thus crystallising the iron out of the mixture at the top of the core. Due to the higher density of the iron "snow" this will sink to lower depths in the core and subsequently remelt, driving convection at depth within the planet. The resulting deep dynamo may then be able to explain the observed weak magnetic field of Mercury (e.g. Christensen, 2006). The crystallising iron will enrich the top of the core in silicon and sulphur and may move the mixture into the immiscible region of the Fe-S-Si phase diagram resulting in a stratified Fe-S layer at the top of the core. Over time, the melting snow will cool the deep core and the system will evolve into a bottom-up crystallising region, growing Mercury's inner core outwards from the centre.

Chapter 10

Conclusions

This thesis has attempted to shed light on the possible structure, composition and evolution of Mercury's core. Due to its dominant abundance in Mercury's interior, the properties of pure liquid iron have been investigated, but the planet's core does not consist of iron alone. So, in addition to pure iron, the same methods were used to study an iron rich mixture containing ten atomic percent sulphur and ten atomic percent silicon.

10.1 Summary of Results

10.1.1 Investigation of Pure Liquid Iron

In Chapters six and seven the thermo-elastic properties of pure liquid iron have been investigated using "free" spin calculations and thermodynamic integration (to include the magnetic entropic contribution to the Helmholtz free energy). Overall, a gradual spin crossover has been found such that the transition from high to low spin is predicted to extend over a far larger pressure range than previously thought, with the transition to low spin possibly occurring at or above $\sim$ 150 GPa, however further calculations would be required to extend the study beyond 150 GPa in order to confirm this transition pressure. Finite atomic moments persisting to such a large pressure will have implications not only for Mercury and the other rocky bodies in the solar system but also for sub-Earth size exoplanets, as it may suggest a high magnetic susceptibility which will impact upon the generation of planetary magnetic fields (Frick et al., 2002). The calculated (using thermodynamic integration) density of liquid iron was found to be higher than experimentally determined values (6800 - 6950 kg/m^3;

Williams, 2009) with a value of 7164 kg/m^3 at 2000 K and 0 GPa. This work has also calculated the mean thermal expansion and mean Grüneisen parameter between 2000 and 4000 K and the isothermal bulk modulus at 2000, 3000 and 4000 K. These together were used to calculate the adiabatic gradient, which, when compared alongside the gradients of published melting curves, can be used to give insight into the evolution and structure of the core of Mercury (see Section 10.2).

10.1.2 Properties of Fe-S-Si

The methods discussed and implemented to study pure liquid iron in Chapters six and seven have also been applied to a more likely composition of Mercury's core, an iron rich mixture of Fe-S-Si (with the relative atomic abundance of 80:10:10; Chapters eight and nine). In a manner similar to that found in Chapter seven, the spin crossover in Fe-S-Si was found to be gradual with a predicted transition to low spin at or above $\sim$ 140 GPa, far exceeding the central pressures of Mercury ($\sim$ 36 GPa, Hauck et al., 2013). The density of $Fe_{0.8}S_{0.1}Si_{0.1}$ has been calculated here to be 6795 kg/m^3 at the approximate conditions of Mercury's core-boundary (5 GPa and 2000 K), significantly less than pure liquid iron at the same conditions (7653 kg/m^3, Chapter seven). The calculated density is, within error, consistent with the results of Hauck et al. (2013) who found a mean core bulk density equal to 6980 $\pm$ 280 kg/m^3. This thesis has also calculated the isothermal bulk modulus of $Fe_{0.8}S_{0.1}Si_{0.1}$ at 2000, 3000 and 4000 K and evaluated the mean thermal expansion and Grüneisen parameter between 2000 - 4000 K. These were then used to calculate the adiabatic gradient of Fe-S-Si, such that it could be compared against the gradient of the liquidus of the same composition (Chapter five). Laser-heated diamond-anvil-cell experiments were conducted both off-line at the University of Bristol Earth Sciences department and *in situ* at the Diamond Light Source in Oxford. A number of measurements were taken which were used alongside the published melting data of Sanloup and Fei (2004) (with the assumption that compositional difference had a negligible effect on melting temperature) to define the solidus and liquidus relationships up to $\sim$ 50 GPa.

10.2 The Evolution of Mercury's Core

10.2.1 Pure Iron

With each chapter in this thesis the predicted evolution of Mercury's core has changed. "Free" spin calculations of a hypothetical pure iron Mercurian core, when compared against the gradient of the recent Anzellini et al. (2013) melting curve of iron, suggest an entirely 'bottom-up' crystallisation, i.e. the growth of a solid inner core from the centre of the planet outwards (as thought to be the regime that governs the evolution of the Earth's inner core). Conversely, when compared against the slope of Shen et al. (1998), a far more complex evolution is predicted, suggesting multiple crystallising regions over the course of the planet's lifetime (e.g. Chapter 6, Figure 6.15). However, the results of Chapter six, the "free" spin calculations of pure liquid iron, neglected the magnetic entropic term in the Helmholtz free energy of the system. This is important as the magnetic entropy is larger for larger atomic moment magnitudes and acts negatively on the Helmholtz free energy and thus it may stabilise the higher spin states to higher temperatures and pressures. Larger moment magnitudes increase the volume and therefore impact upon all of the thermo-elastic properties of the system. This correction was applied in Chapter seven and as a consequence the calculated adiabatic gradient of pure liquid iron increased, resulting in a different predicted evolutionary scenario for Mercury. In particular, comparison with the gradient of the melting curve of Anzellini et al. (2013) suggested a complicated crystallisation regime, as the adiabatic gradient is steeper than the slope of the Anzellini et al. (2013) melting curve at low pressures but becomes the shallower relationship at high pressures (Chapter 7, Figure 7.13). However, the difference between the gradient of the melting curve of Anzellini et al. (2013) and the adiabatic gradient calculated in Chapter seven is marginal (Figure 10.1) and therefore it is possible that because of its greater curvature, both the high-pressure and low-pressure points of the adiabatic curve will cross the liquidus upon cooling. Figure 10.1 indicates that, initially, a pure iron core will begin to crystallise at the top of Mercury's core, but that upon further cooling of the planet, the adiabat will also cross the melting curve at high pressure resulting in both 'bottom-up' and 'top-down' crystallisation regimes occurring simultaneously.

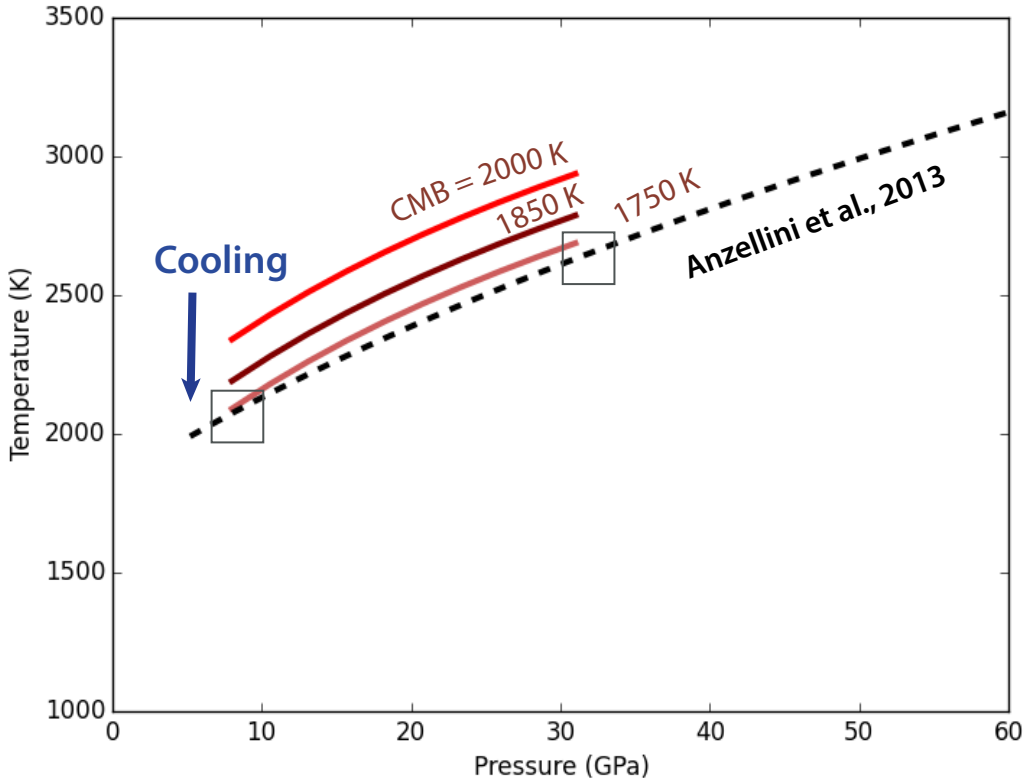

Figure 10.1: The hypothetical pure liquid iron adiabat in Mercury's core. Using the adiabatic gradient calculated in Chapter 7, the theoretical adiabat of Mercury has been estimated using three hypothetical temperatures of planet's core-mantle boundary equal to 2000, 1850 and 1750 K (shades of red). With a core-mantle boundary temperature of 1750 K the adiabat crosses the pure iron melting curve (from Anzellini et al., 2013; dashed back line) at both high and low pressures (indicated by grey boxes).

10.2.2 Fe-S-Si

It is unlikely that the core of Mercury consists of iron alone, instead it is probable that the Mercurian core is made of an iron rich mixture containing light elements in a sufficient abundance to maintain a liquid layer within the planet. In Chapter eight, "free" spin calculations of the adiabatic gradient of $Fe_{0.8}S_{0.1}Si_{0.1}$ in comparison with the slope of the melting curve of Fe-S-Si measured experimentally in Chapter five suggested a 'bottom-up' crystallisation regime deep within the planet. However, as previously discussed, the "free" spin calculations did not account for the magnetic entropy of the system and this was corrected in Chapter nine in which thermodynamic integration and free-energy minimisation were used to map the spin crossover in $Fe_{0.8}S_{0.1}Si_{0.1}$. Including the magnetic entropy increased

the adiabatic gradient of Fe-S-Si such that it lay above the gradient of the Fe-S-Si melting curve at all simulated pressures (Chapter 9, Figure 9.9). In this scenario this suggests total 'top-down' crystallisation of Mercury's core, i.e. initiating crystallisation at the top of the Mercurian core (e.g. Figure 10.2). This is consistent with Dumberry and Rivoldini (2015) who used models of an Fe-FeS alloy in Mercury's core and concluded that a crystallisation scenario involving the formation of iron 'snow' best fitted the geodetic observations of the planet; this is also the regime proposed to be governing the crystallisation of the core of Ganymede (Hauck et al., 2006) and Mars (Stewart et al., 2007).

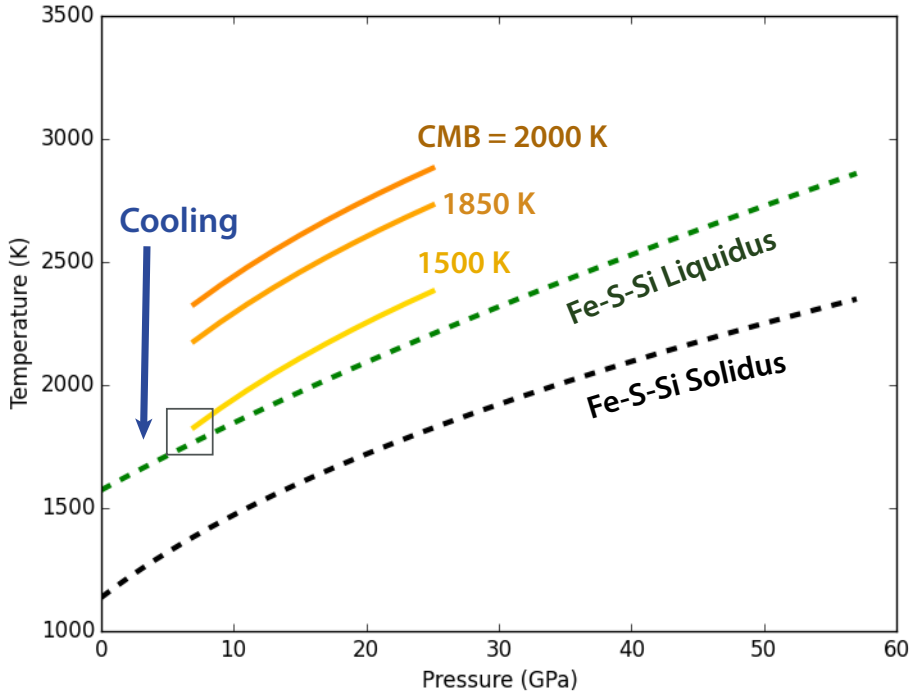

Figure 10.2: The hypothetical Fe-S-Si adiabat in Mercury's core. Using the adiabatic gradient calculated in Chapter 9 the theoretical adiabat of Mercury has been estimated using three hypothetical temperatures of planet's core-mantle boundary equal to 2000, 1850 and 1500 K (shades of orange to yellow). With a core-mantle boundary temperature of 1500 K the adiabat crosses the Fe-S-Si curve (from Chapter five; dashed back line) at low pressures indicating 'top-down' crystallisation in the planet's core (indicated by a grey box).

In the 'top-down' scenario, upon cooling, the adiabat will first cross the liquidus at/near the core-mantle boundary (Figure 10.2). Iron 'snow' will form at the top of the core and due to gravity, precipitate to deeper depths. This will result in the enrichment of the surrounding

liquid in silicon and sulphur (e.g. Chapter 8, Figure 8.9, point 1) which will be buoyantly upwelled as the iron-rich solid sinks. This may explain the presence of Mercury's magnetic field, as chemical buoyancy associated with the iron 'snow' regime may drive a dynamo deep within the planet (e.g. Christensen, 2006). The temperature of the core-mantle boundary region will increase due to the latent heat of crystallisation, and become sub-adiabatic and both thermally and chemically stratified. At greater depths the sinking depleted solid will become superliquidus and remelt, locally increasing the melting temperature. As the top of the core becomes further enriched in silicon and sulphur, the composition may then move into the immiscible region of the Fe-S-Si phase diagram (e.g. Morard and Katsura, 2010), forming two chemically distinct liquids, one silicon enriched and the other sulphur enriched. The sulphur enriched liquid would likely float, which may then have further implications for the generation of the planet's magnetic field (e.g. Cao et al., 2014). As the planet continues to cool, the temperature of the innermost region of Mercury's core (which has become depleted in Si and S relative to the bulk composition) may fall below the liquidus, such that a solid inner core will begin to grow outwards from the centre of the planet. All the while, the crystallising 'snow' regions will continue to extend deeper into the planet, eventually reaching the inner-core boundary. An iron-rich 'snow-forming' region at the top of Mercury's core may explain the observed weak magnetic field, as the deep convecting liquid generating the dynamo will need to diffuse through the conducting stratified layer at the top of the core, reducing the measured field strength (e.g. Christensen, 2006).

10.3 Final Conclusions and Further Work

The aim of this thesis was to investigate Mercury's core structure, composition and evolution. In doing so it has presented a suite of thermo-elastic properties of pure liquid iron and $Fe_{0.8}S_{0.1}Si_{0.1}$, important not only in the modelling of Mercury's interior and magnetic field, but also relevant to the other rocky bodies in the Solar System, notably the Moon, Mars and Ganymede. The same materials and predicted dynamics may also exist in the cores of sub-Earth size exoplanets and so further calculations could extend the study presented here to higher pressures closer to that associated with larger planets. The conclusions drawn in this thesis depend critically on the form of the liquidus (melting curve) and the adiabat; subtle differences in the form of either of these can lead to major differences in the expected core evolution. Hence, further studies are underway to extend the calculations, and the melting

experiments conducted in Chapter five. This work has looked at the influence an Fe-S-Si ternary has on the core of Mercury, but it is likely that other elements exist in the planet's core, e.g. nickel, carbon, oxygen and hydrogen. Performing calculations described in this thesis on more complex iron-rich mixtures may shed further light on the mysterious core of Mercury and further our understanding of the evolution of planetary cores including that of the early Earth.

Appendix A

Convergence Tests

Pure Liquid Iron: k-points

The pure iron k-points were converged with respect to the Brillouin zone sampling. A single step of an *ab initio* molecular dynamics VASP run was conducted with a *2x2x2* grid, a single k-point located at the gamma point and finally located at $\frac{1}{4}\frac{1}{4}\frac{1}{4}$. Tests were run at two volumes (V1,13.54 $\AA^3$/atom and V2, 12.19 $\AA^3$/atom) and converged with respect to the difference between the two volumes. The $\frac{1}{4}\frac{1}{4}\frac{1}{4}$ k-point grid produced values of free energy and pressure closer to the larger *2x2x2* grid.

Table A.1: Pure liquid iron k-points sampling in the Brillouin zone: V1-V2

KPOINT Grid	Free Energy (eV/atom)	Diff (eV/atom)	Pressure (kB)	Diff (kB)
2 x 2 x 2	-0.113258		-117.62	
gamma	-0.103254	0.0100036	-129.34	11.72
$\frac{1}{4}\frac{1}{4}\frac{1}{4}$	-0.115517	-0.00225944	-120.78	3.16

Pure Liquid Iron: energy cut-off

The pure iron energy cut-off was converged with respect to the difference in pressure and energy between two volumes (V1,13.54 $\AA^3$/atom and V2, 12.19 $\AA^3$/atom) within the convergence criterion of $\pm$ 2 GPa, and $\pm$ 5 meV.

Table A.2: Pure liquid iron energy cut-off convergence: V1-V2

ENCUT	Free Energy (eV/atom)	Diff (eV/atom)	Pressure (kB)	Diff (kB)
300	-0.187032088		-235.51	
350	-0.18355804	-0.003474	-209.76	25.75
400	-0.183440176	-0.000179	199.87	9.89
450	-0.182452768	-0.0009874	-200.49	-0.62
500	-0.183697336	0.00124457	-202.74	-2.25
550	-0.182761752	-0.0009356	-214.18	-11.44
600	-0.18385228	0.00109053	211.1	3.08

Fe-S-Si: k-points

The Fe-S-Si k-points were converged with respect to the Brillouin zone sampling. A single step of a *ab initio* molecular dynamics VASP run was conducted with a *2x2x2* grid, a single k-point located at the gamma point and finally located at $\frac{1}{4}\frac{1}{4}\frac{1}{4}$. Tests were run at two volumes and converged with respect to the difference between the two volumes (V1,14.14 $\mathring{A}^3$/atom and V2, 12.73 $\mathring{A}^3$/atom). The $\frac{1}{4}\frac{1}{4}\frac{1}{4}$ k-point grid produced values of free energy and pressure closer to the larger *2x2x2* grid.

Table A.3: Fe-S-Si k-points sampling in the Brillouin zone: V1-V2

KPOINT Grid	Free Energy (eV/atom)	Diff (eV/atom)	Pressure (kB)	Diff (kB)
2 x 2 x 2	-0.019715		-118.17	
gamma	-0.023761	0.004046	-116.85	-1.32
$\frac{1}{4}\frac{1}{4}\frac{1}{4}$	-0.017262	-0.002452	-117.2	-0.97

Fe-S-Si: energy cut-off

The Fe-S-Si energy cut-off was converged with respect to the difference in pressure and energy between two volumes (V1,14.14 $\mathring{A}^3$/atom and V2, 12.73 $\mathring{A}^3$/atom) within the convergence criterion of $\pm$ 2 GPa, and $\pm$ 5 meV.

Table A.4: Fe-S-Si Fe-S-Si energy cut-off convergence: V1-V2

ENCUT	Free Energy (eV/atom)	Diff (eV/atom)	Pressure (kB)	Diff (kB)
400	-0.144577838		-139.29	
500	-0.143981126	0.000596712	-141.25	-1.96
600	-0.143883013	0.000148113	-141.3	0.05
700	-0.143926407	-9.33937 x 10^{-5}	-141.13	-0.17
800	-0.143936886	-2.0479 x 10^{-5}	-141.23	0.1

Appendix B

Pressures and Volumes: Chapter Seven and Nine Supplementary Information

Table B.1: The volumes and pressures computed from *ab initio* molecular dynamics calculations of pure liquid iron at the MS3 spin state.

Temperature (K)	Volume ($Å^3$/atom)	Total Pressure (GPa)	Error ($\pm$ GPa)
2000	14.898	-2.712	0.001
	13.544	7.107	0.001
	12.189	24.678	0.001
	11.512	35.802	0.017
	10.835	55.602	0.016
3000	14.898	3.261	0.002
	13.544	13.582	0.002
	12.189	32.048	0.002
	11.512	46.418	0.004
	10.835	64.887	0.007
4000	14.898	8.123	0.002
	13.544	19.637	0.001
	12.189	38.979	0.002
	11.512	53.857	0.004
	10.835	73.845	0.006

Table B.2: The volumes and pressures computed from *ab initio* molecular dynamics calculations of pure liquid iron at the LS spin state.

Temperature (K)	Volume ($\AA^3$/atom)	Total Pressure (GPa)	Error ($\pm$ GPa)
2000	13.544	-14.388	0.003
	12.189	-6.860	0.002
	11.512	1.220	0.002
	10.835	13.113	0.004
	8.126	138.683	0.005
3000	13.544	-8.056	0.004
	12.189	1.914	0.003
	11.512	11.024	0.007
	10.835	23.526	0.003
	8.126	154.638	0.004
4000	13.544	-1.558	0.005
	12.189	10.051	0.003
	11.512	19.471	0.003
	10.835	32.885	0.004
	8.126	162.235	0.033

Table B.3: The volumes and pressures computed from *ab initio* molecular dynamics calculations of Fe-S-Si at the MS3 spin state.

Temperature (K)	Volume ($\AA^3$/atom)	Total Pressure (GPa)	Error ($\pm$ GPa)
2000	15.556	-2.050	0.006
	14.142	4.705	0.002
	12.728	17.640	0.003
	12.021	28.235	0.002
	11.314	43.489	0.003
3000	15.556	2.603	0.010
	14.142	10.403	0.002
	12.728	24.795	0.001
	12.021	36.156	0.004
	11.314	52.087	0.005
4000	15.556	7.196	0.005
	14.142	16.186	0.002
	12.728	31.262	0.003
	12.021	43.020	0.003
	11.314	60.197	0.002

Table B.4: The volumes and pressures computed from *ab initio* molecular dynamics calculations of Fe-S-Si at the LS spin state.

Temperature (K)	Volume ($\AA^3$/atom)	Total Pressure (GPa)	Error ($\pm$ GPa)
2000	14.142	-6.080	0.003
	12.728	-3.517	0.005
	12.021	2.147	0.003
	11.314	10.634	0.003
	8.485	115.768	0.001
3000	14.142	-4.048	0.003
	12.728	3.411	0.003
	12.021	10.306	0.002
	11.314	19.843	0.004
	8.485	124.335	0.018
4000	14.142	0.789	0.002
	12.728	9.807	0.005
	12.021	17.619	0.003
	11.314	28.663	0.004
	8.485	139.194	0.003

Appendix C

Density of States of Fe-S-Si and Pure Liquid Iron

In Figure C.1 the density of states for both the up and down spins are shown for Fe-S-Si (blue) and pure liquid iron (orange), calculated using "free" spin calculations (for more details on the calculations see Chapters 6 and 8). The peak height at the Fermi level is larger for Fe-S-Si, and therefore, following the Stoner criterion, indicates that the iron in the Fe-S-Si mixture might maintain a larger moment magnitude than pure liquid iron (see Chapter 8).

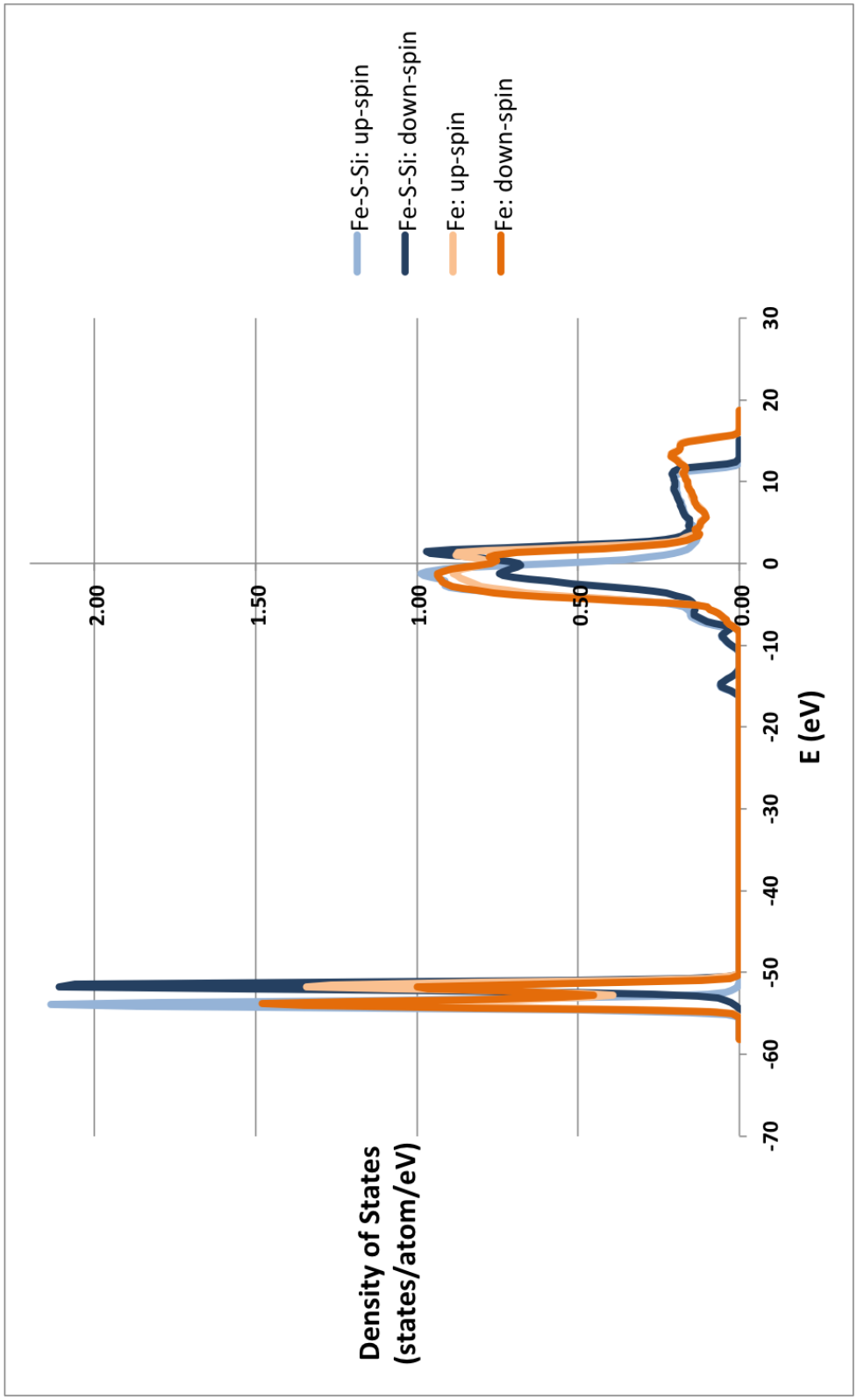

Figure C.1: The up-spin and down-spin densities of state of pure liquid iron (light and dark orange respectively) and $Fe_{0.8}S_{0.1}Si_{0.1}$ (light and dark blue respectively). The densities of states for each material are a snapshot taken from within the equilibrated region of the simulations described in Chapters 6 and 8.

Appendix D

The Properties of Pure Iron and Fe-S-Si

The properties of pure liquid iron and liquid $Fe_{0.8}S_{0.1}Si_{0.1}$ have been calculated in Chapters 7 and 9 using a combination of 'free spin' calculations and thermodynamic integration. Figures D.1 - D.5 show the results of Chapters 7 and 9 (pure liquid iron and $Fe_{0.8}S_{0.1}Si_{0.1}$) for comparison.

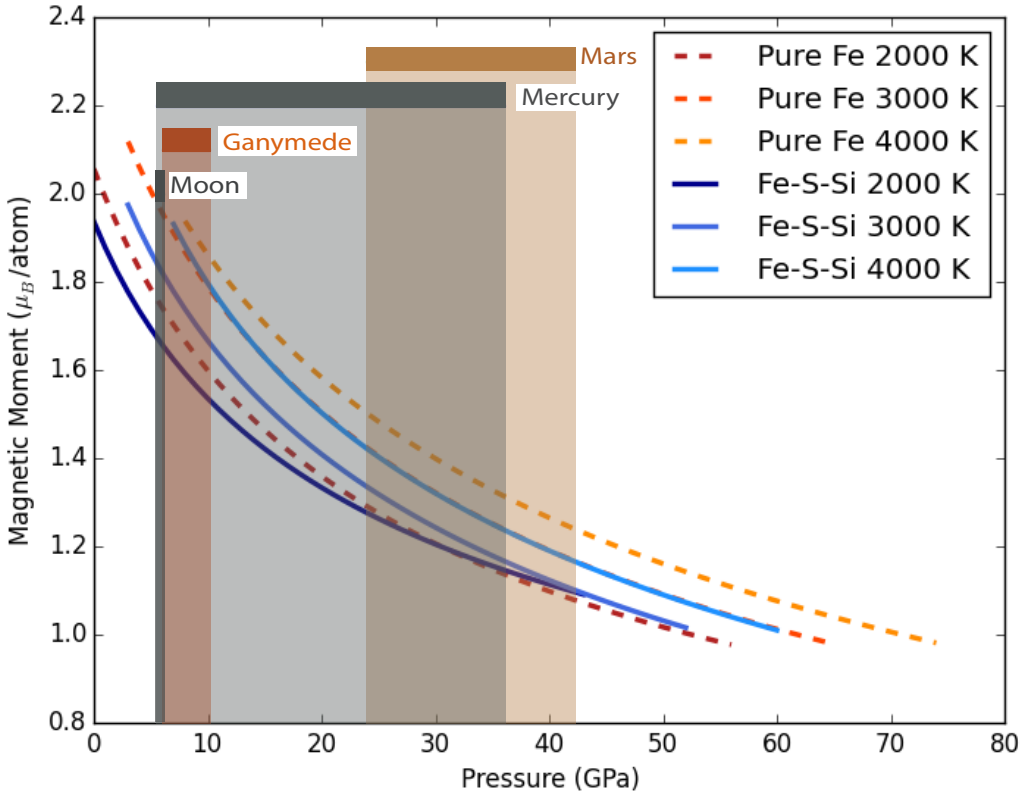

Figure D.1: The magnetic transition of $Fe_{0.8}S_{0.1}Si_{0.1}$ (solid blue lines) and pure liquid iron (dashed orange lines) as calculated in Chapters 7 and 9.

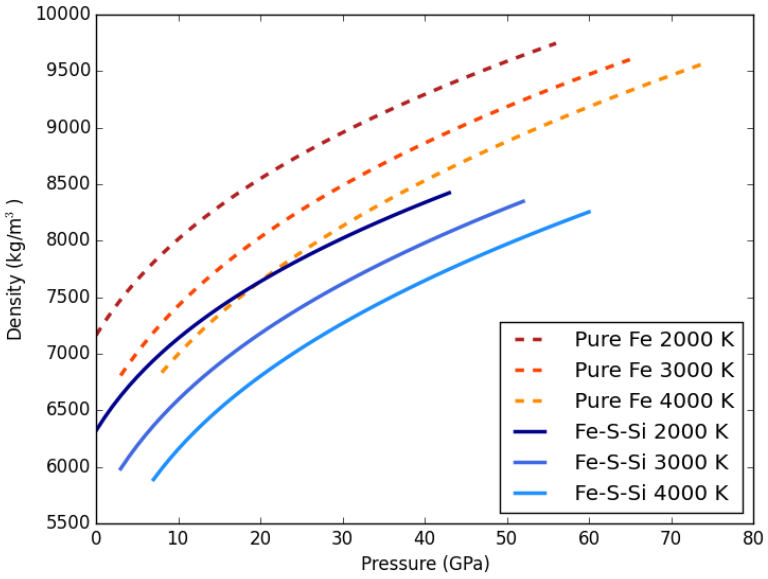

Figure D.2: The equations of state of $Fe_{0.8}S_{0.1}Si_{0.1}$ (solid blue lines) and pure liquid iron (dashed orange lines) as calculated in Chapters 7 and 9.

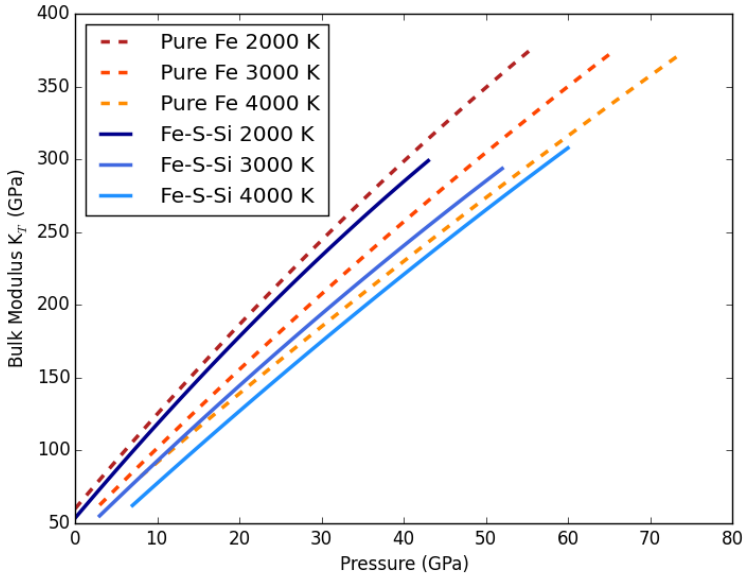

Figure D.3: The isothermal bulk moduli of $Fe_{0.8}S_{0.1}Si_{0.1}$ (solid blue lines) and pure liquid iron (dashed orange lines) as calculated in Chapters 7 and 9.

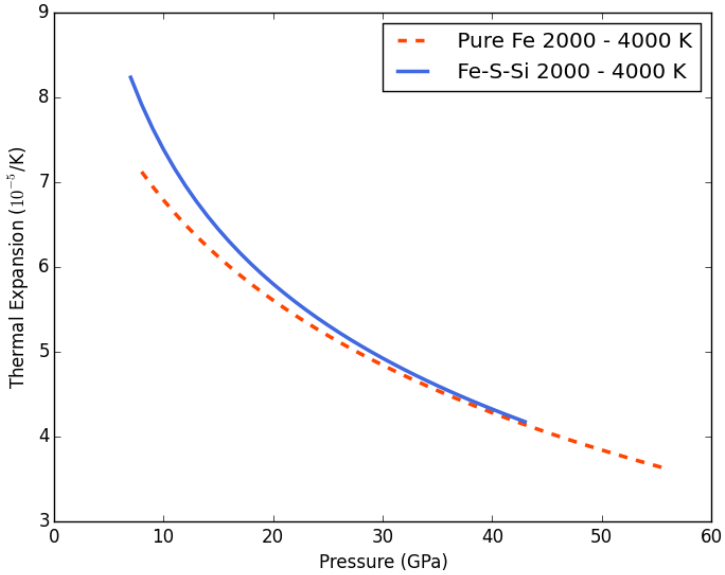

Figure D.4: The thermal expansion of $Fe_{0.8}S_{0.1}Si_{0.1}$ (solid blue lines) and pure liquid iron (dashed orange lines) as calculated in Chapters 7 and 9.

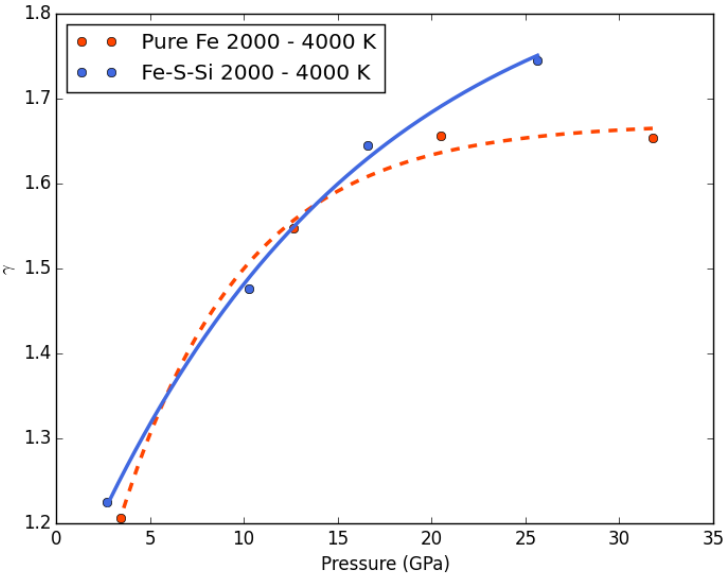

Figure D.5: The mean Grüneisen parameter of $Fe_{0.8}S_{0.1}Si_{0.1}$ (solid blue line) and pure liquid iron (dashed orange line) between 2000 and 4000 K computed using thermodynamic integration in Chapters 7 and 9.

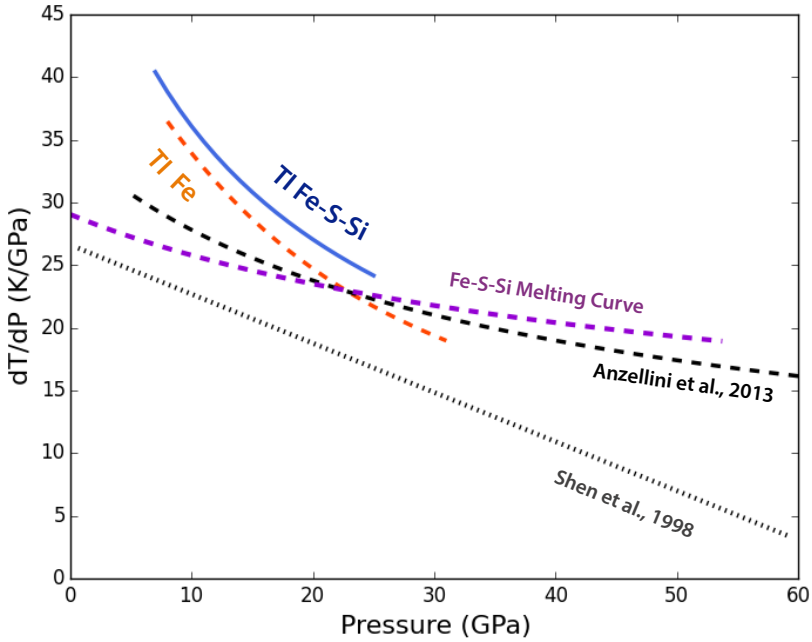

Figure D.6: The adiabatic gradient of $Fe_{0.8}S_{0.1}Si_{0.1}$ (solid blue line) and pure liquid iron (dashed orange line) as calculated in Chapters 7 and 9.

Appendix E

The Radial Distribution Function of Fe-S-Si

In Chapter 7 the radial distribution function is used to determine the state of the calculation and confirm that the $Fe_{0.8}S_{0.1}Si_{0.1}$ is liquid and that the sulphur and silicon atoms have not clustered. Additionally, the Fe-Fe interaction have been used to investigate wether any structural changes have occurred as was found in the pure iron liquid in Chapter 6.

In Figure E.1 the radial distribution functions of the Fe-Fe, Si-Si, S-S, Fe-Si, Fe-S and Si-S interactions are shown at 2000 K and -3 GPa. The Fe-Fe, Fe-Si and Fe-S peaks are distinct but due their is noise in all other peaks shown, to improve this would require longer simulations times which was not possible within the timeframe of this work. All of the g(r) functions of each pattern shown tend to one, this in addition to the snapshot shown in Chapter 8 indicates that the sulphur and silicon atoms did not cluster as if they had the g(r) function would tend to values less than one.

The radial distribution functions were also be used to investigate wether any structural changes occurred in the Fe-Fe interactions as was calculated in pure liquid fe in Chapter 6 (Figure E.2). With increasing pressure the shape of the 2nd neighbour peak becomes distinctly non-gaussian and shifts to shorter distances. This is consistent with that calculated in Chapter 6 for pure liquid iron and may indicate that a structural change is occurring with increasing pressure.

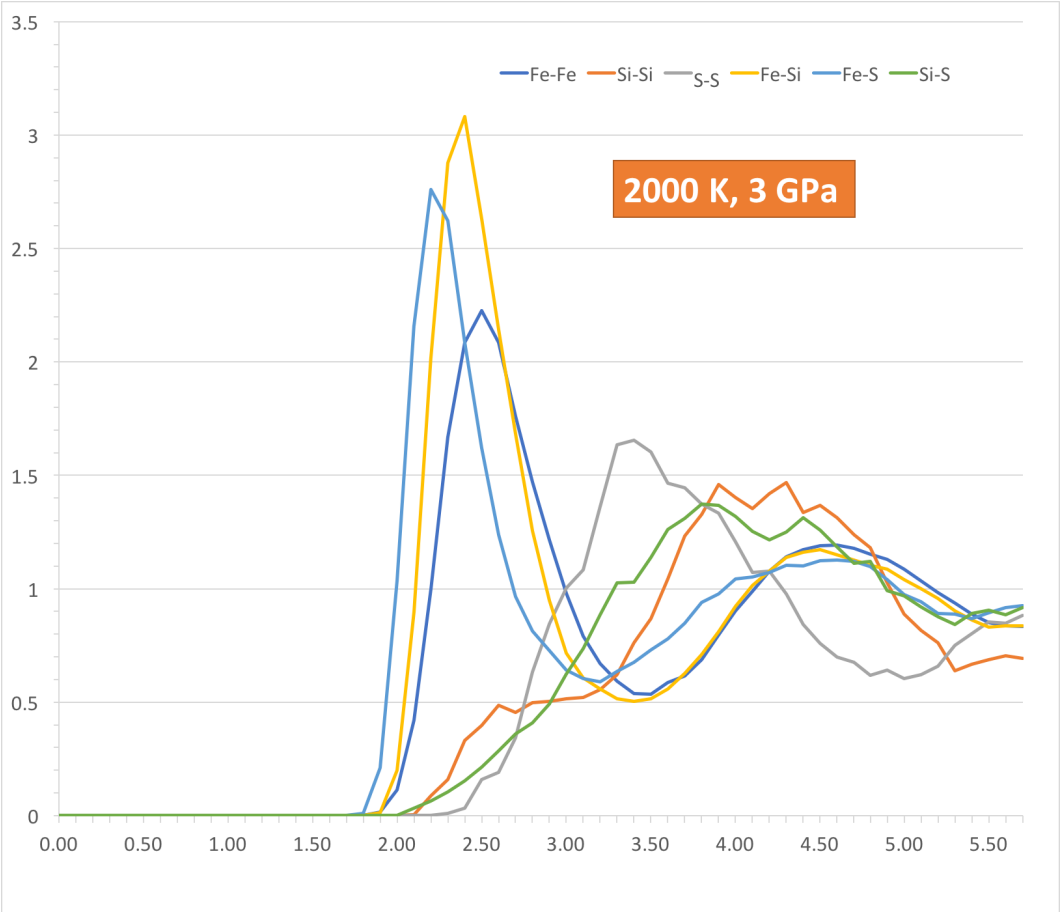

Figure E.1: The radial distribution function of $Fe_{0.8}S_{0.1}Si_{0.1}$ at 2000 K and 3 GPa. The Fe-Fe interactions are outlines in dark blue, Fe-Si in yellow, Fe-S in light blue, Si-Si in red, S-S in grey and Si-S in green.

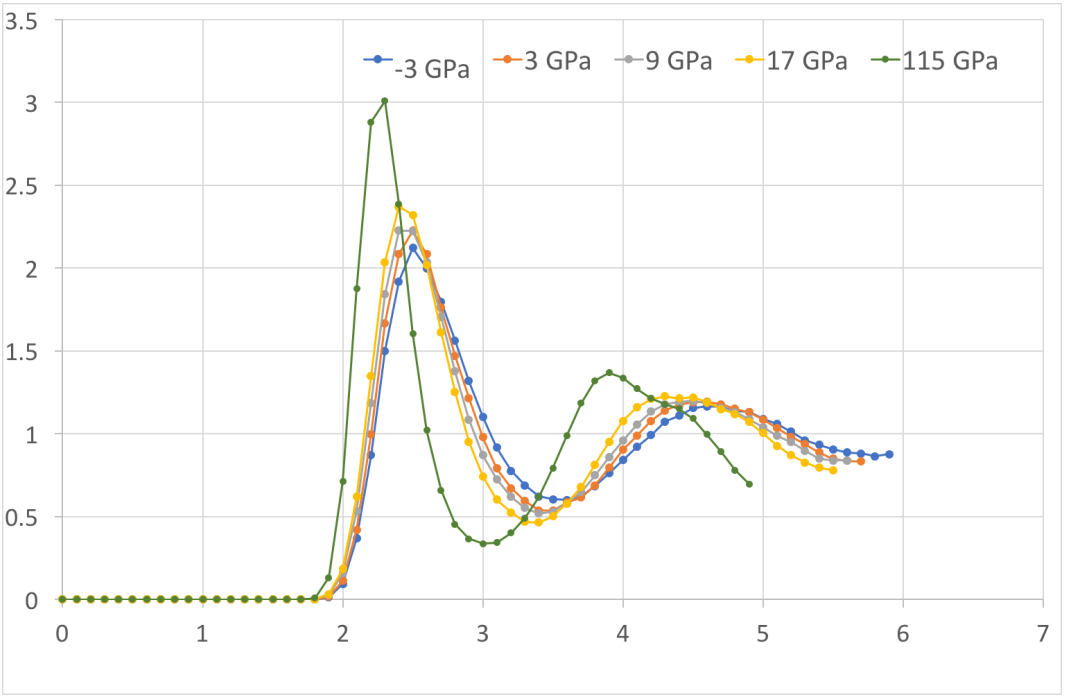

Figure E.2: The radial distribution function of Fe-Fe within the $Fe_{0.8}S_{0.1}Si_{0.1}$ alloy at 2000 K and pressures from -3 - 115 GPa (blue to green respectively). The Fe-Fe interactions are outlined in varying colours (as outlined in the figure). With increasing pressure the shape of the 2nd neighbour peak becomes distinctly non-gaussian which may suggest a structural change in the liquid as was also calculated in Chapter 6.

References

M. Abdellahi, M. Bahmanpour, and M. Bahmanpour. The use of artificial bee colony algorithm to speed up the nanopowders synthesis during high energy ball milling. *Powder Technology*, 264:61–70, sep 2014. ISSN 00325910. doi: 10.1016/j.powtec.2014.05.014.

D. Alfè. Temperature of the inner-core boundary of the Earth: Melting of iron at high pressure from first-principles coexistence simulations. *Phys. Rev. B*, 79(6):60101, feb 2009. doi: 10.1103/PhysRevB.79.060101.

D. Alfè, M. J. Gillan, and G. D. Price. Composition and temperature of the Earth's core constrained by combining ab initio calculations and seismic data. *Earth and Planetary Science Letters*, 195(12):91–98, 2002a. ISSN 0012-821X. doi: http://dx.doi.org/10.1016/S0012-821X(01)00568-4.

D. Alfè, G. D. Price, and M. J. Gillan. Iron under Earth's core conditions: Liquid-state thermodynamics and high-pressure melting curve from *ab initio* calculations. *Phys. Rev. B*, 65(16):165118, apr 2002b. doi: 10.1103/PhysRevB.65.165118.

B. J. Anderson, C. L. Johnson, H. Korth, M. E. Purucker, R. M. Winslow, J. A. Slavin, S. C. Solomon, R. L. McNutt, J. M. Raines, and T. H. Zurbuchen. The Global Magnetic Field of Mercury from MESSENGER Orbital Observations. *Science*, 333(6051):1859–1862, sep 2011.

B. J. Anderson, C. L. Johnson, H. Korth, R. M. Winslow, J. E. Borovsky, M. E. Purucker, J. A. Slavin, S. C. Solomon, M. T. Zuber, and R. L. McNutt. Low-degree structure in Mercury's planetary magnetic field. *Journal of Geophysical Research: Planets*, 117 (E12), dec 2012. ISSN 01480227. doi: 10.1029/2012JE004159.

J. D. Anderson, G. Colombo, P. B. Esposito, E. L. Lau, and G. B. Trager. The mass, gravity

field, and ephemeris of Mercury. *Icarus*, 71(3):337–349, 1987. ISSN 10902643. doi: 10.1016/0019-1035(87)90033-9.

W. W. Anderson and T. J. Ahrens. An equation of state for liquid iron and implications for the Earth's core. *Journal of Geophysical Research: Solid Earth*, 99(B3):4273–4284, 1994. ISSN 2156-2202. doi: 10.1029/93JB03158.

D. Andrault, G. Fiquet, M. Kunz, F. Visocekas, and D. Häusermann. The Orthorhombic Structure of Iron: An in Situ Study at High-Temperature and High-Pressure. *Science*, 278(5339):831–834, oct 1997.

R. J. Angel, J. Gonzalez-Platas, and M. Alvaro. EosFit7c and a Fortran module (library) for equation of state calculations. *Zeitschrift fur Kristallographie*, 229(5):405–419, 2014. ISSN 00442968. doi: 10.1515/zkri-2013-1711.

D. Antonangeli, G. Morard, N. C. Schmerr, T. Komabayashi, M. Krisch, G. Fiquet, and Y. Fei. Toward a mineral physics reference model for the Moon's core. *Proceedings of the National Academy of Sciences*, 112(13):3916–3919, mar 2015. doi: 10.1073/pnas.1417490112.

S. Anzellini, A. Dewaele, M. Mezouar, P. Loubeyre, and G. Morard. Melting of iron at Earth's inner core boundary based on fast X-ray diffraction. *Science (New York, N.Y.)*, 340(6131):464–6, apr 2013. ISSN 1095-9203. doi: 10.1126/science.1233514. URL http://science.sciencemag.org/content/340/6131/464.

G. Aquilanti, A. Trapananti, A. Karandikar, I. Kantor, C. Marini, O. Mathon, S. Pascarelli, and R. Boehler. Melting of iron determined by X-ray absorption spectroscopy to 100 GPa. *Proceedings of the National Academy of Sciences*, 112(39):12042–12045, sep 2015. doi: 10.1073/pnas.1502363112.

H. Asanuma, E. Ohtani, T. Sakai, H. Terasaki, S. Kamada, N. Hirao, N. Sata, and Y. Ohishi. Phase relations of Fe-Si alloy up to core conditions: Implications for the Earth inner core. *Geophysical Research Letters*, 35(12), 2008. ISSN 1944-8007. doi: 10.1029/2008GL033863.

H. Asanuma, E. Ohtani, T. Sakai, H. Terasaki, S. Kamada, T. Kondo, and T. Kikegawa.

Melting of iron–silicon alloy up to the core–mantle boundary pressure: implications to the thermal structure of the Earth's core. *Physics and Chemistry of Minerals*, 37(6): 353–359, 2010. ISSN 1432-2021. doi: 10.1007/s00269-009-0338-7.

E. Asphaug and A. Reufer. Mercury and other iron-rich planetary bodies as relics of inefficient accretion. *Nature Geosci*, 7(8):564–568, aug 2014. ISSN 1752-0894.

M. J. Assael, K. Kakosimos, R. M. Banish, J. Brillo, I. Egry, R. Brooks, P. N. Quested, K. C. Mills, A. Nagashima, Y. Sato, and W. A. Wakeham. Reference Data for the Density and Viscosity of Liquid Aluminum and Liquid Iron. *Journal of Physical and Chemical Reference Data*, 35(1), 2006.

A. Baldereschi. Mean-value point in the Brillouin zone. *Physical Review B*, 7(12):5212–5215, 1973. ISSN 01631829. doi: 10.1103/PhysRevB.7.5212.

W. A. Bassett and M. S. Weathers. Stability of the body-centered cubic phase of iron: A thermodynamic analysis. *Journal of Geophysical Research*, 95(B13):21709, 1990. ISSN 0148-0227. doi: 10.1029/JB095iB13p21709.

A. D. Becke. Density-functional exchange-energy approximation with correct asymptotic behavior. *Phys. Rev. A*, 38(6):3098–3100, sep 1988. doi: 10.1103/PhysRevA.38.3098.

F. Birch. Finite elastic strain of cubic crystals. *Physical Review*, 71(11):809–824, 1947. ISSN 0031899X. doi: 10.1103/PhysRev.71.809.

F. Birch. Finite strain isotherm and velocities for single-crystal and polycrystalline NaCl at high pressures and 300K. *Journal of Geophysical Research: Solid Earth*, 83(B3): 1257–1268, 1978. ISSN 2156-2202. doi: 10.1029/JB083iB03p01257.

M. Birkholz, P. F. Fewster, and C. Genzel. *Thin Film Analysis by X-Ray Scattering*. 2006. ISBN 3-527-31052-5.

P. E. Blöchl. Projector augmented-wave method. *Phys. Rev. B*, 50(24):17953–17979, dec 1994. doi: 10.1103/PhysRevB.50.17953.

R. Boehler. The phase diagram of iron to 430 kbar. *Geophysical Research Letters*, 13(11): 1153–1156, 1986. ISSN 1944-8007. doi: 10.1029/GL013i011p01153.

R. Boehler. Temperatures in the Earth's core from melting-point measurements of iron at high static pressures. *Nature*, 363(6429):534–536, jun 1993.

R. Boehler, D. Santamaría-Pérez, D. Errandonea, and M. Mezouar. Melting, density, and anisotropy of iron at core conditions: new x-ray measurements to 150 GPa. *Journal of Physics: Conference Series*, 121(2):22018, 2008.

M. Born and J. R. Oppenheimer. Born-Oppenheimer approximation. *Ann. Phys. (Leipzig)*, 84:457, 1927.

D. Breuer, S. A. Hauck, M. Buske, M. Pauer, and T. Spohn. Interior Evolution of Mercury. *Space Science Reviews*, 132(2):229–260, 2007. ISSN 1572-9672. doi: 10.1007/s11214-007-9228-9.

D. Breuer, T. Rueckriemen, and T. Spohn. Iron snow, crystal floats, and inner-core growth: modes of core solidification and implications for dynamos in terrestrial planets and moons. *Progress in Earth and Planetary Science*, 2(1):39, 2015. ISSN 2197-4284. doi: 10.1186/s40645-015-0069-y. URL http://dx.doi.org/10.1186/s40645-015-0069-y.

J. M. Brown and R. G. McQueen. Phase transitions, Grüneisen parameter, and elasticity for shocked iron between 77 GPa and 400 GPa. *Journal of Geophysical Research: Solid Earth*, 91(B7):7485–7494, 1986. ISSN 2156-2202. doi: 10.1029/JB091iB07p07485.

P. K. Byrne, C. Klimczak, A. M. Celal Sengor, S. C. Solomon, T. R. Watters, and I. I. Hauck Steven A. Mercury's global contraction much greater than earlier estimates. *Nature Geosci*, 7(4):301–307, apr 2014. ISSN 1752-0894.

H. Cao, J. M. Aurnou, J. Wicht, W. Dietrich, K. M. Soderlund, and C. T. Russell. A dynamo explanation for Mercury's anomalous magnetic field. *Geophysical Research Letters*, 41 (12):4127–4134, jun 2014. ISSN 00948276. doi: 10.1002/2014GL060196.

P. Cassen, R. E. Young, G. Schubert, and R. T. Reynolds. Implications of an internal dynamo for the thermal history of Mercury. *Icarus*, 28(4):501–508, 1976. ISSN 0019-1035. doi: http://dx.doi.org/10.1016/0019-1035(76)90123-8.

N. L. Chabot, E. A. Wollack, R. L. Klima, and M. E. Minitti. Experimental constraints on

Mercury's core composition. *Earth and Planetary Science Letters*, 390:199–208, mar 2014. ISSN 0012-821X. doi: http://dx.doi.org/10.1016/j.epsl.2014.01.004.

B. Chen, J. Li, and S. A. Hauck. Non-ideal liquidus curve in the Fe-S system and Mercury's snowing core. *Geophysical Research Letters*, 35(7), apr 2008. ISSN 00948276. doi: 10.1029/2008GL033311.

U. R. Christensen. A deep dynamo generating Mercury/'s magnetic field. *Nature*, 444 (7122):1056–1058, dec 2006. ISSN 0028-0836.

M. Cococcioni and S. de Gironcoli. Linear response approach to the calculation of the effective interaction parameters in the LDA+U method. *Phys. Rev. B*, 71(3):35105, jan 2005. doi: 10.1103/PhysRevB.71.035105.

M. L. Cohen and V. Heine. The Fitting of Pseudopotentials to Experimental Data and Their Subsequent Application. *Solid State Physics - Advances in Research and Applications*, 24(C):37–248, 1970. ISSN 00811947. doi: 10.1016/S0081-1947(08)60070-3.

J. E. Connerney and N. F. Ness. Mercury's Magnetic Field and Interior. In *Mercury*, pages 494–513. 1988.

G. Di Achille, C. Popa, M. Massironi, E. Mazzotta Epifani, M. Zusi, G. Cremonese, and P. Palumbo. Mercury's radius change estimates revisited using MESSENGER data. *Icarus*, 221(1):456–460, sep 2012. ISSN 00191035. doi: 10.1016/j.icarus.2012.07.005.

M. Dumberry and A. Rivoldini. Mercury's inner core size and core-crystallization regime. *Icarus*, 248:254–268, mar 2015. ISSN 00191035. doi: 10.1016/j.icarus.2014.10.038.

R. P. Feynman. Forces in Molecules. *Phys. Rev.*, 56(4):340–343, aug 1939. doi: 10.1103/PhysRev.56.340.

R. A. Fischer, A. J. Campbell, R. Caracas, D. M. Reaman, P. Dera, and V. B. Prakapenka. Equation of state and phase diagram of Fe-16Si alloy as a candidate component of Earth's core. *Earth and Planetary Science Letters*, 357-358:268–276, dec 2012. ISSN 0012821X. doi: 10.1016/j.epsl.2012.09.022. Reprinted from Earth and Planetary Science Letters, 373, Rebecca A. Fischer, Andrew J. Campbell, Razvan Caracas, Daniel M. Reaman, Przymyslaw Dera, Vitali B. Prakapenka, Equation of state and phase diagram

of Fe-16Si alloy as a candidate component of Earth's core, 268 - 276, Copyright 2012, with permission from Elsevier.

R. A. Fischer, A. J. Campbell, D. M. Reaman, N. A. Miller, D. L. Heinz, P. Dera, and V. B. Prakapenka. Phase relations in the Fe-FeSi system at high pressures and temperatures. *Earth and Planetary Science Letters*, 373:54–64, jul 2013. ISSN 0012-821X. doi: http://dx.doi.org/10.1016/j.epsl.2013.04.035. Reprinted from Earth and Planetary Science Letters, 373, Rebecca A. Fischer, Andrew J. Campbell, Daniel M. Reaman, Noah A. Miller, Dion L. Heinz, Przymyslaw Dera, Vitali B. Prakapenka, Phase relations in the Fe-FeSi system at high pressures and temperatures, 54 - 64, Copyright 2013, with permission from Elsevier.

H. Flyvbjerg and H. G. Petersen. Error estimates on averages of correlated data. *The Journal of Chemical Physics*, 91(1):461–466, 1989.

V. Fock. Naherungsmethode zur Losung des quantenmechanischen Mehrkorperproblems. *Zeitschrift fur Physik*, 61(1-2):126–148, 1930. ISSN 14346001. doi: 10.1007/BF01340294.

R. A. Forman, G. J. Piermarini, J. D. Barnett, and S. Block. Pressure Measurement Made by the Utilization of Ruby Sharp-Line Luminescence. *Science*, 176(4032):284–285, apr 1972.

P. Frick, S. Khripchenko, S. Denisov, D. Sokoloff, and J.-F. Pinton. Effective magnetic permeability of a turbulent fluid with macroferroparticles. *The European Physical Journal B - Condensed Matter and Complex Systems*, 25(4):399–402, 2002. ISSN 1434-6036. doi: 10.1140/epjb/e20020044.

M. J. Gillan. The virtual matter laboratory. *Contemporary Physics*, 38(2):115–130, 1997. ISSN 0010-7514. doi: 10.1080/001075197182450.

M. Grott, D. Breuer, and M. Laneuville. Thermo-chemical evolution and global contraction of mercury. *Earth and Planetary Science Letters*, 307(1-2):135–146, jul 2011. ISSN 0012821X. doi: 10.1016/j.epsl.2011.04.040.

E. Grüneisen. Theorie des festen Zustandes einatomiger Elemente. *Annalen der Physik*, 344(12):257–306, 1912. ISSN 1521-3889. doi: 10.1002/andp.19123441202.

H. Harder. Sulfur in Mercury's Core? *Icarus*, 151(1):118–122, may 2001. ISSN 00191035. doi: 10.1006/icar.2001.6586.

S. A. Hauck, J. M. Aurnou, and A. J. Dombard. Sulfur's impact on core evolution and magnetic field generation on Ganymede. *Journal of Geophysical Research: Planets*, 111 (E9), 2006. ISSN 2156-2202. doi: 10.1029/2005JE002557.

S. A. Hauck, S. C. Solomon, and D. A. Smith. Predicted recovery of Mercury's internal structure by MESSENGER. *Geophysical Research Letters*, 34(18), 2007. ISSN 1944-8007. doi: 10.1029/2007GL030793.

S. A. Hauck, J.-L. Margot, S. C. Solomon, R. J. Phillips, C. L. Johnson, F. G. Lemoine, E. Mazarico, T. J. McCoy, S. Padovan, S. J. Peale, M. E. Perry, D. E. Smith, and M. T. Zuber. The curious case of Mercury's internal structure. *Journal of Geophysical Research: Planets*, 118(6):1204–1220, jun 2013. ISSN 21699097. doi: 10.1002/jgre.20091.

S. A. Hauck II, A. J. Dombard, R. J. Phillips, and S. C. Solomon. Internal and tectonic evolution of Mercury. *Earth and Planetary Science Letters*, 222(3-4):713–728, jun 2004. ISSN 0012821X. doi: 10.1016/j.epsl.2004.03.037.

D. L. Heinz and R. Jeanloz. Temperature Measurements in the Laser-Heated Diamond Cell. In *High-Pressure Research in Mineral Physics: A Volume in Honor of Syun-iti Akimoto*, pages 113–127. American Geophysical Union, 1987. ISBN 9781118664124. doi: 10.1029/GM039p0113.

H. Hellman. Einführung in die Quantenchemie. In *Einführung in die Quantenchemie.*, page 285. 1937.

P. Hohenberg and W. Kohn. Inhomogeneous Electron Gas. *Phys. Rev.*, 136(3B):B864—-B871, nov 1964. doi: 10.1103/PhysRev.136.B864.

J. Holloway and B. J. Wood. *Simulating the earth : experimental geochemistry*. 1988. ISBN 0-04-552023-2.

E. Holmström and L. Stixrude. Spin crossover in ferropericlase from first-principles molecular dynamics. *Physical review letters*, 114(11):117202, 2015. ISSN 0031-9007. doi: https://doi.org/10.1103/PhysRevLett.114.117202.

H. Ichikawa, T. Tsuchiya, and Y. Tange. The P-V-T equation of state and thermodynamic properties of liquid iron. *Journal of Geophysical Research: Solid Earth*, 119(1):240–252, jan 2014. ISSN 21699313. doi: 10.1002/2013JB010732.

T. K. Irifune and T. Pressure generation to 125 GPa using a 6-8-2 type multianvil apparatus with nano-polycrystalline diamond anvils. *Journal of Physics: Conference Series*, 215 (1):12190, 2010. ISSN 1742-6596.

J. Ita and L. Stixrude. Petrology, elasticity, and composition of the mantle transition zone. *Journal of Geophysical Research: Solid Earth*, 97(B5):6849–6866, 1992. ISSN 2156-2202. doi: 10.1029/92JB00068.

J. M. Jackson, W. Sturhahn, M. Lerche, J. Zhao, T. S. Toellner, E. E. Alp, S. V. Sinogeikin, J. D. Bass, C. A. Murphy, and J. K. Wicks. Melting of compressed iron by monitoring atomic dynamics. *Earth and Planetary Science Letters*, 362:143–150, jan 2013. ISSN 0012-821X. doi: http://dx.doi.org/10.1016/j.epsl.2012.11.048.

A. Jain, G. Hautier, S. P. Ong, C. J. Moore, C. C. Fischer, K. A. Persson, and G. Ceder. Formation enthalpies by mixing GGA and GGA + U calculations. *Phys. Rev. B*, 84(4): 45115, jul 2011. doi: 10.1103/PhysRevB.84.045115.

A. Jayaraman. Diamond anvil cell and high-pressure physical investigations. *Rev. Mod. Phys.*, 55:65–108, Jan 1983. doi: 10.1103/RevModPhys.55.65. URL http://link.aps.org/doi/10.1103/RevModPhys.55.65.

B. Johannes, C. Kaestner, P. E. Blöchl, J. Kästner, C. Först, and S. Yip. Electronic Structure Methods: Augmented Waves, Pseudopotentials and The Projector Augmented Wave Method. In *Handbook of Materials Modeling*, pages 93–119. 2005.

C. L. Johnson, R. J. Phillips, M. E. Purucker, B. J. Anderson, P. K. Byrne, B. W. Denevi, J. M. Feinberg, S. A. Hauck, J. W. Head, H. Korth, P. B. James, E. Mazarico, G. A. Neumann, L. C. Philpott, M. A. Siegler, N. A. Tsyganenko, and S. C. Solomon. Low-

altitude magnetic field measurements by MESSENGER reveal Mercury's ancient crustal field. *Science*, 348(6237):892–895, may 2015.

W. Kaula. The interiors of the terrestrial planets : their structure and evolution. In M. G. Kivelson, editor, *The Solar System*, pages 78–93. 1986.

J. Kirkwood. Statistical Mechanics of Fluid Mixtures. *The Journal of chemical physics*, 3 (5):300, 1935. ISSN 0021-9606.

S. Klotz, Y. Le Godec, T. Strässle, and U. Stuhr. The $\alpha\gamma\varepsilon$ triple point of iron investigated by high pressurehigh temperature neutron scattering. *Applied Physics Letters*, 93(9), 2008. doi: http://dx.doi.org/10.1063/1.2976128.

J. S. Knibbe and W. van Westrenen. The interior configuration of planet Mercury constrained by moment of inertia and planetary contraction. *Journal of Geophysical Research: Planets*, 120(11):1904–1923, 2015. ISSN 2169-9100. doi: 10.1002/2015JE004908.

W. Kohn and L. J. Sham. Self-Consistent Equations Including Exchange and Correlation Effects. *Phys. Rev.*, 140(4A):A1133—-A1138, nov 1965. doi: 10.1103/PhysRev.140.A1133.

T. Komabayashi and Y. Fei. Internally consistent thermodynamic database for iron to the Earth's core conditions. *Journal of Geophysical Research: Solid Earth*, 115(B3), 2010. ISSN 2156-2202. doi: 10.1029/2009JB006442.

T. Komabayashi, Y. Fei, Y. Meng, and V. Prakapenka. In-situ X-ray diffraction measurements of the γ-ε transition boundary of iron in an internally-heated diamond anvil cell. *Earth and Planetary Science Letters*, 282(14):252–257, may 2009. ISSN 0012-821X. doi: http://dx.doi.org/10.1016/j.epsl.2009.03.025.

G. Kresse and J. Furthmüller. Efficiency of ab-initio total energy calculations for metals and semiconductors using a plane-wave basis set. *Computational Materials Science*, 6 (1):15–50, 1996a. ISSN 09270256. doi: 10.1016/0927-0256(96)00008-0.

G. Kresse and J. Furthmüller. Efficient iterative schemes for ab initio total-energy calcu-

lations using a plane-wave basis set. *Physical Review B*, 54(16):11169–11186, 1996b. ISSN 0163-1829. doi: 10.1103/PhysRevB.54.11169.

G. Kresse and J. Hafner. Ab Initio Molecular Dynamics of Liquid Metals, 1993. ISSN 01631829.

G. Kresse and J. Hafner. Ab initio molecular-dynamics simulation of the liquid-metalamorphous-semiconductor transition in germanium. *Physical Review B*, 49(20): 14251–14269, 1994. ISSN 0163-1829. doi: 10.1103/PhysRevB.49.14251.

G. Kresse and D. Joubert. From Ultrasoft Pseudopotentials to the Projector Augmented Wave Method. *Phys. Rev. B*, 59(3):1758–1775, 1999. ISSN 1098-0121. doi: 10.1103/PhysRevB.59.1758.

A. Le Bail, H. Duroy, and J. L. Fourquet. Ab-initio structure determination of LiSbWO6 by X-ray powder diffraction. *Materials Research Bulletin*, 23(3):447–452, 1988. ISSN 0025-5408. doi: http://dx.doi.org/10.1016/0025-5408(88)90019-0.

J. S. Lewis. Metal/silicate fractionation in the solar system. *Earth and Planetary Science Letters*, 15(3):286–290, jul 1972. ISSN 0012821X. doi: 10.1016/0012-821X(72)90174-4.

R. C. Liebermann. Multi-anvil, high pressure apparatus: a half-century of development and progress. *High Pressure Research*, 31(4):493–532, dec 2011. ISSN 0895-7959. doi: 10.1080/08957959.2011.618698.

L.-G. Liu and W. A. Bassett. The melting of iron up to 200 kbar. *Journal of Geophysical Research*, 80(26):3777–3782, 1975. ISSN 2156-2202. doi: 10.1029/JB080i026p03777.

O. T. Lord, M. J. Walter, R. Dasgupta, D. Walker, and S. M. Clark. Melting in the FeC system to 70 GPa. *Earth and planetary science letters*, 284(1):157–167, 2009. ISSN 0012-821X.

O. T. Lord, M. J. Walter, D. P. Dobson, L. Armstrong, S. M. Clark, and A. Kleppe. The FeSi phase diagram to 150 GPa. *Journal of Geophysical Research: Solid Earth*, 115(B6), 2010. ISSN 2156-2202. doi: 10.1029/2009JB006528.

O. T. Lord, E. T. H. Wann, S. A. Hunt, A. M. Walker, J. Santangeli, M. J. Walter, D. P. Dobson, I. G. Wood, L. Vočadlo, G. Morard, and M. Mezouar. The NiSi melting curve to 70GPa. *Physics of the Earth and Planetary Interiors*, 233:13–23, 2014a. ISSN 00319201. doi: 10.1016/j.pepi.2014.05.005.

O. T. Lord, I. G. Wood, D. P. Dobson, L. Vočadlo, W. Wang, A. R. Thomson, E. T. H. Wann, G. Morard, M. Mezouar, and M. J. Walter. The melting curve of Ni to 1 Mbar. *Earth and Planetary Science Letters*, 408:226–236, dec 2014b. ISSN 0012-821X. doi: http://dx.doi.org/10.1016/j.epsl.2014.09.046.

S.-N. Luo and T. J. Ahrens. Shock-induced superheating and melting curves of geophysically important minerals. *Physics of the Earth and Planetary Interiors*, 143144:369–386, 2004. ISSN 0031-9201. doi: http://dx.doi.org/10.1016/j.pepi.2003.04.001.

Y. Ma, M. Somayazulu, G. Shen, H.-k. Mao, J. Shu, and R. J. Hemley. In situ X-ray diffraction studies of iron to Earth-core conditions. *Physics of the Earth and Planetary Interiors*, 143144:455–467, jun 2004. ISSN 0031-9201. doi: http://dx.doi.org/10.1016/j.pepi.2003.06.005.

V. Malavergne, M. Tarrida, R. Combes, H. Bureau, J. Jones, and C. Schwandt. New high-pressure and high-temperature metal/silicate partitioning of U and Pb: Implications for the cores of the Earth and Mars. *Geochimica et Cosmochimica Acta*, 71(10):2637–2655, may 2007. ISSN 0016-7037. doi: http://dx.doi.org/10.1016/j.gca.2007.03.011.

V. Malavergne, M. J. Toplis, S. Berthet, and J. Jones. Highly reducing conditions during core formation on Mercury: Implications for internal structure and the origin of a magnetic field. *Icarus*, 206(1):199–209, mar 2010. ISSN 0019-1035. doi: http://dx.doi.org/10.1016/j.icarus.2009.09.001.

H. K. Mao, J. Xu, and P. M. Bell. Calibration of the ruby pressure gauge to 800 kbar under quasi-hydrostatic conditions. *Journal of Geophysical Research*, 91(B5):4673, 1986. ISSN 0148-0227. doi: 10.1029/JB091iB05p04673.

J. L. Margot, S. J. Peale, R. F. Jurgens, M. A. Slade, and I. V. Holin. Large Longitude Libration of Mercury Reveals a Molten Core. *Science*, 316(5825):710–714, may 2007.

J.-L. Margot, S. J. Peale, S. C. Solomon, S. A. Hauck, F. D. Ghigo, R. F. Jurgens, M. Yseboodt, J. D. Giorgini, S. Padovan, and D. B. Campbell. Mercury's moment of inertia from spin and gravity data. *Journal of Geophysical Research: Planets*, 117(E12), dec 2012. ISSN 01480227. doi: 10.1029/2012JE004161.

K. Momma and F. Izumi. VESTA for three-dimensional visualization of crystal, volumetric and morphology data. *Journal of Applied Crystallography*, 44(6):1272–1276, dec 2011. doi: 10.1107/S0021889811038970.

G. Morard and T. Katsura. Pressure-temperature cartography of FeSSi immiscible system. *Geochimica et Cosmochimica Acta*, 74(12):3659–3667, jun 2010. ISSN 0016-7037. doi: 10.1016/j.gca.2010.03.025.

G. Morard, C. Sanloup, B. Guillot, G. Fiquet, M. Mezouar, J. P. Perrillat, G. Garbarino, K. Mibe, T. Komabayashi, and K. Funakoshi. In situ structural investigation of Fe-S-Si immiscible liquid system and evolution of Fe-S bond properties with pressure. *Journal of Geophysical Research: Solid Earth*, 113(B10), 2008. ISSN 2156-2202. doi: 10.1029/2008JB005663.

G. Morard, D. Andrault, N. Guignot, J. Siebert, G. Garbarino, and D. Antonangeli. Melting of Fe–Ni–Si and Fe–Ni–S alloys at megabar pressures: implications for the core–mantle boundary temperature. *Physics and Chemistry of Minerals*, 38(10):767–776, 2011. ISSN 1432-2021. doi: 10.1007/s00269-011-0449-9.

G. Morard, D. Andrault, D. Antonangeli, and J. Bouchet. Properties of iron alloys under the earth's core conditions. *Comptes Rendus - Geoscience*, 346(5-6):130–139, 2014. ISSN 16310713.

F. D. Murnaghan. Finite Deformations of an Elastic Solid. *American Journal of Mathematics*, 59(2):235–260, 1937. ISSN 00029327, 10806377. doi: 10.2307/2371405.

NASA. MErcury Surface, Space ENvironment, GEochemistry and Ranging (MESSENGER), 2014. URL http://www.nasa.gov/directorates/heo/scan/services/missions/solarsystem/MESSENGER.html. Last visited 18/11/2016.

NASA. Labelled Diagram of Mariner 10, 2016. URL http://nssdc.gsfc.nasa.gov/image/spacecraft/mariner10.gif. Last visited 18/11/2016.

NASA/Johns Hopkins University Applied Physics Laboratory/Carnegie Institution of Washington. Ridges and Cliffs on Mercury's Surface, 2008. URL http://www.nasa.gov/mission_pages/messenger/multimedia/ridges_craters.html. Last visited 13/06/16.

NASA/Johns Hopkins University Applied Physics Laboratory/Carnegie Institution of Washington. Colour Composite Image of Mercury, 2013. URL http://www.nasa.gov/multimedia/imagegallery/image_feature_2455.html. Last visited 10/06/2016.

NASA/JPL. Mercury Magnetosphere, 2013. URL http://solarsystem.nasa.gov/galleries/mercury-magnetosphere. Last visited 13/06/16.

NASA/JPL/Caltech. How Was Mercury Made?, 2011. URL http://www.nasa.gov/mission_pages/messenger/multimedia/messenger_orbit_image20110929_7.html. Last visited 13/06/16.

N. Ness. The magnetic field of Mercury. *Physics of the Earth and Planetary Interiors*, 20 (2-4):209–217, nov 1979. ISSN 00319201. doi: 10.1016/0031-9201(79)90044-X.

N. F. Ness, K. W. Behannon, R. P. Lepping, Y. C. Whang, and K. H. Schatten. Magnetic Field Observations near Mercury: Preliminary Results from Mariner 10. *Science*, 185 (4146):151–160, 1974. ISSN 00368075, 10959203.

N. F. Ness, K. W. Behannon, R. P. Lepping, and Y. C. Whang. The magnetic field of Mercury, 1. *Journal of Geophysical Research*, 80(19):2708–2716, jul 1975. ISSN 01480227. doi: 10.1029/JA080i019p02708.

J. H. Nguyen and N. C. Holmes. Melting of iron at the physical conditions of the Earth's core. *Nature*, 427(6972):339–342, jan 2004. ISSN 0028-0836.

L. R. Nittler, R. D. Starr, S. Z. Weider, T. J. McCoy, W. V. Boynton, D. S. Ebel, C. M. Ernst, L. G. Evans, J. O. Goldsten, D. K. Hamara, D. J. Lawrence, R. L. McNutt, C. E. Schlemm, S. C. Solomon, and A. L. Sprague. The Major-Element Composition of Mercury's Surface from MESSENGER X-ray Spectrometry. *Science*, 333(6051):1847–1850, sep 2011.

S. Nosé. A unified formulation of the constant temperature molecular dynamics methods. *The Journal of Chemical Physics*, 81(1), 1984.

S. Odenbach. Recent progress in magnetic fluid research. *Journal of Physics: Condensed Matter*, 16(32):R1135, 2004.

Online Dictionary of Crystallography (IUCr). Structure Factor, 2008. URL http://reference.iucr.org/dictionary/Structure_factor. Last visited 13/06/16.

S. J. Peale. Does Mercury have a molten core? *Nature*, 262(5571):765–766, aug 1976.

P. N. Peplowski, L. G. Evans, S. A. Hauck, T. J. McCoy, W. V. Boynton, J. J. Gillis-Davis, D. S. Ebel, J. O. Goldsten, D. K. Hamara, D. J. Lawrence, R. L. McNutt, L. R. Nittler, S. C. Solomon, E. A. Rhodes, A. L. Sprague, R. D. Starr, and K. R. Stockstill-Cahill. Radioactive Elements on Mercury's Surface from MESSENGER: Implications for the Planet's Formation and Evolution. *Science*, 333(6051):1850–1852, sep 2011.

J. Perdew, J. Chevary, S. Vosko, K. Jackson, M. Pederson, D. Singh, and C. Fiolhais. Erratum: Atoms, molecules, solids, and surfaces: Applications of the generalized gradient approximation for exchange and correlation. *Physical Review B*, 48(7):4978–4978, 1993. ISSN 0163-1829. doi: 10.1103/PhysRevB.48.4978.2.

J. P. Perdew. Density-functional approximation for the correlation energy of the inhomogeneous electron gas. *Phys. Rev. B*, 33(12):8822–8824, jun 1986. doi: 10.1103/PhysRevB.33.8822.

J. P. Perdew and A. Zunger. Self-interaction correction to density-functional approximations for many-electron systems. *Physical Review B*, 23(10):5048–5079, 1981. ISSN 01631829. doi: 10.1103/PhysRevB.23.5048.

J. P. Perdew, J. A. Chevary, S. H. Vosko, K. A. Jackson, M. R. Pederson, D. J. Singh, and C. Fiolhais. Atoms, Molecules, Solids, and Surfaces - Applications of the Generalized Gradient Approximation for Exchange and Correlation. *Phys. Rev. B*, 46(11):6671–6687, 1992. ISSN 0163-1829. doi: 10.1103/PhysRevB.46.6671.

J. C. Phillips. Energy-Band Interpolation Scheme Based on a Pseudopotential. *Phys. Rev.*, 112(3):685–695, nov 1958. doi: 10.1103/PhysRev.112.685.

W. E. Pickett. Pseudopotential methods in condensed matter applications. *Computer Physics Reports*, 9(3):115–197, 1989. ISSN 0167-7977. doi: 10.1016/0167-7977(89)90002-6.

J. P. Poirier. *Introduction to the Physics of the Earth's Interior*. Cambridge University Press, 2000. ISBN 9780521663922.

P. Pulay. Ab initio calculation of force constants and equilibrium geometries in polyatomic molecules. *Molecular Physics*, 17(2):197–204, 1969. doi: 10.1080/00268976900100941.

H. M. Rietveld. Line profiles of neutron powder-diffraction peaks for structure refinement. *Acta Crystallographica*, 22(1):151–152, jan 1967. doi: 10.1107/S0365110X67000234.

H. M. Rietveld. A profile refinement method for nuclear and magnetic structures. *Journal of Applied Crystallography*, 2(2):65–71, jun 1969. doi: 10.1107/S0021889869006558.

M. A. Riner, C. R. Bina, M. S. Robinson, and S. J. Desch. Internal structure of Mercury: Implications of a molten core. *Journal of Geophysical Research: Planets*, 113(E8), 2008. ISSN 2156-2202. doi: 10.1029/2007JE002993.

A. Rivoldini and T. Van Hoolst. The interior structure of Mercury constrained by the low-degree gravity field and the rotation of Mercury. *Earth and Planetary Science Letters*, 377-378:62–72, sep 2013. ISSN 0012821X. doi: 10.1016/j.epsl.2013.07.021.

A. Rivoldini, T. Van Hoolst, and O. Verhoeven. The interior structure of Mercury and its core sulfur content. *Icarus*, 201(1):12–30, may 2009. ISSN 00191035. doi: 10.1016/j.icarus.2008.12.020.

T. Rückriemen, D. Breuer, and T. Spohn. The Fe snow regime in Ganymede's core: A deep-seated dynamo below a stable snow zone. *Journal of Geophysical Research: Planets*, 120(6):1095–1118, 2015. ISSN 2169-9100. doi: 10.1002/2014JE004781.

T. Sakai, E. Ohtani, N. Hirao, and Y. Ohishi. Stability field of the hcp-structure for Fe, Fe-Ni, and Fe-Ni-Si alloys up to 3 Mbar. *Geophysical Research Letters*, 38(9), may 2011. ISSN 00948276. doi: 10.1029/2011GL047178.

C. Sanloup and Y. Fei. Closure of the FeSSi liquid miscibility gap at high pressure. *Physics of the Earth and Planetary Interiors*, 147(1):57–65, oct 2004. ISSN 0031-9201. doi: 10.1016/j.pepi.2004.06.008.

C. Sanloup, F. Guyot, P. Gillet, G. Fiquet, R. J. Hemley, M. Mezouar, and I. Martinez. Structural changes in liquid Fe at high pressures and high temperatures from Synchrotron X-ray Diffraction. *EPL (Europhysics Letters)*, 52(2):151, 2000. URL http://iopscience.iop.org/article/10.1209/epl/i2000-00417-3.

G. Schubert, M. N. Ross, D. J. Stevenson, and T. Spohn. Mercury's thermal history and the generation of its magnetic field. *Mercury*, pages 429–460, 1988.

G. Shen, P. Lazor, and S. K. Saxena. Melting of wüstite and iron up to pressures of 600 kbar. *Physics and Chemistry of Minerals*, 20(2):91–96, 1993. ISSN 1432-2021. doi: 10.1007/BF00207201.

G. Shen, H.-k. Mao, R. J. Hemley, T. S. Duffy, and M. L. Rivers. Melting and crystal structure of iron at high pressures and temperatures. *Geophysical Research Letters*, 25 (3):373–376, 1998. ISSN 1944-8007. doi: 10.1029/97GL03776.

G. Shen, V. B. Prakapenka, M. L. Rivers, and S. R. Sutton. Structure of Liquid Iron at Pressures up to 58 GPa. *Phys. Rev. Lett.*, 92(18):185701, may 2004. doi: 10.1103/PhysRevLett.92.185701.

J. Siebert, V. Malavergne, F. Guyot, R. Combes, and I. Martinez. The behaviour of sulphur in metalsilicate core segregation experiments under reducing conditions. *Physics of the Earth and Planetary Interiors*, 143144:433–443, jun 2004. ISSN 0031-9201. doi: 10.1016/j.pepi.2003.07.022.

R. W. Siegfried and S. C. Solomon. Mercury: Internal structure and thermal evolution. *Icarus*, 23(2):192–205, oct 1974. ISSN 0019-1035. doi: 10.1016/0019-1035(74)90005-0.

F. Simon and G. Glatzel. Bemerkungen zur Schmelzdruckkurve. *Zeitschrift für anorganische und allgemeine Chemie*, 178(1):309–316, 1929. ISSN 1521-3749. doi: 10.1002/zaac.19291780123.

J. C. Slater. Wave Functions in a Periodic Potential. *Phys. Rev.*, 51(10):846–851, may 1937. doi: 10.1103/PhysRev.51.846.

D. E. Smith, M. T. Zuber, R. J. Phillips, S. C. Solomon, S. A. Hauck, F. G. Lemoine, E. Mazarico, G. A. Neumann, S. J. Peale, J.-L. Margot, C. L. Johnson, M. H. Torrence, M. E. Perry, D. D. Rowlands, S. Goossens, J. W. Head, and A. H. Taylor. Gravity Field and Internal Structure of Mercury from MESSENGER. *Science*, 336(6078):214–217, apr 2012.

P. Söderlind, J. A. Moriarty, and J. M. Wills. First-principles theory of iron up to earth-core pressures: Structural, vibrational, and elastic properties. *Phys. Rev. B*, 53(21):14063–14072, jun 1996. doi: 10.1103/PhysRevB.53.14063.

S. C. Solomon. Some aspects of core formation in Mercury. *Icarus*, 28(4):509–521, aug 1976. ISSN 00191035. doi: 10.1016/0019-1035(76)90124-X.

S. C. Solomon. The relationship between crustal tectonics and internal evolution in the moon and Mercury. *Physics of the Earth and Planetary Interiors*, 15(2-3):135–145, nov 1977. ISSN 00319201. doi: 10.1016/0031-9201(77)90026-7.

S. Speziale, A. Milner, V. E. Lee, S. M. Clark, M. P. Pasternak, and R. Jeanloz. Iron spin transition in Earth's mantle. *Proceedings of the National Academy of Sciences of the United States of America*, 102(50):17918–17922, dec 2005. doi: 10.1073/pnas.0508919102.

A. Stark, J. Oberst, F. Preusker, S. J. Peale, J.-L. Margot, R. J. Phillips, G. A. Neumann, D. E. Smith, M. T. Zuber, and S. C. Solomon. First MESSENGER orbital observations of Mercury's librations. *Geophysical Research Letters*, 42(19):7881–7889, oct 2015. ISSN 00948276. doi: 10.1002/2015GL065152.

G. Steinle-Neumann, L. Stixrude, and R. E. Cohen. First-principles elastic constants for the hcp transition metals Fe, Co, and Re at high pressure. *Phys. Rev. B*, 60(2):791–799, jul 1999. doi: 10.1103/PhysRevB.60.791.

A. Stephenson. Crustal remanence and the magnetic moment of Mercury. *Earth and*

Planetary Science Letters, 28(3):454–458, jan 1976. ISSN 0012821X. doi: 10.1016/0012-821X(76)90206-5.

D. Stevenson. Mercury's magnetic field: a thermoelectric dynamo? *Earth and Planetary Science Letters*, 82(1-2):114–120, mar 1987. ISSN 0012821X. doi: 10.1016/0012-821X(87)90111-7.

D. J. Stevenson. Planetary science: Mercury's mysteries start to unfold. *Nature*, 485(7396):52–53, may 2012. ISSN 0028-0836.

D. J. Stevenson, T. Spohn, and G. Schubert. Magnetism and thermal evolution of the terrestrial planets. *Icarus*, 54(3):466–489, jun 1983. ISSN 00191035. doi: 10.1016/0019-1035(83)90241-5.

A. J. Stewart, M. W. Schmidt, W. van Westrenen, and C. Liebske. Mars: A New Core-Crystallization Regime. *Science*, 316(5829):1323–1325, jun 2007.

L. Stixrude and B. Karki. Structure and Freezing of MgSiO3 Liquid in Earth's Lower Mantle. *Science*, 310(5746):297–299, oct 2005.

L. Stixrude, R. E. Cohen, and D. J. Singh. Iron at high pressure: Linearized-augmented-plane-wave computations in the generalized-gradient approximation. *Phys. Rev. B*, 50 (9):6442–6445, sep 1994. doi: 10.1103/PhysRevB.50.6442.

L. Stixrude, N. de Koker, N. Sun, M. Mookherjee, and B. B. Karki. Thermodynamics of silicate liquids in the deep Earth. *Earth and Planetary Science Letters*, 278(34):226–232, feb 2009. ISSN 0012-821X. doi: 10.1016/j.epsl.2008.12.006.

R. G. Strom. Mercury: A post-Mariner 10 assessment. *Space Science Reviews*, 24(1):3–70, 1979. ISSN 1572-9672. doi: 10.1007/BF00221842.

R. G. Strom and A. L. Sprague. *Exploring Mercury. The iron planet*. 2003. ISBN 1852337311 (acid-free paper).

R. G. Strom, N. J. Trask, and J. E. Guest. Tectonism and volcanism on Mercury. *Journal of Geophysical Research*, 80(17):2478–2507, 1975. ISSN 0148-0227. doi: 10.1029/JB080i017p02478.

L. J. Swartzendruber. The Fe (Iron) system. *Bulletin of Alloy Phase Diagrams*, 3(2):161–165, 1982. ISSN 0197-0216. doi: 10.1007/BF02892374.

S. Tateno, K. Hirose, Y. Ohishi, and Y. Tatsumi. The Structure of Iron in Earth's Inner Core. *Science*, 330(6002):359–361, oct 2010. URL http://science.sciencemag.org/content/330/6002/359.

G. Taylor and E. Scott. *Treatise on Geochemistry*. Elsevier, 2003. ISBN 9780080437514. doi: 10.1016/B0-08-043751-6/01071-9.

B. H. Toby. EXPGUI, a graphical user interface for GSAS. *Journal of Applied Crystallography*, 34(2):210–213, 2001. ISSN 00218898. doi: 10.1107/S0021889801002242.

T. Van Hoolst and C. Jacobs. Mercury's tides and interior structure. *Journal of Geophysical Research*, 108(E11):5121, 2003. ISSN 0148-0227. doi: 10.1029/2003JE002126.

D. Vanderbilt. Soft self-consistent pseudopotentials in a generalized eigenvalue formalism. *Physical Review B*, 41(11):7892–7895, 1990. ISSN 01631829. doi: 10.1103/PhysRevB.41.7892.

R. Vilim, S. Stanley, and S. A. Hauck. Iron snow zones as a mechanism for generating Mercury's weak observed magnetic field. *Journal of Geophysical Research: Planets*, 115(E11), 2010. ISSN 2156-2202. doi: 10.1029/2009JE003528.

L. Vočadlo, J. Brodholt, D. Alfè, M. J. Gillan, and G. D. Price. Ab initio free energy calculations on the polymorphs of iron at core conditions. *Physics of the Earth and Planetary Interiors*, 117(1-4):123–137, jan 2000. ISSN 00319201. doi: 10.1016/S0031-9201(99)00092-8.

L. Vočadlo, D. Alfè, M. J. Gillan, and G. D. Price. The properties of iron under core conditions from first principles calculations. *Physics of the Earth and Planetary Interiors*, 140(1-3):101–125, 2003. ISSN 00319201. doi: 10.1016/j.pepi.2003.08.001.

R. Von Dreele and A. Larson. General structure analysis system (GSAS). Technical report, 1994.

Y. Waseda and K. Suzuki. Atomic Distribution and Magnetic Moment in Liquid Iron by

Neutron Diffraction. *physica status solidi (b)*, 39(2):669–678, 1970. ISSN 1521-3951. doi: 10.1002/pssb.19700390235.

T. R. Watters, M. S. Robinson, and A. C. Cook. Topography of lobate scarps on Mercury: New constraints on the planet's contraction. *Geology*, 26(11):991–994, nov 1998. doi: 10.1130/0091-7613(1998)026⟨0991:TOLSOM⟩2.3.CO;2.

M. Weber, S. Steeb, and W. Knoll. Magnetic neutron scattering at small momentum transfer caused by spin fluctuations in molten iron. *Physics Letters A*, 61(1):78–80, 1977. ISSN 0375-9601. doi: 10.1016/0375-9601(77)90271-7.

M. Weber, W. Knoll, and S. Steeb. Magnetic small-angle scattering from molten elements iron, cobalt, and nickel. *Journal of Applied Crystallography*, 11(5):638–641, 1978. ISSN 1600-5767. doi: 10.1107/S0021889878014107.

Q. Williams. Bottom-up versus top-down solidification of the cores of small solar system bodies: Constraints on paradoxical cores. *Earth and Planetary Science Letters*, 284(3-4): 564–569, jul 2009. ISSN 0012821X. doi: 10.1016/j.epsl.2009.05.019.

I. G. Wood, J. Ahmed, D. P. Dobson, and L. Vočadlo. High-pressure phase transitions and equations of state in NiSi. III. A new high-pressure phase of NiSi. *Journal of Applied Crystallography*, 46(1):14–24, 2013. ISSN 1600-5767. doi: 10.1107/S0021889812047085.

C. S. Yoo, N. C. Holmes, M. Ross, D. J. Webb, and C. Pike. Shock temperatures and melting of iron at Earth core conditions. *Phys. Rev. Lett.*, 70(25):3931–3934, jun 1993. doi: 10.1103/PhysRevLett.70.3931.

C. S. Yoo, J. Akella, A. J. Campbell, H. K. Mao, and R. J. Hemley. Phase Diagram of Iron by in Situ X-Ray Diffraction: Implications for Earth's Core. *Science*, 270(5241): 1473–1475, 1995. ISSN 00368075, 10959203.

M. Yseboodt and J.-L. Margot. Evolution of Mercury's obliquity. *Icarus*, 181(2):327–337, apr 2006. ISSN 00191035. doi: 10.1016/j.icarus.2005.11.024.

M. T. Zuber, O. Aharonson, J. M. Aurnou, A. F. Cheng, S. A. Hauck, M. H. Heimpel, G. A. Neumann, S. J. Peale, R. J. Phillips, D. E. Smith, S. C. Solomon, and S. Stanley. The

geophysics of mercury: Current status and anticipated insights from the MESSENGER mission. *Space Science Reviews*, 131(1-4):105–132, 2007. ISSN 00386308. doi: 10.1007/s11214-007-9265-4.